Search for ?+ pentaquark via the π⁻ρ→K⁻X reactionusing 1.92 GeV/c π beam at J-PARC

その他のタイトル	J-PARC における1.92 GeV/cπ 中間子ビームを用いたπ⁻ρ→K⁻X反応によるペンタクォーク ?+ 探索
学位授与年月日	2015-09-14
URL	http://doi.org/10.15083/00072953

学位論文

Search for Θ^+ pentaquark via the $\pi^- p \to K^- X$ reaction using 1.92 GeV/c π beam at J-PARC

（ J-PARC における 1.92 GeV/c π 中間子ビームを用いた
$\pi^- p \to K^- X$ 反応によるペンタクォーク Θ^+ 探索 ）

平成 26 年 1 月博士（理学）申請

東京大学大学院理学系研究科
物理学専攻

高橋 智則

Abstract

An experiment to search for the Θ^+ pentaquark has been carried out in the $\pi^- p \to K^- X$ reaction at the K1.8 beam line of the J-PARC 50 GeV Proton Synchrotron hadron facility as the J-PARC E19 experiment. The experiment was aiming at the confirmation of the existence or nonexistence of Θ^+ in the $\pi^- p \to K^- X$ reaction at 1.92 GeV/c, where the previous experiment KEK-PS E522 found a bump structure with the statistical significance of 2.6σ.

The data were taken from October to November in 2010 with a liquid hydrogen target exposed to 7.8×10^{10} π^- beam with incident momentum of 1.92 GeV/c. The K1.8 beam line spectrometer and the SKS systems were used to obtain high statistics data with high resolution of $\Delta p/p \sim 10^{-3}$. In order to cope with the high intensity beam of 10^7 Hz at the J-PARC, detectors and a data acquisition system were upgraded from those of the KEK-PS K6. This is the first physics experiment at the J-PARC hadron facility. The calibration of the spectrometer systems was conducted using $\Sigma^\pm$ production data which were taken via the $\pi^\pm p \to K^+ \Sigma^\pm$ reactions. The missing mass resolution and the mass accuracy of Θ^+ were estimated to be 1.7$\pm$0.3 MeV/c^2 (FWHM) and 1.7 MeV/c^2 from the $\Sigma^\pm$ data, respectively.

The differential cross section of the $\pi^- p \to K^- X$ reaction was obtained by averaging the events whose scattering angle from 2° to 18° in the laboratory frame. In the missing mass spectrum, no evidence of the Θ^+ was observed around the mass of 1530 MeV/c^2. The upper limit of the differential cross section of Θ^+ production was found to be 0.27 μb/sr at 90% confidence level in the mass range from 1.51 to 1.55 GeV/c^2.

From the present result, we obtained the upper limit of the Θ^+ decay width of 0.72 MeV (3.1 MeV) for the $J^P = 1/2^+(1/2^-)$ state at 90% confidence level with the help of a theoretical calculation based on the effective Lagrangian approach. The obtained upper bound did not exclude the DIANA's measurement of 0.36 ± 0.11 MeV for the decay width in the $K^+\mathrm{Xe} \to K^0_s p \mathrm{Xe}'$ reaction.

To compare the meson induced reaction with the photon induced one, the width was estimated from the measurement of the LEPS experiment which reported the differential cross section of 12nb/sr in the center of mass system for the $\gamma n \to K^- \Theta^+$ reaction. Using a theoretical calculation of the photoproduction, the lower limit of the decay width corresponding to the LEPS data was estimated to be 20-30 MeV ($\sim$150 MeV) for the $J^P = 1/2^+(1/2^-)$ state and $\sim$2.3 MeV ($\sim$0.3 MeV) for $J^P = 3/2^+(3/2^-)$ state. There is a conflict between the experimental results with the meson beam and the photon beam. From the claimed narrow width by the LEPS experiment, the LEPS data favors the spin 3/2 assignment, while the cross section upper limits obtained from the meson beam experiments already excluded that level of production in the case of spin 3/2 and spin 1/2 would be the only possibility left. Therefore, current theoretical models cannot explain the previous LEPS data and the results of meson-induced reactions simultaneously.

Contents

List of Figures

List of Tables

1. Introduction

1.1. Hadrons and Exotics

In the standard model, the elementary particles that form matter in nature are classified into quarks and leptons. The interaction between quarks and leptons are mediated by gauge bosons. As the underlying theory of the interaction of quarks and gluons, Quantum Chromodynamics (QCD), a local $SU(3)$ gauge theory, has been developed. An interesting feature in QCD is asymptotic freedom. The principle of asymptotic freedom states that the effective coupling constant α_s of QCD falls with increasing momentum transfer Q^2, or equivalently with decreasing distance between particles. It has been tested extensively in many experiments at high momentum transfer, or small α_s, where asymptotic freedom justifies the use of perturbative calculations. In low energy region, however, α_s is large and nonperturbative treatments are required. In this region, a variety of phenomena take place, such as color confinement and spontaneous chiral symmetry breaking. There are mainly three different approaches to investigate this region. First one is an approach from first principles, although it is numerical calculations on a discrete space-time grid. The Lattice QCD uses the original degrees of freedom, quarks and gluons, and is generally limited by the available computer power (lattice size and spacing) and discretization procedures. The second class is the chiral perturbation theory. It is called an effective theory since the microscopic QCD description of hadron interaction is left and more adequate (effective) degrees of freedoms are used, in other words, mesons and baryons are considered as the fundamental particles. In this framework, processes are described through the most general Lagrangian for meson and baryon fields compatible with QCD symmetries. This theory was first formulated for the pseudo-scalar meson interaction where the involved momenta and quark masses, instead of the coupling constant, are used for a perturbative treatment. The third approach to the low energy QCD, is the usage of QCD-inspired models capturing certain phenomenological aspects. Examples are the quark model and the chiral quark-soliton model.

The color confinement allows only color singlet states to exist. The strong interaction always binds quarks into composite particles that have no net color charge called hadrons. In the constituent quark model, ordinary mesons and baryons are color-singlet clusters of a $q\overline{q}$ and qqq, respectively. However, QCD does not prohibit the possible existence of exotic states such as glueball (gg, ggg), hybrid ($q\overline{q}g$, $qqqg$), tetraquark ($qq\overline{q}\overline{q}$), pentaquark ($qqqq\overline{q}$), dibaryon ($qqqqqq$), and so on. Therefore, the search for exotic particles beyond the normal quark model is important to understand quark confinement and the nature of the strong force.

1.2. Θ^+ baryon

The recent experimental searches for the pentaquark were triggered by a prediction of Diakonov, Petrov and Polyakov [1]. They made a prediction for the masses and widths of anti-decuplet pentaquark states

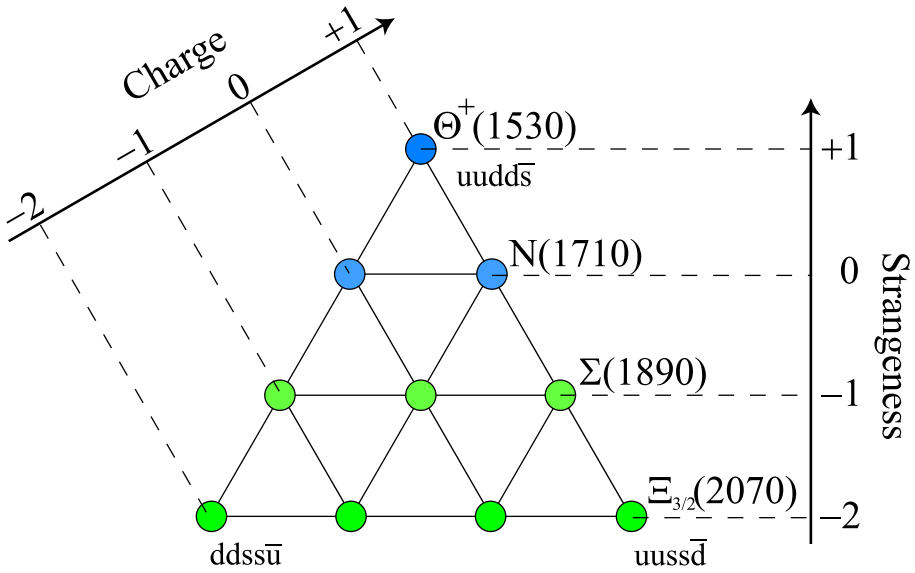

Figure 1.1.: The anti-decuplet baryons with $J^P = 1/2^+$ by chiral soliton model [1]. The anti-decuplet contains the exotic particles at the corners of this diagram ($\Theta^+, \Xi^+, \Xi^{--}$). The quark content and the predicted masses are shown.

in the chiral soliton model. In this model, all baryons are regarded as rotational excitations of the same classical meson-field. Performing the rotation in ordinary and the $SU(3)_{flavor}$ space, the quantizations show that the lowest baryon state is the octet with spin 1/2 and the next is the decuplet with spin 3/2. The masses of these states are reproduced within accuracy of 1%. The third rotational state is $\overline{\mathbf{10}}$ with spin 1/2. The scheme of the anti-decuplet is shown in Fig.1.1. The corners explicitly have quantum numbers of a $qqqq\overline{q}$ state and these states have the anti-quark with the different flavor to the others. They are manifestly exotic since a valence quark content beyond qqq is required, while the inner members of anti-decuplet are called crypto-exotic since their quantum numbers could in principle be built by coupling three quarks. In their paper [1], known nucleon resonance $N(1710)$ was assigned to a member of the anti-decuplet, which consequently led to the prediction of Θ^+ mass to be 1530 MeV/c^2. It turned out that the mass is much lighter than one would expect from the naive quark model. The decay width of the Θ^+ is calculated as Γ <15 MeV, which is unusually small for a strong decaying particle. The narrow width in [1] is explained by the cancellation of the leading order contribution by the subsequent orders. The small decay width is nowadays seen as a main characteristic of the pentaquarks.

After the first measurements in 2003, a lot of attempts were made in order to describe the Θ^+ theoretically. The diquark-model proposed by R. Jaffe and F. Wilczek [2] gives the similar properties in terms of the mass and the width. In this model, the Θ^+ and its anti-decuplet partners are described as a bound state of an anti-quark with two highly correlated spin-zero ud diquarks. Since the decay of Θ^+ requires the change of color, spin and spatial wavefunctions through the re-assignment of the quark configuration from diquark-diquark-quark configuration of $[ud]^2\overline{s}$ to the meson-baryon of K^+n, the width becomes narrow. One of the distinct features of the diquark model is that the Θ^+ is a member of the $8 + \overline{10}$ multiplet. Figures 1.2 and 1.3 show the mass hierarchy of the multiplet. There are both the lighter and the heavier N than the Θ^+, which are tentatively identified as the Roper

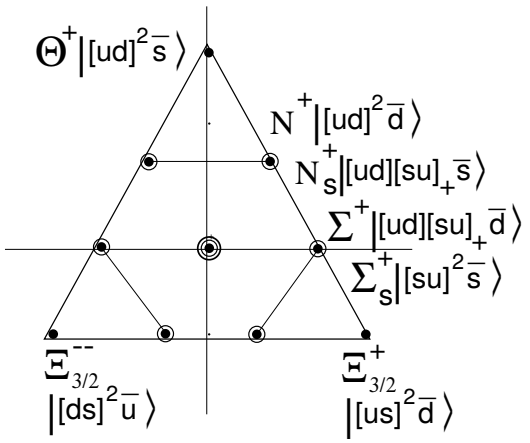

Figure 1.2.: The quark content of the $8 \oplus \overline{10}$ multiplet predicted by the diquark model [2].

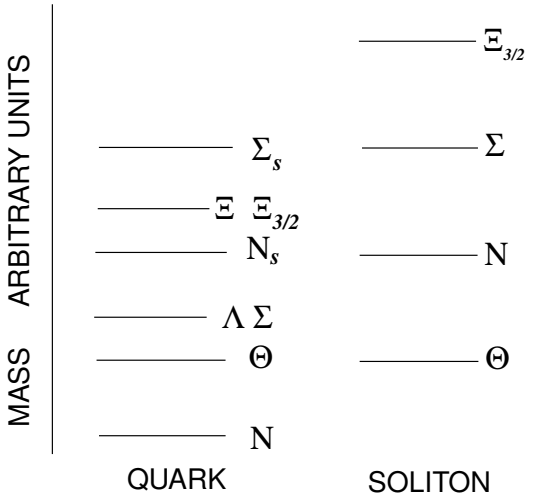

Figure 1.3.: Comparison of the relative mass of the diquark model [2] and chiral soliton model [1].

resonance $N^*(1440)$ and the $N^*(1770)$, respectively. Furthermore, the Ξ state is lighter than Σ state.

T. Kishimoto and T. Sato [3] proposed the Θ^+ as the three body bound state of $K\pi N$ with the binding energy of $\sim$30 MeV. They assume the Θ^+ has the spin-parity of $1/2^+$ and the isospin of 0 and the three particles are in an s-wave to realize the lowest energy state. The narrow width of Θ^+ can be naturally explained as follows. Since the Θ^+ decays into KN, a pion has to be absorbed into a nucleon, where the conservation of the spin-parity requires both the πN system and the kaon with respect to πN system must be excited to the p-wave simultaneously. Thus the decay can take place through the weak mixing of p-waves and the excitation can take place only when particles are within the interaction range. However, such probability is supposed to be small. They roughly estimated the width of $\sim$1 MeV by calculating the interaction range and the radius of the Θ^+. In their calculation, a strongly attractive $K\pi$ system is predicted to reproduce the Θ^+ as a bound state.

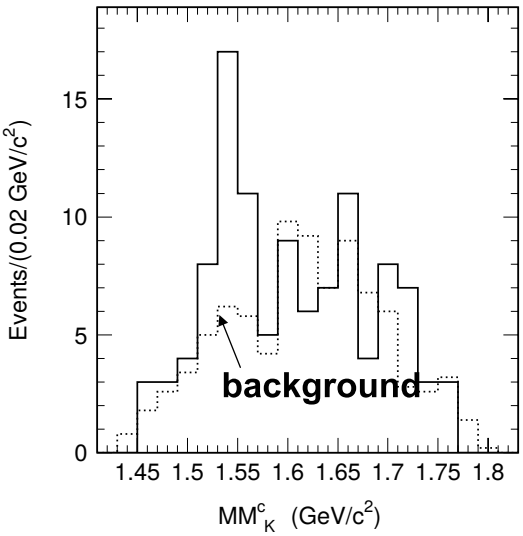

Figure 1.4.: The first evidence of the existence of the Θ^+ reported by SPring-8/LEPS collaboration [5]. The solid histogram is a missing mass spectrum of $\gamma n \to K^- X$ reaction where K^+ is also detected. The hatched histogram is the estimated background from $\gamma p \to K^- K^+ X$ reaction. The peak with a Gaussian significance of 4.6 σ was observed at 1540 $\pm$ 10 MeV/c^2. The only upper limit of the width was reported to be less than 25 MeV/c^2.

1.3. Experimental studies

The first experimental evidence for the production of the Θ^+ was reported from LEPS Collaboration in the photoproduction reaction $\gamma n \to K^+ K^- n$ on ^{12}C with a mass of $M = 1.54 \pm 0.01$ GeV/c^2 and a decay width of $\Gamma < 25$ MeV/c^2 as shown in Fig. 1.4 [5]. Independently, in the same year, the DIANA collaboration found a resonance in the reaction $K^+\mathrm{Xe} \to K^0 p \mathrm{Xe}'$ at the mass $M = 1.539 \pm 0.002$ GeV/c^2 with a width of $\Gamma \leq 9$ MeV/c^2. Further support came from the NA49 collaboration, claiming the observation of the $S = -2$ partner of the Θ^+, $\Xi^{--}(ddss\bar{u})$, at a mass of $M = 1.862 \pm 0.002$ GeV/c^2 with a width < 18 MeV/c^2. The H1 collaboration published their results for $\Theta_c(uudd\bar{c})$, of $M \approx 3.099$ GeV/c^2 and a width of ≈ 12 MeV/c^2.

At the same time, additional groups performed their searches for the Θ^+. However, a growing number of experiments could not confirm the initial findings. References on numerous other positive and null reports can be found [4]. A series of high energy experiments with high statistics did not confirm a Θ^+ signal. The high energy experiments can be divided into two main groups. First one is e^+e^- annihilation experiments (e.g. $e^+e^- \to pK^0X$). The simplest explanation of why pentaquarks have not been observed in e^+e^- experiments is given by the fact that there are no hadronic parts in the initial state. Since a pentaquark requires five quarks to be glued together by a soft fragmentation mechanism, which might be different from the conventional hadronisation mechanisms, the production of the pentaquark state should be significantly suppressed. Second one is proton-induced reactions on several nuclei. In the high energy experiments, we do not have enough knowledge of the production mechanism of hadrons, especially for the excited states. Furthermore, according to Titov *et al.* [6], the pentaquark production cross section can be suppressed with increasing energy faster than the conventional three quark hyperons, although this depends on the kinematic region. At the same time

they pointed out there will be no suppression with increasing energy in the central rapidity regions in inclusive reactions. Therefore the production at low energy is more suitable for the study of the property of Θ^+.

Among the low energy experiments, the photon induced reaction was investigated by the LEPS, SAPHIR and CLAS collaborations.

The first positive report of the CLAS collaboration at TJNAF/JLAB was announced in 2003, where they searched for the Θ^+ in the $\gamma d \to pK^-K^+n$ reaction with photon beams produced by 2.474 and 3.115 GeV incident electron beam. A signal was detected at 1.542 ± 0.005 GeV/c^2 with $\Gamma < 21$ MeV/c^2 [7]. However, since a series of dedicated experiments with CLAS had been performed, the situation became complicated. the repeat measurement with more than 30 times the integrated luminosity of the earlier one was performed in the photon energy range from 0.8 to 3.6 GeV [8]. Figure 1.5(b) shows the comparison of the original CLAS data (points) and the repeat measurement, which is rescaled down by a factor of 5.92 (solid histogram). The repeat measurement turned out with a null result and they found the upper limit (95% C.L.) for the total cross section of Θ^+ production ranges from 0.15 to 3 nb, depending on its angular distribution, for a mass of 1.54 GeV/c^2.

Recently, a new experiment was done at LEPS on a deuteron target with more statistics and the photon energy range of 2.0-2.4 GeV was analyzed [9]. Figure 1.5 shows the Fermi-motion-corrected nK^+ invariant mass distribution. A clear peak was observed at $1524 \pm 2 \pm 3$ MeV/c^2 with the statistical significance of 5.1 σ. The cross section was estimated to be 12 ± 2 nb/sr in the center-of-mass frame by assuming the isotropic production.

SAPHIR collaboration at ELSA observed a peak in the nK^+ invariant distribution using the $\gamma p \to nK^+K^0_s$ reaction [10]. The incident photon energies from 0.87 to 2.63 GeV were used for the data described in [10]. They applied a cut $\cos\theta_{K^0_s} > 0.5$ to reduce the $\Lambda(1520)$ background and obtained a narrow peak in nK^+ spectrum, which is shown in Fig. 1.6(a). The peak position was at $1540 \pm 4 \pm 2$ MeV with a statistical significance of 4.8σ.

The same reaction was measured by the CLAS collaboration with the photon energy range of 1.6 - 3.8 GeV [11, 12]. They accumulated more than 10 times higher statistics than that of SAPHIR. For better comparison, the kinematic cuts used in SAPHIR were applied. The photon energy was limited to be below 2.6 GeV and an angular selection of $\cos\theta_{K^0_s} > 0.5$ was applied. The nK^+ invariant mass spectrum is shown in 1.6(b) with two different bin sizes reflecting the CLAS and the SAPHIR resolutions [12]. There is no evidence of the Θ^+.

The status of the Θ^+ is rather uncertain and the situation is complicated by the fact that there are no data sets from independent groups with exactly overlapping conditions. For example, the LEPS setup covers the acceptance in the forward region, while the CLAS detector does not. Nam *et al.* [13] proposed the theoretical explanation that the Θ^+ has spin 3/2, which gives the large cross section at forward kaon angle in the $\gamma N \to \overline{K}\Theta^+$ reaction.

Note that there are still several early pentaquark searches that have positive results with high statistical significance. The DIANA collaborations confirm their earlier claims. The pK^0_s invariant mass spectrum in [14] is shown in Fig. 1.7. Belle collaboration reported a negative evidence in the same production reaction of DIANA using secondary kaons [34]. The upper limit of the decay width is estimated to be 0.64 MeV, which is slightly higher than the DIANA result. CLAS also reported the positive result on $\gamma p \to \pi^+K^+K^-n$ [15]. The nK^+ invariant mass spectrum is presented in Fig.

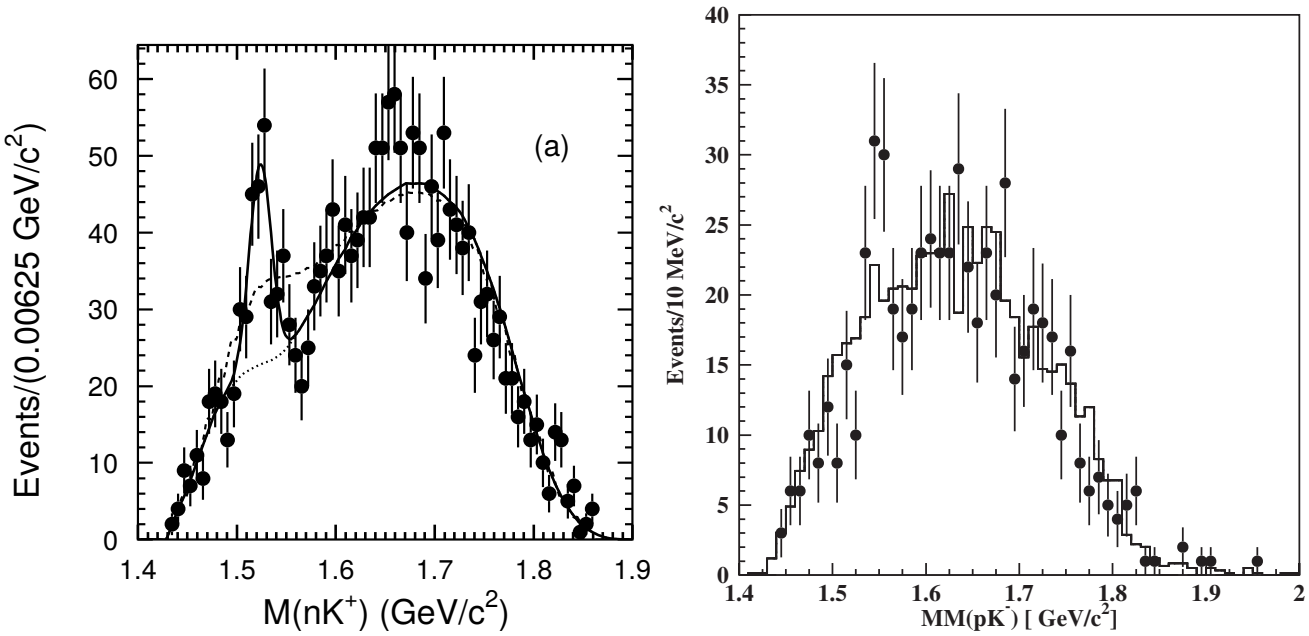

(a) For the LEPS data [9]. (b) For the CLAS data [8].

Figure 1.5.: The nK^+ invariant mass spectrum of the $\gamma d \to K^+K^-X$ reaction reported by LEPS in 2009 (a) and of the $\gamma d \to pK^+K^-n$ reaction reported by CLAS (b). The points and the solid histogram in (b) are the original data [7] and the high statistics data scaled down by a factor of 5.92, respectively.

1.8(a). Figure 1.8(b) shows the nK^+K^- invariant mass spectrum. A peak structure suggests that Θ^+ may be produced through the decay of an intermediate N^* resonance.

The other positive and negative results are listed in Tables 1.1 and 1.2.

1.4. Θ^+ production with meson beams

Hadron-induced production has an advantage of relatively large cross section, because all the vertices are described by the strong interaction and less ambiguous while there is uncertainty in the photoproduction reactions from the anomalous magnetic moment of Θ^+. On the other hand, in general, the beam quality is not very good, especially for the low energy region. In addition, there are non-resonant backgrounds with large cross sections. However, since the confirmation by various reactions is crucial to establish a new state, it is important to study the meson-induced reactions.

1.4.1. Theoretical calculation for the meson induced reactions

Figure 1.9 shows the tree level diagram of the Θ^+ production via the $\pi^-p \to K^-\Theta^+$ and the $K^+p \to \pi^+\Theta^+$, where Θ^+ is assumed as isosinglet. The involved coupling constants are $g_{\pi NN}$, $g_{K^*K\pi}$, $g_{KN\Theta}$ and $g_{K^*N\Theta}$. The latter two are not determined experimentally. Y. Oh *et* al. [47] calculated the cross section for the Θ^+ with spin-parity of $1/2^+$ case, using $g_{KN\Theta} = 2.2$, which corresponds to 5 MeV/c^2 width of the Θ^+, and several values were examined for $g_{K^*N\Theta}$. In addition, form factor which reflects the finite sizes of the hadrons is introduced. In their calculation, two types of form factors were used.

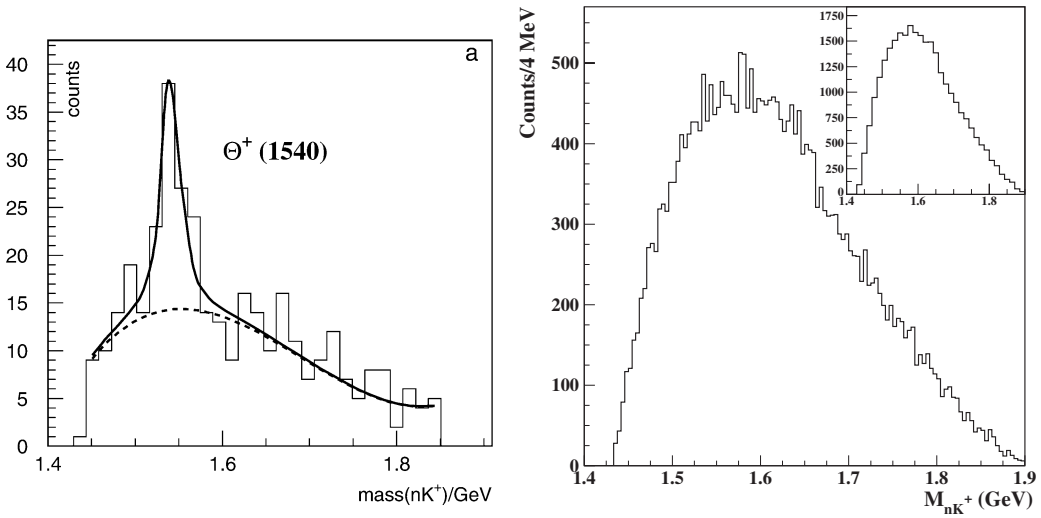

(a) For the SAPHIR data [10]. (b) For the CLAS data [12].

Figure 1.6.: The nK^+ invariant mass spectra of the $\gamma p \to K^0_s K^+ n$ reaction by SAPHIR and CLAS. The latter is plotted with the same analysis cut as that of SAPHIR. The inset shows the same spectrum with the binning used by SAPHIR.

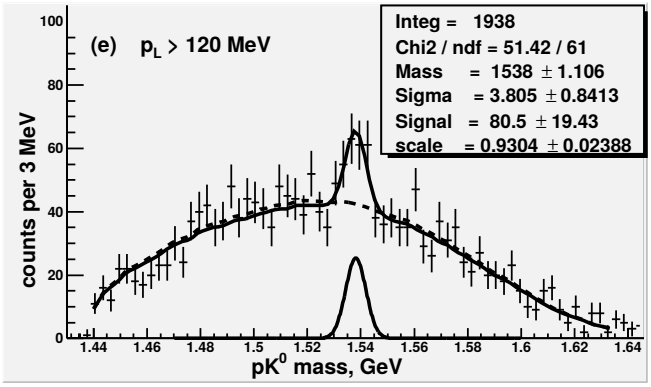

Figure 1.7.: The pK^0_s invariant mass spectrum of the $K^+\mathrm{Xe} \to K^0_s pX$ reaction reported by DIANA in 2013 [14].

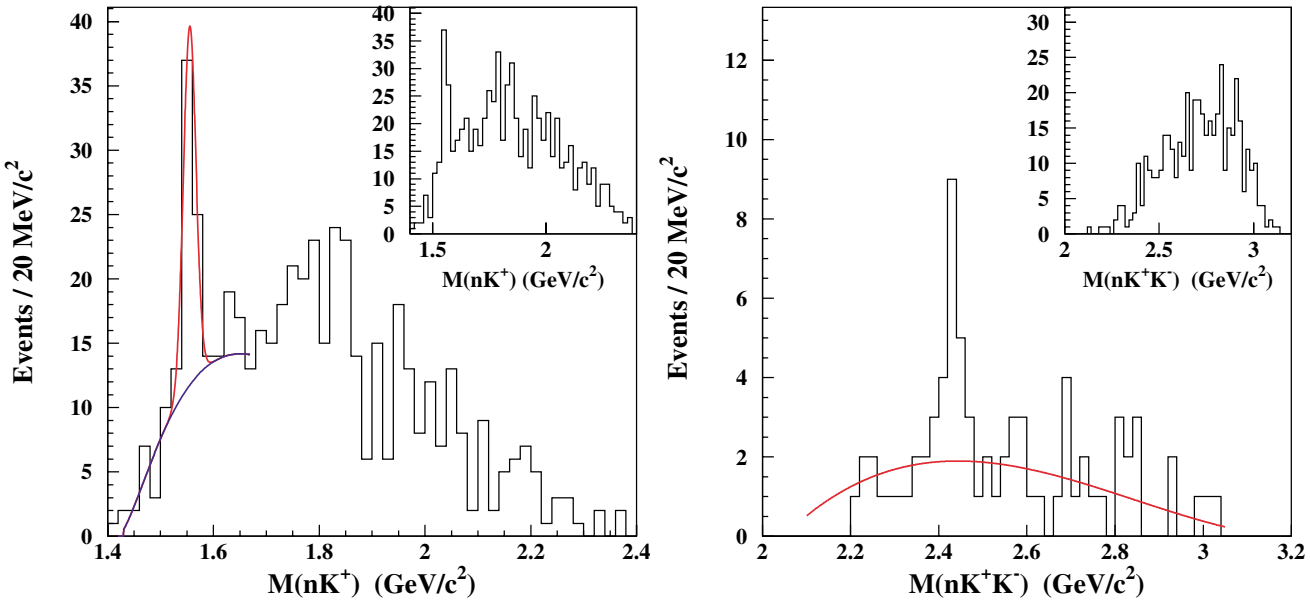

(a) The nK^+ invariant mass spectrum.

(b) The nK^+K^- invariant mass spectrum.

Figure 1.8.: The nK^+ and nK^+K^- invariant mass spectra measured by CLAS in the $\gamma p \to \pi^+ K^- K^+ n$ reaction [15].

Table 1.1.: Summary of the experiments with positive result for the Θ^+ baryon.

Group	Reaction	Mass [MeV/c^2]	Width [MeV/c^2]	σ	Reference
LEPS	$\gamma^{12}\mathrm{C} \to K^+K^-X$	1540 ± 10	< 25	4.6	[5]
LEPS	$\gamma d \to K^+K^-X$	1524 ± 2	< 25	5.1	[9]
DIANA	$K^+\mathrm{Xe} \to K^0_s pX$	1539 ± 2	< 9	4.4	[16]
DIANA	$K^+\mathrm{Xe} \to K^0_s pX$	1537 ± 2	0.36 ± 0.11	7.3	[17]
DIANA	$K^+\mathrm{Xe} \to K^0_s pX$	1538 ± 2	0.39 ± 0.10	8	[18]
DIANA	$K^+\mathrm{Xe} \to K^0_s pX$	1538 ± 2	0.36 ± 0.11	6.3	[14]
CLAS(d)	$\gamma d \to K^+K^-pn$	1542 ± 5	< 21	5.2	[7]
CLAS(p)	$\gamma p \to \pi^+K^-K^+n$	1555 ± 10	< 26	7.8	[15]
SAPHIR	$\gamma p \to K^0_s K^+ n$	1540 ± 6	< 25	4.8	[10]
ITEP	$\nu A \to K^0_s pX$	1533 ± 5	< 20	6.7	[19]
JINR	$p\ \mathrm{C_3H_8} \to K^0_s pX$	1540 ± 8	9.2	5.5	[20]
HERMES	$e^+d \to K^0_s pX$	1528 ± 3	12 ± 9	4.2	[21]
COSY-TOF	$pp \to K^0_s p\Sigma^+$	1530 ± 5	< 18	4.7	[22]
ZEUS	$e^+p \to e^+K^0_s pX$	1522 ± 3	8 ± 4	4.6	[23]
NOMAD	$\nu A \to K^0_s pX$	1529 ± 3	2-3	4.3	[24]
SVD	$pA \to K^0_s pX$	1526 ± 5	< 24	5.6	[25]
SVD	$pA \to K^0_s pX$	1523 ± 5	< 14	8.0	[26]

Table 1.2.: Summary of the experiments with negative result for the Θ^+ baryon.

Experiments	Reaction	Limit	Reference
BES	$e^+e^- \to J/\Psi \to \overline{\Theta}\Theta$	1.1×10^{-5} B.R. (90% C.L.)	[27]
BES	$e^+e^- \to \Psi(2S) \to \overline{\Theta}\Theta$	8.4×10^{-6} B.R. (90% C.L.)	
ALEPH	$e^+e^- \to Z \to pK^0_sX$	6.2×10^{-4} B.R. (95% C.L.)	[28]
DELPHI	$e^+e^- \to Z \to pK^0_sX$	$< 0.67 \times \Lambda^*$ (95% C.L.)	[29]
L3	$e^+e^- \to e^+e^-pK^0_sX \;\; (\gamma\gamma \to \Theta^+X)$	< 1.8 nb (95% C.L.)	[30]
BaBar	$e^+e^- \to \Upsilon(4S) \to pK^0_sX$	1.0×10^{-4} B.R. (90% C.L.)	[31]
BaBar	$e^-\text{Be} \to pK^0_sX$	not given	[32]
Belle	$e^+e^- \to B^0\overline{B^0} \to p\overline{p}K^0_sX$	$< 2.3 \times 10^{-7}$ B.R. (90% C.L.)	[33]
Belle	$K^+n \to K^0_spX$	$\Gamma < 0.64$ MeV (90% C.L.)	[34]
CDF	$p\overline{p} \to K^0_spX$	$< 0.03 \times \Lambda^*$ (90% C.L.)	[35]
SPHINX	$p\text{C} \to K^0_spX$	$< 0.1 \times \Lambda^*$ (90% C.L.)	[36]
HERA-B	$pA \to K^0_spX$	$< 2.7\% \times \Lambda^*$ (90% C.L.)	[37]
HyperCP	$p\text{Cu} \to K^0_spX$	$< 0.3\% \times K^0_sp$	[38]
FOCUS	$\gamma\text{BeO} \to K^0_spX$	$< 0.02 \times \Sigma^*$ (95% C.L.)	[39]
PHENIX	$d\text{Au} \to K^-\overline{n}X$	not given	[40]
WA89	$\Sigma^+A \to K^0_spX$	$< 1.8\mu$b/A (99% C.L.)	[41]
WA89	$\Sigma^-A \to K^0_spX$	$< 16\mu$b/A (95% C.L.)	[42]
CLAS	$\gamma p \to K^0_sK^+n$	< 0.8 nb (95% C.L.)	[11]
CLAS	$\gamma p \to K^0K^+n, K^0K^0_sp$(combined)	< 0.7 nb (95% C.L.)	[12]
CLAS	$\gamma d \to K^-pK^+n$	< 0.15 - 3 nb (95% C.L.)	[8]
CLAS	$\gamma d \to K^+n\Lambda$	< 5 - 25 nb (95% C.L.)	[43]
COSY-TOF	$pp \to K^0_sp\Sigma^+$	< 0.15 μb (95% C.L.)	[44]
NOMAD	$\nu\text{A} \to K^0_spX$	$< 2.13 \times 10^{-3}$ νCC (95% C.L.)	[45]
LASS	$K^+p \to K^+n\pi^+$	not given	[46]

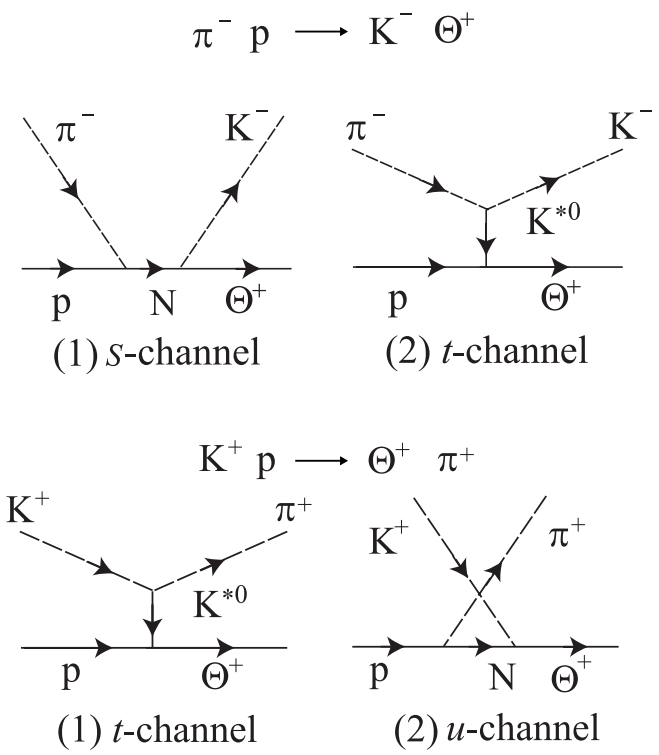

Figure 1.9.: Tree level diagrams for the $\pi^- p \to K^- \Theta^+$ reaction (Top) and the $K^+ p \to \pi^+ \Theta^+$ reaction (Bottom).

One is the static form factor F_s, the three-momentum monopole type, which is a function of $\sqrt{s}$ only,

$$F_s = \frac{\Lambda_s^2}{\Lambda_s^2 + |\mathbf{q}|^2} \tag{1.1}$$

where Λ_s is the cut off parameter and $\mathbf{q}$ is the three-momentum of the initial state particles in the center-of-mass frame. The other is the covariant form factor F_c

$$F_c = \frac{\Lambda_c^4}{\Lambda_c^4 + (x - M_{ex}^2)^2} \tag{1.2}$$

where x and and M_{ex} are the momentum squared and the mass of the exchanged particle. Figure 1.10 shows their results of the $\pi^- p \to K^- \Theta^+$ reaction. Due to the interference between the amplitudes of s-channel and t-channel, the cross section of the $\pi^- p \to K^- \Theta^+$ reaction is quite dependent on the magnitude of $g_{K^* N\Theta}$. In the calculation of the cross section of the $K^+ p \to \pi^+ \Theta^+$ reaction, $g_{NK\Theta} = 1.0$ was employed and three values of $g_{K^* N\Theta} = 0, \pm g_{KN\Theta}$ were considered [48]. Figure 1.11 shows the differential cross section for $K^+ p \to \pi^+ \Theta^+$. K^* exchange plays an important role in angular dependence. With K^* exchange, the differential cross section has a peak at forward and backward angle while there is only a backward peak with $g_{K^* N\Theta} = 0$. The small coupling to $K^* N$ is favored by dedicated experiments. One is the CLAS experiment to search for Θ^+ in the $\gamma p \to \overline{K}^0 K^+ n$ reaction, and other experiment was performed at KEK which is described in the next subsection.

The decay width of Θ^+ is related to the coupling constant $g_{KN\Theta}$. Without K^* exchange, the differential cross section is simply proportional to the width of Θ^+ as follows:

$$\frac{d\sigma}{d\Omega} \propto g_{KN\Theta}^2 \propto \Gamma_{\Theta^+ \to K^+ n + K^0 p} \tag{1.3}$$

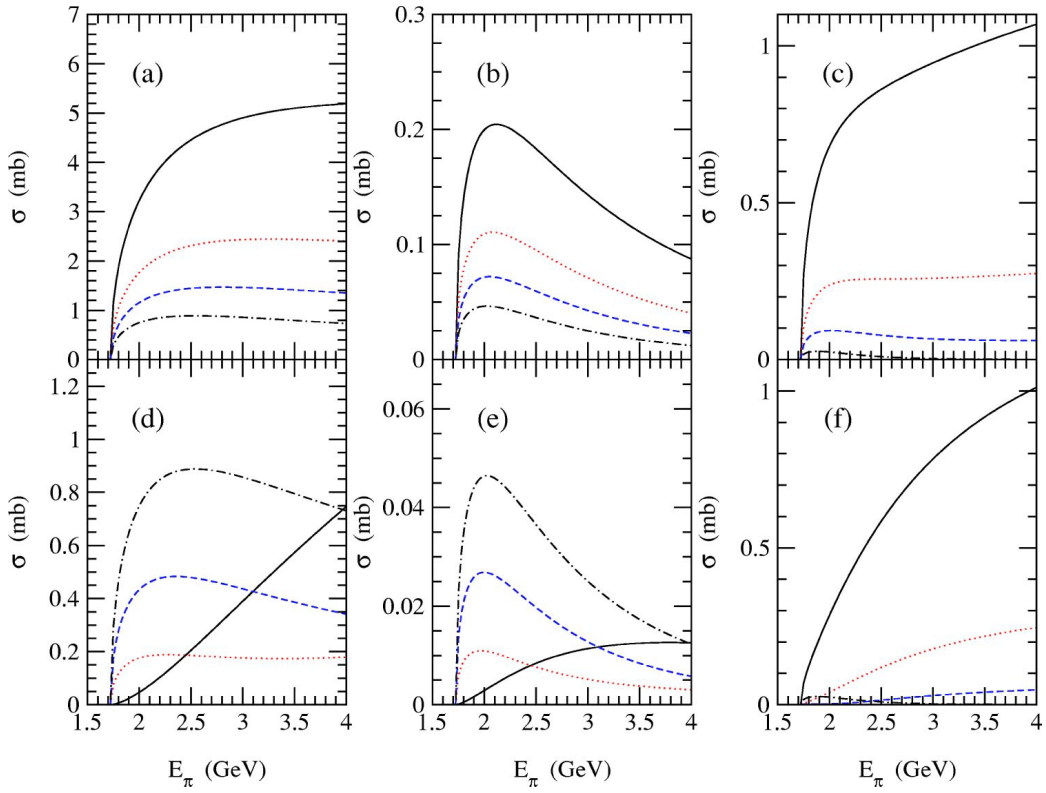

Figure 1.10.: Calculated differential cross sections for the $\pi^- p \to K^- \Theta^+$ reaction by Y. Oh *et* al [47]. (a,d): without form factors. (b,e) with the form factors of Eq.1.1 with $\Lambda = 0.5$ GeV. (c,f) with the form factors of Eq.1.2 with $\Lambda = 1.8$ GeV. In (a,b,c), the solid, dotted dashed, and dot-dashed lines are with $g_{K^*N\Theta} = -2.2, -1.1, -0.5$, and 0.0, respectively. In (d,e,f), the solid, dotted, dashed, and dot-dashed lines are with $g_{K^*N\Theta} = 2.2, 1.1, 0.5$, and 0.0, respectively.

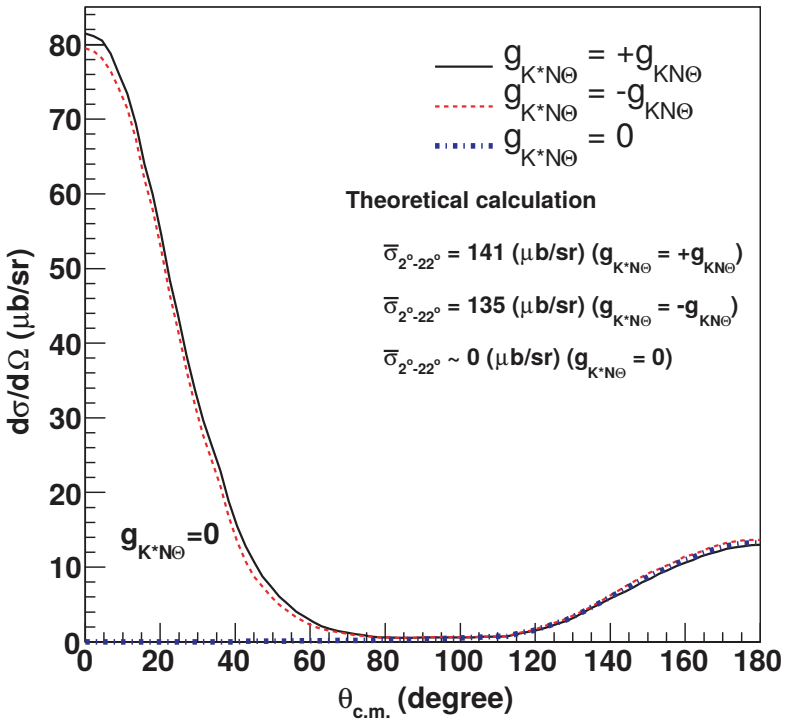

Figure 1.11.: Calculated cross sections for the $K^+p \to \pi^+\Theta^+$ reaction by Y. Oh *et* al [48].

Thus, the measurement of the production cross section and/or the decay width is important to understand the production mechanism of Θ^+.

1.4.2. KEK-PS E522 and KEK-PS E559

KEK-PS E522

The KEK-PS E522 [49] conducted the search for Θ^+ via the $\pi^-p \to K^-X$ reaction at the K2 beam line of the KEK 12 GeV Proton Synchrotron. A polyethylene target ($(CH2)_n$) was exposed to the π^- beam with the momentum of 1.87 GeV/c and 1.92 GeV/c. While any structure corresponding to the Θ^+ was not observed for 1.87 GeV/c, a hint of a bump whose width was consistent with the experimental resolution was found at the mass of $M = 1530.6^{+2.2}_{-1.9}(\text{stat.})^{+1.9}_{-1.3}(\text{syst.})$ MeV/c^2 as shown in Fig. 1.12. However the statistical significance of the bump was only 2.5 $\sim$ 2.7σ which was not enough to claim the evidence of the Θ^+. Therefore, they derived the upper limit of the production cross sections averaged over 0^o to 20^o in the laboratory frame to be 1.6 μb/sr and 2.9 μb/sr at the 90 % confidence level at the beam momentum of 1.87 and 1.92 GeV/c, respectively.

The obtained upper limits are quite smaller than the theoretical calculations and give a strong constraint to the unknown parameters such as the coupling constant $g_{K^*N\Theta}$ used in the calculations.

KEK-PS E559

The existence of Θ^+ via the $K^+p \to \pi^+\Theta^+$ reaction was examined in the KEK-PS E559 [50] at the KEK K6 beam line. K^+ beam with the momentum of 1.2 GeV/c was irradiated on a liquid hydrogen target. In the missing mass spectrum of the reaction, no peak structure was observed. A 90 % confidence

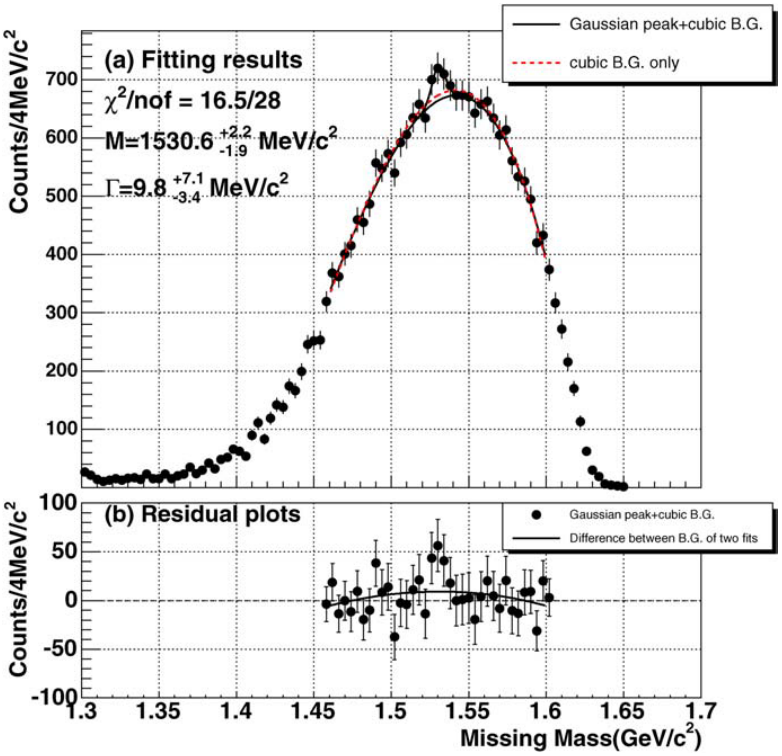

Figure 1.12.: The missing mass spectrum of the $\pi^- p \to K^- \Theta^+$ reaction at the beam momentum of 1.92 GeV/c obtained in the KEK-E522. [49].

level upper limit of 3.5 μb/sr was obtained for the differential cross section averaged over 2^o to 22^o in the laboratory frame as shown in Fig. 1.13. From the small differential cross section at forward angles, the t-channel process, where K^{0*} is exchanged, is excluded. However, the acceptance of E559 is not sensitive to the backward angles, therefore there is a possibility that the Θ^+ is produced via the u-channel process. It should be noted that the CLAS measurement in the $\gamma p \to \overline{K}^0 \Theta^+$ reaction [11,12] suggests that the contribution to the K^* exchange process is highly suppressed.

1.4.3. Present experiment: J-PARC E19

In order to establish the Θ^+ state, it is necessary to confirm the existence in experiments with higher statistics. The present experiment, J-PARC E19, was designed to confirm the existence of Θ^+ via the $\pi^- p \to K^- X$ reaction at the J-PARC 50 GeV Proton Synchrotron with better mass resolution and higher statistics than the previous experiment, KEK-PS E522. Since the peak structure was found only at the beam momentum of 1.92 GeV/c in E522, the study of the energy dependence of the cross section was planned with three beam momenta of 1.87, 1.92, and 1.97 GeV/c. The experiment with the beam momentum of 1.92 GeV/c was conducted from October to November in 2010 as the first run of J-PARC E19. Compared to E522, we took the data 10 times more statistics using the spectrometers with 10 times higher momentum resolution realized with K1.8 beam lien spectrometer and the SKS spectrometer.

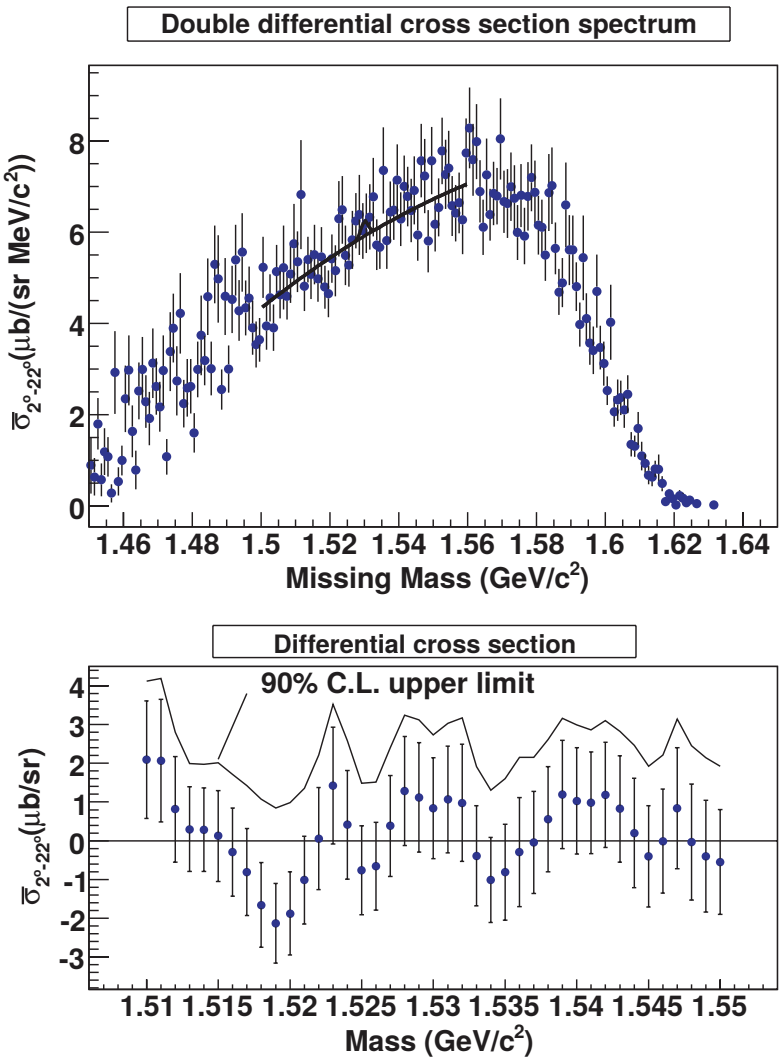

Figure 1.13.: The missing mass spectrum of the $K^+p \to \pi^+\Theta^+$ reaction at the beam momentum of 1.2 GeV/c obtained in the KEK-E559 [50].

1.4.4. Thesis outline

In this thesis, we report the study of the production cross section and the width of Θ^+ through the missing mass spectroscopy via the $\pi^- p \to K^- X$ reaction with the beam momentum of 1.92 GeV/c. The experimental apparatus is described in Chap.2. The procedure of data analysis is described in Chap.3. The experimental results and discussion are given in Chap.4. Finally, a conclusion is given in Chap.5.

1.4.5. Major contributions

The author studied the production of Θ^+ pentaquark in the $\pi^- p \to K^- X$ reaction at J-PARC. The author participated in the present experiment from the construction stage and contributed to both the hardware and software work. The author developed the multi-wire proportional chambers (MWPC) for beam tracking and the data acquisition system for the J-PARC K1.8 experiment. In the data analysis, the author carried out the beam and scattered particle track reconstruction and measurements of the missing mass of the $p(\pi, K)$ reaction and the production cross section of Θ^+. Since the author improved the beam tracking efficiency and evaluations of the acceptance of the spectrometer and the missing mass resolution, more reliable results were obtained.

2. Experimental apparatus

2.1. Overview

The J-PARC E19 experiment was performed at the K1.8 beam line in the hadron hall of the 50 GeV Proton Synchrotron at J-PARC (Japan Proton Accelerator Research Complex) to search for the pentaquark Θ^+ in the $\pi^- p \to K^- X$ reaction.[1] The K1.8 beam line was constructed for experimental studies of strangeness nuclear physics using high intensity hadron beams (pions, kaons or protons). Two spectrometer systems with a good momentum resolution, the K1.8 beam line spectrometer and the Superconducting Kaon Spectrometer (SKS), were built to analyze incoming particles and outgoing ones, respectively.

In the present experiment, the intensity of π^- beam is 10^6 per spill, spill cycle is typically 2 seconds with 6 seconds repetition. The π^- beam with the momentum of 1.92 GeV/c were delivered to a liquid hydrogen target to search for Θ^+ by missing mass spectroscopy in the $\pi^- p \to K^- X$ reaction. The Θ^+ was searched for with the missing mass technique by using beamline and SKS spectrometers. The first physics run was performed in October and November 2010. The comparison of the experimental conditions of KEK-E522 to that of J-PARC E19 are listed in Table 2.1.

2.2. Accelerator and beam line

J-PARC (Japan Proton Accelerator Research Complex) is an international research facility aiming at 1 MW class power, by the joint project of JAEA and KEK. Figure 2.1 shows a schematic view of J-PARC. The proton accelerator consists of three stages, a 400 MeV (currently 181 MeV) LINAC, a 3 GeV Rapid Cycling Synchrotron (RCS) and a 50 GeV (30 GeV in phase-1) Main Ring (MR).

[1] It is also important to note that the present experiment is the first physics experiment at the K1.8 beam line.

Table 2.1.: The experimental conditions of the KEK-E522 and that of J-PARC E19 1st RUN. N_{Beam} is the number of π^- beam delivered to the target.

	E522	E19 (1st RUN)
momentum [GeV/c]	1.87, 1.92	1.92
mass resolution [MeV/c^2]	13.6	<2.0
K^- spectrometer	KURAMA	SKS
target material	polyethylene ($(CH_2)_n$)	liquid hydrogen (H_2)
target thickness [g/cm^2]	10 (1.4 for H_2)	0.85
N_{Beam}	7.4×10^9	7.8×10^{10}

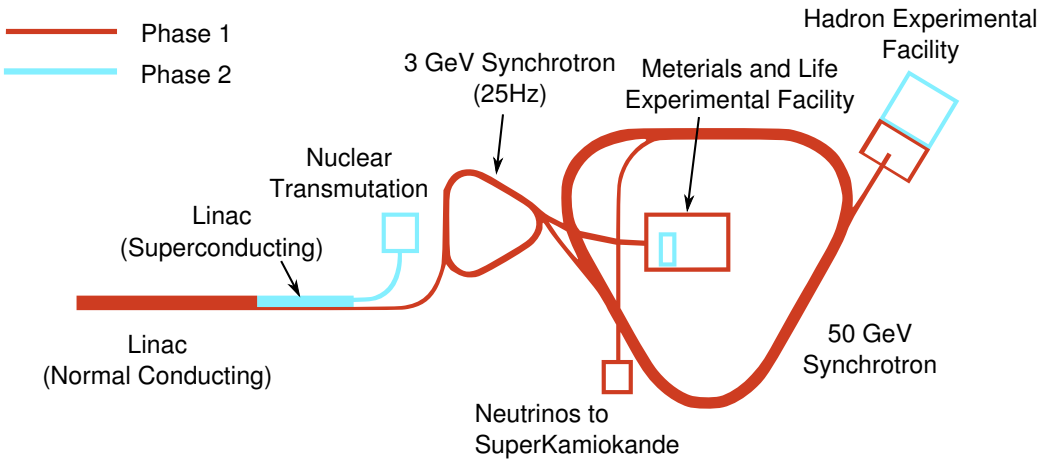

Figure 2.1.: Schematic view of J-PARC [51].

The accelerated beam is applied to the several experimental facilities that make use of the variety of secondary-particle beams produced from the collisions between the high intensity proton beams and target materials.

A cross-sectional view of the present J-PARC ion source is shown in Fig. 2.2. A volume production type ion source is used to produce H^- ions. The source plasma is produced by an arc discharge using the LaB_6 filament having a cylindrical double-spiral structure. (Fig. 2.3)

The H^- extracted from the plasma chamber is followed by the LINAC, which has about 50 cavity modules to accelerate the beam up to 181 MeV. Table 2.2 and Fig. 2.4 are basic parameters and a layout of the LINAC, respectively. The Radio-Frequency Quadrupole (RFQ) LINAC accelerates the 50 keV beams from the ion source up to 3 MeV. The Medium Energy Beam Transport (MEBT) is comprised of 8 quadrupole-magnets and two bunchers to match the RFQ beams to the following Drift Tube LINAC (DTL). In addition, the RF deflector (RF chopper) is installed in the MEBT to chops the 500 μs long macropulse beam into the medium-bunches at the RCS revolution frequency of 1 MHz. The three DTL cavities accelerate the beams from 3 MeV up to 50 MeV. The $30 + 2$ Separated-type DTL (SDTL) cavities accelerate the beams up to 181 MeV. The RF frequency is 324 MHz in this low β section. In the present phase, the LINAC provides 181 MeV beam to the RCS. In this case, the last 2 cavities of the SDTL are applied as the debunchers.

For the injection to the RCS, the H^- ions are charge exchanged using the Hybrid type thick Boron-doped Carbon (HBC) stripping foil. The H^- beam from the LINAC is stripped directly to H^+, while the unstripped H^- and H^0 beams are converted to protons by a couple of foils placed at downstream and then transported to the beam dump. Table 2.3 and Fig. 2.5 are basic parameter and a layout of the RCS. In normal operation mode, over 90 % of the protons accelerated in the RCS are directed to the muon and neutron production targets in the Materials and Life Science Experimental Facility (MLF). The remaining protons are transported to the MR for further acceleration before being extracted.

The MR has three-folded symmetry and its circumference is 1567.5 m. Each arc section and straight section is 406.4 m long and 116.1 m long, respectively. The three straight sections are dedicated to "injection and beam collimators", "slow extraction", and "rf cavities and fast extraction". A layout of the MR is shown in Fig. 2.6. Main parameters of the MR is summarized in Table 2.4

The slow extraction (SX) port directs the primary protons to the Hadron Experimental Facility

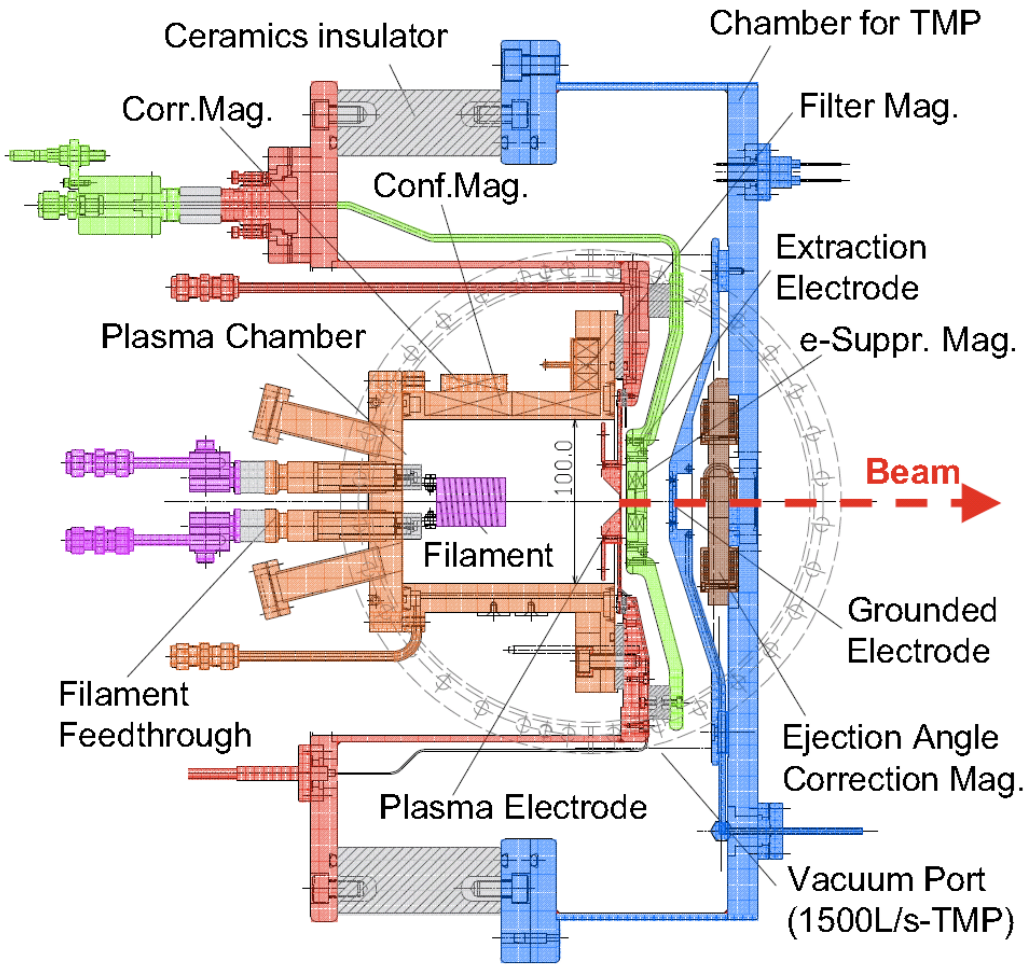

Figure 2.2.: Cross sectional view of the J-PARC ion source [52].

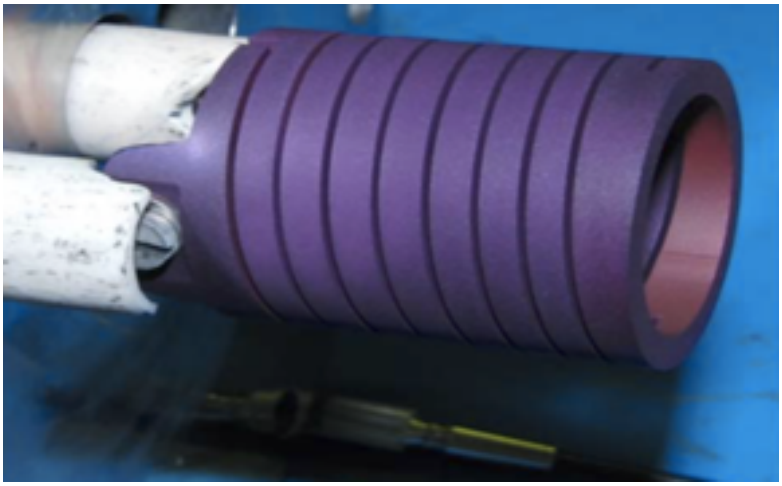

Figure 2.3.: Photograph of the LaB_6 filament for the ion source [52].

Table 2.2.: Basic parameters of the J-PARC LINAC.

acc. ions row	H^- (negative hydrogen)
output energy	400 MeV (present: 181 MeV)
peak current	50 mA (present: 30 mA max)
repetition	25 Hz (+ 25 Hz for ADS)
beam pulse width	500 μs (macro pulse)
RF pulse width	650 μs (with build up time)
RF frequency	324 MHz ($\sim$ 191 MeV)
	972 MHz ($\sim$ 400 MeV)
LINAC length	300 m
number of klystrons	45

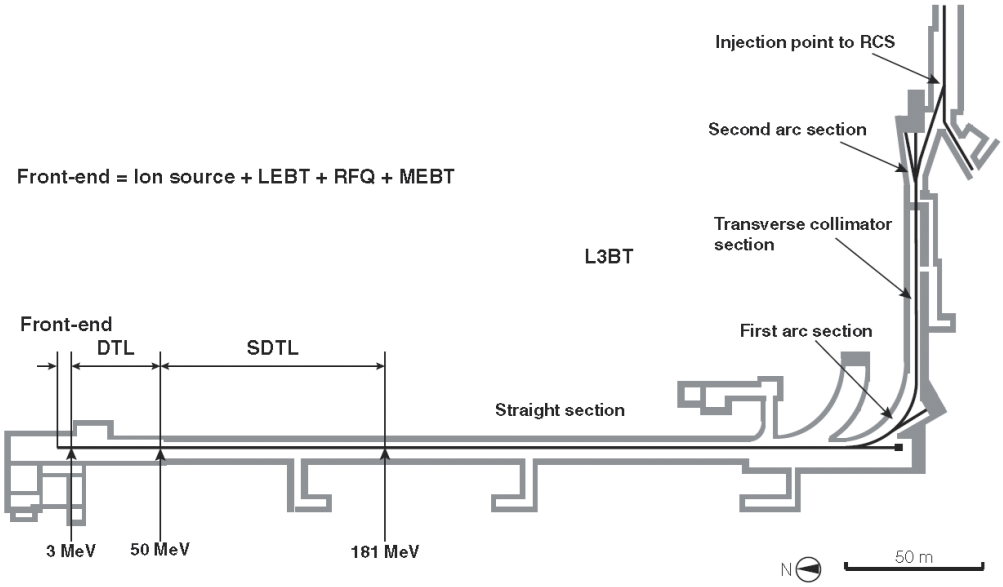

Figure 2.4.: Layout of LINAC [53].

Table 2.3.: Basic parameters of the J-PARC RCS.

circumference	348.3 m
injection energy	181 MeV (phase I, day=1)
	400 MeV (phase I, 2nd stage)
extraction energy	3 GeV
beam power	0.6 MW (181 MeV LINAC)
	1.0 MW (400 MeV LINAC)
number of protons	5.0×10^{13} ppp (181 MeV LINAC)
	8.3×10^{13} ppp (400 MeV LINAC)
repetition	25 Hz
harmonic	2
nominal tune	(6.72, 6.35)
acceptance	480π mm·mrad
painting area	214π mm·mrad (max)

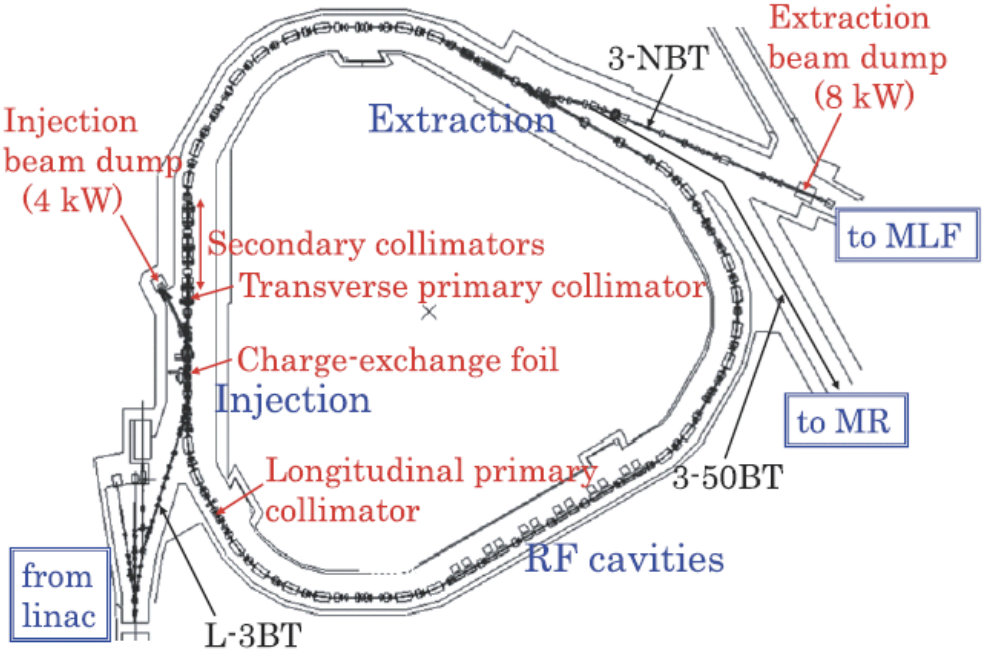

Figure 2.5.: Layout of 3 GeV RCS [54].

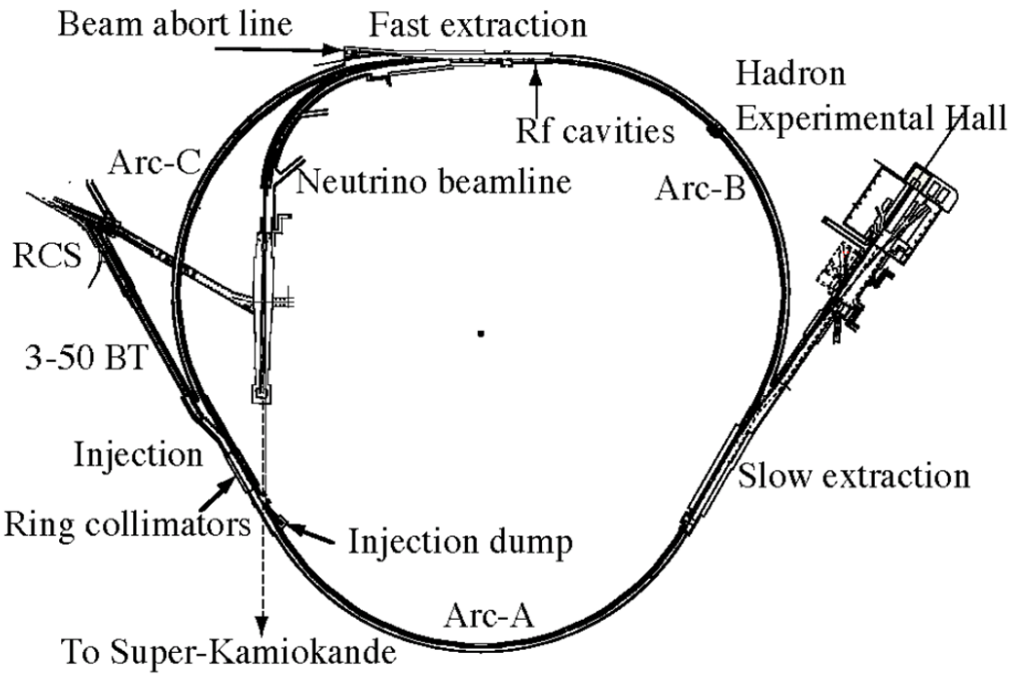

Figure 2.6.: Schematic view of 50 GeV Main Ring [55].

Table 2.4.: Main parameters of the MR.

circumference	1567.5 m
injection energy	3 GeV
extraction energy	30 GeV (phase-I)
	50 GeV (phase-II)
beam power	0.67 MW (phase-I)
	0.75 MW (phase-II)
number of protons	3.3×10^{14} ppp (phase-II)
repetition	$\sim$ 0.3 Hz
harmonic	9 (normal)
bunch	8 (normal)
nominal tune	(22.4, 20.8)
acceptance	81 π mm·mrad

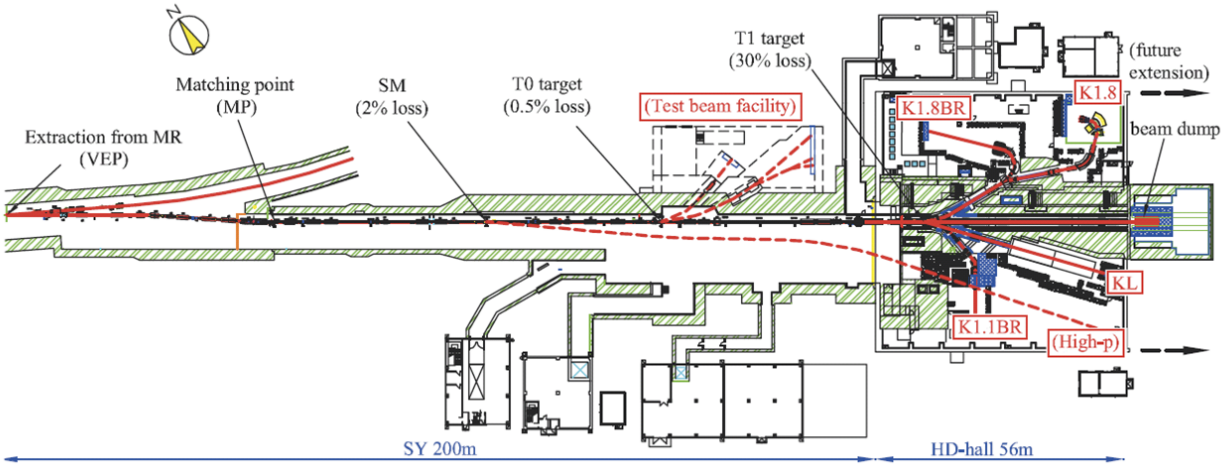

Figure 2.7.: Schematic layout of hadron experimental facility [56]. Additional beam lines at future extension are shown by dashed lines.

(HD-hall) where a variety of nuclear physics experiments are carried out using hadron (kaons, pions etc.) beams. The typical beam intensity was 3×10^{12} per spill at the moment. The repetition period is 6 seconds and the flat top of the spill was about 2.2 seconds.

2.2.1. Hadron experimental facility and K1.8 beam line

The layout of the HD-hall is shown in Fig. 2.7. The extracted primary beam is transported to the HD-hall through the beam switching yard (SY). The length of SY is about 200 m. In the first 80 m section of the SY, the beam line has a slope and the proton beam is elevated by 2.9 m. The size of the HD-hall is 60^W m $\times$ 56^L m. The primary proton beam is focused on the secondary-particle-production target, called T1. In the early stages of the accelerator commissioning, the proton beam power was poor as a few kW. Therefore, materials whose melting point was rather low compared with that of Ni was able to be prepared as the production target to increase the secondary particle yield. In the present experiment, a platinum rod of 6 mm in diameter and 60 mm length which corresponds to 50 % beam loss were installed at the T1 site(Fig. 2.8). At the downstream of the T1, three charged secondary beam lines (K1.8, K1.8BR, and K1.1BR) and a neutral secondary beam line (KL) are operational so far, though the beam extraction to K1.8 and K1.8BR are mutually exclusive. The K1.8 beam line transports separated charged secondaries with the central momentum of 2 GeV/c at maximum. It was designed mainly for Ξ hypernuclear spectroscopy and a systematic study of the double strangeness system using the (K^-, K^+) reaction. It was optimized for the momentum of 1.8 GeV/c, since the Ξ^- production cross section reaches maximum at about 1.8 GeV/c. Furthermore, the extraction angle was chosen to be 6 degrees, since the K^- production cross section is maximum around such angle according to an empirical formula by Sanford and Wang [59].

Figure 2.9 shows a schematic layout of K1.8 beam line components. The K1.8 beam line is composed of four sections: the front-end section, the first mass separation section, the second mass separation section, and the beam spectrometer section. This two-stage mass separation scheme is quite effective for K1.8 to transport required particles. Magnet layout and field strengths are designed using TRANS-

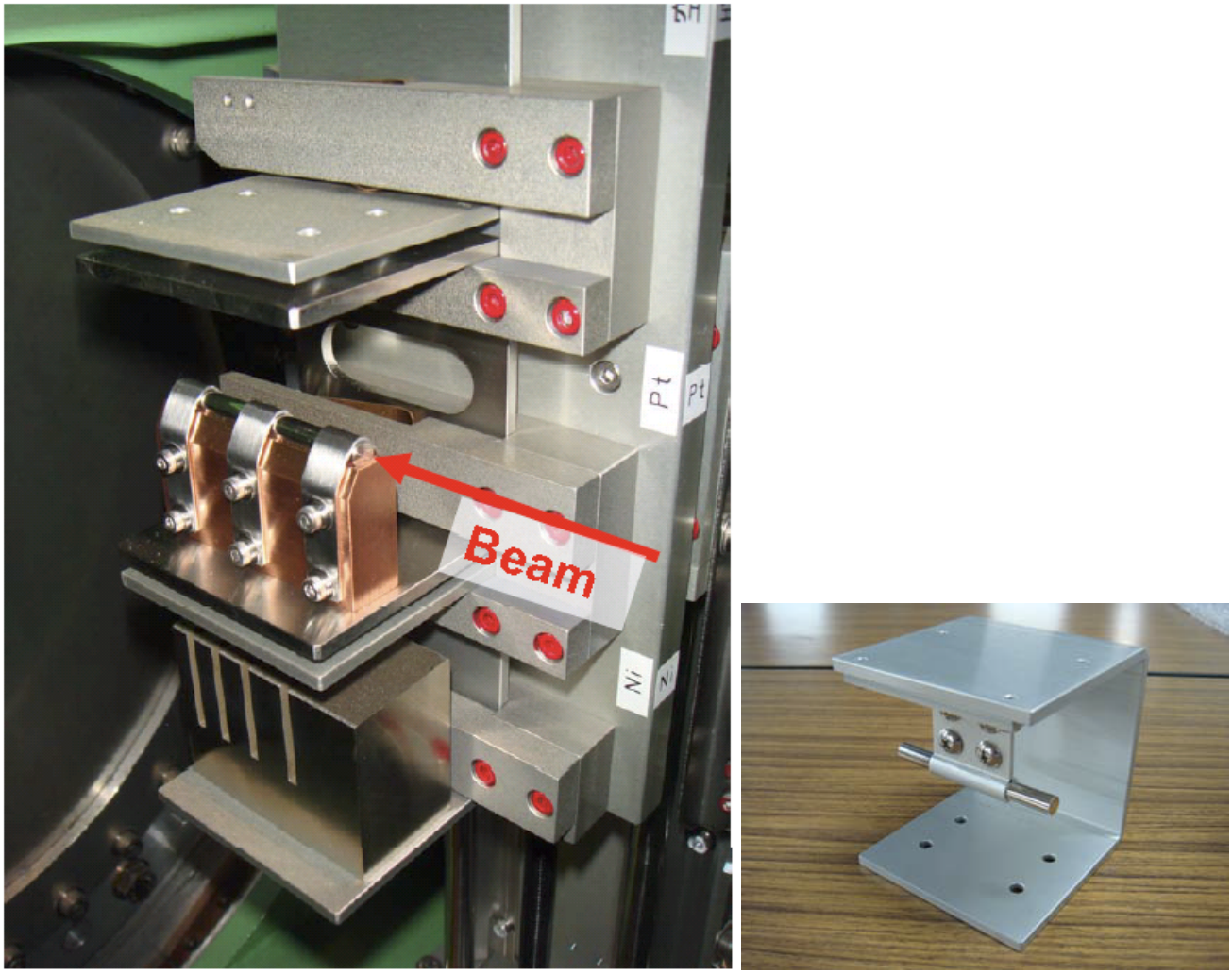

(a) Pt and Ni target for up to 5 kW. (b) Pt target for up to 2 kW.

Figure 2.8.: A picture of the Pt and Ni fixed target for a beam power of up to 5 kW (a) [57]. The Pt target is a platinum rod of $\phi 6 \times 60$ mm and is attached to the copper block for the indirect cooling. The Ni target is made of a nickel block of 35 mm wide, 50 mm height and 54 mm thickness with four slits, which are same as rotating one. In the present experiment, the Pt target was used. To make it easier to see the target shape, the Pt target without the copper block is shown together, which was used for a beam power of up to 2 kW (b) [58].

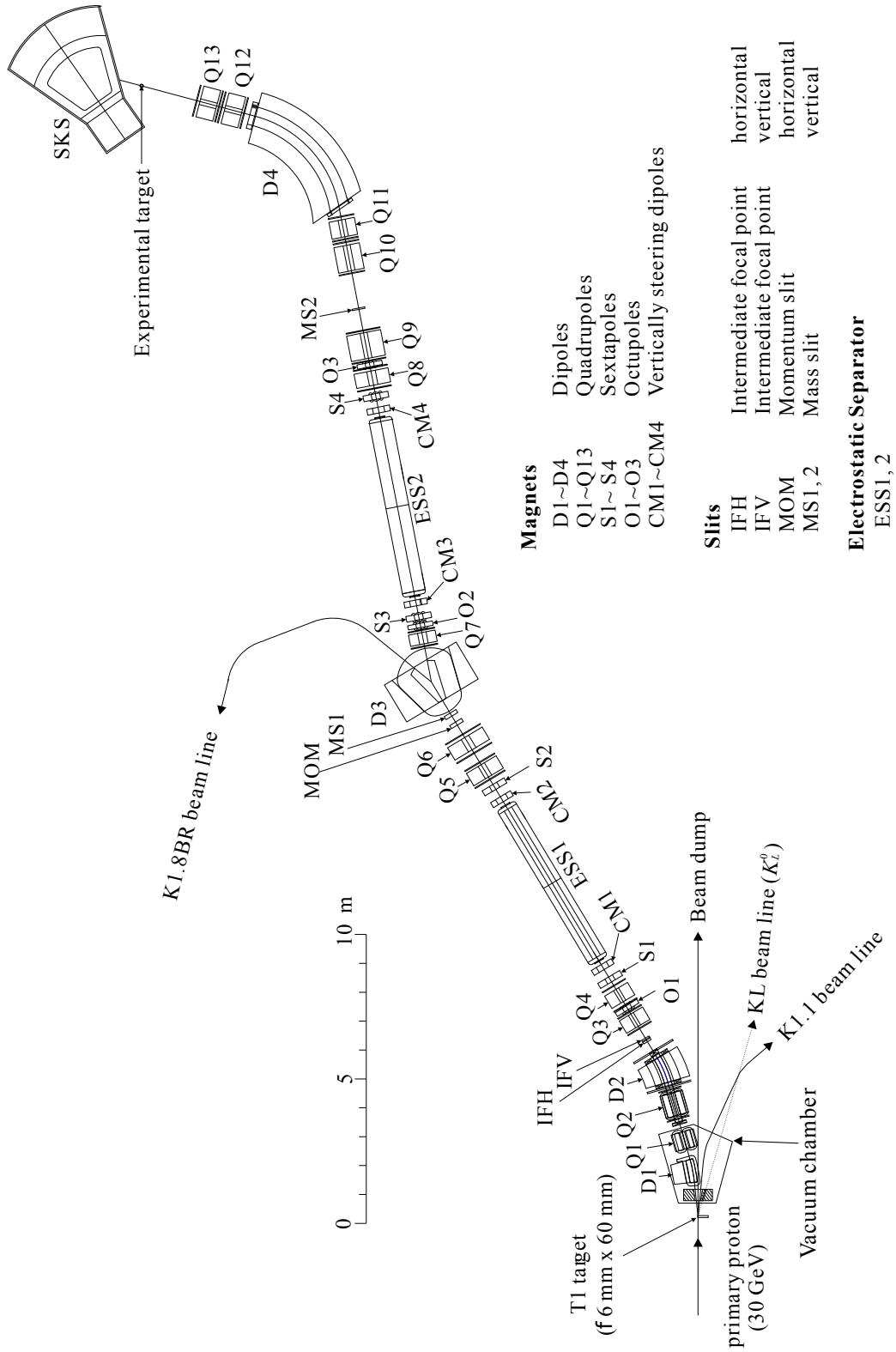

Figure 2.9.: The schematic layout of K1.8 beam line components [63].

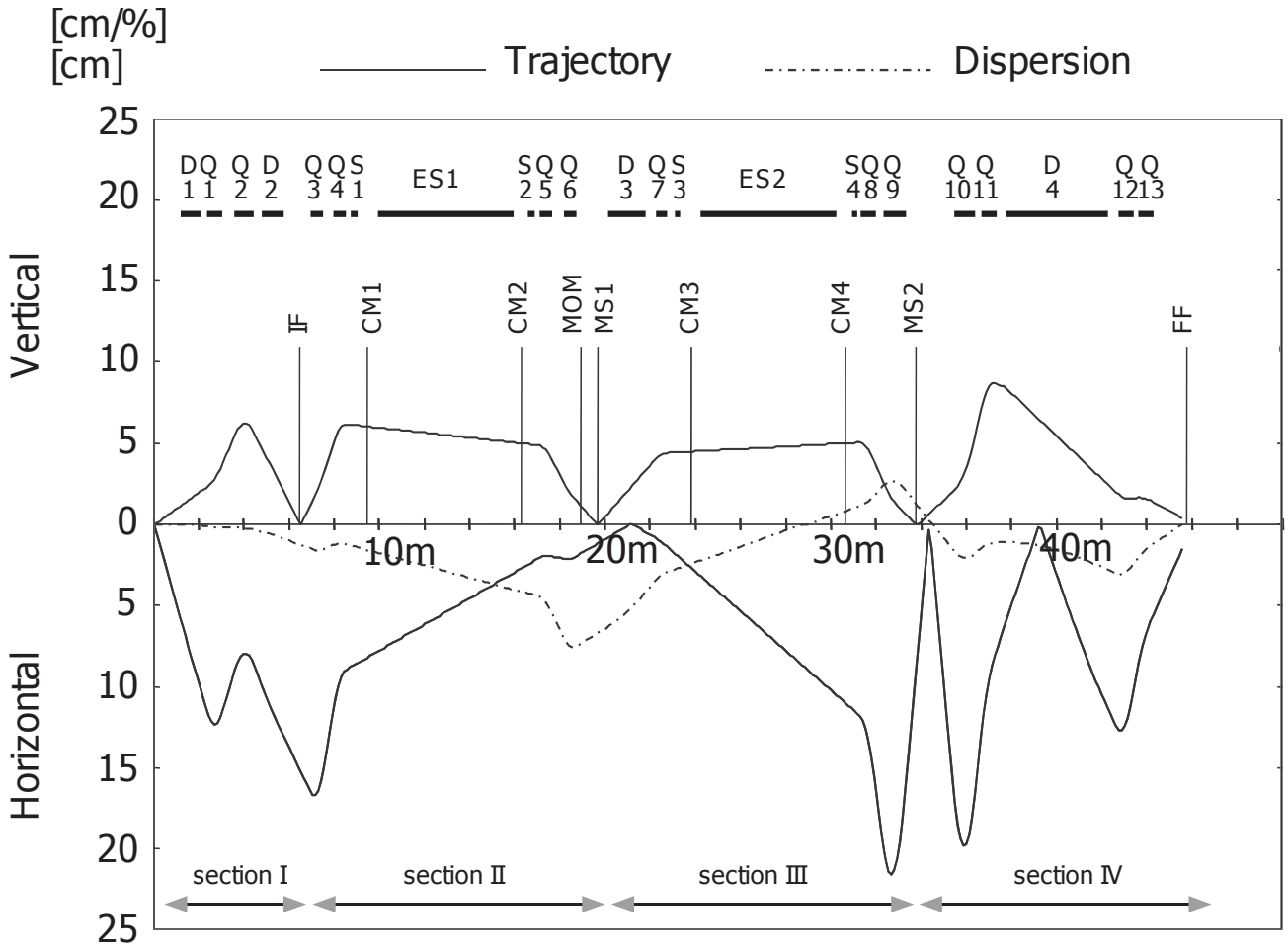

Figure 2.10.: The beam envelopes to the first order and the dispersion function of the K1.8 beam line [62].

Table 2.5.: Beam line elements of the K1.8 beam line [62]. The element names beginning 'D', 'Q', 'S' and 'O' denote dipole, quadrupole, sextupole, and octupole magnets, respectively. 'CM' is a correction magnet to compensate deflection of orbit in the electrostatic separator. The sections in the right-hand column corresponds to sections I-IV in Fig. 2.9. $(y|\phi)$, $(y|y)$, $(y|\theta\phi)$, $(y|\phi\delta)$ denote beam transfer matrix elements [60, 61].

Beam line element	J-PARC designation	Gap or bore/2 (cm)	Effective length (cm)	Field at pole at 1.8 GeV/c (kG)	Bend (deg)	Section
D1	5C216SMIC	8	88.46	11.846	10	
Q1	NQ321MIC	8	67.84	5.5		I
Q2	Q416MIC	10	87.04	−6.929		
D2	8D218SMIC	15	99.65	15.774	15	
IF-H	movable horizontal slit for acceptance control					
IF-V	movable vertical slit, $(y\|\phi)$					
Q3	Q410	10	54.72	7.4		
O1	O503	12.5	15	1.		
Q4	Q410	10	54.72	−8.2		
S1	SX504	12.5	27.6	0.419		
CM1	4D604V	10	20	3.76	0.743	II
ES1	Separator	10	600	$E = -750$ kV/10 cm		
CM2	4D604V	10	20	3.76	0.743	
S2	SX504	12.5	27.6	−1.141		
Q5	NQ510	12.5	56	−7.201		
Q6	NQ510	15	57.2	8.1		
MOM	movable horizontal slit for momentum acceptance control					
MS1	movable vertical slit for K–π separation $(y\|\phi) = 0.0$, $(y\|y) = 0.632$, $(y\|\theta\phi) = (y\|\phi\delta) = 0$					
D3	6D330S	15	165.1	−12.696	−20	
Q7	Q408	10	47	−4.511		
O2	O503	12.5	15	0.2		
S3	SX604	15	20	−1.05		
CM3	4D604V	10	20	3.76	−0.743	III
ES2	Separator	10	600	$E = 750$ kV/10 cm		
CM4	4D604V	10	20	3.76	−0.743	
S4	SX604	15	20	0.24		
Q8	NQ512	12.5	66.8	−7.9605		
Q9	NQ518	12.5	96.2	9.8799		
MS2	movable horizontal slit for K–π separation $(y\|\phi) = 0$, $(y\|y) = -0.713$, $(y\|\theta\phi) = (y\|\phi\delta) = 0$					
Q10	NQ412	10	66	9.5589		
Q11	NQ412	10	66	−7.5032		
D4	12D489	20	446.8	15.0102	64	IV
Q12	NQ412	10	66	7.6768		
Q13	NQ413	10	66	−5.2168		

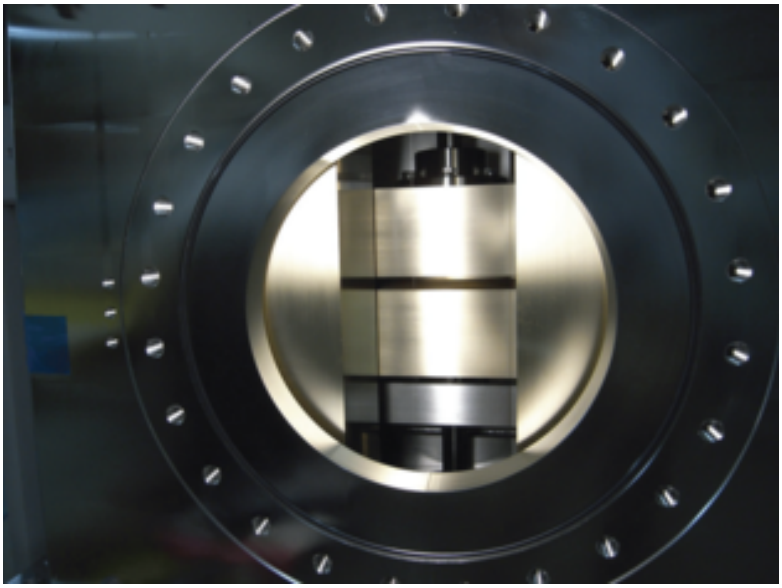

Figure 2.11.: Photograph of the intermediate focus (IF) slit [62]. IF slit has the horizontal component (IFH) and the vertical component (IFV). The blocks in IF are made of brass (70 % copper and 30 % zinc, with a density 8.5 g/cm^3).

PORT [60, 61]. The beam envelopes of first order optics are shown in Fig. 2.10. The total length to the final focus point (FF) of the beam line is 45.8 m. The beam is focused vertically at intermediate focus slit (IF), and at mass slit (MS1, MS2) before the FF where the experimental target is placed.

Details of the beam line elements are listed in Table 2.5. The frontend section consists of two dipole magnets (D1, D2) and two quadrupole magnets (Q1, Q2) with DQQD configuration, which select the central momentum of the secondary beam. The T1 target is followed by the water-cooled copper collimator to protect the magnets from the heat deposit caused by the primary proton beam. D1 and Q1 magnets and the copper collimator, are placed in the vacuum chamber in order to avoid having additional beam pipes, which otherwise might add further materials to be cooled. The K/π separation is very sensitive to the beam size at the production target. Pions from K^0_s decays and rescattered or produced at target-peripheral materials enlarge the beam size of the pion beam projected onto the production target. They are the so-called cloud pions and make the K/π separation worse. To keep the K/π separation good, IF is installed and it redefines the beam image at the production target. The IF is composed of the horizontal slit (IF-H) and the vertical slit (IF-V). For the IF-H (IF-V), a brass block of 20 (30) cm length is used. (Fig. 2.11)

Secondary particles are purified with two electrostatic separators, ESS1 and ESS2. Figure 2.12 shows a photograph of ESS1. Both of ESS1 and ESS2 have the effective length of 6 m and the electrode gap of 10 cm, in which vertical electrostatic field of 75 kV/cm is applied. Each of ESS1 and ESS2 is sandwiched by two dipole magnets, CM1/CM2 and CM3/CM4, respectively, which generate horizontal magnetic fields. After the ESS and CM, the selected beam is focused in the vertical direction by quadrupoles (Q5-Q6, Q8-Q9). Unwanted secondary particles are deflected by the combination of electrostatic and magnetic fields and absorbed by the mass slits (MS1 and MS2) located downstream of ESS1 and ESS2, respectively. The MS1 and MS2 are vertical-type slit which is made of tungsten alloy of 50 cm length. The sextapoles (S1-S4) and octapoles (O1-O3) are used to correct the second and

Figure 2.12.: Photograph of the first stage electrostatic separator of the K1.8 beam line viewed from upstream [62].

third order aberrations, respectively. The momentum slit (MOM) is a horizontal slit, which is used for the selection of momentum bite of the secondary beam and is located at a large momentum-dispersion point.

In October and November 2010, the yield of K^- at 1.8 GeV/c was measured with 3kW primary beam (3.75×10^{12} ppp) using Pt target. Although the beam line magnets and offset positions of the slits were not fine tuned, the yield and purity were obtained to be 45k kaons/spill with the kaon ratio of 5%. Table 2.6 summarizes the electric field of the separators and the slit conditions used in autumn 2010 together with the designed values.

For π^- beam used in the E19 experiment, the separators were operated with 30 kV/cm and narrower slit openings than the kaon case were used. Typical π^- intensity was 1 M/spill.

The momentum analyzer part is located after the MS2. It is described in the Sec. 2.3.

2.2.2. Spill structure

In physics experiment, extraction spill structure is very important since the acceptable counting rate of detectors and data acquisition (DAQ) system is limited. In some situation, high multiplicity environment gives rise to increases of signal pileup, event overlay, dead time of detectors and DAQ. In severe cases, too many charge deposit might destroy a detector, for instance, wires in gas chambers. Therefore, the beam spill structure should be flat and stable during an extraction. In the present J-PARC, the spill feedback control devices are installed, which consists of two kinds of quadrupole magnets; extraction quadrupole magnet (EQ) to shape the beam structure from a Gaussian like form to flat one and ripple quadrupole magnet (RQ) to reject the high frequent ripple noise. However, the magnet power supplies of MR have a large ripple even at extraction period. It causes serious spikes in

Table 2.6.: Electric field of the Separators and slit conditions for the yield and purity measurement of kaon beam at 1.8 GeV/c in autumn 2010. (V) and (H) denotes the vertical and horizontal slits.

	In the measurement	Design
ESS1	40 kV/cm	± 75 kV/cm
ESS2	40 kV/cm	± 75 kV/cm
slit opening		
IFY (V)	2.0 mm	4.0 mm
MS1 (V)	± 2.35 mm	± 2.25 mm
MS2 (V)	± 2.5 mm	± 2.4 mm
IFX (H)	± 130 mm (full)	± 130 mm (full)
MOM (H)	± 180 mm (full)	± 180 mm (full)

the beam spill and brings the bad effects described above.

The spill duty factor is a measure of the quality of extracted beam. It is given as the ratio of the actual amount of time extracted beam is on to the extraction time of 2.2 sec. We monitored it using the accidental coincidence counting rate of two counters. For example, a counter located at upstream of the beam line, which used for monitoring the beam intensity by counting the number of scattered particles from T1 target, and a counter installed at the beam momentum analyzer were utilized for this purpose. According to the above definition, the duty factor η can be expressed as

$$\begin{aligned} \eta &= \frac{N_1}{R_1 \times T} \\ &= \frac{N_2}{R_2 \times T} \\ &= \frac{N_{acc}}{R_{acc} \times T}, \end{aligned} \tag{2.1}$$

where the subscript (1, 2 or acc) means the quantity for each counter or the accidental coincidence of the two counter, T is time duration of spill-on (= 2.2 sec), N's (N_1, N_2, N_{acc}) and R's (R_1, R_2, R_{acc}) are the number of hits in time T and counting rate, respectively. R_{acc} is calculated by

$$R_{acc} = R_1 \times R_2 \times \Delta_T \tag{2.2}$$

where Δ_T is the coincidence gate width of two counters. Using Eq.(2.1) and (2.2), the duty factor was described as

$$\eta = \frac{\Delta_T}{T} \times \frac{N_1 N_2}{N_{acc}} \tag{2.3}$$

In the present experiment, the duty factor was measured to be $\sim$ 16%. However, the instantaneous intensity often reached at 500 counts per 100 μsec (i.e. 5 MHz), which was an order of magnitude higher than the averaged one and an example is shown in Fig. 2.13. In order to keep the detection efficiency and to protect the wire chambers from the damage, we restricted the beam intensity to $\sim 1.0 \times 10^6$/spill for the present experiment.

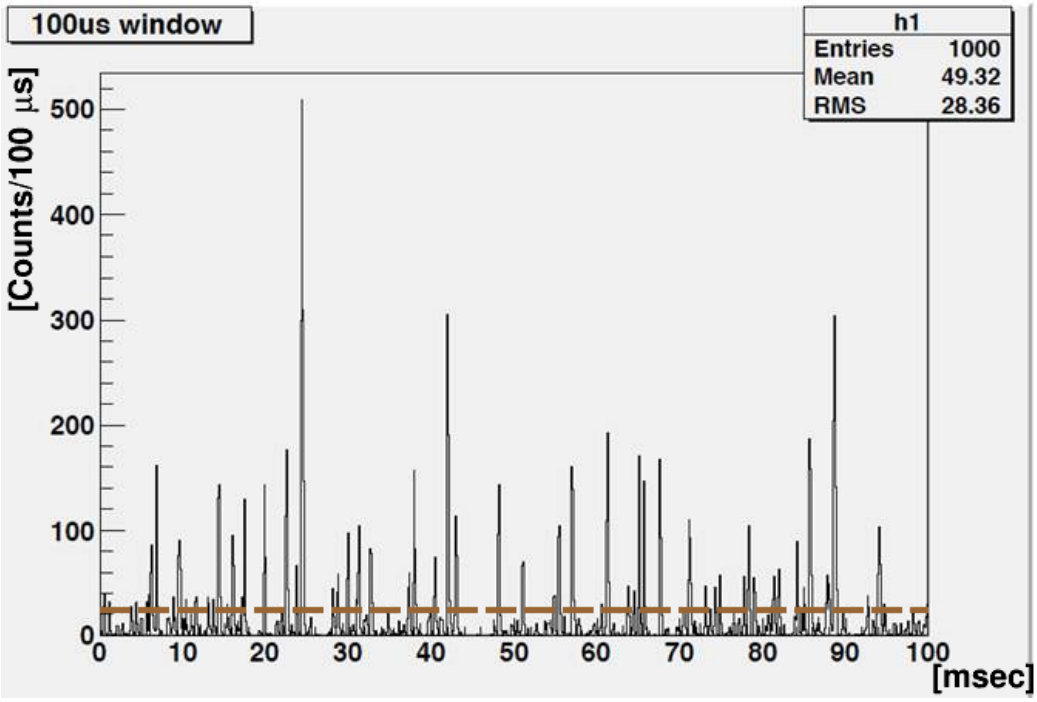

Figure 2.13.: Typical signal rate of BH1 during the engineering run with the beam intensity of $\sim$ 0.5M /2.2 sec [63]. Each bin content corresponds to the number of counts in the 100 μs time window. The dashed line means the averaged intensity which is expected for the duty factor of 100%.

2.3. Beam spectrometer

The beam spectrometer consists of a QQDQQ magnetic system , tracking wire chambers and trigger counters as shown in Fig. 2.14. The dipole magnetis called D4. A series of wire chamber installed at the entrance and exit of QQDQQ determines the particle trajectory and momentum, which are used for reaction vertex reconstructions. Point-to-point optics is realized between VI (40 cm upstream to the Q10 pole edge) and VO (30 cm downstream from the Q13 pole edge). Therefore, the multiple scattering at the entrance and exit of the QQDQQ does not affect the momentum resolution to the first-order matrix. The expected momentum resolution is $\Delta p/p = 1.4 \times 10^{-4}$ in 1σ, assuming the tracking devices have the position resolution of 200 μm in 1σ. Table 2.7 shows design specifications of the beam momentum analyzer.

Figure 2.15 shows the measured excitation curves for the K1.8 components. D4 consists of the main coil and the sub coil. When the beam momentum exceeds around 1.6 GeV/c, the sub coil is turned on together with the main coil.

The magnetic field of the D4 is monitored using a high-precision Hall effect sensor (Digital Teslameter 151, DTM-151 of Group3 Technology) [65]. The field values were logged with time-stamps during the data-taking period for the time-dependent correction in the offline analysis. The resolution and the accuracy of the meter is 1.7×10^{-6} and 0.01 %, respectively. The fluctuation was observed due to the power supply noise of D4 suffered from the MR, which was less than 0.05 %.

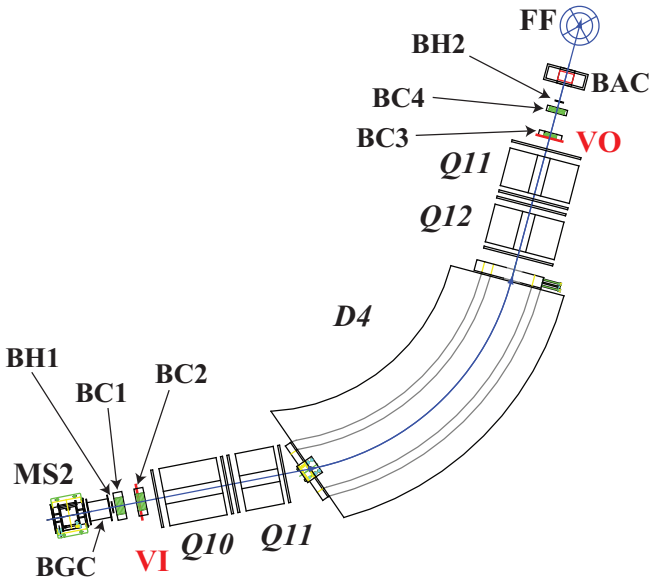

Figure 2.14.: The schematic layout of K1.8 beam spectrometer [64]. BAC was removed in the E19 experiment.

Table 2.7.: Design specifications of the K1.8 beam analyzer

Momentum resolution	3.3×10^{-4} (FWHM)
Momentum bite	$\pm 3\%$
Maximum momentum	2.0 GeV/c
Bending angle	64^o
Flight path (BH1–BH2)	10.4 m
Radius of curvature of D4	4 m

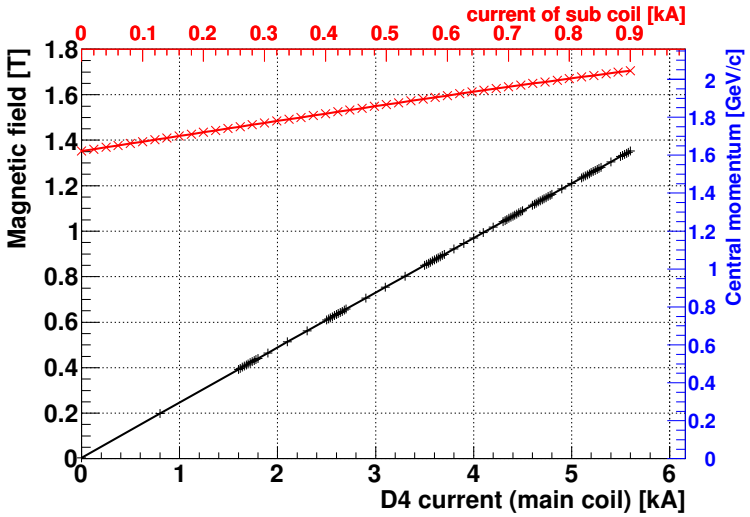

(a) K1.8 D4.

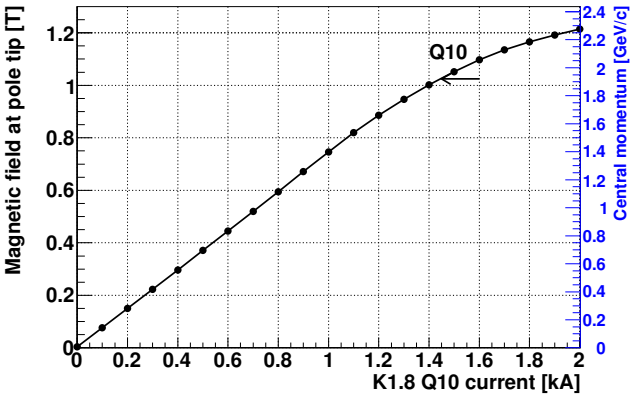

(b) K1.8 Q10.

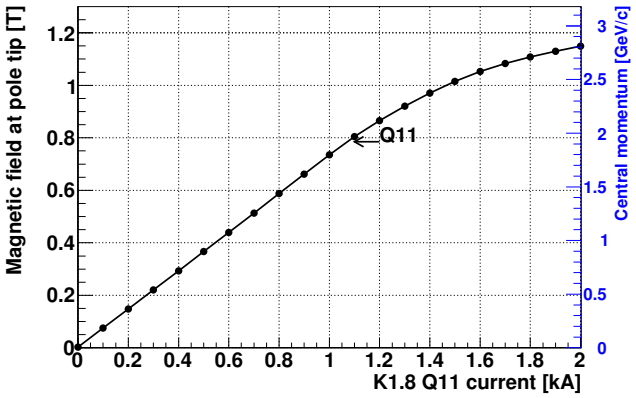

(c) K1.8 Q11.

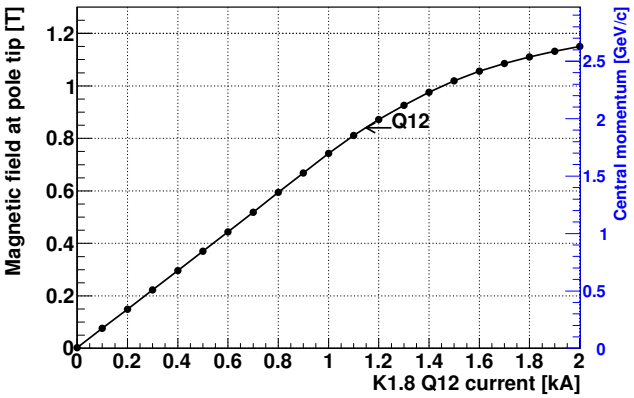

(d) K1.8 Q12.

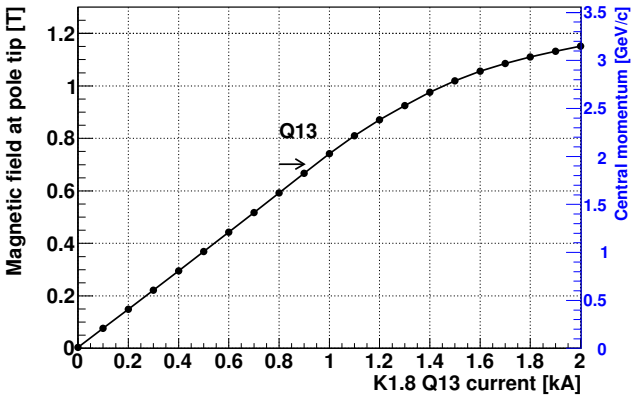

(e) K1.8 Q13.

Figure 2.15.: The measured magnetic field excitation curves of the K1.8 components [63]; (a) D4, (b) Q10, (c) Q11, (d) Q12 and (e) Q13. The central momentum of K1.8 corresponding to the field value is shown in the blue axis, where the required field for Q magnets are optimized for the target position of E19.The black and red line in (a) mean the magnetic field generated by the only main coil and by both the main coil with the maximum current and the sub coil, respectively. The arrows in the plots of the Q magnets indicate the magnitude of the field used for the central momentum of 1.92 GeV/c.

Beam trigger counters

The particle identification at an online trigger level was performed with a Time-of-Flight method and the threshold type Čerenkov counters. The characteristics of trigger counters are listed in Table 2.8.

Gas Čerenkov Counter (BGC)

The Gas Čerenkov counter, BGC [66] was located just downstream of the second mass slit and used for electron/positron rejection in the momentum range above 1 GeV/c, where it is difficult to separate pions from electrons by a Time-of-Flight method. Iso-butane gas of 0.15 MPa, which corresponds to the refractive index of 1.002, was filled as the Čerenkov photon radiator. The reflection mirror was made of aluminum evaporated on a borosilicate glass substrate (Yamada Kogaku Kogyo) of 6 mm thickness. The aluminum layer was coated with MgF_2, which is transparent to the UV-photons, in order to prevent aluminum oxidation. The mirror shape was paraboloidal with the focal length of 195 mm. Čerenkov photons were detected by a phototube with a UV-transparent window with a diameter of 5 inch (Hamamatsu R1250-03). Figure 2.16 shows a schematic view of BGC.

The measured number of photo-electrons was approximately 5 for higher than 0.5 GeV/c. The detection efficiency for electrons was found to be 99.5%, which was enough to reject unwanted electrons existing the fraction of 12-14% in the pion beam.

Beam Hodoscopes (BH)

To perform the time-of-flight measurement for beam particles, two hodoscopes, BH1 and BH2, were installed in the beam spectrometer. The BH1 was a segmented scintillation counter, which was located just downstream of BGC. Figure 2.17 shows a schematic view of BH1. It was divided into eleven vertical pieces of 5 mm-thick plastic scintillators in order to balance the counting rate of each segment. To avoid any dead space, each segment was overlapped with its adjacent segments by 1.0 mm. Each segment was equipped with photomultipliers on both ends. The phototubes had additional high voltage (HV) supplier, so called booster, on last three dinode stages to keep their gain under the high counting rate.

The BH2 was located 120-cm upstream of the experimental target. This counter provided a time origin of the counter whole system. It was segmented into seven vertical pieces of 5 mm-thick plastic scintillators as shown in Fig. 2.18. Each segment was overlapped by 2 mm due to the same reason as BH1. The same kind of phototubes as those of BH1 were attached to each segment.

Beam tracking chambers (BC)

For the beam tracking devices, two multi-wire proportional chambers (MWPC, BC1-BC2) and two multi-wire drift chambers (MWDC, BC3-BC4) were used. BC1 and BC2 were located at the entrance of the QQDQQ system while BC3 and BC4 were placed at the exit of the QQDQQ. Their specifications are summarized in Table 2.9.

BC1-2

At the upstream part of the K1.8 beam spectrometer, a single counting rate is estimated to be 10–20 MHz for the J-PARC full intensity operation. According to the past experience at the KEK K6

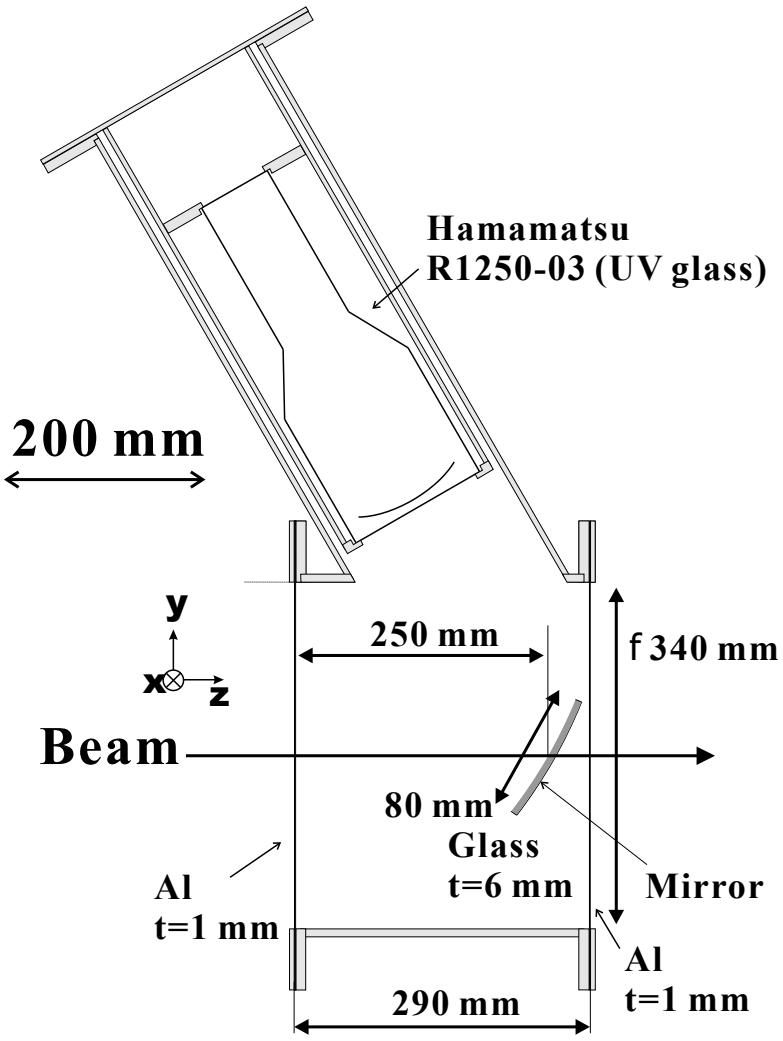

Figure 2.16.: Schematic view of the BGC [63].

Table 2.8.: Specifications of the trigger counters.

Name	Sensitive area (mm)	Spec.	PMT
BGC	$340^W \times 80^H$(mirror), 290^L	iso-C_4H_{10}, n$\sim$1.002 (1.5 atm)	R1250-03 (UV glass)
BH1	$170^W \times 66^H \times 5^T$	BC420, 11 segments, 3-stage booster	H6524MOD
BH2	$133^W \times 60^H \times 5^T$	BC420, 7 segments, 3-stage booster	H6524MOD
TOF	$2240^W \times 1000^H \times 30^T$	BC410, 32 segments	H1949
AC1	$1050^W \times 1200^H \times 113^T$	Silica aerogel, n=1.05	R1584-01
AC2	$1400^W \times 1400^H \times 113^T$	Silica aerogel, n=1.05	R1584-01
LC	$2800^W \times 1400^H \times 40^T$	Acrylic, 28 segments, n=1.49	H1949, H6410

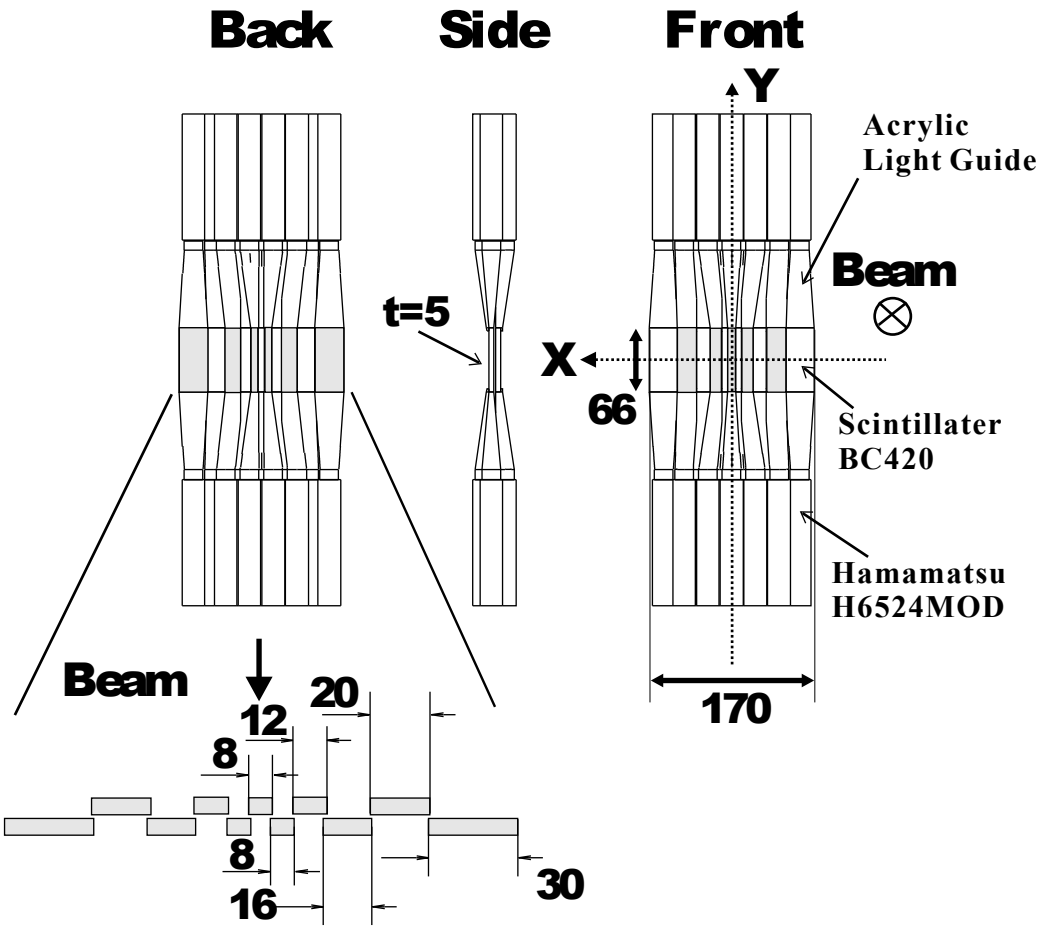

Figure 2.17.: Schematic view of BH1 [63].

Table 2.9.: Specification of the tracking devices. Wire direction is listed in the order from upstream to downstream.
Gas mixture;
BC1-4, SDC1-2 $\cdots$ Ar : i-C_4H_{10} : Methylal = 76 : 20 : 4.
SDC3-4 $\cdots$ Ar : C_2H_6 = 50 : 50.

Name	Active area (X × Y mm^2)	spacing (mm)	Wire direction	Tilt angle X, U, V (Deg.)	Resolution (μm in rms)
BC1	256 × 100	1.0	$X-V-U-X-V-U$	$0, +15, -15$	300
BC2	256 × 100	1.0	$V-U-X-V-U-X$	$0, +15, -15$	300
BC3	192 × 100	3.0	$XX'-VV'-UU'$	$0, +15, -15$	200
BC4	240 × 150	5.0	$VV'-UU'-XX'$	$0, +15, -15$	200
SDC1	192 × 100	3.0	$VV'-UU'$	$0, +15, -15$	200
SDC2	400 × 150	5.0	$VV'-UU'-XX'$	$0, +15, -15$	200
SDC3	2140 × 1140	20	$V-X-U-V-X-U$	$0, +30, -30$	300
SDC4	2140 × 1140	20	$V-X-U-V-X-U$	$0, +30, -30$	300

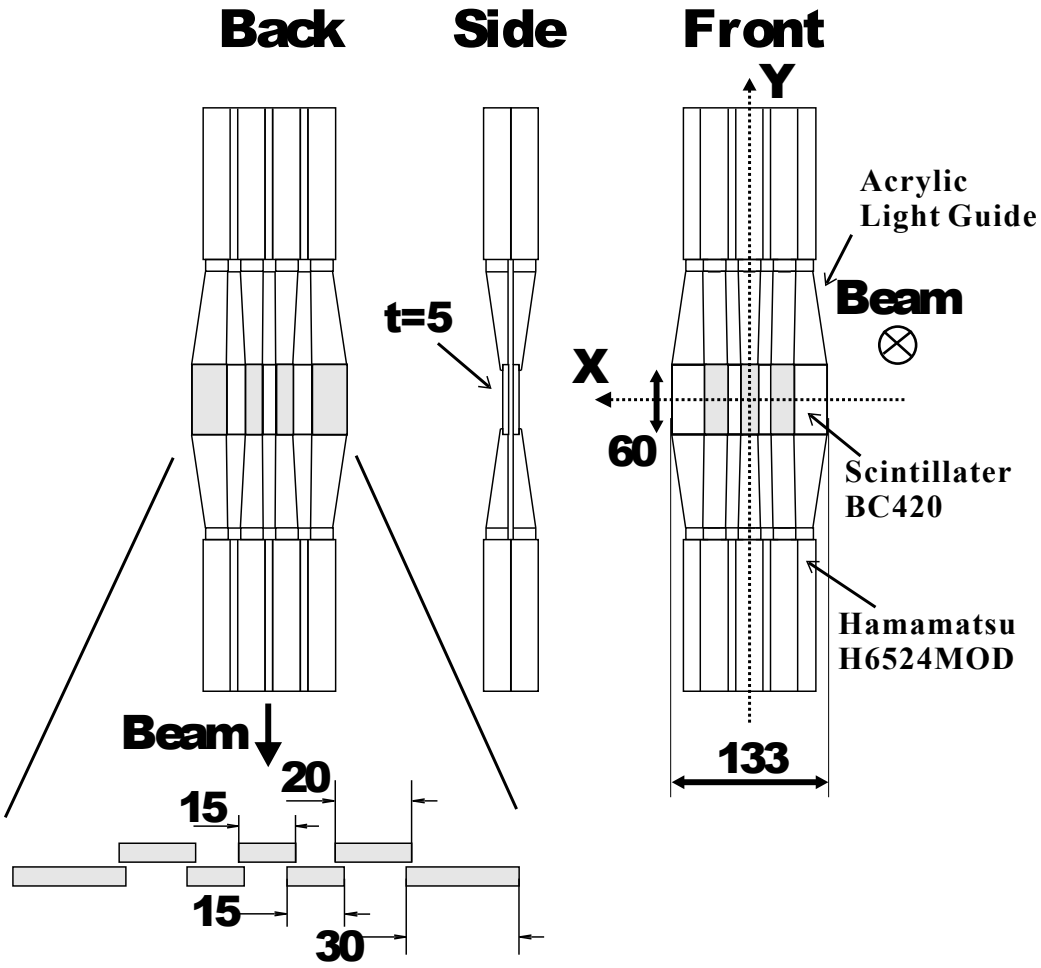

Figure 2.18.: Schematic view of BH2 [63].

beam line, where the wire chambers with 2.5 mm drift space had been used for the beam tracking, a deterioration in the detection efficiency became non-negligible with the counting rate over 200 kHz per wire. This situation required the wire chamber with the sense wire pitch of ≤ 1 mm in the J-PARC K1.8 case. Thus, we constructed MWPC with 1 mm anode pitch. Note that there is the practical difficulties of precisely stringing and soldering wires at a pitch below 1 mm. The schematic view of a cell structure and an anode wire plane of the MWPC is shown in Fig. 2.19. The sense wire is a gold-plated tungsten alloyed with 3% rhenium and its diameter is 15 μm. These wires are tensioned by ~ 20 gram-force per wire and fixed on the printed circuit board (PCB) made of Flame Retardant type 4 grade (FR-4) glass-reinforced epoxy with a thickness of 3 mm, which corresponds to anode-cathode gap. The cathode planes are made of 12 μm Mylar film coated with 20 μm-thick graphite paste (MRX-713J-A, a carbon conductive ink) which is used to reduce damage of the cathode caused by discharge. The cathode films are fixed on the G10 frames and connected to an HV line. Although the active area of a sense plane is $256^H \times 100^V$ mm^2, there are additional wires (guard wires) at both sides even outside the window, which moderate the change of electrostatic field in the edge region. The signal readout lines are drawn out to eight half-pitch connectors, HIROSE FX2-68P-1.27DSL(71), on both the top and bottom of the anode frame. All guard wires are grounded directly.

The assembled structure of the MWPC is shown in Fig. 2.20(a). Each MWPC had six sense-wire planes (X, U, V, X, U, V), where wire directions of X, U and V were tilted by 0^o, $+15^o$ and -15^o from the vertical direction, respectively. The distance between the layers is 20 mm, which is required to mount the frontend electronics and its noise shield. The window frame was covered by the 9-μm-thick aluminized aramid film for the gas seal and the electric shield. The precision pins were inserted through the registered holes and served to lock the relative wire positions between the sense planes.

The frontend read-out electronics of MWPC consisted of Amplifier-Shaper-Discriminator (ASD) IC's (CXA3183Q TGCASD) on a PCB mounted on MWPC. The ASD IC was developed for the Thin Gap Chambers in the forward muon trigger system of the LHC ATLAS experiment [67]. The specifications of the ASD IC is listed in Table 2.10 and its block diagram is shown in Fig. 2.21. An analog signal from a wire chamber is received by the preamplifier section with the integration time constant of 16 nsec. The gain of its preamplifier stage is ≈ 0.8 V/pC and output is further amplified by the shaper stage with a gain of 7. The threshold voltage for discriminator section is common to the 4 channels and their digital output level is LVDS-compatible. One IC chip contains 4 channels in a QFP48 package. Fig. 2.22 shows the ASD card (GNA-200) we developed, which had 8 ASD IC's, thus, 32-channel analog input. The input connector was a half-pitch one (HIROSE FX2-68S-1.27DSL), which matches the connector on the chamber, and fast switching diodes were placed for the electrostatic discharge protection. The differential output pair was pulled down with resistor networks on the card. The output connector was a half-pitch connector, KEL 8831E-068-170L-F. Power for +3.3 V(0.82 A), -3.0 V(0.11 A), threshold bias, and ground were supplied by other cables. A test input signal of NIM logic level could be injected through the RG-174/U coaxial cable. The LVDS output signal from the ASD card was sent to a newly developed MWPC encoder via 10 m-long twisted-pair cables. In the actual operation, the ASD IC's were covered with noise shield case as schematically shown in Fig. 2.20(a). The threshold voltage of signal-noise separation we applied to the ASD IC's was about 20 mV. [2] The

[2]The threshold voltage is magnified by 10 times compared to the pulse height before the comparator. The actual set up values were about 200 mV.

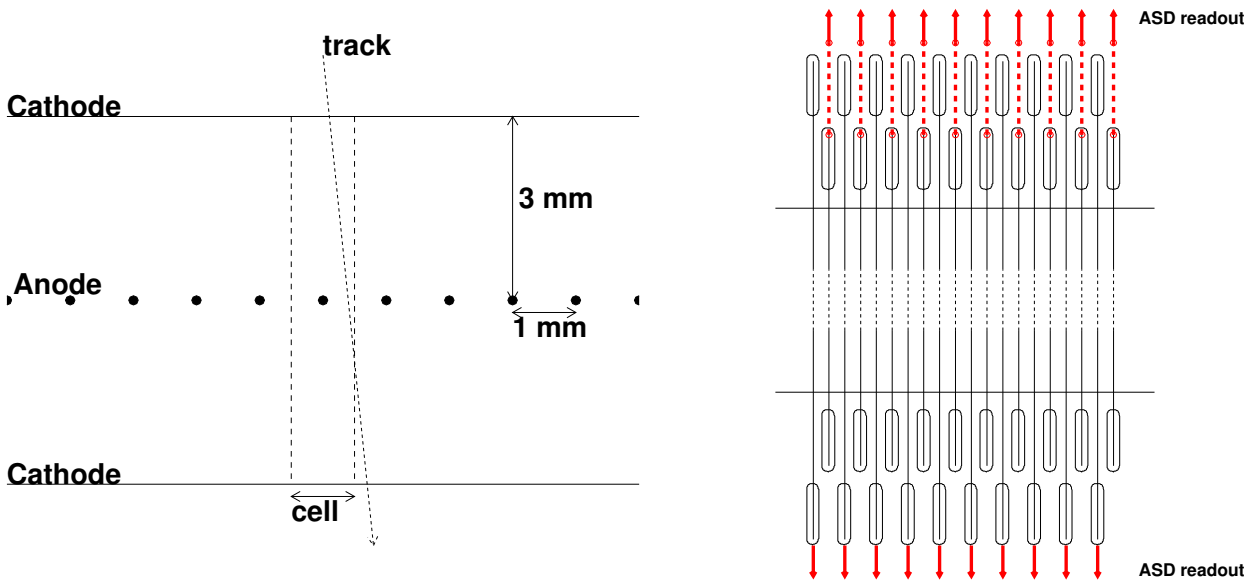

(a) (b)

Figure 2.19.: Schematic view of the structure of BC1 and BC2 [63]. (a) The cell structure of BC1, BC2. (b) Front view of the anode plane of BC1, BC2. Soldering pads, through-holes and direction of signal readout are shown by round boxes, red circles and red arrows, respectively.

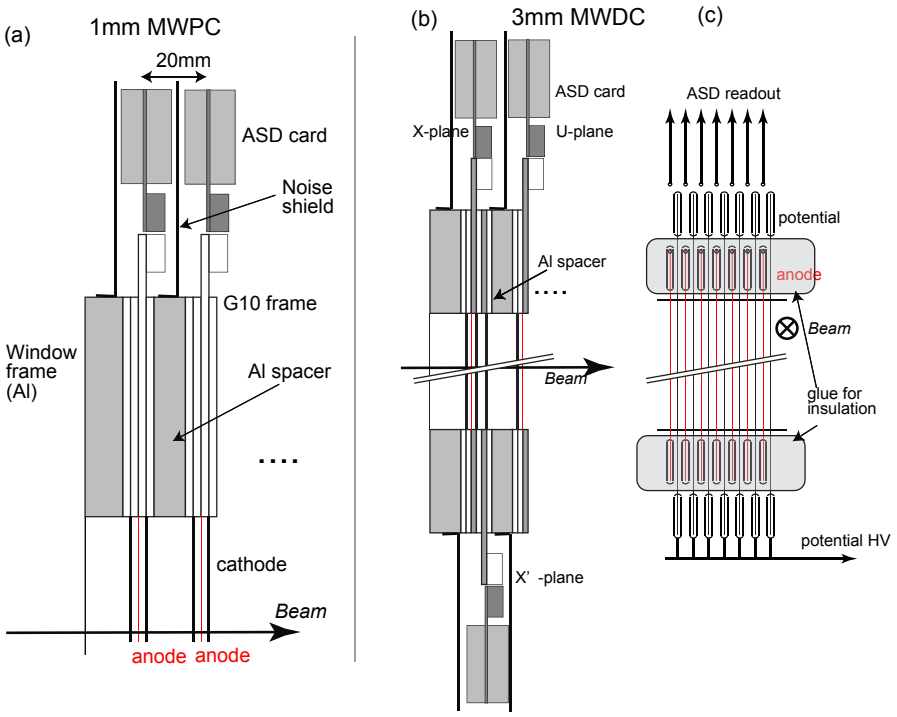

Figure 2.20.: Side view of the beam line chambers and the wire frame of the 3 mm spacing MWDC [64]. (a) Side view of the 1 mm spacing MWPC. (b) Side view of the 3 mm spacing MWDC. (c) Front view of the wire frame of the 3 mm spacing MWDC.

Table 2.10.: CXA3183Q TGC ASD chip characteristics.

process	SONY Analog Master Slice (bipolar semi-custom)
package	QFP48
preamplifier gain	0.8 V/pC
integration time constant	16 nsec
input impedance	$\sim 80\ \Omega$
open-emitter analog outputs	
main amplifier gain	$\times 7$
Baseline restoration circuits	
Comparator with LVDS-compatible outputs	
noise	ENC $\approx$ 7500 at $C_D = 150$ pF
threshold voltage	common for all 4 channels
required voltage	$\pm$ 3 V, GND
power consumption	59 mW/ch when driving a 100 Ω load
	(+3 V: 16.4 mA, $-$3 V: 3.25 mA, 46 mW in ASD chip
	and 13 mW at LVDS receiver end)

digitizer part is described in Sec. 2.6.

BC3-4

In order to cope with several MHz counting rate at the downstream part of the K1.8 beam spectrometer, a new drift chamber with an anode pitch of 3 mm was fabricated and used as BC3, while a drift chamber with 5 mm anode spacing was recycled from the KEK-PS K6 beam line and used as BC4 [68]. The schematic view of the cell structure of the drift chamber BC3 is shown in Fig. 2.23. Each chamber consisted of three units of a double-plane (or pair-plane) structure. Namely, one plane and another plane whose wire alignment was shifted by a half wire spacing formed one unit and the two anode planes faced one of the three cathode layers from both sides. This structure was useful to resolve the left-right (L-R) ambiguity. The wires were aligned in the orientation of $XX'(0^o)$, $UU'(+15^o)$ and $VV'(-15^o)$. The sense and potential wires were made of gold-plated tungsten plus 3% rhenium (ϕ12.5 μm) and gold-plated copper beryllium (ϕ75 μm), respectively. Those wires were soldered on the FR-4 frame. Epoxy glue was used for the electrical insulation between the potential wires and the anode pads as shown in Fig. 2.20(c), where HV of $\sim$1.2 kV was applied in a very narrow space. The gap between the sense plane and the cathode plane was 2 mm, which was limited by technical reasons related to the gas seal and frame distortion. The cathode material of BC3 was the 12-μm-thick mylar film coated with 20-μm-thick carbon ink on both sides, while the cathode planes of BC4 were made of 7.5 μm-thick kapton coated with 0.1 μm aluminum and 0.0025 μm chromium for preventing oxidation of the aluminum coating on both sides. The window region of the outermost layers were sealed with aluminized film for the electric shield.

The ATLAS ASD IC's were commonly used for the frontend electronics of the all beam line chambers. 32-ch ASD cards, which was the same type used for the BC1-2, were attached to BC3, while 16-ch ASD cards (GNA-140) were mounted on BC4. The LVDS output signal of the ASD card mounted on

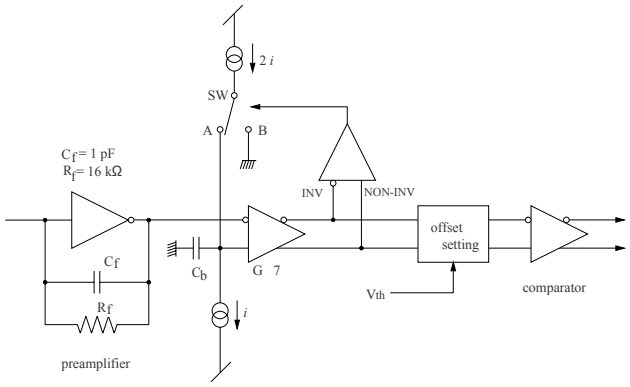

Figure 2.21.: Block diagram of the ASD chip [67].

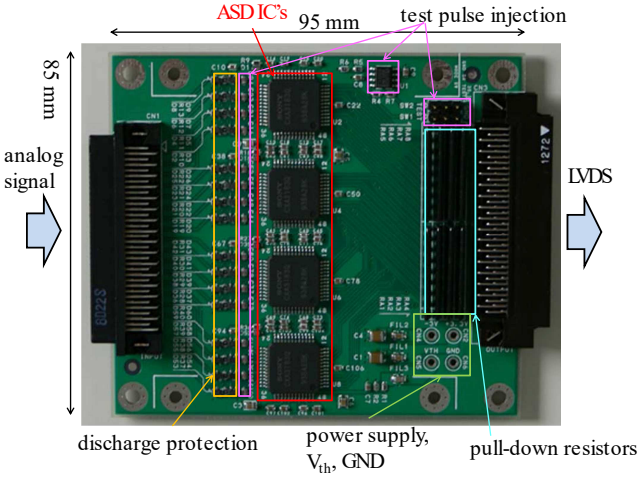

Figure 2.22.: ASD card for wire chamber frontend readout electronics [64].

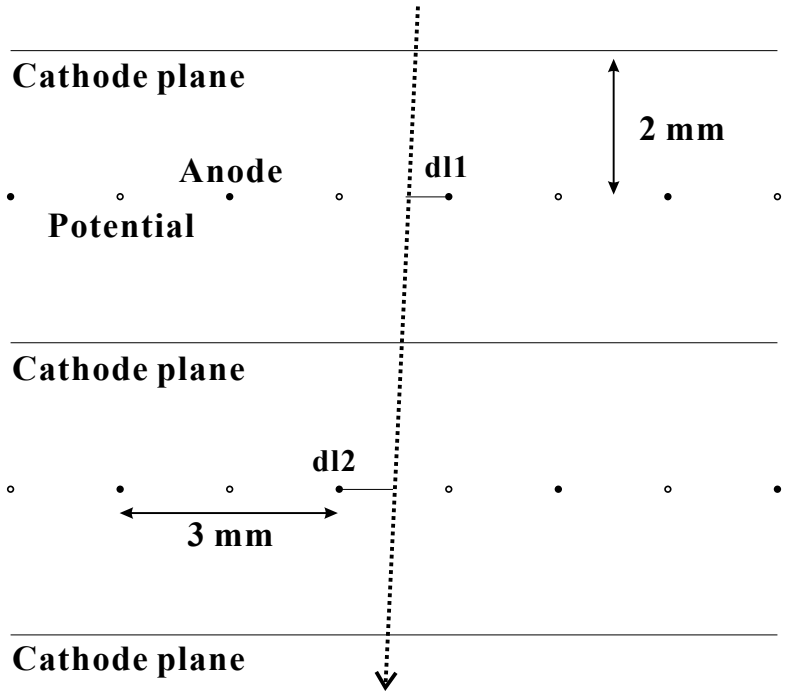

Figure 2.23.: Cell structure of BC3 [63].

BC3 and BC4 was transferred to TKO Multi-Hit TDC via 15 m-long twisted pair cables. The detail of the TKO Multi-Hit TDC is described in Sec. 2.6

Operation of MWPC and MWDC

The gas mixture of argon(76%) + isobutane(20%) + methylal (4%) at atmosphere pressure flowed through the beam line chambers (BC1,2,3,4) individually. Figure 2.24 shows the detection efficiency curve of one of the layer of MWPC (BC1) (a) and MWDC (BC3) (b) as a function of the cathode high voltage. It was measured using a low-intensity pion beam (∼10 kHz). At the beginning of the present experiment, we applied HV of −2.55 kV to MWPCs, where the detection efficiency was thoroughly in the plateau region. However, spikes in the beam structure cause the over current and wires broken, thus, we found it was difficult to keep that voltage. The operation voltages of BC1 and BC2 were set to −2.51 kV for the stable operation. For BC3, HVs of −1.23 and −1.25 kV were applied to the cathode planes and potential wires, respectively. BC4 was operated at −1.40 kV for both cathode and potential wire.

2.4. Scattered particle Spectrometer

The Superconducting Kaon Spectrometer (SKS) was originally designed and constructed for the study of Λ hypernuclei via the (π^+, K^+) reaction [69] at KEK K6 beam line. The remarkable feature in this system was a simultaneous realization of both of its outstanding momentum resolution of 0.1% and a large acceptance of 100 msr around 1 GeV/c. In addition, it keeps the flight path as short as 5 m, and has a powerful kaon identification ability.

The SKS was transferred to the J-PARC K1.8 beam line. The cooling system was modified to

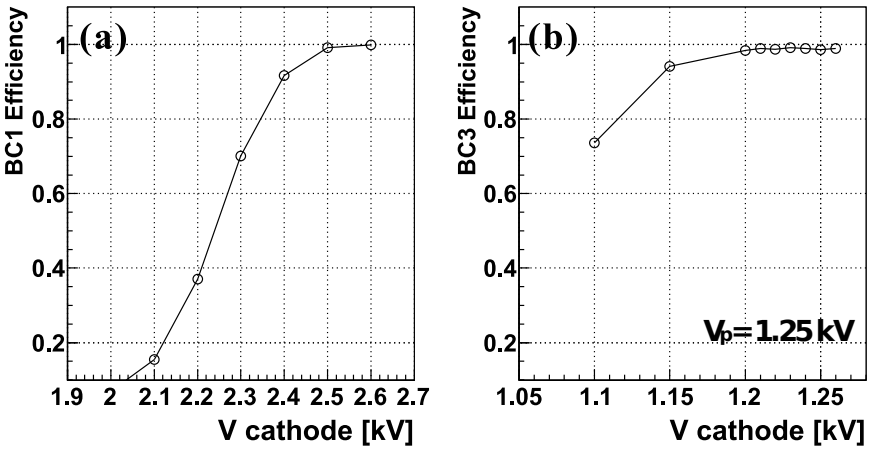

Figure 2.24.: The efficiency versus high voltage of cathode plane [64]. (a) 1-mm spacing MWPC (BC1). (b) 3-mm spacing MWDC (BC3).

Table 2.11.: Parameters of SKS.

	Present SKS	SKS at KEK-K6
Momentum resolution (@ 0.8 GeV/c)	0.1% (FWHM)	0.1% (FWHM)
Momentum coverage [GeV/c]	0.75 – 1.1	0.75 – 0.8
Angular acceptance [msr]	120	100
Bending angle [1]	100^o	100^o
Flight path [1]	$\sim$ 6.0 m	$\sim$ 5.5 m

[1] for the central trajectory

use a GM-JT cryo-coolers [70]. The SKS consisted of four sets of drift chambers (SDC1, 2, 3, 4) and superconducting dipole magnet (SKS magnet) and three types of particle identification counters (TOF, AC1,2 and LC). The detectors used in the SKS system except AC1,2 were upgraded for the J-PARC experiments to increase the momentum acceptance and the high rate capability. Figure 2.25 shows the detector setup of SKS in the present experiment. The parameters of the magnet are listed in Table 2.11. The particle trajectory and its momentum were determined by the Runge-Kutta method and fitting the track candidates particle-by-particle over the magnetic-field map, which was calculated by a finite element method (ANSYS [72]). The SKS pole gap and the open space from SKS to SDC3 were occupied with helium bags to reduce multiple scattering effects. The magnetic field at the central region was measured with an NMR teslameter (EFM-3000AX of Echo Electronics) [71] during the experiment for the correction of the field fluctuation in the offline analysis. The precision of the NMR probe is 1.0×10^{-6}. The magnetic field was set to 2.5 T, which corresponded to the current of 400 A, in the present experiment. The details of those detectors will be given in the following subsections.

Trigger and particle identification counters

In order to select the particles on the hardware trigger, three kinds of trigger counters (TOF, AC1–2, and LC) were used. The specifications of the trigger counters were listed in Table 2.8. Charged particles

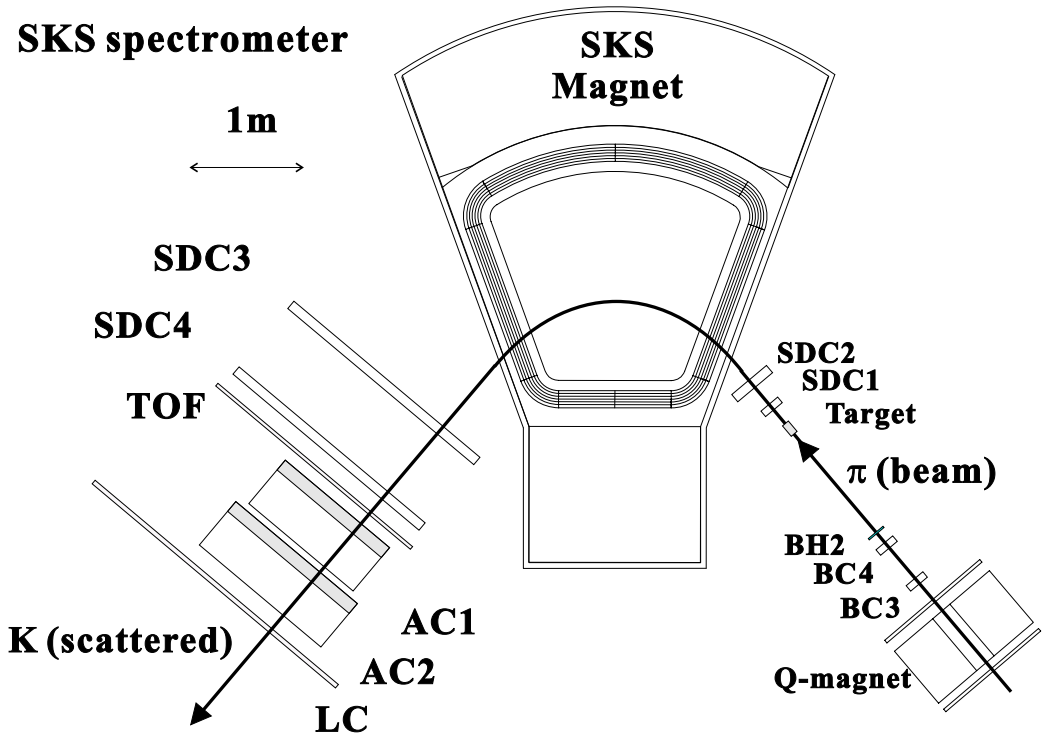

Figure 2.25.: Detector setup of SKS [64].

are detected by TOF. A Lucite counter (LC) and Aerogel counters (AC1–2), of which refractive indices are 1.49 and 1.05, respectively, function as threshold-type Čerenkov counter. Since the momentum of scattered kaon ranged in 0.75–1.1 GeV/c in the present experiment, kaon was over the threshold of Lucite and under the threshold of Aerogel counter, as shown in Fig. 2.26. Thus, a Lucite and Aerogel counters were served to distinguish proton from kaon and kaon from pion, respectively. Further, the time-of-flight between TOF and BH2 was used to identify the particle in an offline analysis.

Time-of-Flight Counter (TOF)

The time-of-flight wall counter (TOF) was used for the scattered particle identification, which was located just behind of SDC4, the most downstream tracking device. Figure 2.27 shows a schematic view of the TOF counter. It was segmented into 32 vertical pieces of $70 \times 1000 \times 30$ mm^3 plastic scintillators. Two fast photo multiplier tubes (Hamamatsu H1949) viewed each scintillator from both ends through 200 mm-long light guides. The typical time resolution between BH2 and TOF was about 200 ps in rms, including the two counters and readout electronics, which is good enough to separate the scattered pions, kaons and protons.

Aerogel Čerenkov Counter (AC)

The aerogel Čerenkov counters (AC1 and AC2) are silica aerogel Čerenkov counters to veto pions with a threshold of 0.4 GeV/c, as shown in Fig. 2.26. They were installed behind of the TOF wall. Figure 2.28 shows a schematic view of AC2. The sensitive area of AC1 was $1050 \times 1200 \times 113$ mm^3 and that of AC2 was $1400 \times 1400 \times 113$ mm^3. The Čerenkov radiator was composed of silica aerogel tiles (SP-50 of Matsushita Electric Works). The refractive index of a silica aerogel was 1.05. Each tile was

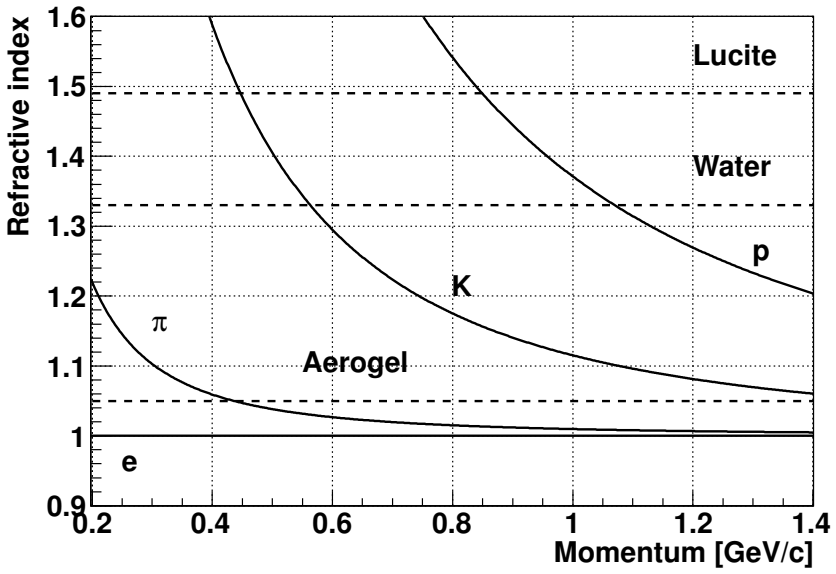

Figure 2.26.: Threshold of refractive index for Čerenkov radiation as a function of the particle momentum [63].

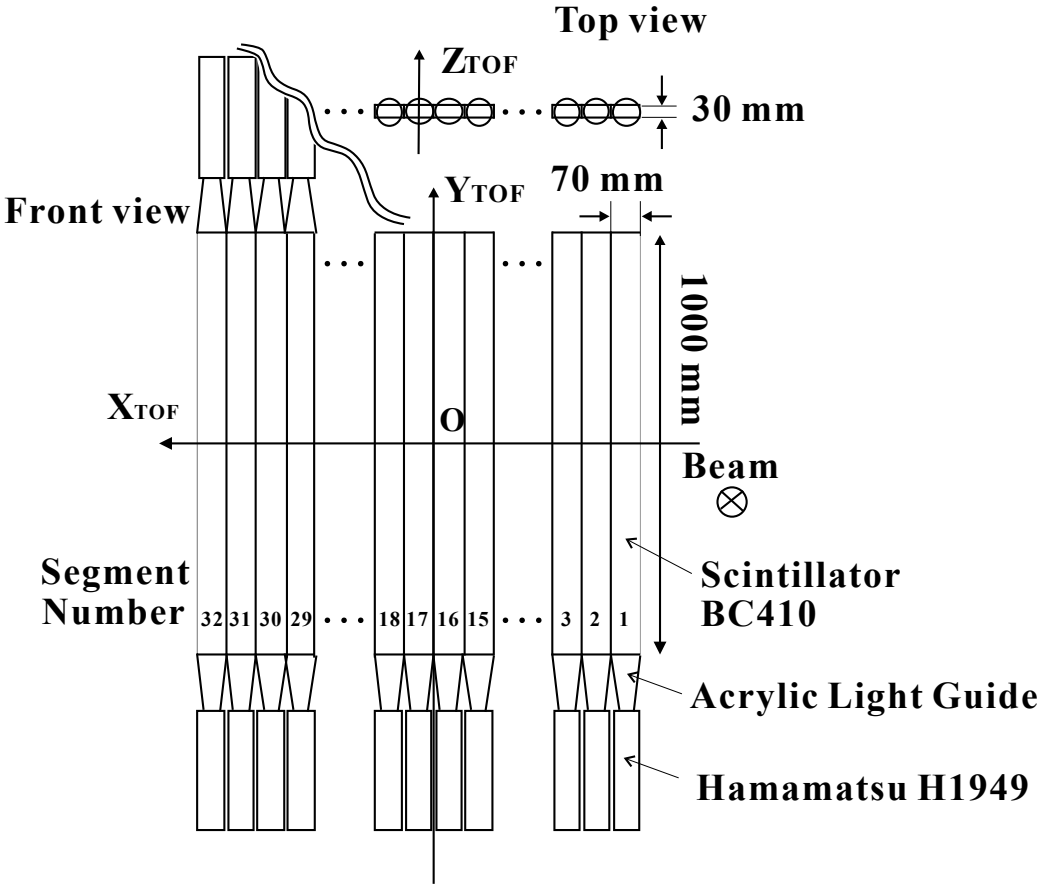

Figure 2.27.: The schematic view of TOF [63].

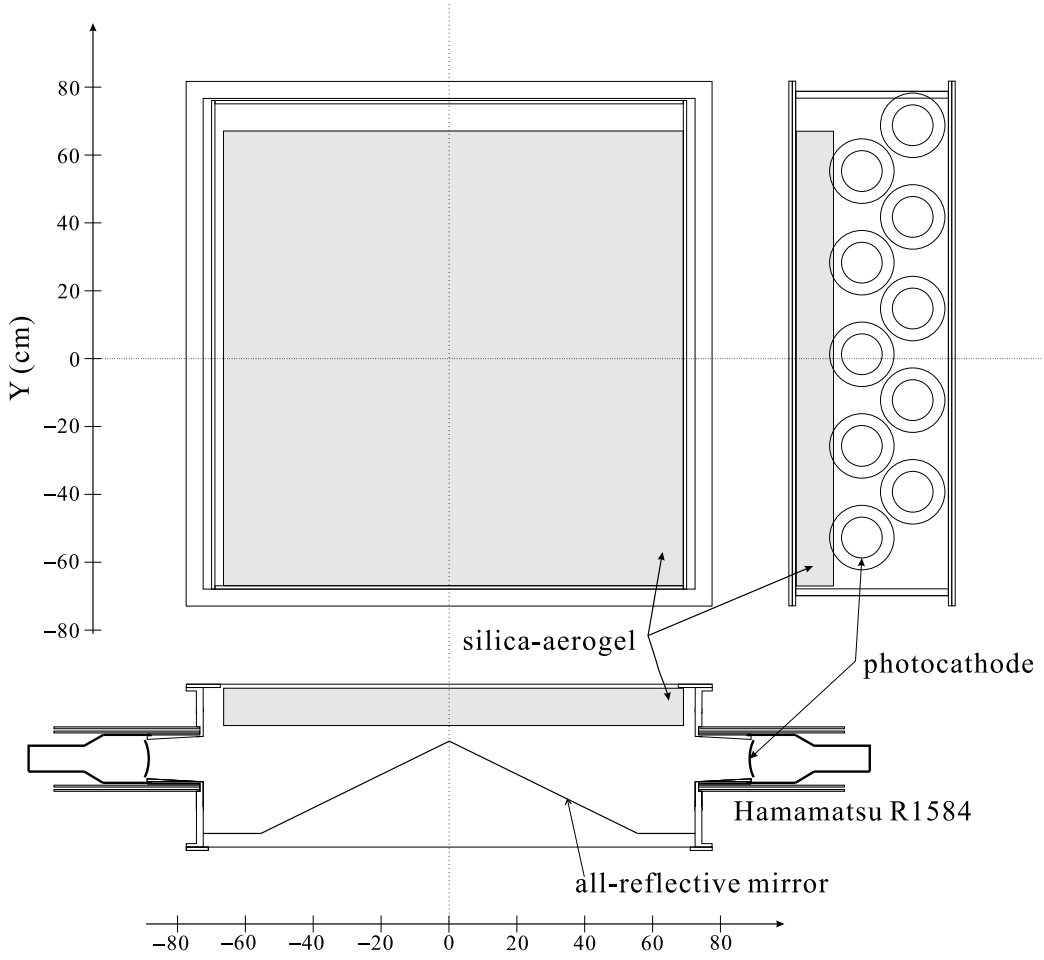

Figure 2.28.: The schematic view of AC2 [63].

a rectangular shape of 113×113 mm^2 with the thickness of 10 mm. About 1400 and 1600 tiles were packed in AC1 and AC2. The inner surfaces of the counter boxes were covered with aluminized Mylar sheets [92]. For AC1 and AC2), we used 18 and 20 phototubes (Hamamatsu R1584-02) which were sensitive to single photo electron. The mean photo-electron number was about six.

Lucite Čerenkov Counter (LC)

The lucite Čerenkov counter (LC) is a threshold-type Čerenkov counter comprising 28 vertical pieces of $100 \times 1400 \times 40$ mm^3 Lucite radiator with the refractive index of 1.49. Figure 2.29 shows a schematic view of LC. Each segment is equipped with fast phototubes on the top and bottom sides. It was installed just down stream of AC2. A wave-length shifter of bis-MBS was mixed by 10 ppm in weight in the lucite radiator in order to keep the detection efficiency for pions and kaons with various incident angles. Although the threshold momentum for protons is 0.85 GeV/c, LC is slightly sensitive to protons below the threshold due to the scintillation of the wavelength shifter.

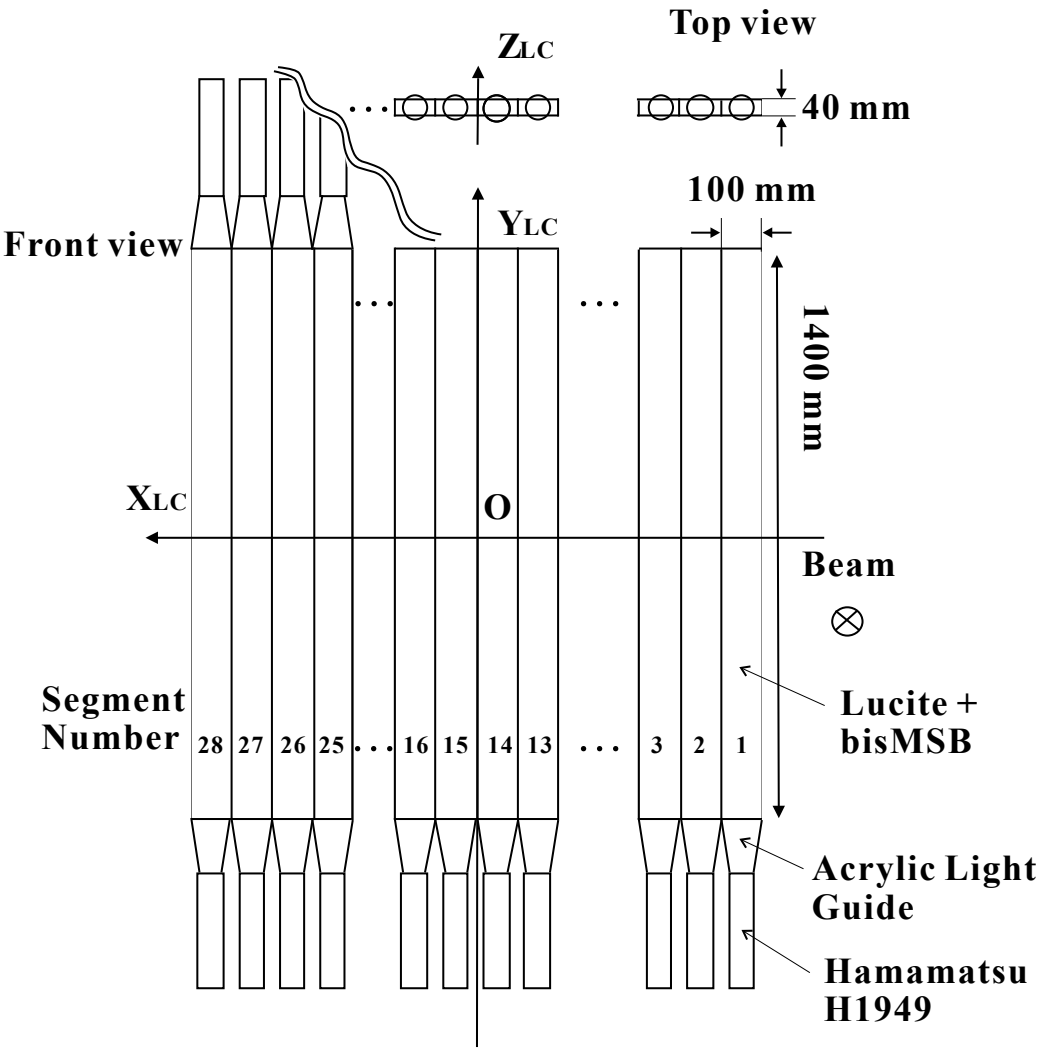

Figure 2.29.: The schematic view of LC [63].

Drift chambers (SDC)

SDC1-2

The drift chambers (SDC1 and SDC2) were installed at the entrance of the SKS magnet. Since they were exposed to the beam, they must have the high rate capability in the same level as that of BC3, 4. The structure of SDC1 and that of BC3 were identical but only two sets of pair planes ($UU' - VV'$) were included for SDC1 instead of three sets. In contrast, the SDC2 had a larger active area to detect scattered particles effectively and composed of three sets of pair planes ($XX' - UU' - VV'$) whose anode spacing was 5 mm. The gas mixture and readout electronics for SDC1, 2 were also same as those of BC3.

The operation of SDC1, 2 was the same as that of BC3, 4.

SDC3-4

In order to detect the particle trajectory after a bent by the SKS magnet covering the wide acceptance for the scattering angle and momentum, large drift chambers were placed as SDC3 and SDC4. They were reuse of BD chambers at the Brookhaven National Laboratory Alternating Gradient Synchrotron (BNL-AGS) D6 beam line. The active area was a square window of $2140^W \times 1140^H$ mm^2, which is twice as large as the horizontal length of the previous ones at KEK. Each chamber had six layers with three different wire orientation ($V - X - U - V - X - U$), where X, U and V wires were tilted by 0^o, $+30^o$ and -30^o from the vertical direction, respectively. Figure 2.30 shows its cell structure. The anode wire was a gold-plated tungsten wire ($\phi 25$ μm). All anode wires were replaced with the thicker ones (20 μm $\rightarrow$ 25 μm) for more strength. The neighboring sense wires were 20.0 mm apart. The field and cathode wires were gold-plated copper-beryllium ($\phi 80$ μm). The cathode wire pitch was 2 mm. The cathode wires were grounded, while the field wires and the anode wires had a negative and a positive potential difference, respectively.

The frontend readout electronics of SDC3 consisted of preamplifier boards (PA board, type FPF-229B) attached to the chamber and postamplifier/discriminator boards (PAD board, type FPF-227B) plugged into a 6U Eurocard height crate, which were located near SDC3 with twisted-pair cables of 3-7 m length bridged between PA boards and PAD boards. The PA board employed the Fujitsu MB43468 monolithic charge-sensitive amplifier chip [74]. This chip had four channels housed in a package. Each PA board contained four of these chips. The preamplifier chip converted a negative input charge pulse into a positive output voltage pulse, then the voltage was transformed into differential signals. These signals were further amplified and discriminated by the PAD board. The discriminator part used a LeCroy MVL407, four-channel high-speed voltage comparator chip, which output ECL signals. As for the SDC4, four channels of preamplifier, mainamplifier and discriminator were integrated in a mountable board (pre-/main-amplifier discriminator, PMD type FPF-244B) and attached to the chamber[3]. Figures 2.31(a), (b) and (c) show pictures of the frontend electronics cards.

The characteristic of the frontend electronics was summarized in Table 2.12. The ECL output signal was transferred to the K1.8 counting house with 45 m-long twisted-pair cables. The timing information of the SDC3-4 was digitized by the TKO Dr.T II TDC module as described in Sec. 2.6.

[3]LeCroy MVL407S, the smaller package of MVL407 was used on the FPF-244B.

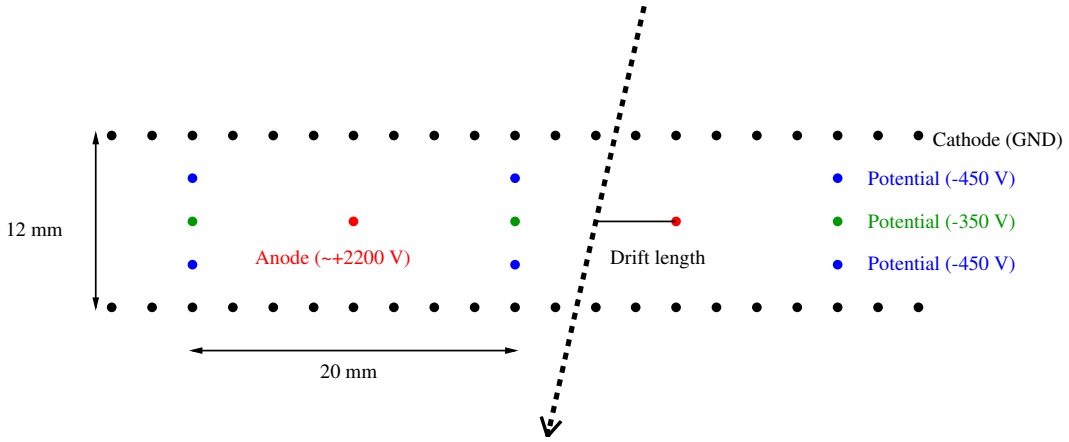

Figure 2.30.: Cell structure of SDC3 and SDC4 [64].

Table 2.12.: The characteristic of frontend electronics of SDC3·4

input	
amplifier type	charge sensitive
input polarity	negative
input coupling	AC
dynamic input capacity	375 pF
preamp gain	333 mV/pC
rise time	13 nsec
fall time	18 nsec
discriminator output	
logic	ECL (low: -1.6 V, high: -0.8 V)
hysteresis voltage	5 mV
minimum pulse width	10 nsec
power requirements	
+8.0 V / 13 mA	
+5.6 V / 140 mA	
+6.0 V / 200 mA	

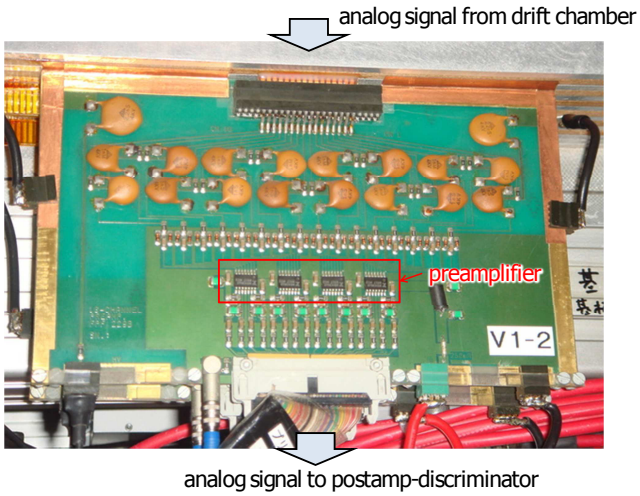

(a) preamplifier (PA) board FPF-229B.

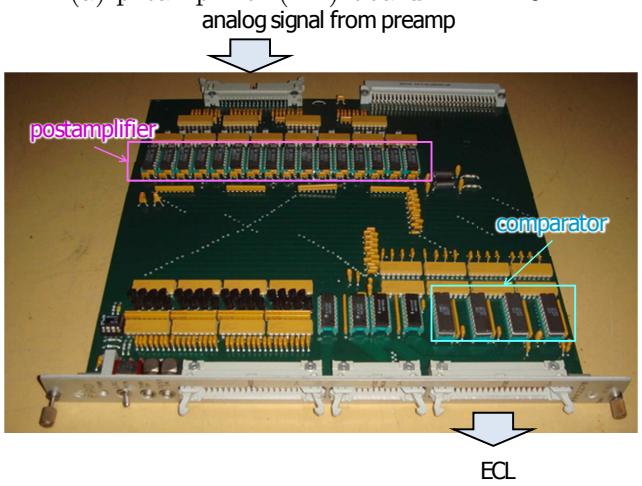

(b) postamplifier and discriminator (PAD) board FPF-227B.

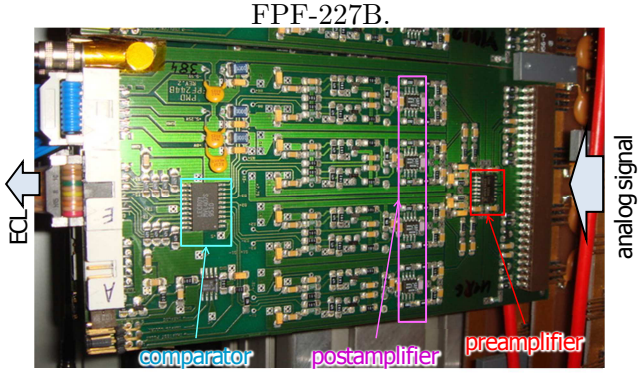

(c) preamp-/postamp- discriminator (PMD) board FPF-244B.

Figure 2.31.: Pictures of frontend electronics for SDC3·4 [63]. (a) preamplifier board (PA board, type FPF-229B). (b) postamplifier and discriminator board (PAD board, type FPF-227B). (c) preamp-/postamp- discriminator (PMD board, type FPF-244B).

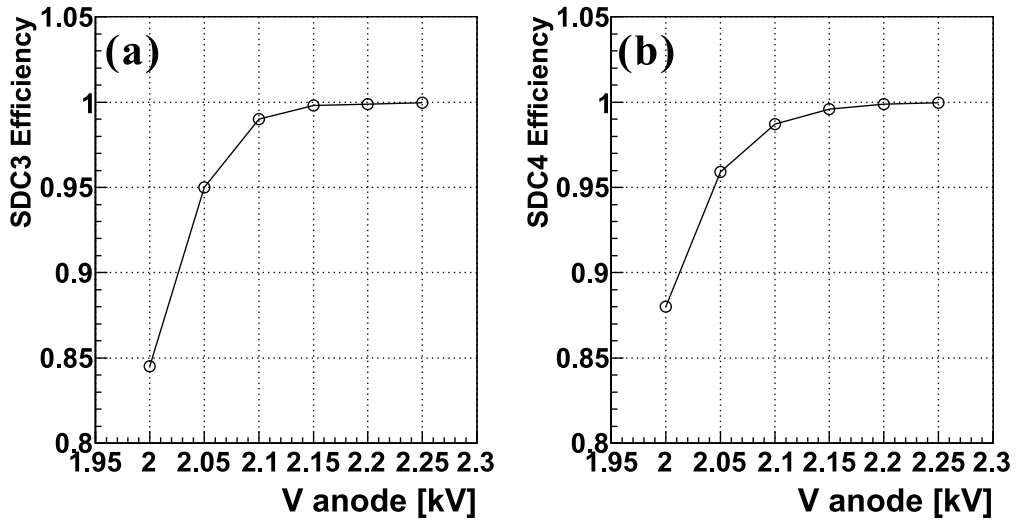

Figure 2.32.: The detection efficiency versus high voltage on anode [64]. (a) SDC3. (b) SDC4.

Operation of SDC3-4

Figure 2.32 shows the detection efficiency curves of one of the SDC3 and SDC4 layers as a function of the anode wire potential measured for a low-intensity π beam ($\sim$ 10 kHz). The gas mixture of argon(50%) + ethane(50%) was flowed. The high voltage was set to +2.2 kV for the anode and -450 and -350 V for the potential wires as shown in Fig. 2.30 in the present experiment. The HV lines were modified so that the operation can be partly turned off the beam passing area according to the experimental conditions.

2.5. Trigger

In this experiment, we used the (π, K) and several other triggers for obtaining various kinds of calibration data, all of which consisted of only the Level-1 (hardware) trigger. Since cross section of the background reactions, such as the (π, π) and (π, p) reactions, are typically two or three orders of magnitude larger than that of the (π, K) reaction, a powerful trigger system for scattered kaon detection was adapted for the efficient data acquisition. Since the beam particles have almost the same momentum, the particle identifications were performed by the velocity β, using scintillation counters and threshold type Čerenkov counters. In this experiment, the (π, K) trigger was comprised of three kinds of counters in the beam spectrometer (BH1, BH2, BGC), and three kinds of counters in the SKS system (TOF, AC1·2 and LC), as mentioned above. In addition, the 2-dimensional matrix coincidence trigger, which was made of a particular combination of the TOF and LC segment, was used to reduce a trigger rate.

The π beam trigger was defined as:

$$\mathrm{BEAM} \equiv \overline{\mathrm{BGC}} \times \mathrm{BH1} \times \mathrm{BH2} \tag{2.4}$$

BH1 and BH2 had two PMTs at both end, and then mean timer modules were used to remove the incident position dependence of the trigger timing. The proton contamination was completely rejected

by precisely adjusting the coincidence timing between BH1 and BH2 with a coincidence width of about 5 nsec. This was possible for the momentum of less than 1.5 GeV/c, where the delay of protons to pions was $\sim$7 ns for the path length between BH1 and BH2.

As described in Sec. 2.4, the TOF is sensitive to any charged particles, the AC1 and the AC2 are sensitive only to pions, and the LC is insensitive to protons with the slow or moderate momentum region (less than 0.85 GeV/c). Therefore the definitions of triggers which include π, K, p as scattered particles are represented as follows;

$$\begin{aligned} \mathrm{PION} &\equiv \mathrm{TOF} \times \mathrm{AC1} \times \mathrm{AC2} \times \mathrm{LC} \\ \mathrm{KAON} &\equiv \mathrm{TOF} \times \overline{\mathrm{AC1}} \times \overline{\mathrm{AC2}} \times \mathrm{LC} \\ \mathrm{PROTON} &\equiv \mathrm{TOF} \times \overline{\mathrm{AC1}} \times \overline{\mathrm{AC2}} \times \overline{\mathrm{LC}} \end{aligned} \tag{2.5}$$

The (π, K) trigger was defined as

$$\mathrm{PIK} \equiv \mathrm{BEAM} \times \mathrm{KAON} \tag{2.6}$$

Mean timer modules were also used to remove the time fluctuation of the TOF and LC counters. The PIK trigger logic diagram is shown in Fig. 2.33. Note that not the all segments of TOF and LC were involved in the trigger. Since the sensitive area of AC1,2 was smaller than those of TOF and LC counters in the present experiment, the TOF and LC segments used in the trigger were restricted after precise adjustment of their coverage considering the scattered particle momentum and the trigger rate. The active segment ID of TOF and LC ranged from 11 to 32 (last) and from 10 to 28 (last), respectively.

The (π, π) trigger was defined as

$$\mathrm{PIPI} \equiv \mathrm{BEAM} \times \mathrm{PION} \tag{2.7}$$

The BH2 timing was used as the common-START/STOP signal of the TDC modules and determined the gate timing of the ADC modules, except for SDC3-4. The TOF counters' timing was used for the common-stop of SDC3-4's TDC because the flight time from BH2 to TOF extended over a wide range according to a variety of flight paths and momenta of scattered particles.

Matrix trigger

For the (π^-, K^-) reaction with the momentum of 1.92 GeV/c, we found background particles which were produced after the beam hit the coil vessel of the SKS magnet. Those particles passed the TOF and LC counters and contaminated the (π^-, K^-) trigger, because they were mostly of low momentum pions whose velocity was higher than that of the LC threshold, but below the threshold of AC1 and AC2 resulting in a fake kaon. Figure 2.34 shows beam trajectories with a momentum of 1.92 GeV/c which are generated by the Geant4 code by taking account of the beam profile and momentum bite measured in the experiment. From this simulation, about 10% beam particles hit the SKS magnet.

Figure 2.35 shows the hit pattern of TOF for the (π^-, K^-) reaction data. The black and red lines were all the PIK trigger and the true scattered K events, respectively. The true K events were selected by the SKS tracking analysis. The typical trigger rate of the (π^-, K^-) reaction with the beam

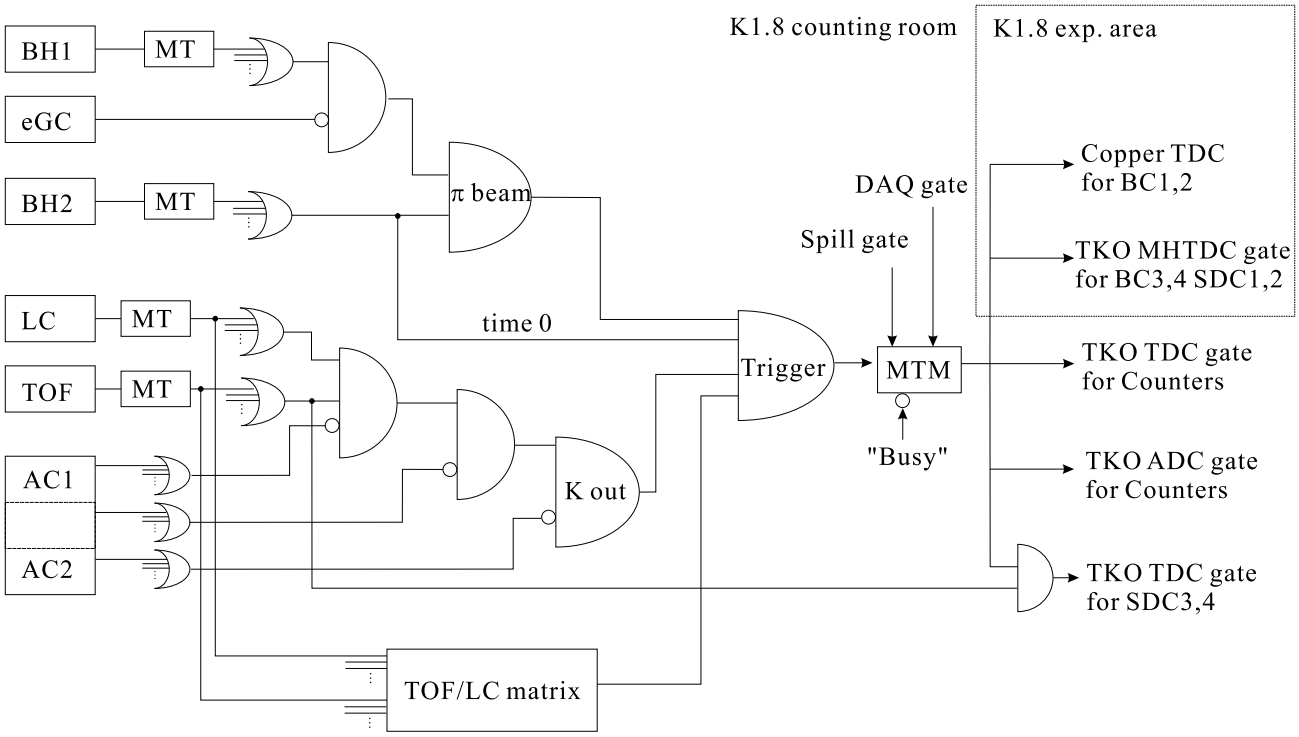

Figure 2.33.: The trigger logic diagram of the (π, K) reaction [63].

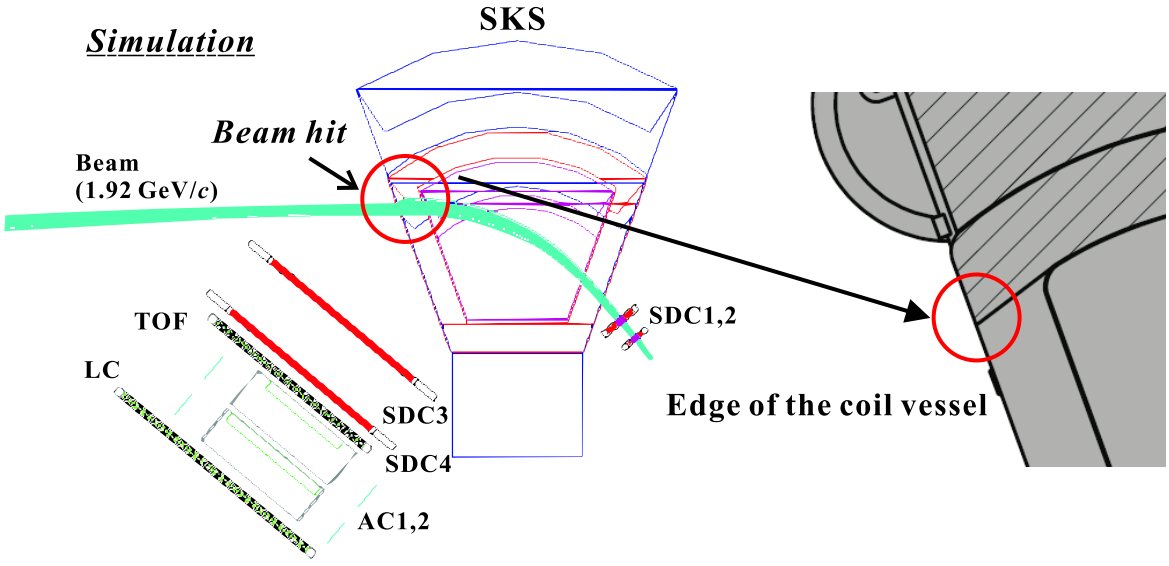

Figure 2.34.: The beam trajectories with the momentum of 1.92 GeV/c (simulation) [63].

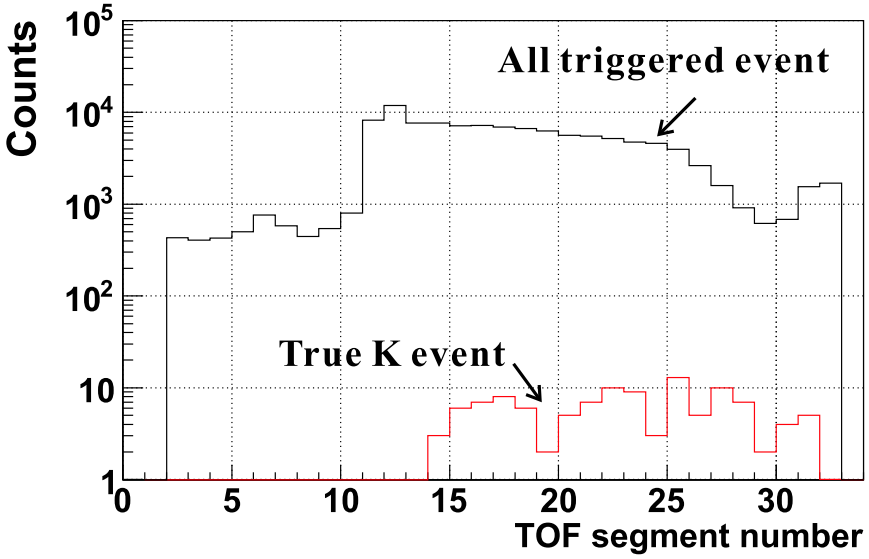

Figure 2.35.: The hit pattern of TOF for the (π^-, K^-) reaction [63]. The vertical axis corresponds to the typical statistics for 3×10^8 beam pions.

momentum of 1.92 GeV/c was $\sim$ 1k/spill, which could not be acceptable for the present DAQ system. The trigger rate had to be less than 0.4 k/spill.

Since those events could not be rejected by using the PIK trigger only, we applied a matrix coincidence trigger using the hit combinations between the TOF and LC counter. The trajectories of the background particles were localized and thus are reflected as a particular correlated hits of TOF and LC counters. Figure 2.36 shows typical trajectories of the background particles and the relation between the segment ID of TOF (TOF$_i$) and LC (LC$_j$) counters.

For constructing a matrix trigger, we used not the conventional NIM modules but a FPGA module, TUL-8040 (Tohoku Universal Logic Module) [75], which utilized a FPGA of Altera APEX EP20K300EQC240-1X as shown in Fig. 2.37. The logic is programmable and can be generated with a delay of 20 ns. Figure 2.38 shows the hit correlation of TOF and LC segments. In this figure, the events which contributed to the true (π, K) trigger were illustrated by red solid lines, while the background events was surrounded by a circle.The trigger rate was decreased from $\sim$800/spill to $\sim$150/spill at the beam intensity of 1 M/spill for the (π^-, K^-) reaction with the liquid hydrogen target. This trigger rate was acceptable for the present DAQ system. In the (π^-, K^-) data, we included the 1/10-prescaled PIK trigger without the matrix coincidence to study inefficiency of the matrix trigger.

In the present experiment, typical Level-1 trigger latency was $\sim$ 600 nsec and the trigger rate for the (π^-, K^-) data was $\sim$350/spill including the prescaled PIK, (π^-, π^-) and BEAM trigger.

2.6. Data acquisition system (DAQ)

The data acquisition system (DAQ) was constructed with the TKO [76], VME [77] and COPPER [78] based front-end electronics. Figure 2.39 illustrated a diagram of the data acquisition system.

The signal pulses of trigger counters were digitized with high resolution TDC (RPT-140) and charge

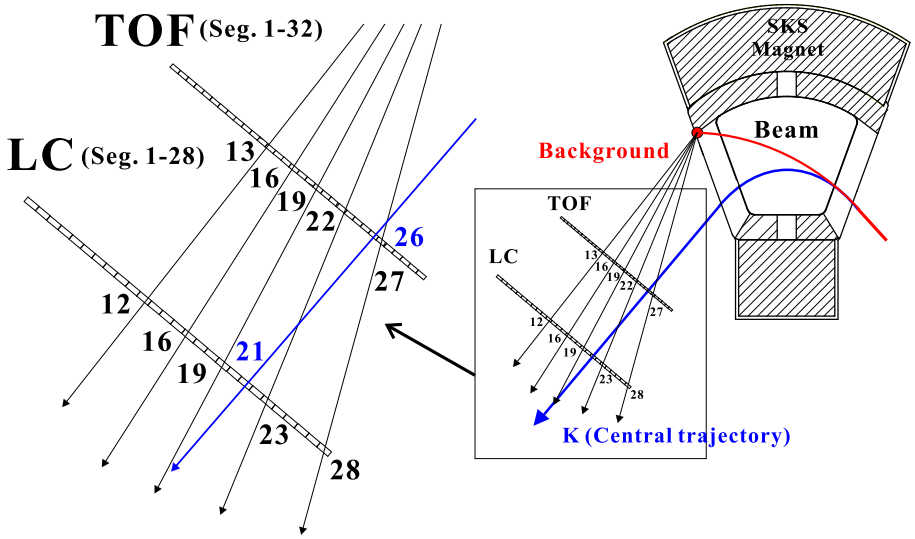

Figure 2.36.: Typical trajectories of the background particles and the relation between the TOF and LC segment [63].

sensitive ADC (Hoshin electronics) modules in the TKO (TRISTAN/KEK Online) boxes. The TKO is a standard developed at KEK. The signals from SDC3-4 were fed into the TKO drift chamber TDC (Dr.T II, RPT-040) modules while those from BC3-4 and SDC1-2 were sent to TKO Multi-hit TDC (MHTDC, GNT-050) modules, on which the ATLAS Muon TDC version 2 (AMT-2) chip [79] was used to digitize the leading-edge information. The common signals in a TKO-box, such as a ADC/ TDC gate signal, a fast clear signal and threshold voltage of the BC4's ASD cards, are distributed via the TKO-GONG (GO/NoGo). The VME-SMP (Super Memory Partner) [80] modules work as an interface module between the VME (Versa Module Eurocard) bus and the TKO bus via the SCH (Super Controller Head) module which was installed in each TKO box. There were nine SMP and TKO boxes, two of them handled high resolution TDC and ADC, three of them for Dr.T II and four of them for MHTDC. Once the trigger signal was supplied to the ACCEPT input in the front panel of SMP, data scan for all the channels of ADC's and TDC's in the TKO box was performed by SCH, and the scanned data were stored in the local memories in SMP's. A busy signal was issued by SMPs during the scanning of the data, and further triggers were prohibited by the trigger control system. The stored data in SMPs were transferred to a VME single board computer (1.8 GHz Intel Pentium M processor on GE Fanuc V7807RC) which was installed in each VME subrack. There were three VME-CPUs, two of them dealt with TKO modules event by event and the other read the VME-scaler (V820/ V830) at the spill end. The scalers recorded single counts of each trigger counter. Unfortunately, TKO MHTDC had a problem that a trigger matching time window for hit signals was not adjustable. All hit information after the last clear signal occupied the buffer of AMTs or a FIFO chip on the board, which caused a buffer overflow and/or long data transfer time from MHTDCs to a VME-CPU. In order to prevent the overflow and to recover DAQ live time, fast clear signals were sent to all DAQ modules periodically every 10 μsec. BUSY time caused by the clear sequence needed about 800 nsec duration including the time of signal distribution to all the end points, thus, we lost about 8% beam time in the present experiment due to the MHTDC-problem.

The hit information on the BC1-2 were sampled by the MWPC encoder mounted on the COPPER

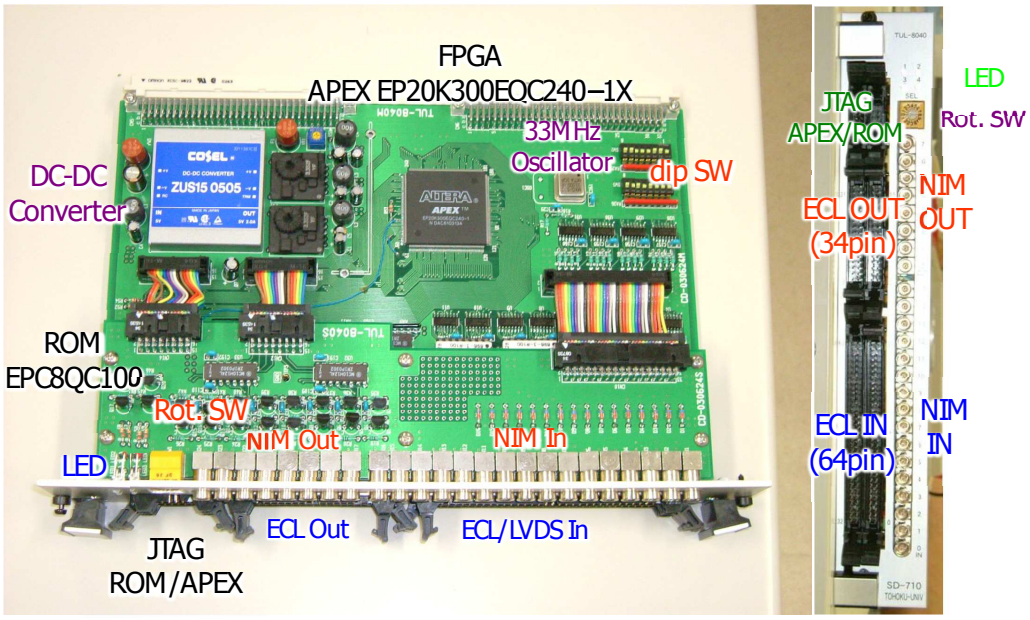

Figure 2.37.: A photograph of TUL-8040 [75].

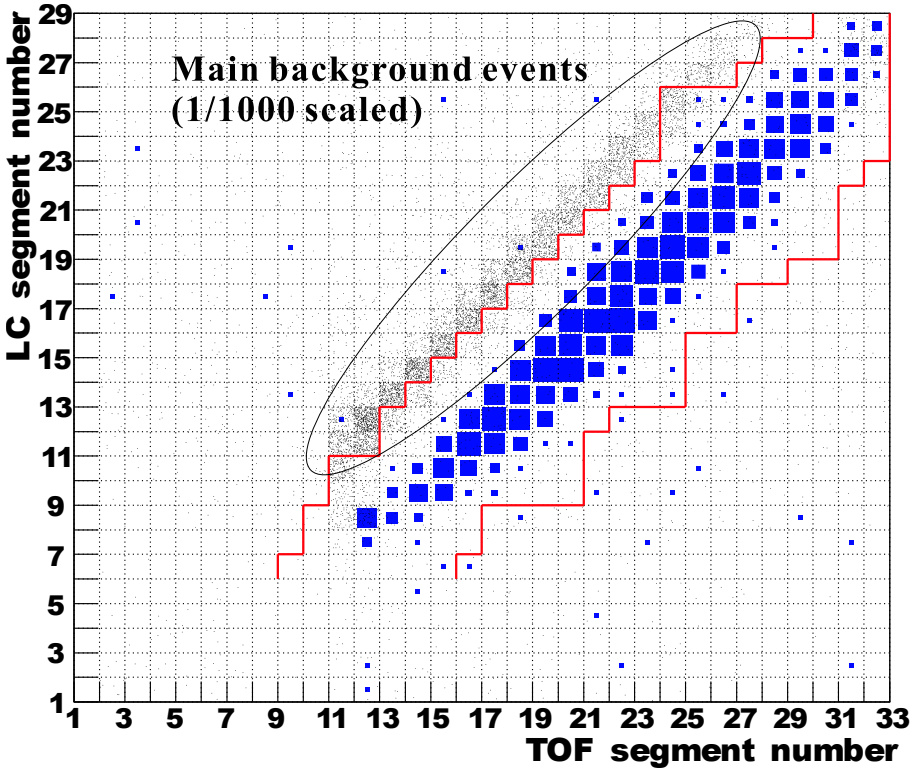

Figure 2.38.: The selected region for the matrix trigger is indicated in red lines [63]. The K^- events are shown in blue squares. The main distribution of the background events are indicated by circle.

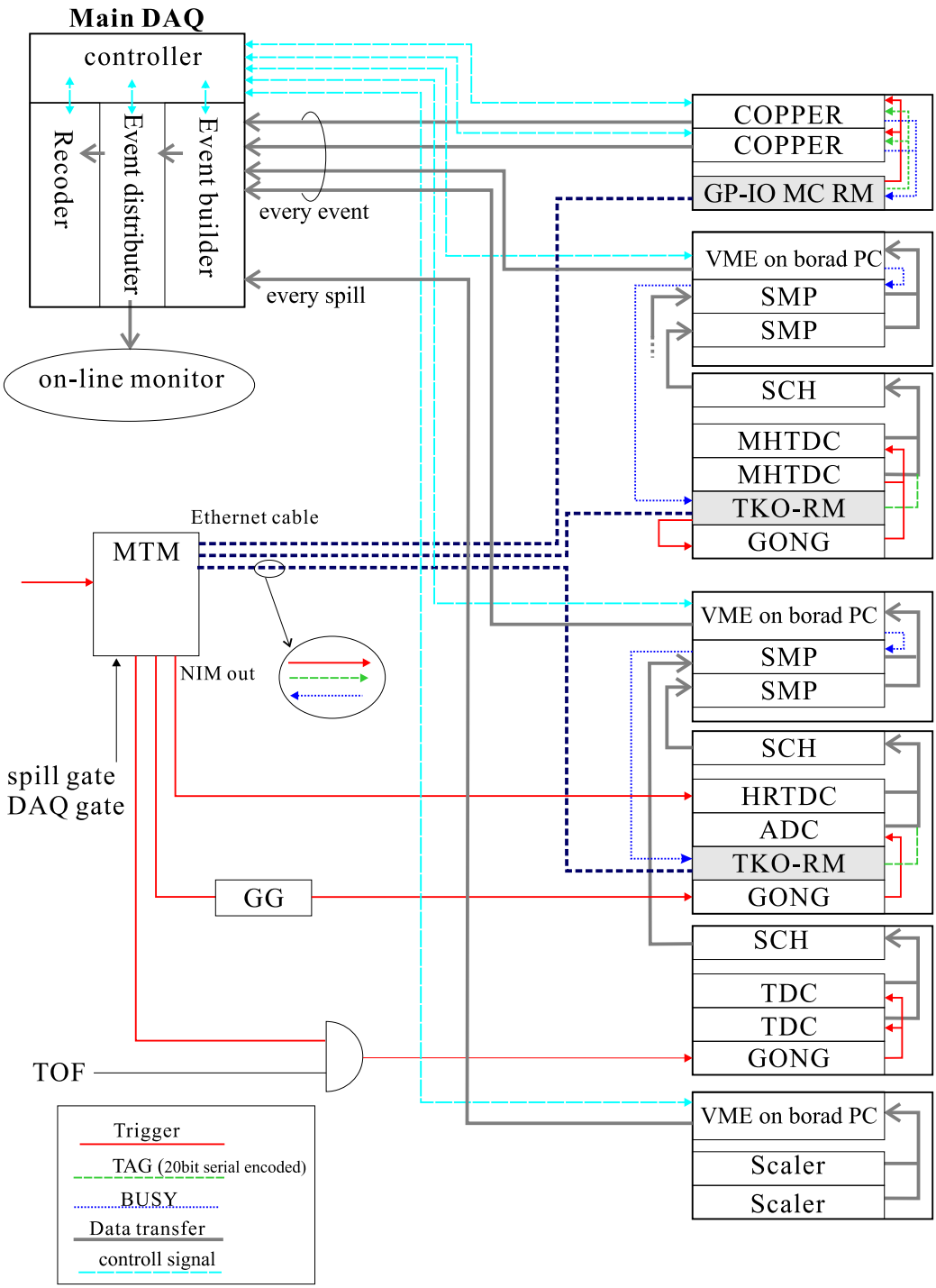

Figure 2.39.: Diagram of the data acquisition system [64].

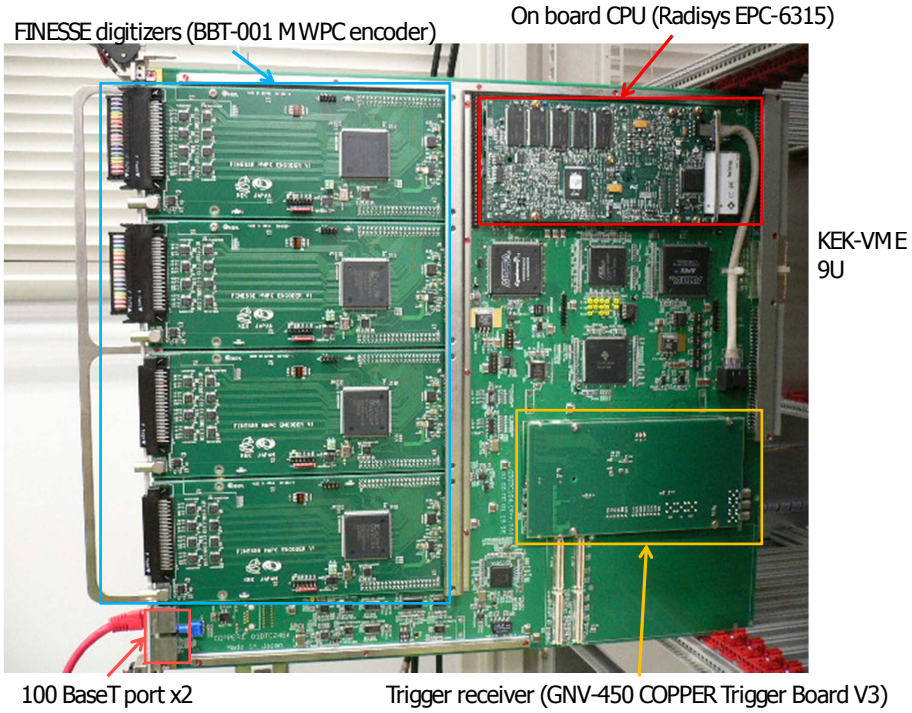

Figure 2.40.: Picture of a COPPER-II board [63]. A prPMC, four FINESSE MWPC encoder cards and a trigger card are shown together.

boards. COPPER (COmmon Pipelined Platform for Electronics Readout)is a new unified data acquisition platform based on the KEK-VME specification that realizes various types of analog-to-digital conversion and pipelined digital data processing functions. The FINESSE (Front-end INstrumentation Entity for Sub-detector Specific Electronics) card of 100 MHz sampling MWPC encoder (BBT-001) was developed in collaboration with the KEK electronics system group. The data from FINESSE's on each COPPER were collected to the processor PCI Mezzanine Card (prPMC, 800 MHz Intel Pentium III processor-M on RadiSys EPC-6315) and sent through FastEthernet to the event builder host. 24 COPPER boards were used to process the signals from BC1-2. A picture of a COPPER-II board with 4 FINESSE cards is shown in 2.40.

Since we have to use several types of the readout systems based on CAMAC/FERA, VME bus, TKO, and KEK-VME/COPPER at the early stage of J-PARC hadron experiments, we have developed network-based DAQ software [81]. The TCP/IP and Ethernet have been widely used in readout systems and the traditional systems can be used together with the KEK-VME system by using network bridges. The DAQ software works with a number of simple function processes (Event-Builder process, Event-Distributor process and Recorder process) and they communicate with each other using two pathways that we call DATA PATH and MESSAGE PATH as shown in Fig. 2.41. The DATA PATH consists of the Front End process (FE), the Event Builder process (EB), the Event Distributor process (ED), the Recorder process and the online monitor process. FE is defined as the process which reads data from A/D conversion devices and sends them to a next stage process; for example, the DAQ process on the COPPER and the VME-CPU correspond to the FE. The EB collects the data fragments from each FE node and builds events, then sends them to the ED. The ED has two ports of data output; one is a recorder port and the other is a monitor port. The former sends all

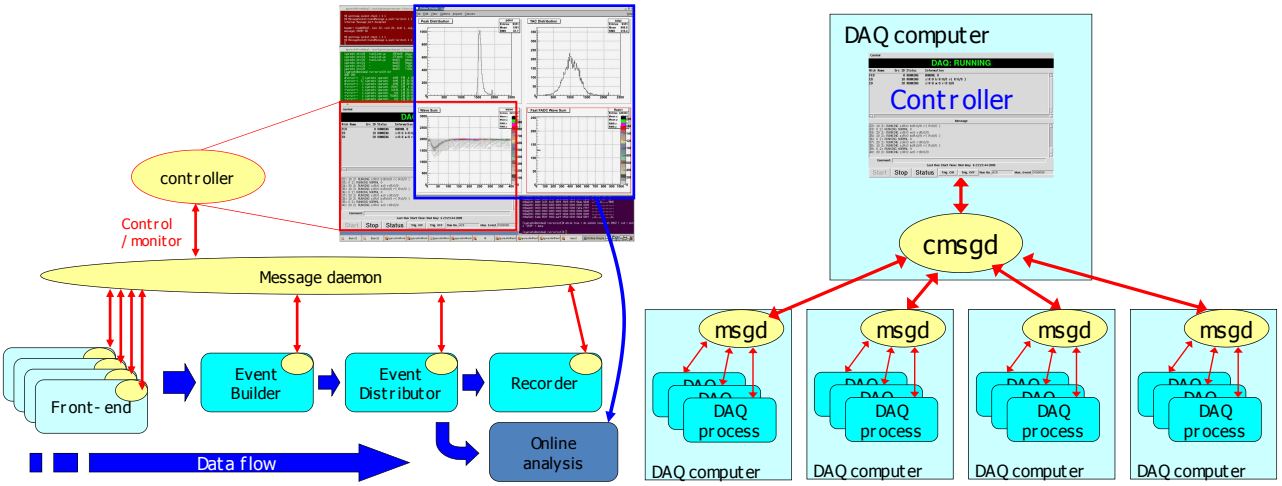

(a) DATA PATH. (b) MESSAGE PATH.

Figure 2.41.: Schematic view of the DAQ software [81]. (a) DATA PATH. (b) MESSAGE PATH.

data to the connected process. On the other hand, the latter is a best-effort service type and may skip some events when the connected process do not finish reading the previous event. The recorder process receives all data from the ED and write them to the storage device of the hard disk drive, The online monitor is not controlled by the Message-handling scheme and it can start and connect to the ED output port anytime. The MESSAGE PATH is a pathway for the slow control and the monitoring DAQ processes. It consists of three types of processes; MSGD, CMSGD and Controller. The MSGD works on each computer and mediates between the DAQ process on the DATA PATH and the CMSGD. The CMSGD works uniquely in the DAQ system and passes a message from the Controller to each MSGD and vice versa. The Controller is the control center of all the DAQ process. It manages the DAQ START/STOP and the global information such as the run number , and also displays the warning or alert messages when needed. All of the inter process communications use the TCP/IP protocol. These programs were developed in the standard C/C++ and POSIX library while the Graphical User Interface process to control and monitor these processes was written in the script language Python/Tkinter. The online monitor process was developed with the ROOT library [82]. The standard Linux operating systems were used in the DAQ processes. Scientific Linux 3 and 4 were used for the COPPER and the VME-CPU, respectively. The Event-Builder, the Event-Distributor, the Recorder and the online monitors were running on Scientific Linux 5 and/or 6.

In order to assure the data integrity of events built from the fragments of network distributed subsystems, we developed a trigger/tag distribution system (TDS) [81]. The TDS works with three types of modules, Master Trigger Module (MTM), Repeater and Receiver Module (RM). Figures 2.42(a), (b), (c) and (d) show photographs of TDS modules. The asynchronous timing signals and the serial data were driven by multipoint-LVDS (M-LVDS) drivers and transmitted through the pair of category-7 standard network cables. The global event tag consisted of the 12 bit event number and the 8 bit spill number, which were serialized and transferred by National Semiconductor DS99R105(Driver)/ DS99R106(Receiver) [83]. The speed of the serialized line is 224 Mbps. The data transfer delay time of the global event tag is 1.3 μs.

If the condition of the trigger logic described in Sec. 2.5 was satisfied, the logic signal was fed into

(a) MTM.

(b) TKO-RM.

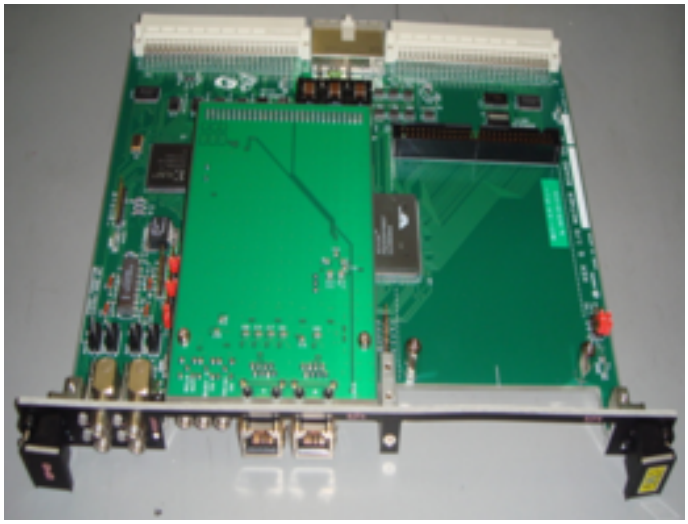

(c) KEK-VME GPIO-RM.

(d) Repeater module.

Figure 2.42.: Pictures of electronics modules for a trigger/tag distribution system [63]. (a) Master Trigger Module (MTM, GNN-570). (b) TKO Receiver Module (TKO-RM, GNT-060). (c) KEK-VME GPIO board (GNV-250) with a mezzanine card of Receiver Module (KEK-VME-RM, GNV-490). (d) Repeater module (GNF-0840).

MTM as the Level-1 trigger (L1), then MTM set the event latch as ”busy” and the L1 trigger were distributed to all RMs. When the RMs received the L1 trigger, the gates for ADC were opened and the common start (or stop) timing signals for TDC were generated and the digitization started. The ”busy” state of the event latch was kept until the clear signal was issued by the Level-2 trigger (L2). In the present experiment, all events which accepted at the L1 were also accepted at the L2. Therefore the L2 trigger was generated just after the A/D conversion of all modules in each subsystem, which took typically 100 μs. When the L2 trigger was sent to MTM, MTM serialized and transmitted the global event tag together with the L2 trigger to all RMs. Then, KEK-VME-RM distributed the L2 trigger and the global event tag to all FINESSE cards via the KEK-VME bus line, while the TKO-RM and VME-RM output the L2 trigger from the front panel and stored the global event tag at the own register. When the L2 trigger was passed to the frontend modules, the digitized data of detector signals were transferred together with the corresponding global event tag to the readout buffer on each subsystem.

In addition to the main DAQ, the monitor system for the magnetic field of spectrometer dipoles, K1.8 D4 and SKS, was running independently. A timestamp at the L1 accept was counted by a FPGA card (GN-0951-1) in a 10 ns unit and read out via the SiTCP [84] card (SOY-100M, BBT-006), which

Figure 2.43.: A picture of the timestamp counting cards (GN-0951-1 and BBT-006) [63].

Table 2.13.: Specifications of the liquid hydrogen target.

Size (mm)	ϕ 67.3 $\times$ 120^L
Capacity	427 cm^3
Target vessel	PET t=0.3 mm (cylinder)
	Mylar t=0.25 mm (end cap)
Chamber	aluminium t=3 mm, ϕ 270 mm
Window	Mylar t=0.25 mm
vacuum	$\sim 1.0 \times 10^{-7}$
LH_2 thickness	0.85 g/cm^2 = 0.0708 g/cm^3 $\times$ 12 cm
Mylar thickness	0.0695 g/cm^2 = 1.39 g/cm^3 $\times$ 0.025 cm $\times$ 2

is shown in Fig. 2.43. The recorded magnetic field values and corresponding timestamps were used in the offline analysis as described in Sec. 3.8.4.

2.7. Liquid hydrogen target

For the previous KEK-E522 experiment, a polyethylene target [$(CH_2)_n$] was used and the quasi-free K^- production from the ^{12}C nucleus made a background in the missing mass spectrum. We learned from the second experiment, KEK-E559 in which the $p(K^+, \pi^+)$ reaction was used, that it is advantageous to use a pure proton target for suppressing the background. Thus, J-PARC E19 used a liquid hydrogen target which was used in E559 [50].

Figure 2.44 shows a schematic view of the liquid hydrogen target. Its cooling system uses liquid helium. The hydrogen vessel was made from PET (polyethylene terephthalate) of 0.30 mm thick for the cylinder part, and Mylar of 0.25 mm thick for the end cap. The target dimensions were 67.3 mm in diameter and 120 mm in length. During the experimental period, the volume and the pressure of the target were monitored and the stability of the density was $\Delta\rho/\rho \sim 10^{-5}$. Specifications of the liquid hydrogen target were listed in Table 2.13.

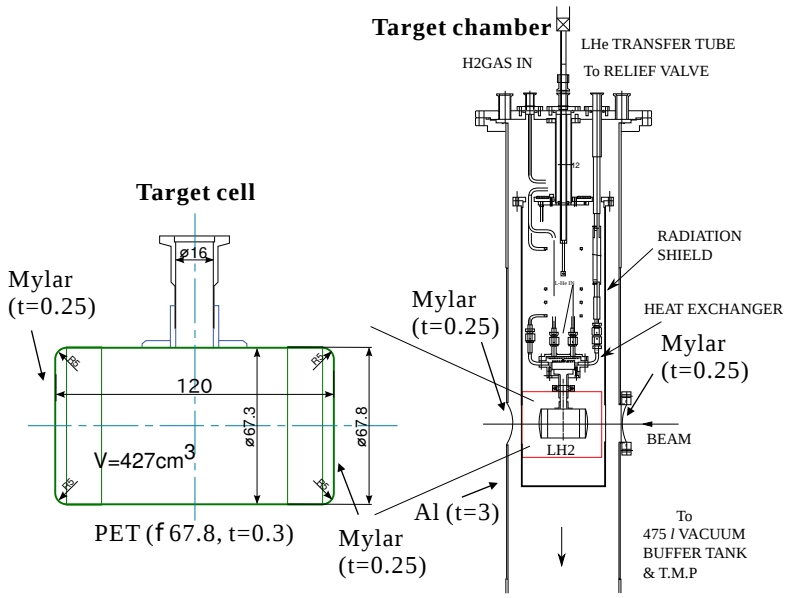

Figure 2.44.: Schematic view of the liquid hydrogen target (unit in mm) [63].

2.8. Data summary

The Θ^+ production data were taken in two cycles from October to November in 2010, as listed in Table 2.14. The total number of pions irradiated on the liquid hydrogen target was 7.8×10^{10}. At the beginning of the October beam time, we took $\Sigma^{\pm}$ production data using the liquid hydrogen target. The mass and cross section of $\Sigma^{\pm}$ are well known and thus the data serve as calibration for the missing mass and check of an entire system. Empty target data were also taken in the October cycle.

In the empty target run, we took beam-through data for the calibration of both spectrometers. Since the π beam passed through both spectrometers, we could estimated the difference of the scale and offset of the reconstructed momenta between the beam line spectrometer and SKS. The beam-through data were also taken with the liquid hydrogen target to check the energy loss effect in the target. To check the alignment of chambers at upstream and downstream of the target, we took the beam-through data without exciting the SKS magnet. The beam-through data were taken with the trigger in which the LC counter hit was not required so that the LC efficiency could be checked by this data. To check the efficiency of TOF and the over kill ratios of AC1·2, we took data with the trigger in which the hits of TOF or AC1·2 were not required. The control data were listed in Table 2.15.

Table 2.14.: Data summary. P_{Beam} is the beam momentum and N_{Beam} is the number of pions irradiated on the target. The $\Sigma^{\pm}$ production data, the empty target data and the 1st Θ^{+} production data taken in October. The 2nd Θ^{+} production data was taken in November after a week interval.

data	P_{Beam} [GeV/c]	reaction	target	N_{Beam} ($\times 10^9$)	data taking time (hours)
Σ^{+}	1.37	(π^{+}, K^{+})	LH_2	2.9	5
Σ^{-}	1.37	(π^{-}, K^{+})	LH_2	12	20
Empty	1.92	(π^{-}, K^{-})	–	4.6	10
Θ^{+} 1st	1.92	(π^{-}, K^{-})	LH_2	30	50
Θ^{+} 2nd	1.92	(π^{-}, K^{-})	LH_2	48	82

Table 2.15.: Data summary of the control data.

data	P_{Beam} [GeV/c]	reaction	target	comments
π^{-} beam through	0.75 – 0.95	—	—	calibration
π^{-} beam through	0.85	—	LH_2	target energy loss
π^{+} beam through	0.85	—	—	calibration
π^{+} beam through	0.85	—	LH_2	target energy loss
π^{-} beam through without SKS	0.85	—	—	alignment of chambers
TOF efficiency	1.92	(π^{-}, π^{-})	LH_2	TOF not required
AC1·2 over kill	1.37	(π^{-}, K^{+})	LH_2	AC1·2 not required

3. Data Analysis

3.1. Outline

Our purpose is the search for the Θ^+ through the missing mass measurement in the $\pi^- p \to K^- X$ reaction. In this chapter, the detailed procedures of the analysis are described.
The missing mass (M) of the (π, K) reaction is given as follows;

$$M = \sqrt{(E_\pi + M_A - E_K)^2 - (p_\pi^2 + p_K^2 - 2p_\pi p_K \cos\theta_{\pi K})} \tag{3.1}$$

where E_π and p_π are the total energy and momentum of a beam π, E_K and p_K are those of a scattered kaon, M_A is the mass of a target nucleus, and $\theta_{\pi K}$ is the scattering angle of the reaction, respectively. The missing mass can be obtained through the measurement of the three kinematic variables, p_π, p_K and $\theta_{\pi K}$, with the event by event track and momentum reconstruction.
Figure 3.1 shows a flow chart of the event reconstruction process. First, good (π, K) events were roughly selected from the PIK triggered events. An incident π was selected using the time-of-flight between BH1 and BH2 (Beam-TOF). A scattered K was roughly selected only using TOF and LC counters' information. The momentum measurements of π and K were carried out from the position and track information on BCs and SDCs, respectively. After the reconstruction of the particle trajectory inside the SKS magnet, the identification of K was performed through the mass calculation with the time-of-flight, the flight path between BH2 and TOF and the momentum. Then, the scattering angle and the event vertex point of the (π, K) reaction was calculated from the trajectories of π and K.
Before obtaining the missing mass distribution, the horizontal scale and the vertical scale of the spectrum were calibrated. The accuracy and the resolution of the measured missing mass were studied using the $\Sigma^\pm$ in the $\pi^\pm p \to K^+ X$ reactions. As for the cross section, various efficiencies and factors were evaluated. For the estimation of correction factors such as the spectrometer acceptance, the decay factor and the background level in the (π, K) events, the Monte Carlo simulation program based on the Geant4 [85] was used. Finally, search for a peak structure in the missing mass spectrum were carried out.

3.2. Analysis of beam particle

3.2.1. Particle identification of π^-

In the off-line analysis, the beam πs were selected by the time-of-flight between BH1 and BH2 (Beam-TOF). The time walk effect of the PMT output pulse height V on the time of particle hit t was calibrated as following,

$$t = t_0 + \frac{p_0}{\sqrt{V - p_1}} + p_2 \tag{3.2}$$

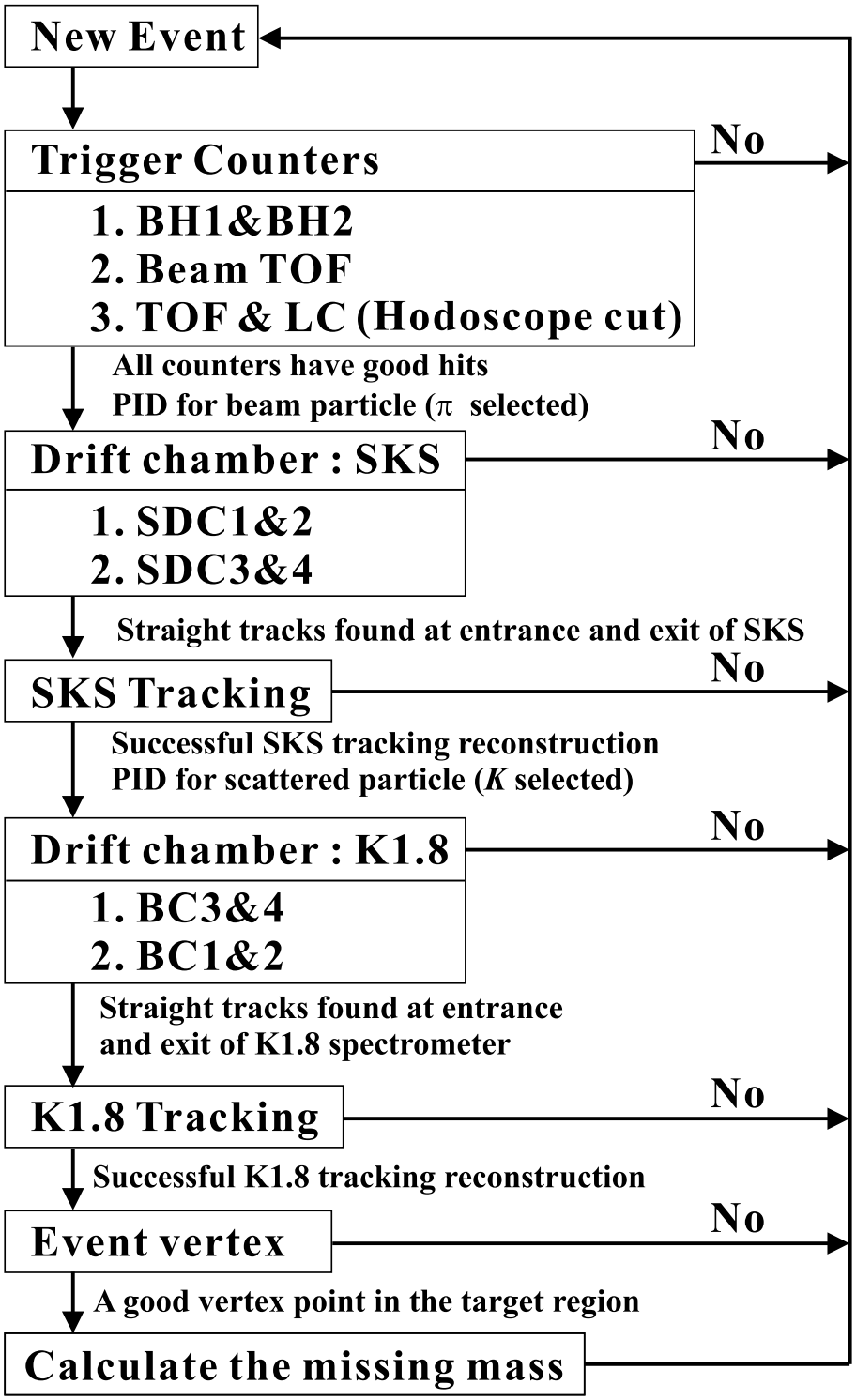

Figure 3.1.: Flow chart of the offline analysis [90].

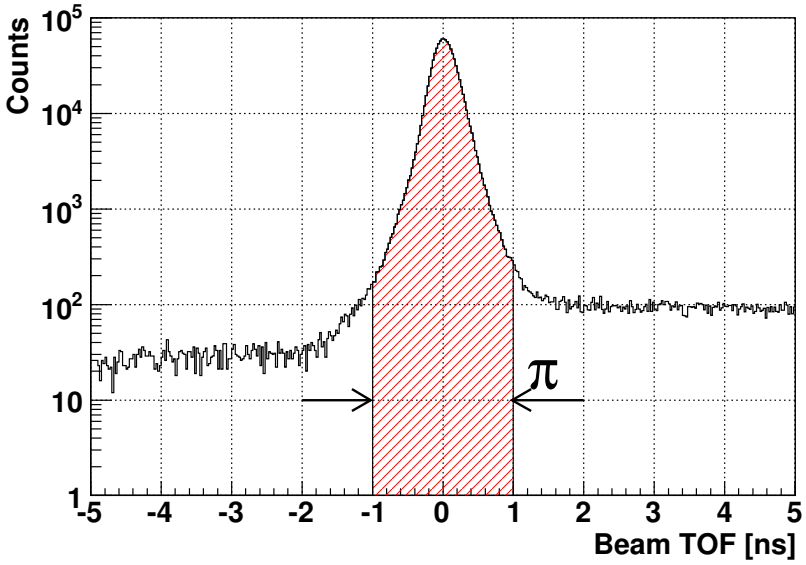

Figure 3.2.: Typical Beam-TOF spectrum of the incident particles. The arrows indicate the selection window for π^- meson, which corresponds to $\sim 5\sigma$ of its resolution.

where t_0 is the time information before slewing correction, and p_0, p_1 and p_2 are constant parameters determined by the data. Figure 3.2 shows the Beam-TOF spectrum of the incident particles after the pulse height correction, where the π peak was adjusted to be zero in the horizontal axis. A typical time resolution was 0.2 nsec (rms). $\pm 5\sigma$ region of its time resolution was selected as good events.

3.2.2. Beam track reconstruction

The beam momentum calculation begins with searching straight tracks locally at the entrance and the exit of QQDQQ using the data of BC1-2 and BC3-4, respectively.

MWPC hit clustering

The hit positions of each layer were calculated in a following procedure. The fired cell and time information was encoded in bit maps by the MWPC encoder. Since the encoder sampled logic signals from ASD cards with 100 MHz clock, the timing information in a unit of 10 nsec of leading edge, trailing edge and signal width (in other words, time-over-threshold, TOT) for each wire were obtained. Figure 3.3 shows a typical leading-edge time spectrum of one of the MWPC layers before and after clustering. Particles traversing the chamber at an angle to the anode plane generally produce a cluster of electrons as they cross over several wires. In such case, the signals are spread out over a time period corresponding to the drift times of the electrons. The first peak and second peak in Fig 3.3 were considered to be due to the closest event of first electrons and late arriving electrons, respectively. In order to extract position information where a charged particle crossed, signals in the same layer were clusterized using the time information. At first, two adjacent signals were marked as belonging to the same cluster, if the two signals overlapped with $\pm$ 10 nsec tolerance and the difference of the wire-ID was within 2. Once the check for all combinations of adjacent signals was done, the boolean table or

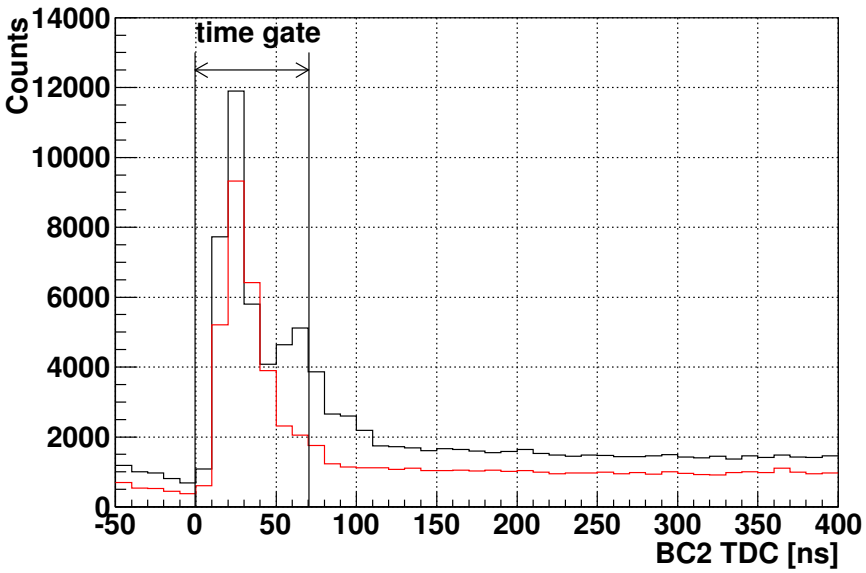

Figure 3.3.: Typical leading-edge timing spectrum of one of the BC1-2 layer before (black) and after (red) clustering. The lower accidental counts in the region before the time gate than those in the region after the time gate is interpreted as the effect of the trigger veto gate.

matrix was obtained as

$$\langle i|j\rangle_1 = \begin{cases} 1 & \text{if } i-\text{th signal and } j-\text{th signal are connected} \\ 0 & \text{if } i-\text{th signal and } j-\text{th signal are unconnected} \end{cases} \tag{3.3}$$

Subscripts represent the order of iterations of the cluster search. Next, the connectivity of not adjacent signals were examined by multiplying the boolean matrix;

$$\langle i|k\rangle_{2m} = \bigvee_j \langle i|j\rangle_m \langle j|k\rangle_m \quad (m = 1, 2, 4, 8, ...) \tag{3.4}$$

In this way, the hit cluster search was continued until updating of the boolean table converged. Then, the cluster was selected by the leading edge timing. A leading edge timing of hit clusters is also shown in Fig. 3.3. The time gate of 70 ns width was set as indicated. For the tracking analysis, the crossed point P on an anode plane was estimated by calculating the weighted mean of each wire position

$$P = \frac{\sum T_i W_i}{\sum T_i} \tag{3.5}$$

where T_i and W_i are a time-over-threshold and wire position of i-th signal in the hit cluster, respectively.

Tracking algorithm of BC1-2

The tracking procedure had two main components. One of them was the track finding and the other was the track fitting. The track finding was the process of the collecting all hits associated with a track. On the other hand, the track fitting was a purely mathematical computation.

The most naive algorithm for track finding is to take account of the all combinations of the data points on the chambers, which is named as a brute force method. The brute force method maximizes

an efficiency of tracking, while it consumes a lot of CPU time and memory usage. To reduce the computing resource, some sophisticated algorithms should be applied before executing the brute force one.

For the straight track finding of BC1-2, the Hough transformation [86], a common technique for pattern recognition, was adopted at the first step. Hough transformation projects a point in normal *pattern* space into a certain *feature* space which is called Hough space. The idea is based on a simple transformation of the equation of a straight line in an x-y plane, $y = kx + m$, to another straight line in a k-m plane, $m = -xk + y$. The points along the line in the k-m plane correspond to all possible lines going through the point (x, y) in the x-y plane, and vice versa. Hit information of the chambers along a track are overlapping at a certain point in the feature space. Therefore, Hough transformation converts "track finding in the pattern space" to "peak search in the feature space".

The 2-dimensional Hough transformation for the x-, u- and v- wire configuration were performed, respectively. Then, all the combinations of the 2-D tracks and other hits, which fired at least 8 planes, were used to three-dimensional track fitting with the least square method. The reduced χ^2 of a straight line fitting was defined as following,

$$\chi^2 = \frac{1}{n-4}\sum_{i=1}^{12} H_i \left(\frac{P_i - f(z_i)}{\sigma_i}\right)^2 \tag{3.6}$$

$$H_i = \begin{cases} 1 & \text{if } i\text{−th plane has a hit} \\ 0 & \text{if } i\text{−th plane has no hit} \end{cases} \tag{3.7}$$

$$n = \sum_{i=1}^{12} H_i \tag{3.8}$$

$$f(z_i) = x_i \cos\theta_i + y_i \sin\theta_i \tag{3.9}$$

$$x_i = x_0 + \frac{dx}{dz} z_i \tag{3.10}$$

$$y_i = y_0 + \frac{dy}{dz} z_i \tag{3.11}$$

where subscript i means the i-th plane of chambers, P_i is the hit position estimated by TDC information, σ_i is the position resolution, θ_i is the wire tilt angle, n is the number of the hits used in the fitting, (x_i, y_i, z_i) is the crossed point of i-th plane in local coordinate (shown in Fig. 3.4), $(x_0, y_0, \frac{dx}{dz}, \frac{dy}{dz})$ is the track parameter to be determined (the direction and the position of the straight track at VI), respectively. If there were any hits of which deviation from the fit is greater than 5σ of the spatial resolution, such kind of track candidate was discarded. Figure 3.5(a) shows the reduced-χ^2 distribution of the BC1-2 tracking. The slight deviation was seen between the reduced-χ^2 of the multi-track events and that of the single-track events, which came from the combinatorial error of hits in the track reconstruction. In the present analysis, the tracks with χ^2 less than 5 were accepted as good ones.

To remove fake tracks, a detector with better time resolution than the wire chamber was used in the tracking analysis. In this case, the track candidates were required that they pass through the BH1 segments whose timing corresponds to the time-of-flight of πs. This track matching with the BH1 reduced the time gate width from 70 ns to 2 ns. Figure 3.6 shows typical track multiplicity of the BC1-2 local tracking with and without requiring the track matching with BH1. The ratio of the single-track events to the total events was improved from $\sim 86\%$ to $\sim 97\%$ by using the time information of BH1

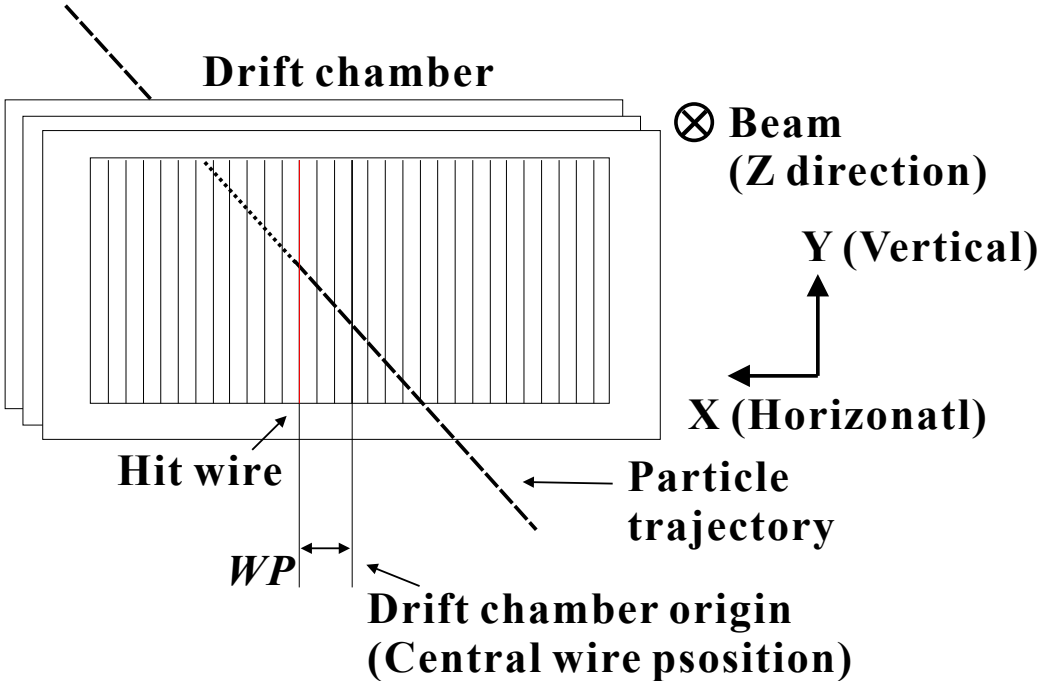

Figure 3.4.: Local coordinate system for the local straight tracking [90].

compared the previous analysis [90, 99]. The track reconstruction efficiency is discussed in Sec. 3.4.3.

Figure 3.7 shows the typical residual distributions of the beam line chambers. The residual was defined as $Residual = X_{hit\ position} - X_{track\ position}$ on the layer. In the residual calculation, the track fitting was performed without the corresponding layer. The residual width of 300 μm and 200 μm in rms were obtained for BC1-2 and BC3-4, respectively.

MWDC drift length calculation

Drift times were obtained from the TKO Multi-hit TDC (MHTDC) data. Owing to the good non-linearity of the AMT implemented on the MHTDC, the time calibration was neglected. The TDC channels were converted to the time with the LSB (least-significant-bit) of 0.78 nsec (= 1/(40 MHz $\times$32)). Figure 3.8 shows the typical leading-edge distributions of (a) BC3 (3 mm anode pitch) and (b) BC4 (5 mm anode pitch). The time gate was set from 0 to 55 ns for BC3 and from 0 to 65 ns for BC4 as indicated in the figure. If one of the planes had more than ten hits within the time gate, the event was rejected in the tracking process. Then, the drift length, which was defined as a distance from the sense wire in the anode plane, was estimated by using the $x - t$ relation. The $x - t$ relation was obtained through the following two steps. At first, assuming that tracks uniformly pass each wire cell, the drift length is proportional to the cumulative distribution of the drift time of single track events,

$$DL(t) \propto \int_0^t DT(t')dt' \tag{3.12}$$

where t, $DT(t)$ and $DL(t)$ are the drift time, the drift time spectrum and a candidate for the $x - t$ relation, respectively. In other words, the drift time distribution is almost equivalent to the drift velocity except for the normalization. The normalization factor is chosen to meet the boundary

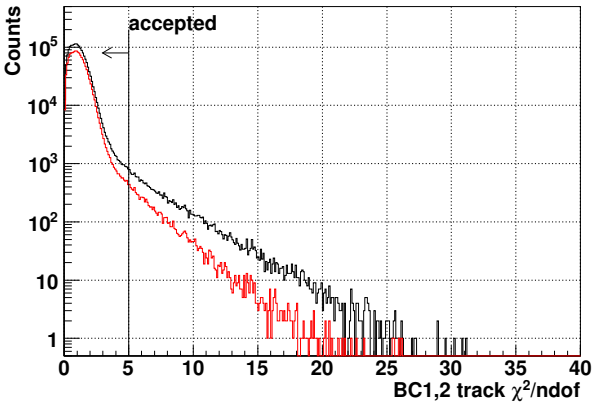

(a) BC1-2.

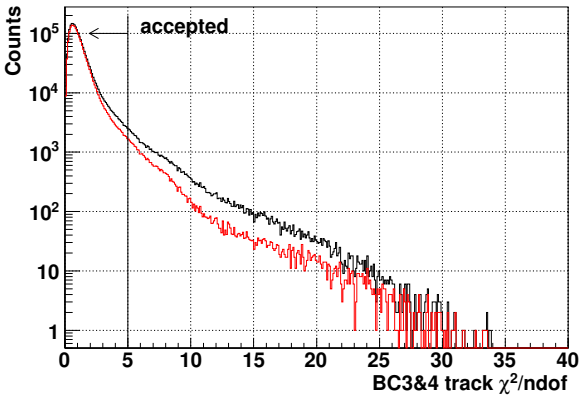

(b) BC3-4.

Figure 3.5.: Reduced χ^2 distribution of BC1-2 straight track fitting (a) and that of BC3-4 (b). The black and red lines show the χ^2 distribution of all and the single-track events, respectively.

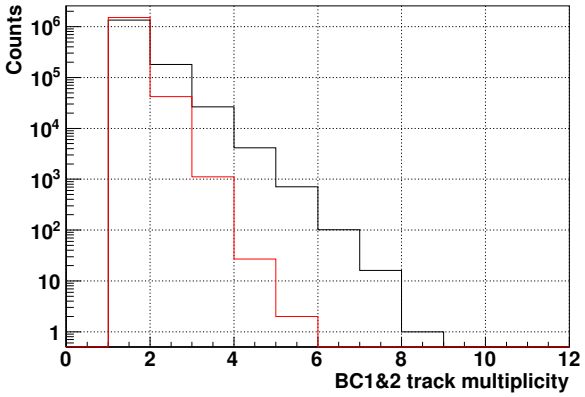

(a) BC1·2.

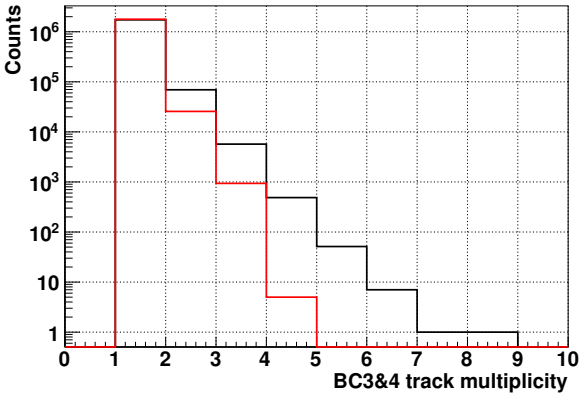

(b) BC3·4.

Figure 3.6.: Typical track multiplicity of the local straight track. (a): BC1·2 with (red) and without (black) the BH1 timing information. (b): BC3·4 with (red) and without (black) the BH2 timing information.

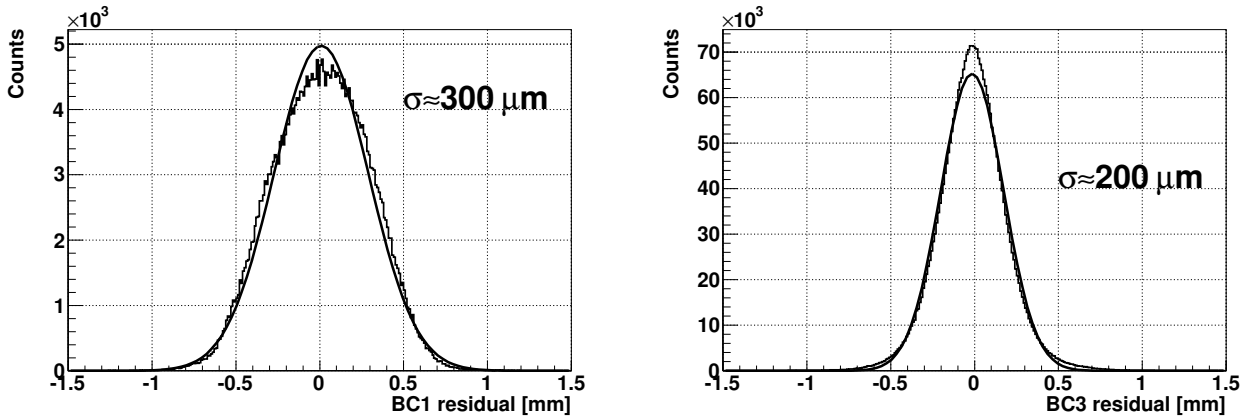

(a) BC1. (b) BC3.

Figure 3.7.: Typical residual distribution of one of the tracker planes. (a): BC1. (b): BC3.

condition of the wire cell.

$$DL(t) = \frac{\int_0^t DT(t')dt'}{\int_0^{t_{max}} DT(t')dt'} \times \frac{L_{cell}}{2} \tag{3.13}$$

where L_{cell} is the cell size of the sensitive plane and t_{max} is the maximum drift time in the cell. Figure 3.9 shows the scatter plot between the drift time and the distance of the track from the sense wire. The magenta curve indicates $DL(t)$. Then, in order to improve the position resolution, the drift length function was optimized by fitting the scatter plot, where the function $dl(t)$ was assumed to be 5th-order polynomial of the drift time,

$$dl(t) = \sum_{k=0}^{5} p_k t^k \tag{3.14}$$

The parameters p_k were adjusted by fitting the track iteratively. An example of $dl(t)$ is shown as the blue line in Fig.3.9. For the events whose drift time was around the maximum value, the drift length $dl(t)$ was truncated to half the cell width whereas for the events with $t < 0$, $dl(t)$ was rounded down to 0. Figure 3.10 shows typical $x - t$ plots of the BC3 layer and that of the BC4. The hit position P on the anode plane was calculated as $P = W \pm dl(t)$, where W is the wire position of the fired cell. The double sign originates from left-right ambiguity.

Tracking algorithm of BC3-4

In the BC3-4 straight track finding, chamber hits were clusterized on a pair of planes. Figure 3.11 show a typical distribution of the drift length sum of a pair of planes. Requiring the drift length sum of a pair was less than a certain threshold, which was set to half a wire-spacing plus 4σ of the position resolution, the hit-pair was considered to belong to the same track and the left-right assignment was solved for the corresponding pair. Then, hit-pairs and the other hits were grouped in each 2-dimensional coordinate systems (x, u and v, respectively), and all combinations were examined for 2-D track candidates. In

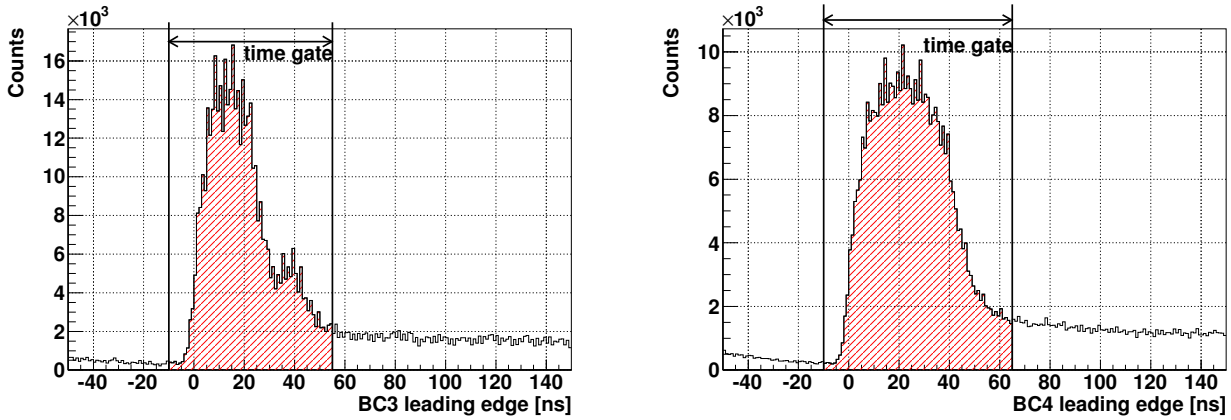

(a) BC3. (b) BC4.

Figure 3.8.: Typical leading-edge timing distribution of (a) one of the BC3 layers and (b) one of the BC4 layers. The bump structure in (a) came from the ringing of the frontend electronics. The red hatched regions correspond to the drift time spectra used in the drift time analysis.

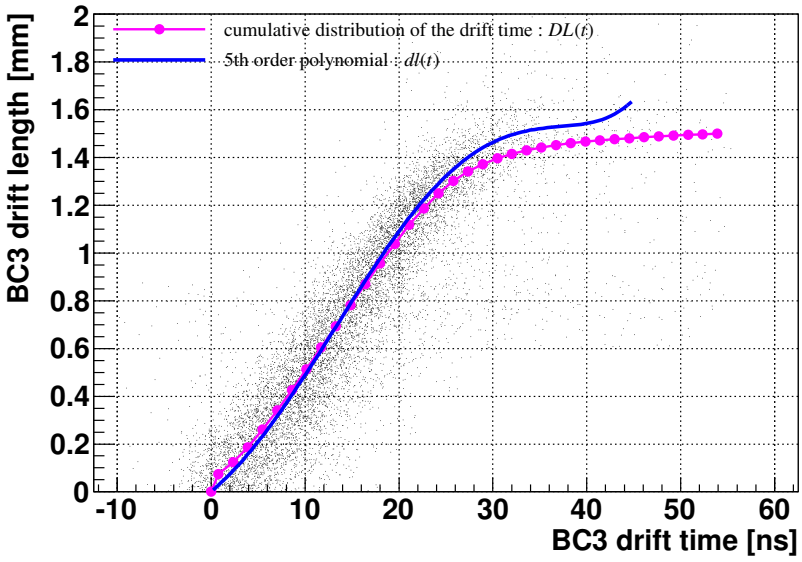

Figure 3.9.: The drift length as a function of the drift time of one of the BC3 layer. The magenta curve is a cumulative distribution of the drift time. The blue line is the optimized $x - t$ relation by fitting the scatter plot with a 5th order polynomial function.

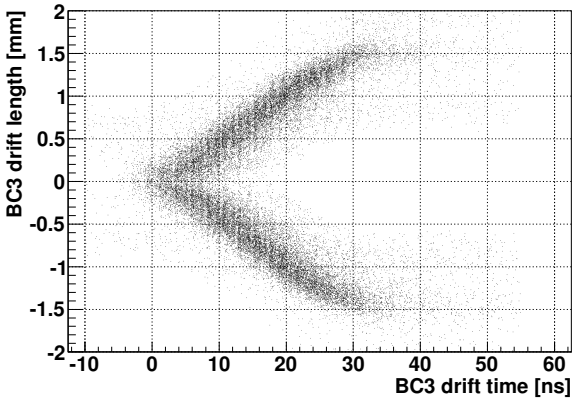

(a) BC3.

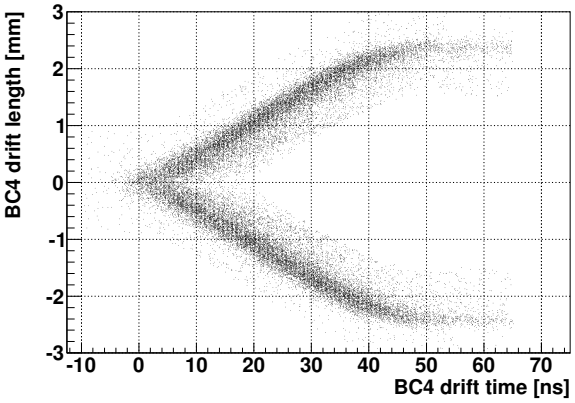

(b) BC4.

Figure 3.10.: Typical $x - t$ plots of (a) BC3 and (b) BC4. The scatter plots were the sum of all the hits in a layer.

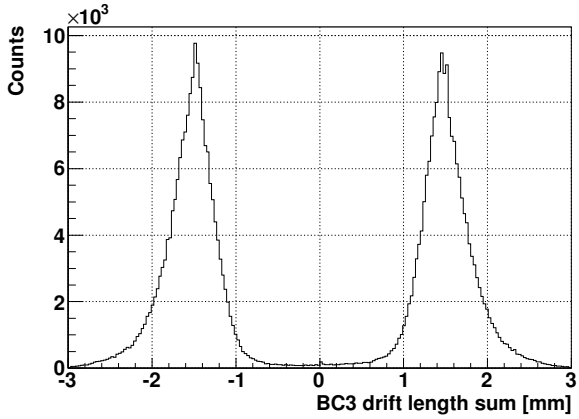

(a) BC3

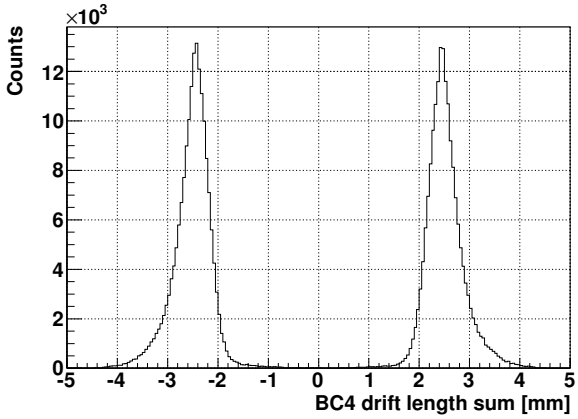

(b) BC4

Figure 3.11.: Typical distribution of the drift-length sum for a pair of planes which are displaced by a half cell to each other.

the two-dimensional fit, the reduced χ^2 was defined as follows;

$$\chi^2 = \frac{1}{n-2} \sum_{i \in \text{same tile angle}} H_i \left(\frac{P_i - f_{2D}(z_i)}{\sigma_i} \right)^2 \tag{3.15}$$

$$H_i = \begin{cases} 1 & \text{if } i-\text{th plane has a hit} \\ 0 & \text{if } i-\text{th plane has no hit} \end{cases} \tag{3.16}$$

$$f_{2D}(z_i) = a_0 + a_1 z_i \tag{3.17}$$

where (a_0, a_1) is the 2-D track parameter. Then, three-dimensional fit was applied in the similar way as the BC1-2 track fitting. Figure 3.5 (b) shows the reduced χ^2 distribution of the BC3-4 tracking. The events which had the tracks with $\chi^2 < 5$ were accepted as good events. Finally, track candidates were required to go through BH2 segments which invoked the trigger.

Momentum analysis of beam

The straight tracks determined at the entrance and exit of the QQDQQ magnet (VI and VO as shonw in Fig. 3.12, respectively) were connected using a 3rd order transport matrix calculated by ORBIT [87]. The matrix $\mathcal{M}$ is formulated as following equations.

$$\vec{X}_{out} = \mathcal{M}(\vec{X}_{in}) \tag{3.18}$$

$$\vec{X} = \begin{pmatrix} x \\ y \\ \dfrac{dx}{dz} \\ \dfrac{dy}{dz} \\ \delta \end{pmatrix} \tag{3.19}$$

$$X_i^{out} = \sum_j R_{ij} X_j^{in} + \sum_{jk} T_{ijk} X_j^{in} X_k^{in} + \sum_{jkl} U_{ijkl} X_j^{in} X_k^{in} X_l^{in} \tag{3.20}$$

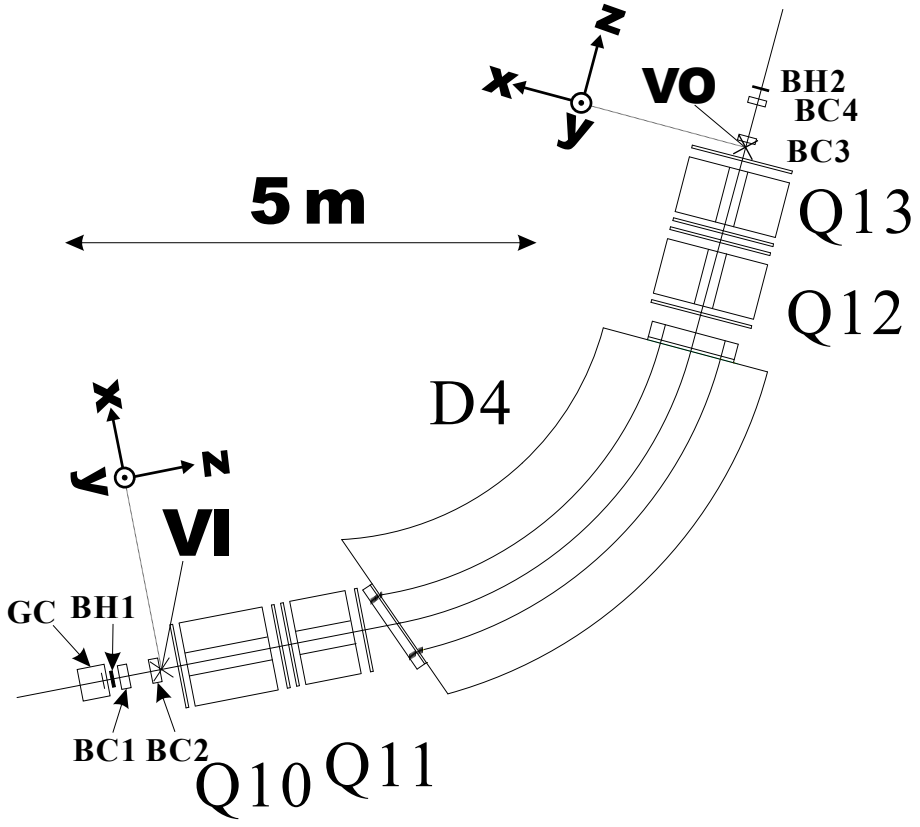

Figure 3.12.: The position of VI and VO which were the origin of the local coordinate systems [90].

$\vec{X}$ = the positions, angles and momentum of the particle with respect to the reference trajectory;
the subscripts (*in* and *out*) stand for the entrance and exit of QQDQQ

x = the horizontal displacement of the arbitrary ray with respect to the assumed central trajectory

y = the vertical displacement of the ray with respect to the assumed central trajectory

dx/dz = the angle that this ray makes in the horizontal plane with respect to the assumed central trajectory

dy/dz = the vertical angle of the ray with respect to the assumed central trajectory

δ = the fractional momentum deviation of the ray from the assumed central trajectory;
The particle momentum p is denoted by $p = p_0(1 + \delta)$, where p_0 is the central momentum calculated from the magnetic field and the effective length of D4, the dipole magnet in the QQDQQ system.

X_i = $i-$th component of a vector $\vec{X}$

R_{ij} = (i, j) component of the first order transfer matrix

T_{ijk} = (i, j, k) component of the second order transfer matrix

U_{ijkl} = (i, j, k, l) component of the third order transfer matrix

The particle momentum was determined by minimizing the following reduced χ^2 value. The MINUIT package [88] was used as the minimization tool, in which the fit free parameters were $\vec{X}_{in}$. For multi-

track events, only one combination which gave the least χ^2 was chosen. The χ^2 value of each track was defined as

$$\chi^2_{K1.8} = \frac{1}{n-5}\left(\underbrace{\sum_{i=1}^{12} H_i \left(\frac{P_i - f_i(\vec{X}_{in})}{w_i} \right)^2}_{BC1-2} + \underbrace{\sum_{i=13}^{24} H_i \left(\frac{P_i - f_i(\vec{X}_{out})}{w_i} \right)^2}_{BC3-4} \right) \tag{3.21}$$

$$n = \sum_{i=1}^{24} H_i \tag{3.22}$$

$$H_i = \begin{cases} 1 \text{ if } i-\text{th plane has a hit.} \\ 0 \text{ if } i-\text{th plane has no hit.} \end{cases} \tag{3.23}$$

P_i = the hit position of the $i-$th plane in BC$'$s

w_i = the appropriate weights determined by the position resolution of the $i-$th plane in BC$'$s

f_i = the estimated points with transport matrix at the $i-$th plane

n = the number of hit planes

The ORBIT uses the features of the beam line element as its input. Among them, the parameters related to the magnetic field were derived from the measured excitation curve. When the central beam momentum was set for 1.92 GeV/c, the field estimated from the excitation curve turned out to be not enough to realize the designed beam profile. Therefore, the applied current of Q10 was increased by 2% to reproduce designed optics. The reason of the deviation was considered as magnetic saturation of Q10 (the first quadrupole in QQDQQ), which in general shorten the effective length of the magnetic field. Figure 3.13 (a) and (b) show the scatter plot of the horizontal position of the track at VI vs. K1.8 tracking χ^2 for 1.37 GeV/c and for 1.92 GeV/c, respectively. A strong correlation was seen in the outer side of the horizontal position of 1.92 GeV/c data. To improve the transport matrix for the momentum of 1.92 GeV/c, the effective length of Q10 was optimized so that the difference between the horizontal position measured by BC1·2 local straight tracking and by that of K1.8 tracking is minimized. Figure 3.13 (c) shows the scatter plot after the optimization, where the effective length was decreased by 3%. The same analysis quality was kept for both the data of 1.37 GeV/c and that of 1.92 GeV/c by optimizing the magnetic field of Q10. The events with χ^2 less than 20 were accepted as good events as shown in Fig. 3.14.

3.3. Analysis of outgoing particles

3.3.1. Track reconstruction of outgoing particles

MWDC drift length calculation

Drift times of SDC1-2 were obtained in the same way as the BC3-4 while SDC3-4 used the TKO Dr.T II as the TDC module. The data of the latter were calibrated by using the TDC calibrator (ORTEC 462). The LSB of the Dr.T II was obtained to be $\sim 576 \pm 12$ psec. The $x - t$ relation was calculated

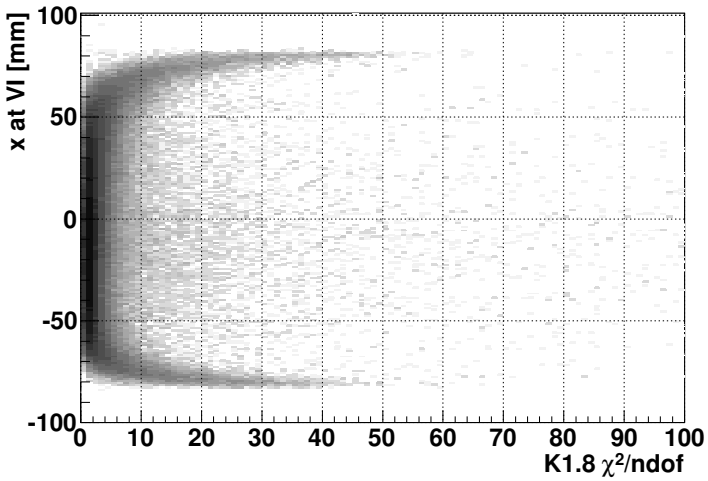

(a) 1.37 GeV/c.

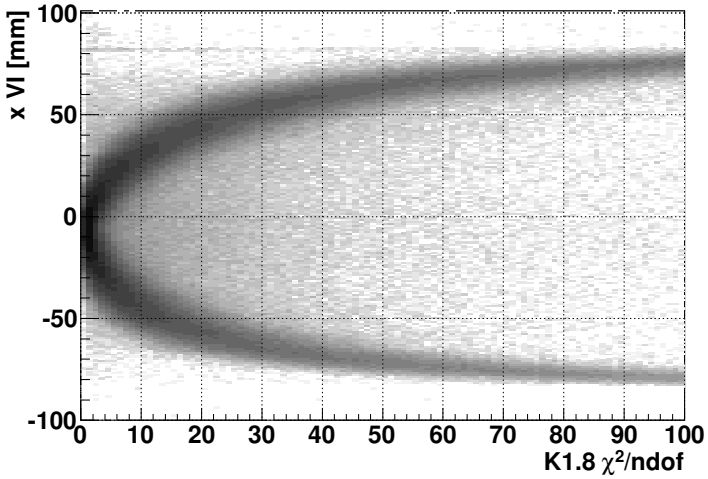

(b) 1.92 GeV/c before optimization.

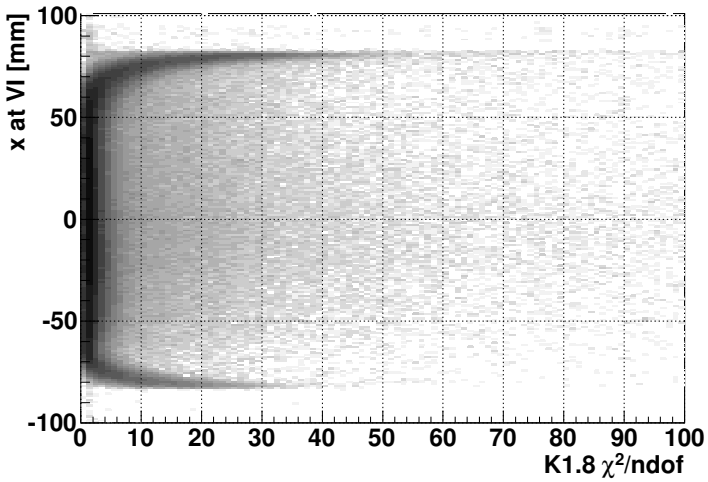

(c) 1.92 GeV/c after optimization.

Figure 3.13.: Scatter plot between χ^2 and the horizontal position at VI position of beam track. (a) For the beam momentum of 1.37 GeV/c and (b) 1.92 GeV/c before the optimization of the transport matrix. (c) For the momentum of 1.92 GeV/c after the optimization.

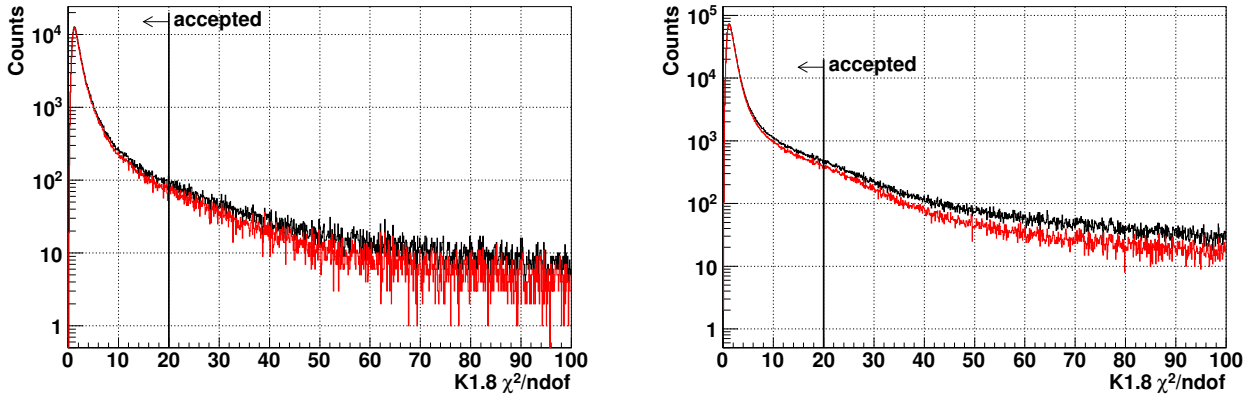

(a) (b)

Figure 3.14.: Reduced χ^2 distribution of the K1.8 beam track of (a) 1.37 GeV/c and (b) 1.92 GeV/c. The black line corresponds to the all track candidates which pass the criteria for both BC1-2 and BC3-4 local tracks. The red line shows the χ^2 of single-track events.

by the same procedure as in the BC3-4 analysis. Figure 3.15 shows a typical drift time spectrum and the $x-t$ plot of one of the SDC3 layers. A typical residual distribution of SDC2 (SDC3) is shown in Fig. 3.16.

Momentum analysis of outgoing particles

The momentum of the scattered particle was calculated from a drift-chamber hit information as follows. At first, straight tracks were constructed both at the entrance and exit of the SKS magnet with SDC1-2 and SDC3-4 hits using a least-square method, respectively. In track finding for the SDC1-2 hits, the same procedure as the BC3-4 track finding was adopted except for the pair plane analysis. As for the SDC3-4 track finding, the pair plane analysis could not be performed due to the chamber structure. Thus all combinations of the left/right ambiguity were examined. Figures 3.17(a) and (b) show reduced χ^2 distributions of SDC1-2 and SDC3-4 tracks, respectively. In both the SDC1-2 and SDC3-4 tracking, χ^2 was required to be less than 5.

The trajectory reconstruction inside the SKS magnetic field was performed by using the fast Runge-Kutta tracking method [89]. Figure 3.18 shows coordinate systems for the SKS track analysis. In this calculation, the hit positions associated with the local straight tracks were used and the path tracing started from the TOF counter to the LH2 target. The momentum was determined by requesting the following reduced χ^2 to be minimized

$$\chi^2_{SKS} = \frac{1}{n-5}\sum_i \left(\frac{x_i^{tracking} - x_i^{data}}{w_i} \right)^2 \tag{3.24}$$

where n is the number of chamber planes with hits, w_i is the weight of the i-th plane, x_i^{data} and $x_i^{tracking}$ are the hit positions on the i-th plane of the data and those of the trajectory to be determined, respectively. The Levenberg-Marquardt method was used in the iteration of the minimum χ^2 search, which was considered to have converged and terminated when the relative χ^2 difference $\delta\chi^2$ satisfies $\delta\chi^2 = \left|(\chi^2_{k+1} - \chi^2_k)/\chi^2_k\right| < 2 \times 10^{-4}$, where k is the number of iterations and χ^2_k is the tracking χ^2

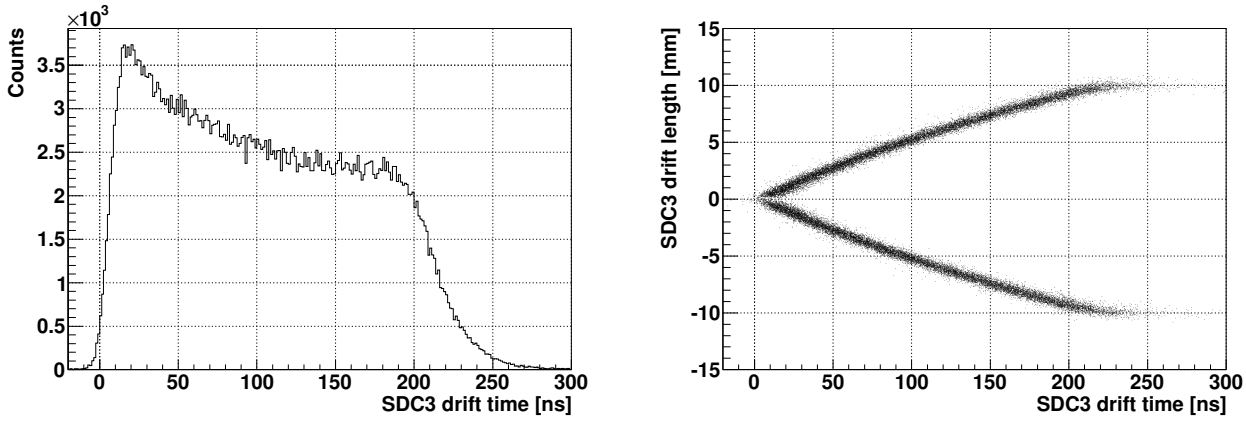

(a) (b)

Figure 3.15.: (a) Typical drift time distribution of one of the SDC3 layers and (b) the scatter plot between the drift time and the drift length of one of the SDC3 layers.

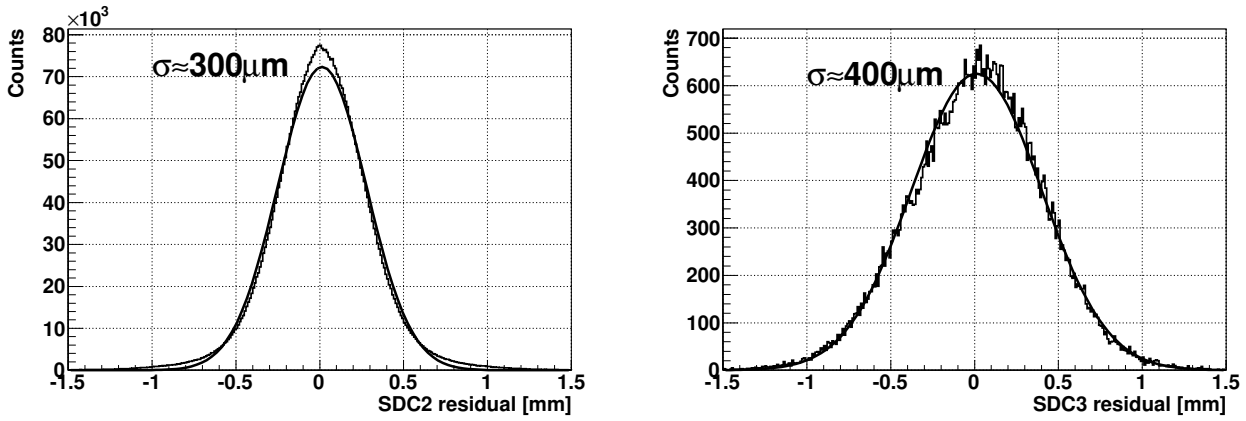

(a) (b)

Figure 3.16.: Typical residual distribution of one of the tracker planes. (a): SDC2. (b): SDC3.

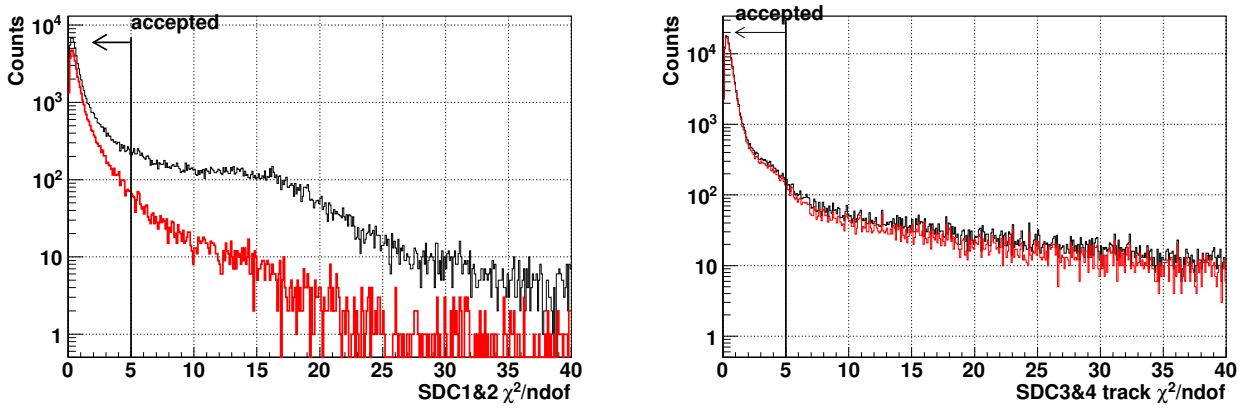

(a) (b)

Figure 3.17.: Reduced χ^2 distribution of the local straight track of (a) SDC1-2 and (b) SDC3-4. The black and red lines show the χ^2 distributions of all and the single-track events, respectively.

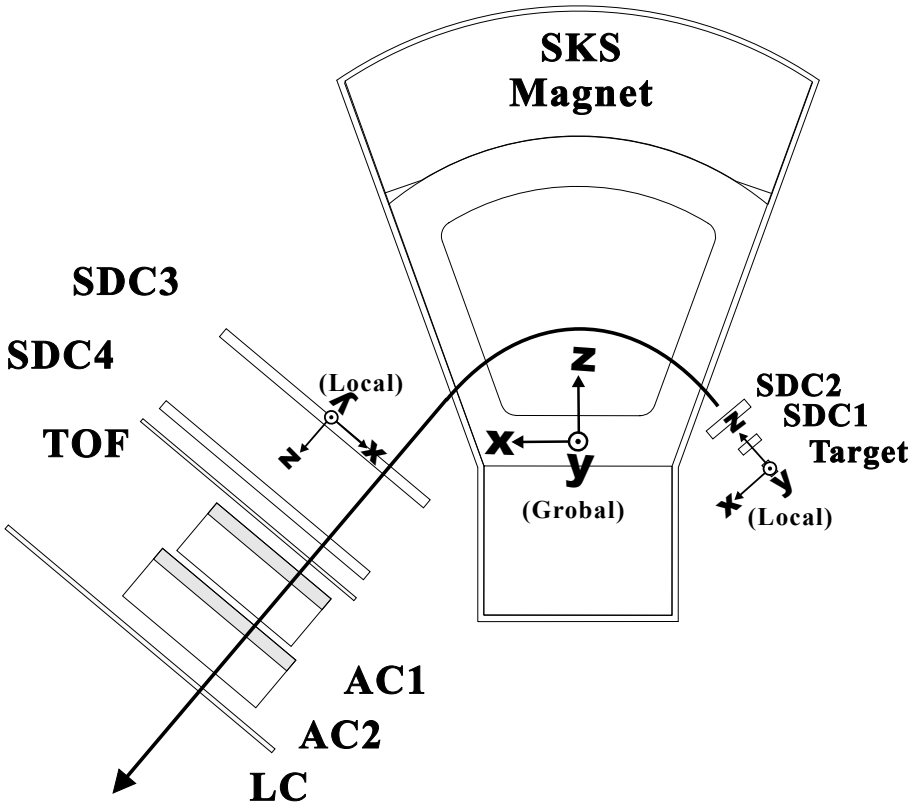

Figure 3.18.: Coordinate systems for the SDC1·2 local tracking, the SDC3·4 local tracking and the SKS tracking [90].

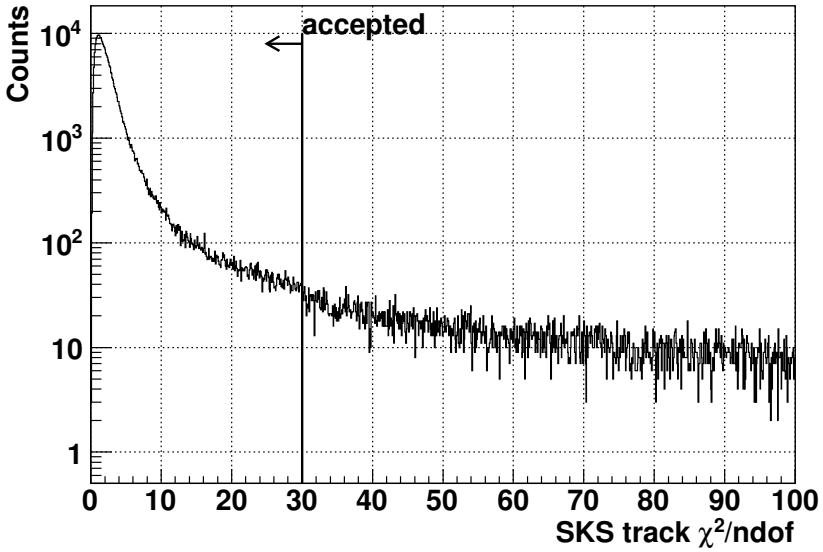

Figure 3.19.: Reduced χ^2_{SKS} distribution of the scattered track. The accepted region is indicated with the arrow.

value for the kth iteration. Figure 3.19 shows a typical χ^2_{SKS} distribution. In the present analysis, events with $\chi^2_{SKS} < 30$ were accepted as good tracks.

3.3.2. Particle identification of K^-

The scattered particle mass ($M_{scattered}$) was calculated using

$$M_{scattered} = \frac{p}{\beta}\sqrt{1-\beta^2} \tag{3.25}$$

$$\beta = \frac{L}{cT} \tag{3.26}$$

where p, c, T, and L stand for the the particle momentum, light velocity, the time-of-flight and the flight path length to the TOF counter, respectively. The time-of-flight T was calibrated to reproduce the known mass of scattered particles. The calibration was done using the scattered π. The outgoing π were selected using only the time-of-flight information. Then the predicted time-of-flight (T_{pred}) was calculated using the momentum, flight length, and PDG mass of π. The time difference ΔT between the T_{pred} and the measured time-of-flight $T_{measure}$ was obtained as

$$\Delta T = T_{pred} - T_{measure} \tag{3.27}$$

The time offset was adjusted to make ΔT zero.

Background particles other than kaons were separated using the ADC and TDC information of the TOF counter, TOF-ADC and TOF-TDC, the ADC and TDC information of the LC counter, LC-ADC and LC-TDC. At first, the simple criteria using TOF-TDC, ADC and LC-TDC, ADC. Figure 3.20, 3.21 show scatter plots between the $M_{scattered}$ and TOF-TDC, ADC and LC-TDC, ADC, respectively.

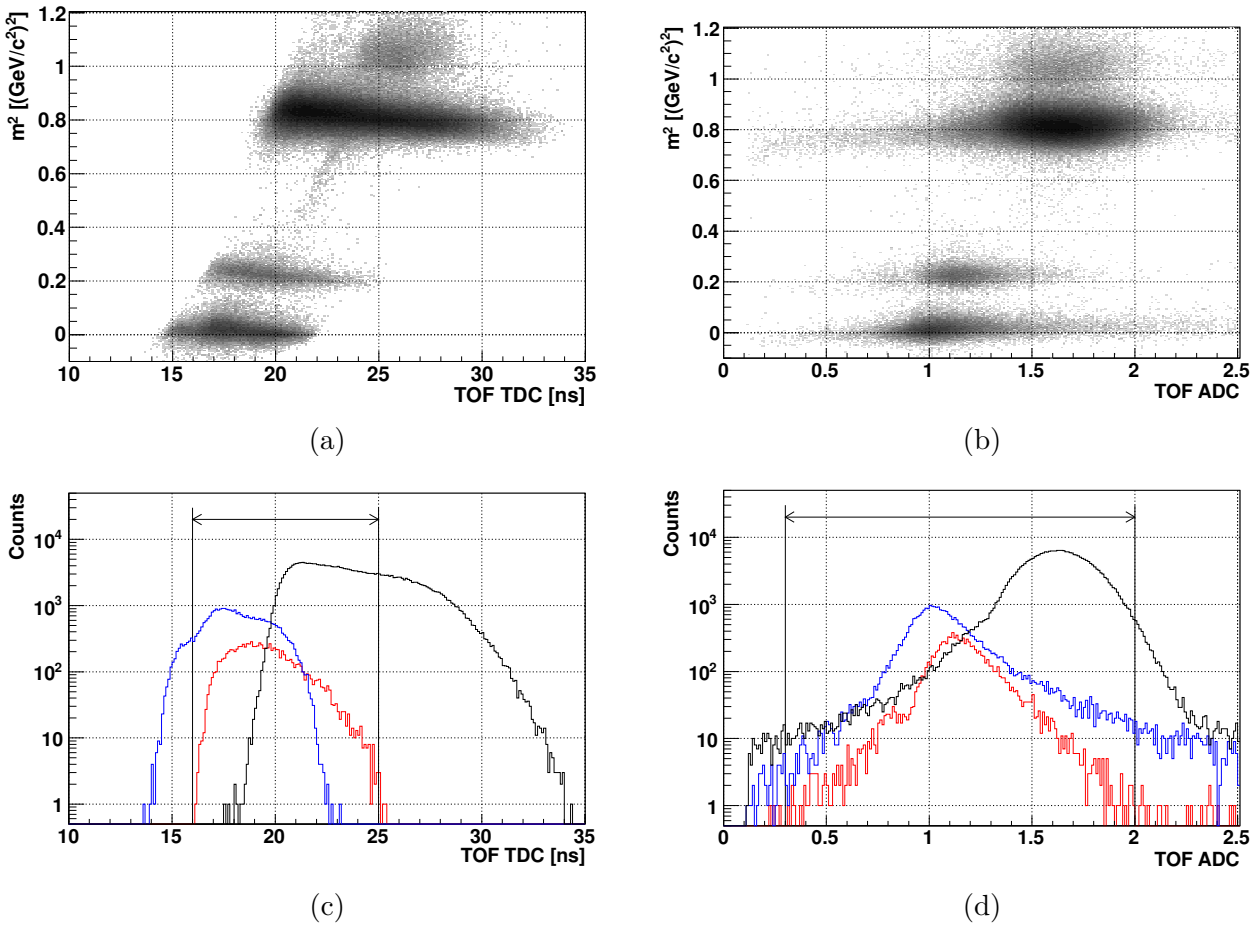

Figure 3.20.: The scatter plots of the mass of outgoing particle versus (a) TDC and (b) ADC of the TOF counter. The projection are shown in (c) and (d). The black, red, blue curves correspond to protons, kaons and pions, respectively. The cut region for the kaon is indicated by the arrows.

The event-selection criteria were;

$$
\begin{aligned}
0.3 &< \mathrm{TOF(ADC)} < 2.0 \\
16.0 &< \mathrm{TOF(TDC)} < 25.0 \text{ ns} \\
0.0 &< \mathrm{LC\ \ (ADC)} < 4.0 \\
19.0 &< \mathrm{LC\ \ (TDC)} < 35.0 \text{ ns}
\end{aligned}
$$

which are indicated by arrows in the figures. The ADC and TDC cut were applied before the local track reconstruction to reduce the CPU time. Second, a correlation of the horizontal scattering angle measured by SDC1-2 and the time-of-flight T was used to select kaon events as shown in Fig. 3.22. This cut was performed just after the local track search of the SDC1-2. Furthermore, the particles were chosen by the $M_{scattered}$ to reduce the background. Fig 3.29(a) shows a squared mass of scattered particles for the (π, K) data. The (π, K) events are shown in the black histogram and the K events selected by the TOF information and the scattering angle cuts in red one. The selected region was

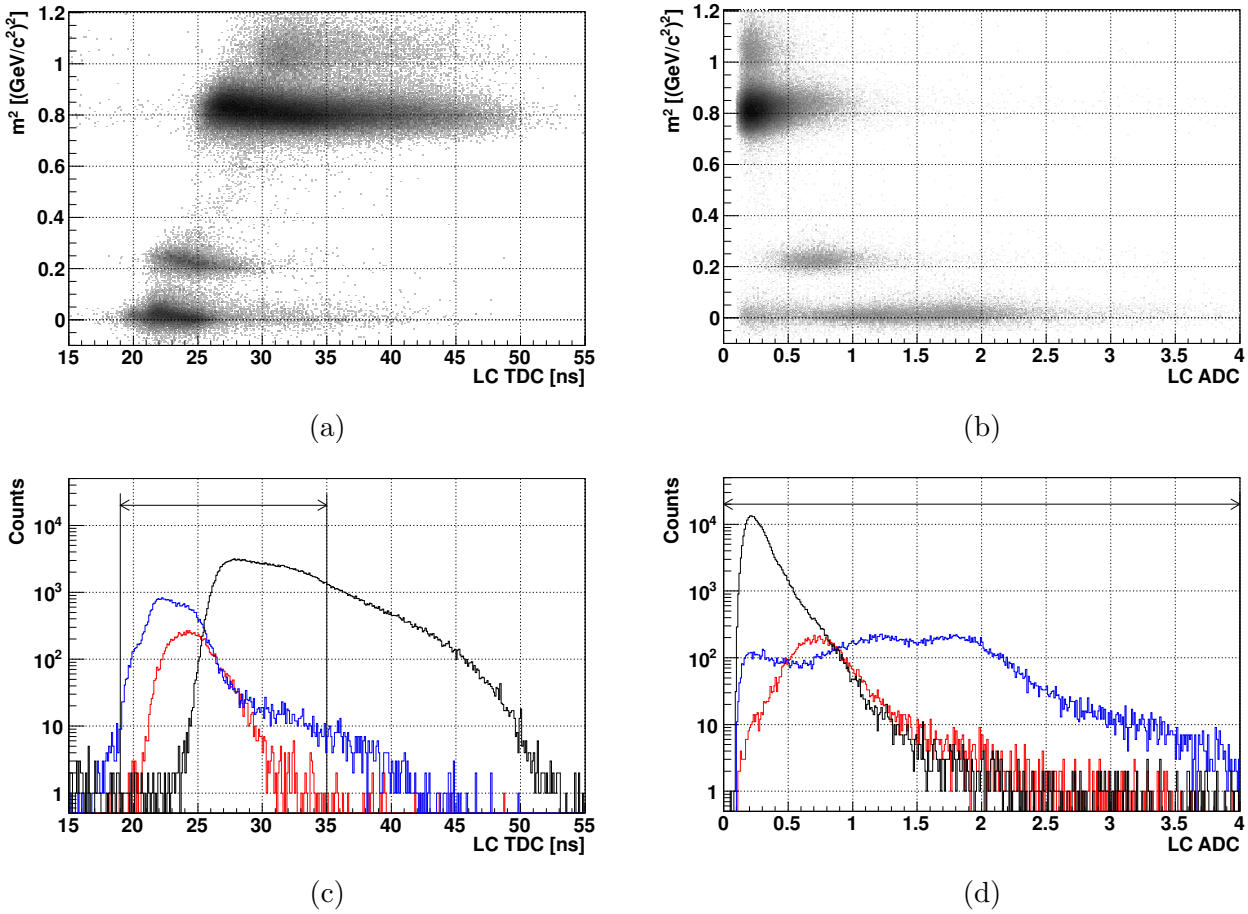

Figure 3.21.: The scatter plots of the mass of outgoing particle versus (a) TDC and (b) ADC of the LC counter. The projection are shown in (c) and (d). The black, red and blue curves correspond to protons, kaons and pions, respectively. The cut region for the kaon is indicated by the arrows.

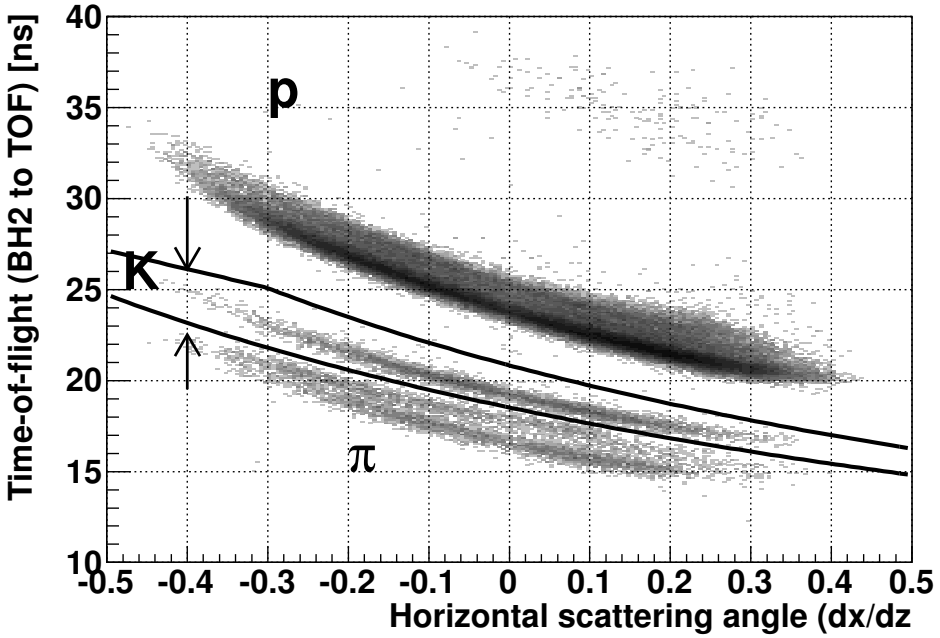

Figure 3.22.: Scatter plot between the horizontal scattering angle measured by SDC1·2 and the flight time between BH2 and TOF. The cut condition for kaon is indicated in the figure.

expressed by the intersection of the following two constraints;

$$18.4 < T + 10.3 \times \frac{dx}{dz} < 22$$
$$0.0480 < \frac{1}{T} - 0.0271 \times \frac{dx}{dz} < 0.0540$$

Scattering angle and vertex point

The scattering angle θ was determined by two tracks respectively defined in BDC3-4 and SKS tracking.

$$\cos\theta = \frac{\boldsymbol{p}_{\mathrm{K1.8}} \cdot \boldsymbol{p}_{\mathrm{SKS}}}{|\boldsymbol{p}_{\mathrm{K1.8}}||\boldsymbol{p}_{SKS}|} \tag{3.28}$$

Figure 3.23 shows typical horizontal and vertical scattering angle resolutions; they are 4.0 mrad and 4.7 mrad in rms, respectively. Because of the special wire configuration of the drift chambers, the vertical resolution was worse than the horizontal one. Figure 3.24 shows the scattering angle distribution of the beam through data, where $\Delta\theta$ should have the peak at zero if there was no deterioration due to the multiple scattering and all degrees of freedom of the alignment of the trackers (BDC3-4 and SDC1-2) were completely resolved. The peak was obtained at 3.2 mrad and the upper side of the half maximum was 5.9 mrad, which was used as the angle resolution $\Delta\theta$ in the estimation of the missing mass resolution.

Figure 3.26(d) shows the correlation between the z-vertex and the scattering angle. Since the vertex resolution was quite poor in a small angle, the angle region of $> 2^\circ$ was accepted. The vertex position of reaction was determined when the distance of closest approach (DCA) of each track was the minimum. Figures 3.25(a)(b)(c) shows the distribution of the vertex position for (π^-, K^-) data. In addition to

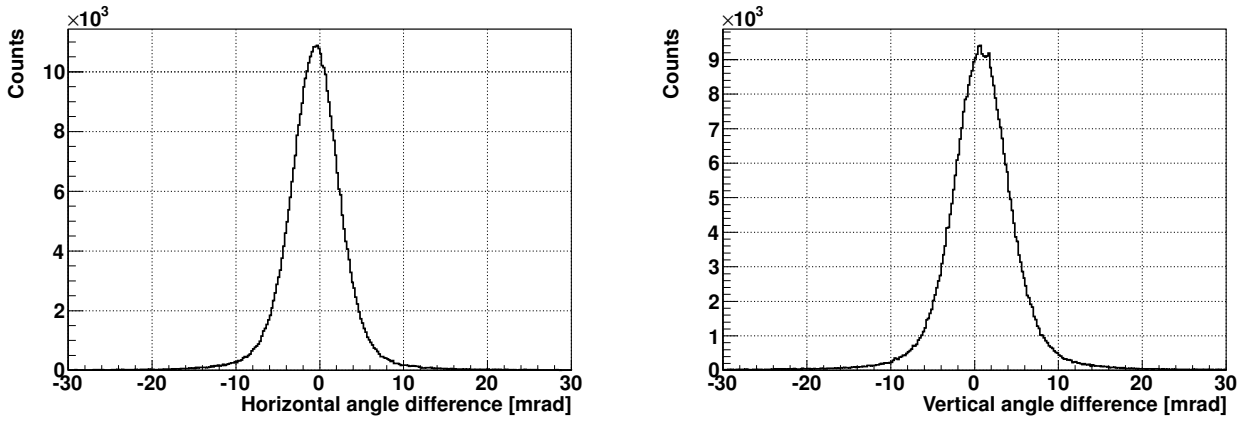

(a) (b)

Figure 3.23.: Typical distribution of the scattering angle difference measured in the beam through data without LH2 target. (a): horizontal direction (rms = 4.0 mrad). (b): vertical direction (rms = 4.7 mrad).

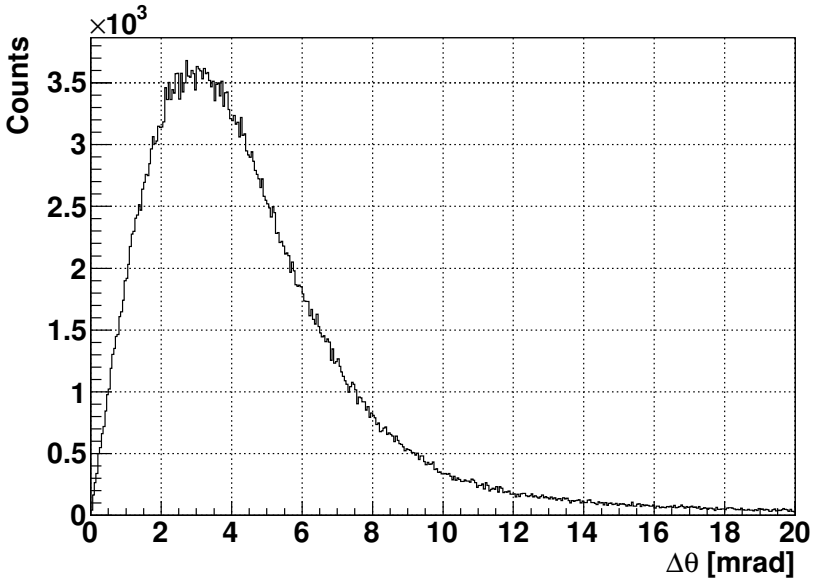

Figure 3.24.: Typical distribution of the scattering angle difference measured in the beam trough data without LH2 target.

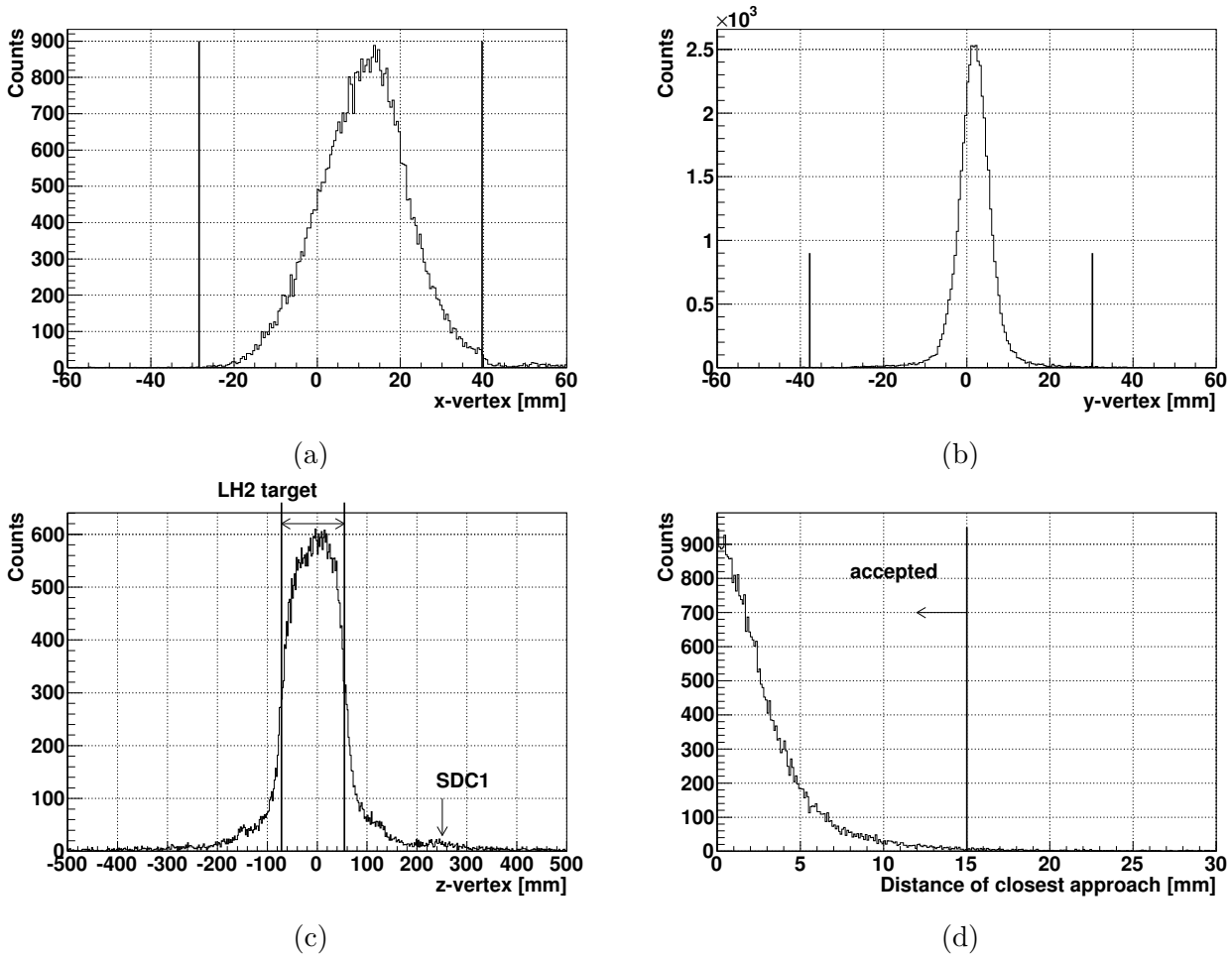

Figure 3.25.: Vertex distribution for the (π^-, K^-) data with the beam momentum of 1.92 GeV/c. (a): x-vertex. (b): y-vertex. (c): z-vertex. (d): distance of closest approach. The selected region is indicated by vertical lines.

the target, a contribution from SDC1 is shown in the z-vertex (Z_{VTX}) distribution. The cut condition in the Z_{VTX} distribution will be described in section 3.4.12. The region from -71.7 mm to 54.3 mm was selected as the reaction events from the LH2 target. The cut on distant of the closest approach was applied to select the track candidates of beam and scattered particle as shown in Fig. 3.25(d). The distance is required to be less than 15 mm. The cut region in the xy-plane formed the circle whose diameter corresponded to that of the LH2 target vessel (i.e. $\phi = 68$ mm), as shown in Fig. 3.26(c). The background contamination was estimated to be $3.9 \pm 0.4\%$ after the vertex cut. The contribution was included as a systematic error.

3.4. Cross Section

The cross section was calculated by the experimental efficiencies and the estimated acceptance of SKS as

$$\frac{d\sigma}{d\Omega} = \frac{A}{\rho x \cdot N_{Avo}} \cdot \frac{1}{N_{Beam} \cdot f_{Beam} \cdot \epsilon_{K1.8}} \cdot \frac{1}{\epsilon_{DAQ} \cdot f_{decay} \cdot f_{absorb} \cdot \epsilon_{vertex}} \cdot \frac{N_K}{\epsilon_{SKS} \cdot \Delta\Omega} \tag{3.29}$$

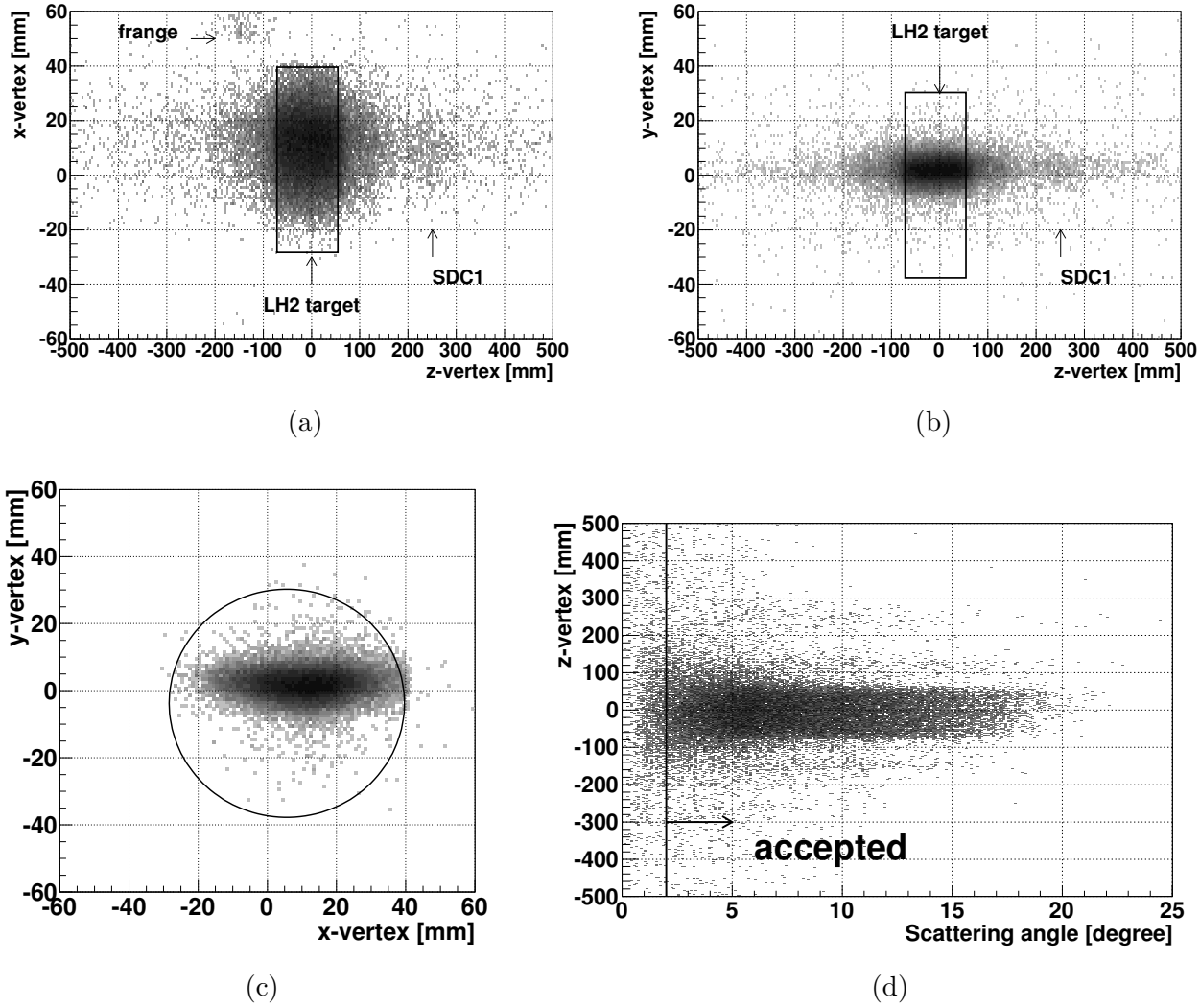

Figure 3.26.: Scatter plot of the vertex point for the (π^-, K^-) data with the beam momentum of 1.92 GeV/c. (a): z-vertex vs. x-vertex. (b): z-vertex vs. y-vertex. (c): x-vertex vs. y-vertex. (d): scattering angle vs. z-vertex.

$$\epsilon_{K1.8} = \epsilon_{BC1-2} \cdot \epsilon_{BC3-4} \cdot \epsilon_{K1.8-track} \cdot \epsilon_{K1.8\ single-track} \tag{3.30}$$

$$\epsilon_{SKS} = \epsilon_{TOF} \cdot \epsilon_{LC} \cdot f_{AC} \cdot \epsilon_{SDC1-2} \cdot \epsilon_{SDC3-4} \cdot \epsilon_{SKS-track} \cdot f_{matrix} \cdot \epsilon_{PID} \tag{3.31}$$

where the symbols are defined in Table 3.1. In this section, brief procedures of the efficiency estimation together with SKS acceptance estimation by a Monte Carlo simulation are described. The values of $\epsilon_{K1.8}$, ϵ_{SKS} and the product of them $\epsilon_{K1.8} \cdot \epsilon_{SKS}$, were 83.6±0.2%, 49.2±2.3%, and 41.1±2.2%, respectively. Note that the previous results for those efficiencies were 68.5±1.9%, 56.0±1.0% and 38.4±1.2% [90], respectively. The analysis efficiency for the beam part was improved in the present analysis since the tracking algorithm has been improved to save events with higher multiplicity.

3.4.1. Data acquisition efficiency

The DAQ efficiency (ϵ_{DAQ}) stands for the live time of the DAQ system. The factor was calculated as the ratio of the number of accepted events to that of requested triggers. The value of ϵ_{DAQ} was 75.3 $\pm$ 0.1% at the trigger rate of $\sim$ 350 per 2.2 sec spill. ϵ_{DAQ} was mainly limited by the data transfer time of the TKO MHTDCs.

3.4.2. Beam normalization factor

The beam normalization factor f_{beam} represents the fraction of π beam out of N_{Beam}. The $e^-(e^+)$ contamination of the beam was 12-14 %, which was rejected by BGC with an efficiency of 99.5 % at the trigger level. The proton contamination in the π^+ beam was also rejected by requiring timing coincidence between BH1 and BH2. However, muons in the beam, which are the decay products of πs, could not be separated from πs. The μ fraction at 1.92 GeV/c in the beam (f_μ) was estimated to be 3.5 $\pm$ 2.0 % by the Decay TURTLE simulation [91]. In the present experiment, the consistency between the beam profile expected from the TURTLE simulation and that of the measured one was confirmed, whereas the validity of the simulation had not been examined with the μ measurement. The systematic error was estimated from the previous KEK experiment [92], assuming that the Decay TURTLE calculation achieved the same accuracy.

The accidental coincidence factor ($f_{BH1\cdot2}$) was estimated by using the BEAM trigger events mixed in the (π, K) data as $f_{BH1\cdot2} = N_{BH1\cdot2}/N_{Beam}$, where $N_{BH1\cdot2}$ is the number of events for which the time of flight between BH1 and BH2 are proper for π. The value of $f_{BH1\cdot2}$ was 97.8 $\pm$ 0.8 %.

Finally, f_{Beam} can be written as

$$f_{Beam} \equiv (1 - f_\mu) \cdot f_{BH1\cdot2} \tag{3.32}$$

In total, the result is $f_{Beam} = 93.3 \pm 2$ %.

3.4.3. Track-finding efficiency of beam particles

The efficiency in the beam momentum reconstruction was estimated as a ratio of the number of events accepted as a good trajectory to that of good beam particles defined with BH1 and BH2. It is composed of the BC1-2 efficiency (ϵ_{BC1-2}), the BC3-4 efficiency (ϵ_{BC3-4}), the K1.8 tracking efficiency ($\epsilon_{K1.8-track}$) and the multiplicity cut efficiency ($\epsilon_{single-track}$). They were estimated by using the BEAM trigger mixed in the (π, K) data. The BC1-2 efficiency and the BC3-4 efficiency are the total efficiency including the detection efficiency and the analysis efficiency to get straight tracks at the entrances and exit of the QQDQQ magnets, respectively. The values of $\epsilon_{BC1-2} = 99.0 \pm 0.1\%$ and $\epsilon_{BC3-4} = 96.2 \pm 0.2\%$ were obtained. The K1.8 tracking efficiency is the analysis efficiency to reconstruct a good particle trajectory in the beam spectrometer, which was $94.3 \pm 0.3\%$.

Unfortunately the bad beam structure caused an increase of the events with multi-tracks, which made the combinatorial background in the missing mass spectrum. Therefore, the tracks crossing neither BH1 nor BH2 were rejected to reduce the background as mentioned in Sec. 3.2.2. The single track efficiency $\epsilon_{single-track}$ denotes the number of single-track events divided by the number of events with good K1.8 tracks. $\epsilon_{single-track}$ was estimated to be $99.8 \pm 0.1\%$.

In total, the tracking efficiency of the beam particles was $89.6 \pm 0.4\%$.

Table 3.1.: List of the experimental efficiency factors and constants used in the calculation of the cross section.

variables or constants	name	values
A	mass number of the target	—
ρx	target thickness in g/cm^2	—
N_{Avo}	Avogadro's number	—
N_{Beam}	scaler count of the BEAM trigger	—
N_K	K yield	—
ϵ_{DAQ}	DAQ live time	75.3 ± 0.1 %
ϵ_{BC1-2}	BC1-2 efficiency	99.0 ± 0.1 %
ϵ_{BC3-4}	BC3-4 efficiency	96.2 ± 0.2 %
$\epsilon_{K1.8-track}$	K1.8 tracking efficiency	94.3 ± 0.3 %
$\epsilon_{K1.8\ single-track}$	single track ratio	99.8 ± 0.1 %
$\epsilon_{K1.8}$	total analysis efficiency of the beam particle	83.6 ± 0.2 %
ϵ_{TOF}	efficiency of TOF-wall	99.3 ± 0.1 %
ϵ_{LC}	efficiency of LC	92.0 ± 0.1 %
f_{AC}	AC1,2 accidental veto factor	$97.3^{+2.6}_{-3.6}$ %
ϵ_{SDC1-2}	SDC1-2 efficiency	96.3 ± 0.3 %
ϵ_{SDC3-4}	SDC3-4 efficiency	85.2 ± 0.2 %
$\epsilon_{SKS-track}$	SKS tracking efficiency	93.9 ± 0.3 %
ϵ_{vertex}	vertex cut efficiency	77.9 ± 1.0 %
ϵ_{PID}	PID efficiency in SKS	93.2 ± 2.0 %
ϵ_{matrix}	matrix trigger efficiency	99.0 ± 0.1 %
ϵ_{SKS}	total analysis efficiency of the scattered particle	49.2 ± 2.3 %
f_{Beam}	beam normalization factor	93.3 ± 2.0 %
f_{μ}	muon fraction in BEAM trigger	3.5 ± 2.0 %
$f_{BH1\cdot2}$	beam accidental coincidence factor	96.6 ± 0.2 %
f_{decay}	decay factor of scattered kaons	44.9 ± 2.0 %
$f_{absorb}(K^+)$	K^+ absorption factor	95.7 ± 0.5 %
$f_{absorb}(K^-)$	K^- absorption factor	88.8 ± 0.5 %

3.4.4. Efficiency of TOF and LC

The detection efficiency of TOF ϵ_{TOF} was estimated by using the beam through data, where the momentum of π ranged from 0.75 GeV/c to 0.95 GeV/c and the beam particles were defined by BEAM, SDC3, SDC4, and LC. ϵ_{TOF} was obtained to be $99.3 \pm 0.1\%$. The same efficiency is assumed for K because of the small energy-loss difference between π and K.

The detection efficiency of LC ϵ_{LC} was estimated to be 92.0 ± 0.1 % in the same way, where the beam particles were defined by BEAM, SDC3, SDC4, and TOF. The μ events from the π decay after passing through TOF was included in the efficiency. The efficiency was assumed to be the same for K because the yield of Čerenkov photons by K was high enough than the discriminator threshold in the momentum range from 0.75 – 0.95 GeV/c.

3.4.5. Track-finding efficiency of scattered particles

The SCD1,2 efficiency $\epsilon_{SCD1,2}$ is the total efficiency including the detection efficiency and the analysis efficiency to get straight track at the entrance of the SKS magnet. It was estimated in a similar way as that of BC3-4's by using the BEAM trigger events. The value of ϵ_{SDC1-2} averaged on the incident position was $90.9 \pm 0.3\%$. Since the energy-loss difference between π (1.37-1.92 GeV/c) and K (0.75-1.00 GeV/c) was small, the same result is assumed for K.

The SDC3-4 efficiency (ϵ_{SDC3-4}) is the total efficiency including the detection efficiency and the analysis efficiency to get straight tracks at the exit of the SKS magnet. It was estimated by using the (π, p) events, in which the particle decay in flight was negligible, in the PIK trigger events. The value of ϵ_{SDC3-4} averaged on the incident position was 86.1 ± 0.2 %. For scattered K, the same efficiency was assumed because of the small energy-loss difference between a proton and K at 0.75–1.00 GeV/c.

The SKS tracking efficiency $\epsilon_{SKS-track}$ was estimated by the (π, p) events recorded in the PIK trigger events because the proton does not decay in flight. Figure 3.27 shows the SKS tracking efficiency with respect to the track incident angle to SDC1,2. The value of $\epsilon_{SKS-track}$ was 93.9 ± 0.3 %.

3.4.6. Overkill of the outgoing K^- with Aerogel Čerenkov counter

The coefficient f_{AC} represents the correction factor due to the overkilling rates of AC1,2. This factor was estimated from the controlled trigger data in which the AC1·2 were not involved. The trigger condition was defined as,

$$\text{BEAM} \times \text{TOF} \tag{3.33}$$

The AC1·2 overkilling factor was obtained as

$$f_{AC} = 1 - \frac{N(AC1 \cdot 2 \times TOF \times LC)}{N(TOF \times LC)} \tag{3.34}$$

where $N(TOF \times LC)$ is the number of events which require the timing coincidence between TOF and LC, while $N(AC1 \cdot 2 \times TOF \times LC)$ is those which require the timing coincidence between TOF, LC and AC1·2 within the corresponding timing gate width. $f_{acc.}$ was estimated to be $97.3^{+2.6}_{-3.6}\%$.

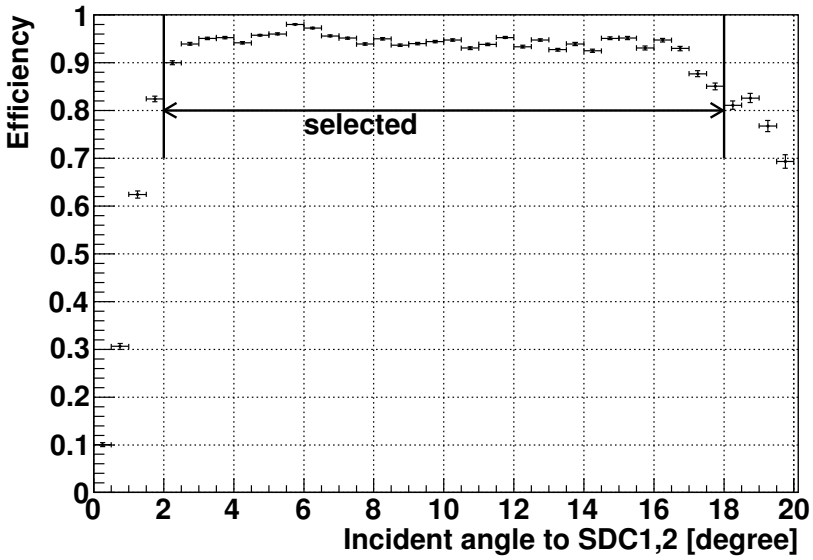

Figure 3.27.: The SKS tracking efficiency as a function of the angle of incident to SDC1-2.

3.4.7. K^- decay factor

f_{decay} represents the correction factor due to the decay of the scattered K. In the present analysis, it is assumed that f_{decay} is decomposed into two factors as follows.

$$f_{decay} = f_{\mathrm{LH2}\to\mathrm{TOF}} \times (1 - f_{\mathrm{TOF}\to\mathrm{LC}}) \tag{3.35}$$

$$f_{\mathrm{LH2}\to\mathrm{TOF}} = e^{-\frac{L}{\beta\gamma c\tau}} \tag{3.36}$$

$$f_{\mathrm{TOF}\to\mathrm{LC}} = \frac{\text{Number of decay products which fired AC1 or AC2}}{\text{Number of kaons reaching the TOF wall}} \tag{3.37}$$

The first component $f_{\mathrm{LH2}\to\mathrm{TOF}}$ is the correction factor due to the decay of kaons until the TOF detector. It depends on $\beta\gamma c\tau$ of the K and its flight length L. The typical value of $e^{-\frac{L}{\beta\gamma c\tau}}$ was estimated to be 41–51 $\pm$ 2.0 % and typical flight lento is 5.1 m for the K in the momentum range of 0.75–1.0 GeV/c. For the calculation of the cross section, $e^{-\frac{L}{\beta\gamma c\tau}}$ was corrected event-by-event taking into account the momentum and the flight path length from the event vertex to the TOF counter. The second factor $f_{\mathrm{TOF}\to\mathrm{LC}}$ expresses the K rejection rate of after passing through the TOF counter. When the velocity of decay products is high enough to make a signal at AC1 or AC2, such are rejected with these detector. $f_{\mathrm{TOF}\to\mathrm{LC}}$ was estimated by the Monte Carlo simulation program based on the Geant4. Figure 3.28 illustrates regions concerned with those factors. The survival rates on the blue and red trajectories correspond to $f_{\mathrm{LH2}\to\mathrm{TOF}}$ and $1 - f_{\mathrm{TOF}\to\mathrm{LC}}$, respectively. The survival rate of scattered K is summarized in Table 3.2. A main contribution comes from the $f_{\mathrm{LH2}\to\mathrm{TOF}}$, which is the survival rate of K from its decay. It should be noted that kaons which decay between the SDC4 and TOF have been also accepted as the kaon events, since decay products make a hit at the TOF with the same time difference as that of kaon. Therefore, the real flight length was the path length from the LH2 target to the SDC4, however, the flight length was calculated from the target to the TOF counter in the current analyses. The effect of the current treatment for the flight length on the f_{decay} was estimated through the Geant4 simulation. It is found to be $\sim$1%, which is negligibly small in the

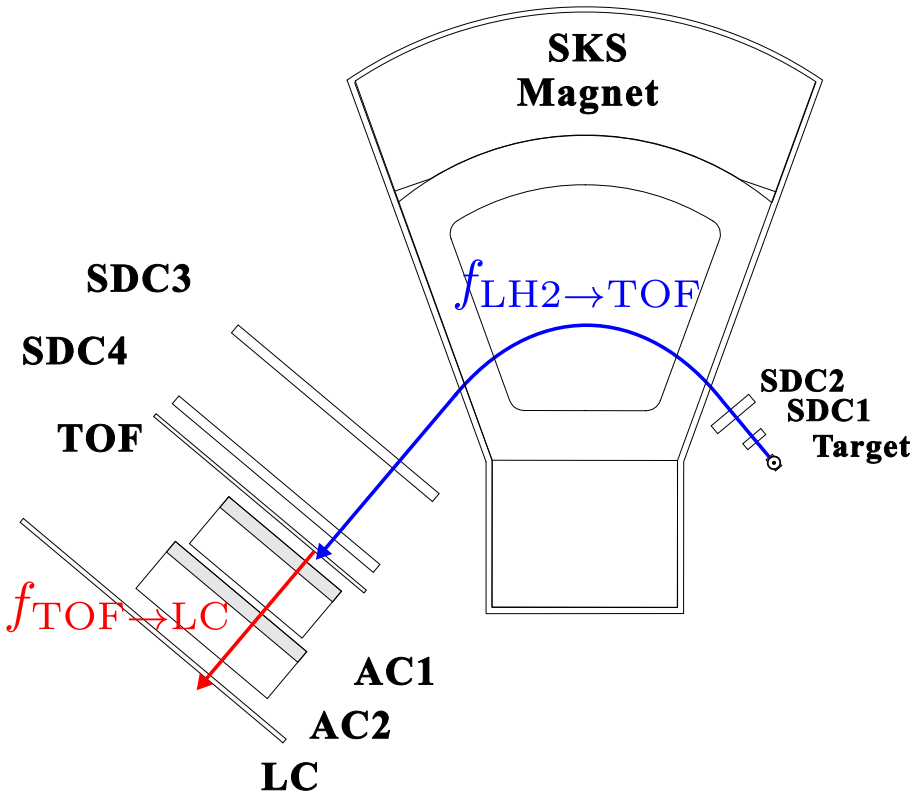

Figure 3.28.: Regions of two kaon survival rate concerned. $f_{\mathrm{LH2}\to\mathrm{TOF}}$ is evaluated from the decay rate of kaons until the TOF counters. $f_{\mathrm{TOF}\to\mathrm{LC}}$ denotes the rejection factor originates from a fake hit at AC1/AC2 caused by decay particles of kaons.

Table 3.2.: The K survival rate.

variable	description	fraction
$f_{\mathrm{LH2}\to\mathrm{TOF}}$	K reached at TOF	(typ.) 0.449
$f_{\mathrm{TOF}\to\mathrm{LC}}$	K rejected by AC1·2 due to the daughter with enough β	0.037± 0.0002
Total survival rate		0.432

calculation of the cross section upper limit.

3.4.8. K^- absorption factor

f_{absorb} represents the correction factor due to the absorption rate of K in the materials. Here, the absorption means the kaon loss by both inelastic and elastic interactions with the materials. The estimation of f_{absorb} was performed by the Monte Carlo simulation based on the Geant4. The rate was estimated to be 4.2 ± 0.5 % for K^+ and 11.2 ± 0.5 % for K^-, respectively.

3.4.9. Efficiency of matrix trigger

In the Θ^+ production data, the pre-scaled PIK trigger events without the matrix trigger was also taken with the pre-scale factor of 10. The efficiency of the matrix trigger ϵ_{matrix} was estimated by a

following equation,

$$\epsilon_{matrix} = \frac{N_{on}}{10 \times N_{off}} \tag{3.38}$$

where N_{on} and N_{off} are the number of kaons selected in the mass distribution of scattered particles with and without the matrix trigger, respectively. The efficiency was found to have no dependence on the scattering angle and the scattered particle momentum so that the matrix trigger made no bias on the missing mass spectrum. The efficiency of the matrix trigger was estimated to be $\epsilon_{matrix} = 99.0 \pm 0.1$ %. The error come from the statistical one.

3.4.10. Efficiency of the PID in the SKS

Three-step cuts were applied to the identification of the outgoing particle. The cut bu the TOF and LC counter's ADC and TDC and the cut by the correlation between TOF and the scattering angle were described in Sec. 3.3.2. The blue open histogram in Fig. 3.29(a) shows kaons selected by those two cut. The third criterion used the measured mass square $M^2_{scattered}$. Particles with the mass of range in $0.15 < M^2_{scattered} < 0.35$ $(\mathrm{GeV}/c^2)^2$ were accepted as kaons, which are shown as the red hatched histogram in Fig.3.29. The efficiency of the outgoing particle identification was estimated as

$$\epsilon_{PID} = \frac{N_{good\ M_{scattered}}}{N_{PIK[0.15<M^2_{scattered}<0.35]}} \tag{3.39}$$

where the denominator $N_{PIK[0.15<M^2_{scattered}<0.35]}$ is the number of PIK triggered events within the range of $0.15 < M^2 < 0.35$ $(\mathrm{GeV}/c^2)^2$. The numerator $N_{good\ M_{scattered}}$ is the number of events passing through the three criteria. The result was $\epsilon_{PID} = 93.1 \pm 2.0$ %. A fluctuation of the production runs was included in the error estimation.

3.4.11. Acceptance

The geometrical acceptance of the SKS was calculated with the Monte Carlo simulation as a function of scattering angle θ and momentum p. In the event generator, the distribution of the beam profile defined as a function of (x_b, y_b, u_b, v_b) was produced from the experimental data, where x_b, y_b, u_b and v_b were the horizontal and vertical positions and their derivatives of a beam particle at the target, respectively. The outgoing Ks were generated uniformly from $\theta - \frac{1}{2}\Delta\theta$ to $\theta + \frac{1}{2}\Delta\theta$ in the polar angle, from 0 to 2π in the azimuthal angle and from $p - \frac{1}{2}\Delta p$ to $p + \frac{1}{2}\Delta p$ in the momentum interval. The effective solid angle $d\Omega(\theta, p)$ was represented as follows,

$$\Delta\Omega(\theta, p) = \int_0^{2\pi} d\phi \int_{\theta'=\theta-\frac{1}{2}\Delta\theta}^{\theta'=\theta+\frac{1}{2}\Delta\theta} d\cos\theta' \left(\frac{N_{accept}(\theta', p)}{N_{generate}(\theta', p)} \right) \tag{3.40}$$

$$= 2\pi \times \int_{\theta'=\theta-\frac{1}{2}\Delta\theta}^{\theta'=\theta+\frac{1}{2}\Delta\theta} d\cos\theta' \left(\frac{N_{accept}(\theta', p)}{N_{generate}(\theta', p)} \right), \tag{3.41}$$

where $N_{accept}(\theta, p)$ and $N_{generate}(\theta, p)$ are the number of accepted events and those of generated events, respectively. The results of fractional acceptance and effective solid angle are shown Figs 3.30 and 3.31, respectively. In this calculation, it was assumed that the Θ^+ was produced isotropically in the center of mass system. The events with the scattering angle from 2° to 18° were chosen so that the efficiency of the SKS tracking is flat as shown in Fig. 3.27. To eliminate kaons with interact with the AC counter,

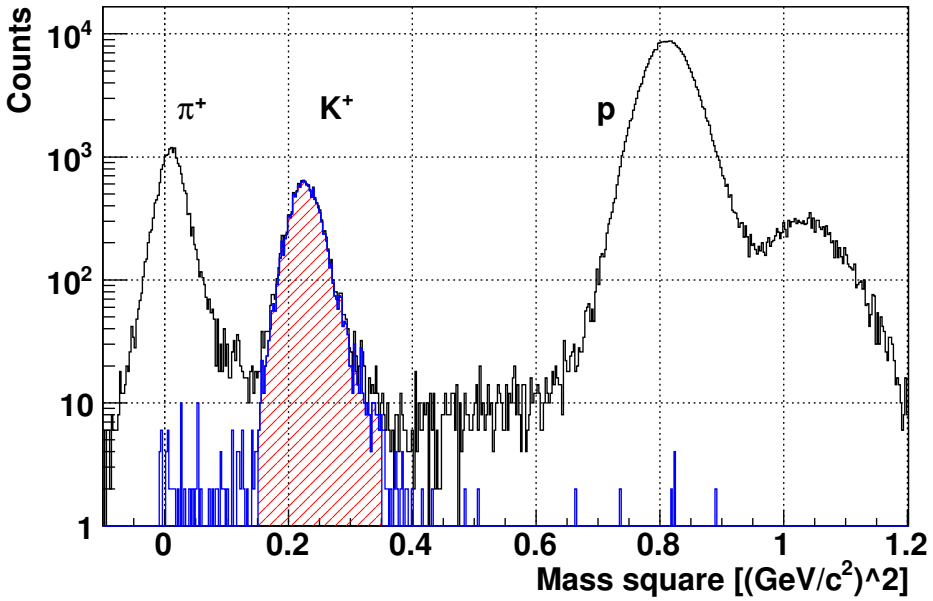

Figure 3.29.: Scattered particle mass distribution for the $(\pi^-, K^+)\Sigma^-$ data. The blue histogram corresponds to the kaons survived after the TOF and LC cut condition. The ratio of the entries in the red-hatched histogram to that of black histogram in the $0.15 < M^2 < 0.35$ were used to calculate the PID efficiency ϵ_{PID}.

the range of 11 to 30 and 11 to 26 segment was used for the TOF and LC counter, respectively. The selected regions is same as the previous analysis [99]. Therefore, the effective solid angle within $2^\circ \leq \theta \leq 18^\circ$ were used in the calculation of the cross section.

3.4.12. Target fiducial volume cut

The liquid hydrogen target was surrounded by the PET vessel and mylar films as described in Sec. 2.7. In order to reduce the background events from those target cell materials, the fiducial volume of the target was defined, comparing the reaction vertex image of the empty target data and the LH2 filled data. Note that the (π^-, π^-) reaction rather than the (π^-, K^-) reaction was used to reconstruct a large number of events.

Figure 3.32 shows the vertex distribution along the beam axis (a), the horizontal (b) and vertical (b) directions. The red and black histograms correspond to the data with and without the LH2, where the entries were normalized according to the beam flux.

Figure 3.33(a) shows the z distribution, where the distribution of the empty target data were subtracted from that of the LH2 filled data. The cut points were set at the FWHM ($-71.7 < z < 54.3$ (mm)) as shown in Fig. 3.33(a). For the xy-distribution, the events were required to be within the circle which had the same radius of the target container. The center of the circle was determined from the beam-through data without LH2. Figure 3.33(b) shows the scatter plot between the x position and the momentum loss of the beam-through data. The loci which were placed at the momentum loss of $-10 < (P_{SKS} - P_{K1.8}) < -5$ GeV/c and the x position of $x \sim 40$ mm or $x \sim -30$ mm is thought

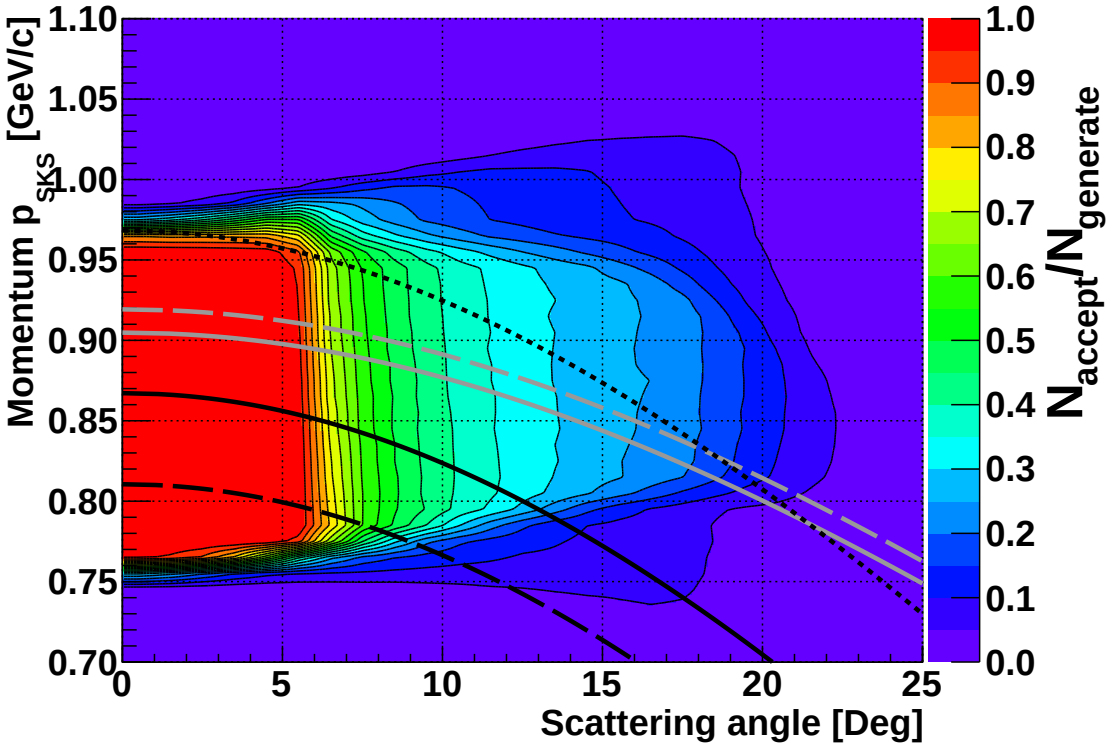

(a)

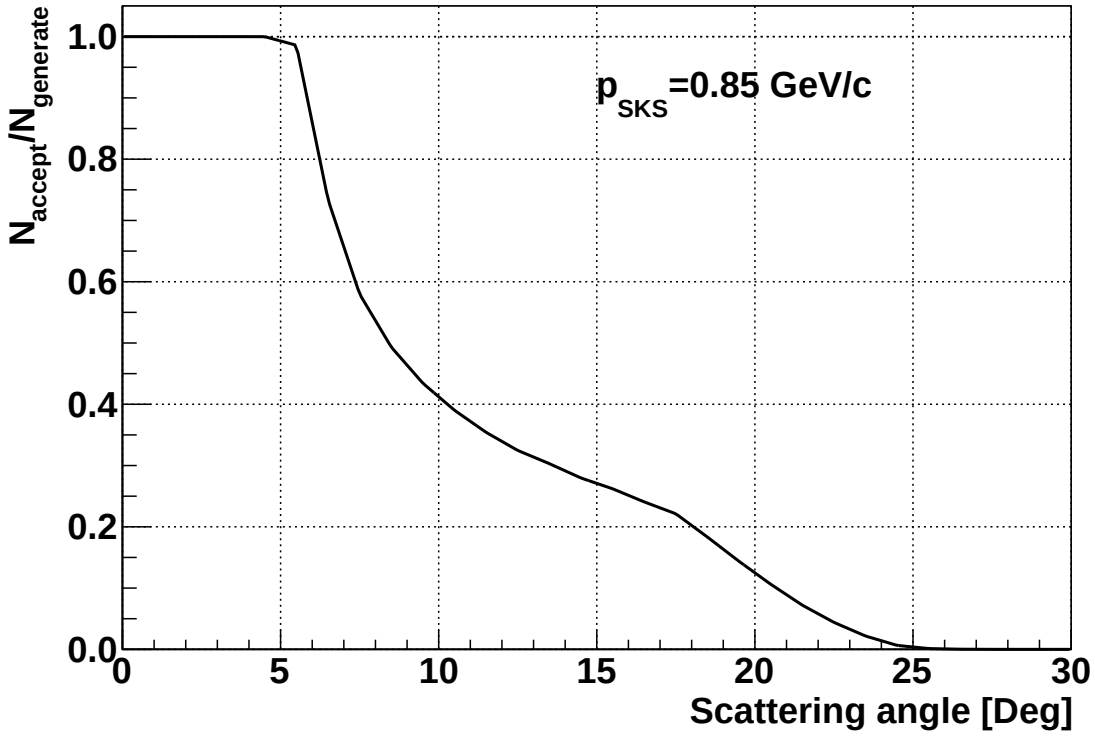

(b)

Figure 3.30.: The acceptance of SKS in the 2.5 T mode. The acceptance is defined as the ratio of the number of accepted events to the number of generated events. (a) The black dotted, solid and dashed lines correspond to the kinematics of the $\pi^- p \to K^- \Theta^+$ reaction at $p_\pi = 1.92$ GeV/c with the Θ^+ masses of 1500, 1540 and 1560 MeV/c^2, respectively. The gray dashed and solid lines correspond to the kinematics of the $\pi^+ p \to K^+ \Sigma^+$ and $\pi^- p \to K^+ \Sigma^-$ reactions at $p_\pi = 1.37$ GeV/c, respectively. (b) A projection plot at $p_{SKS} = 0.85$ GeV/c.

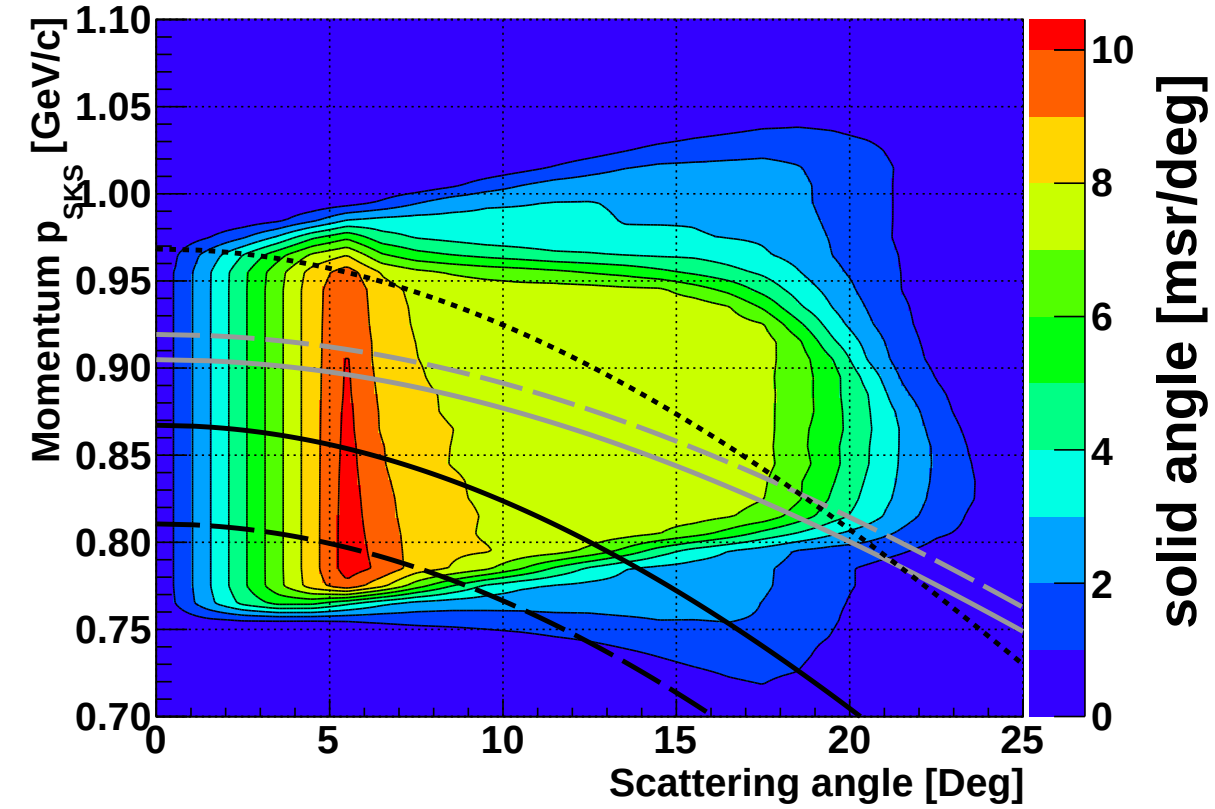

(a)

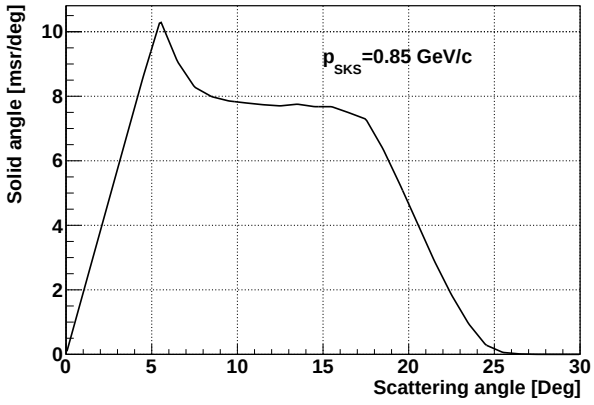

(b)

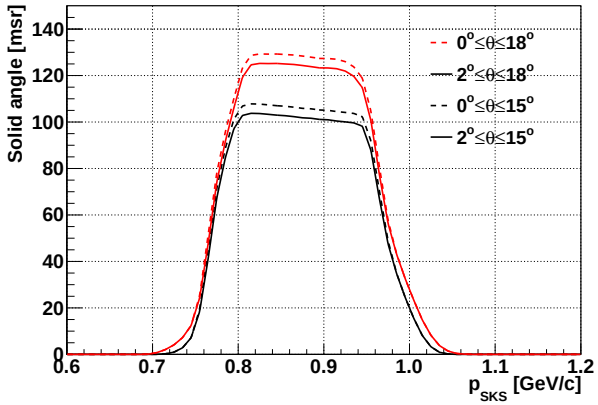

(c)

Figure 3.31.: Effective solid angle of the SKS in the 2.5 T mode. (a) The black dotted, solid and dashed lines correspond to the kinematics of the $\pi^- p \to K^- \Theta^+$ reaction at $p_\pi = 1.92$ GeV/c with the Θ^+ masses of 1500, 1540 and 1560 MeV/c^2, respectively. The gray dashed and solid lines correspond to the kinematics of the $\pi^+ p \to K^+ \Sigma^+$ and $\pi^- p \to K^+ \Sigma^-$ reactions at $p_\pi = 1.37$ GeV/c, respectively. (b) A projection plot at $p_{SKS} = 0.85$ GeV/c. (c) Solid angle as a function of the momentum. red dashed : $0° \leq \theta \leq 18°$. red solid : $2° \leq \theta \leq 18°$. black dashed : $0° \leq \theta \leq 15°$. black solid : $2° \leq \theta \leq 15°$.

to originate from the PET wall of the LH2 container. The blue colored region in Fig. 3.33(b) was selected to see the target cylinder image on the xy-plane as shown in Fig. 3.33(c). The blue circle in Fig. 3.33 indicates the xy-vertex selection in the present analysis. The circle in Fig. 3.26(c) shows the same xy-selection for the (π^-, K^-) reaction vertex.

The vertex selection efficiency was obtained as

$$\epsilon_{vertex} = \frac{N_{[with\ vertex\ selection]}}{N_{[without\ vertex\ selection]}} \tag{3.42}$$

where $N_{[with\ vertex\ selection]}$ is the number of events after the vertex selection and $N_{[without\ vertex\ selection]}$ is that of before the selection. In the (π, K) reaction, 77.9 ± 1.0 % of the events remain after this fiducial volume cut. As shown in Fig. 3.34(b), the vertex cut efficiency had a scattering angle dependence. For the calculation of the cross section, this effect was taken into account.

3.5. Background

The main background processes in the $p(\pi^-, K^-)\Theta^+$ reaction were the three-body final states via the ϕ production, the $\Lambda(1520)$ production and the phase space of K^-K^+n and K^-K^0p. The background spectra of those reactions were estimated by the Geant4 based Monte Carlo simulation. The cross section and the branching ratio used in the simulation are listed in the Table 3.3.

For the ϕ production, the total cross section of 30 ± 8 μb [93] was used. In [95], it was pointed out that there were two possibilities for the angular dependence in the case of ϕ production. Figure 3.35(a) shows the the angular distribution for ϕ production in the center-of-mass system at incident pion momenta from 1.6 to 2.0 GeV/c. Their data is consistent with the isotropic angular dependence though it also consistent with a slight dependence on cosθ with in the statistics. Both cases were considered in the present simulation study. The fit results with a constant and a linear function are shown as a dotted line and a solid line in Fig.3.35(a), respectively. The branching ratio of 0.489 was used for the $\phi \to K^-K^+$ decay [94]. The decay angle distribution for $\phi \to K^-K^+$ was assumed to be isotropic as described in [95].

In the simulation for K^- via of the $\Lambda(1520)$, the $\Lambda(1520)$ was produced in p-wave backward distribution with the total cross section of 20.8 ± 5 μb [93]. Figure 3.35(b) shows the angular dependence for $\Lambda(1520)$ production in the center-of-mass system, where the production angle $\theta_{\rm prod}$ is defined as the angle between the momentum vector of the target proton and that of the produced $\Lambda(1520)$. A half of the $\Lambda(1520)$ decayed to pK^- in the $N\bar{K}$ channel, and decayed kaon had the angular dependence of $\propto \cos^2\theta_{CM}$ as indicated in Fig. 3.35 (c) [93]. Those angular dependences were fitted with a linear and a quadratic functions, respectively (solid lines in Fig. 3.35(b) and (c)). The fit results used in the present analysis are summarized in Table 3.4.

The phase space contribution was estimated by subtracting the cross section of the resonance component from the total cross section of the same final state. The total cross section of the $\pi^-p \to K^-K^+n$ reaction was reported as 39 ± 10 μb [93] and that of the $\pi^-p \to K^-K^0p$ reaction was 30 ± 6 μb [93]. Therefore, the phase space contributions to K^-K^+n and K^-K^0p were calculated to be $39 - 30 \times 0.489 = 24 \pm 11$ μb and $30 - 20.8 \times 0.5 = 20 \pm 10$ μb, respectively.

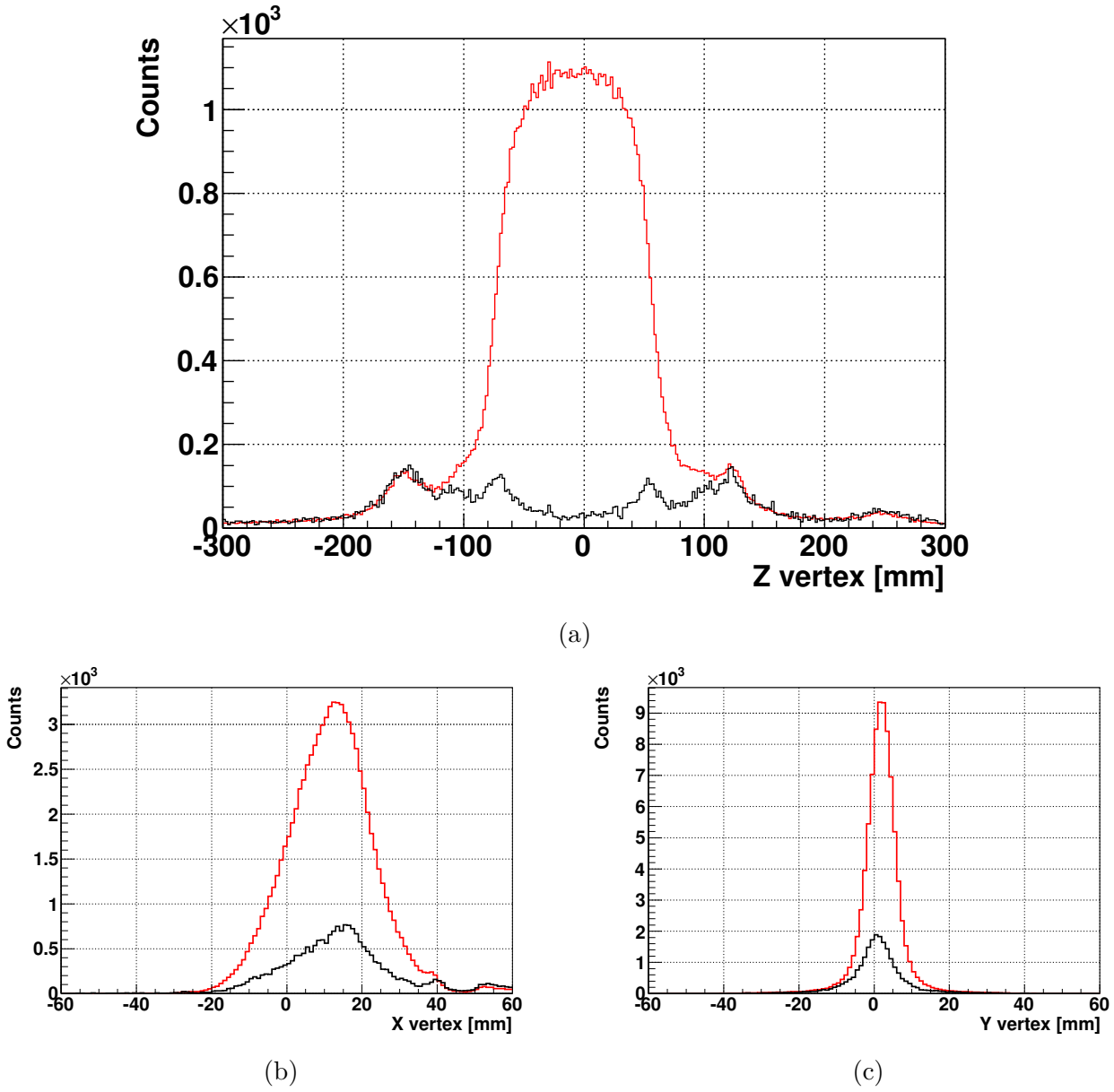

Figure 3.32.: The (π, π) vertex distribution. Each vertical axis is scaled according to the number of beam trigger events. (black): the empty target data. (red): LH2 target data.

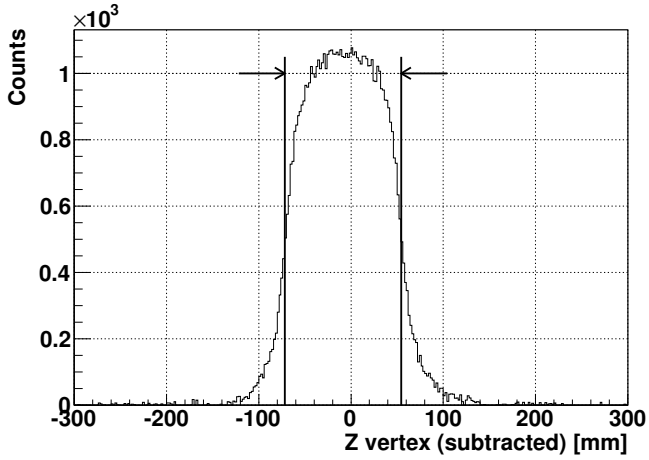

(a)The subtracted z-vertex distribution of the (π, π) reaction.

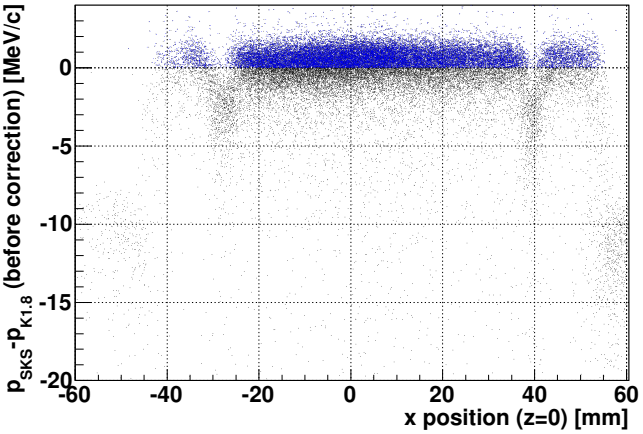

(b) The x position dependence of the momentum drop of the π^+ beam-through data with the momentum of 0.85 GeV/c.

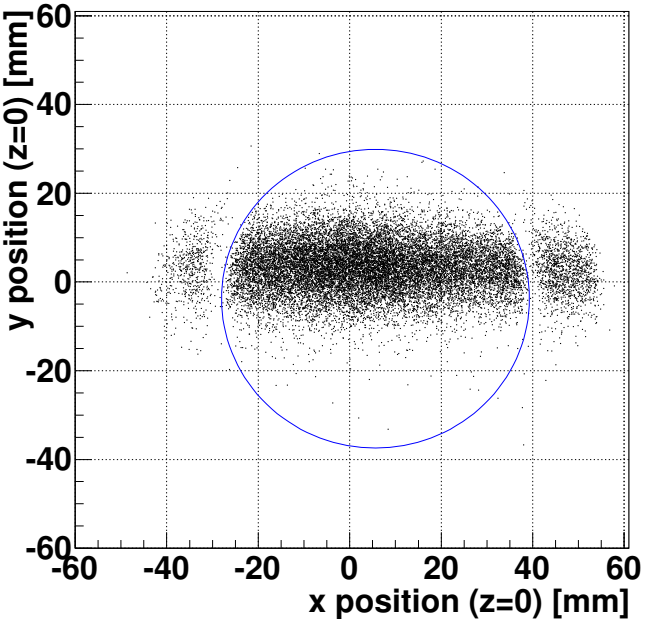

(c) xy beam profile of the blue colored region of (b). The diameter of the blue circle is 67.3 mm, which corresponds to the size of the LH2 target cylinder.

Figure 3.33.: The vertex cut condition for (a) z and for (b),(c) xy

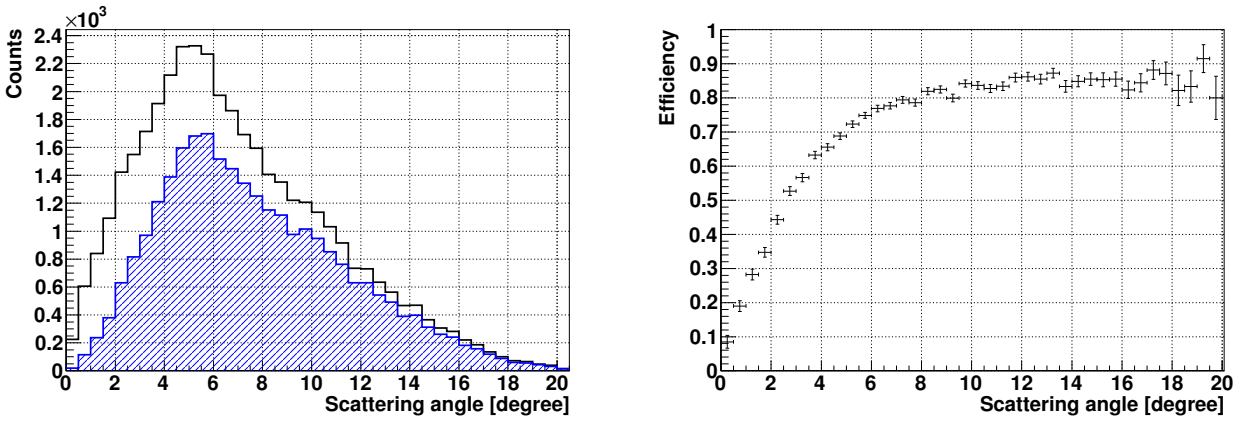

(a) (b)

Figure 3.34.: (a) The scattering angle distribution of the (π^-, K^-) reaction. The blue hatched region indicates the events which survived after the vertex selection. (b)The vertex reconstruction efficiency as a function of the scattering angle of the (π^-, K^-) reaction.

Table 3.3.: Main background processes.

ϕ production				
	$\pi^- p$	$\rightarrow$	ϕn	30 ± 8 μb
	ϕ	$\rightarrow$	$K^- K^+$	BR $= 0.489 \pm 0.005$
$\Lambda(1520)$ production				
	$\pi^- p$	$\rightarrow$	$\Lambda(1520) K^0$	20.8 ± 5 μb
	$\Lambda(1520)$	$\rightarrow$	$p K^-$	BR $= 0.5$
phase space				
	$\pi^- p$	$\rightarrow$	$K^- K^+ n$	$\sim 24 \pm 11$ μb
	$\pi^- p$	$\rightarrow$	$K^- K^0 p$	$\sim 20 \pm 10$ μb

The acceptance of SKS, the decay rate of scattered K^-, the tracking efficiency, the vertex reconstruction efficiency, the distribution of the beam profile and the momentum bite were taken into account in the calculation as same in the data analysis. The relative yield of those processes was normalized by the ratio of each measured cross section. Figures 3.36(a) and (b) show the simulation results of ϕ production with isotropic distribution and with a forward peaking, respectively. The comparison with the simulation and the present experiment will be discussed in Sec. 4.1.

3.6. Consistency check by the $\Sigma^{\pm}$ production reaction

Using the elementary Σ production, the cross section obtained for the present experiment and those in the references was compared. The overall efficiencies and acceptance evaluation are examined. Figure 3.37(a) and (b) show the missing mass spectrum for the $p(\pi^+, K^+)$ and $p(\pi^-, K^+)$ data, respectively. The cross section reported in the old experiments [96, 97] were converted from the center of mass system to the laboratory system and plotted with the open circle, while the present data were plotted with the filled circle. The statistics was much improved with the present experiment. The measured

Table 3.4.: Fit results for the angular distributions of the background processes used in the present analysis. The parameters p_0 and p_1 are the coefficients of the polynomial functions determined in the fit.

	parameterization	fit results	
ϕ production	p_0	$p_0 = 18.5$	
ϕ production	$p_0 + p_1 \cos\theta$	$p_0 = 12.3$	$p_1 = 11.1$
$\Lambda(1520)$ production	$p_0 + p_1 \cos\theta$	$p_0 = -19.2$	$p_1 = 19.1$
$\Lambda(1520)$ decay	$p_0 + p_1 \cos^2\theta$	$p_0 = 14.8$	$p_1 = 17.4$

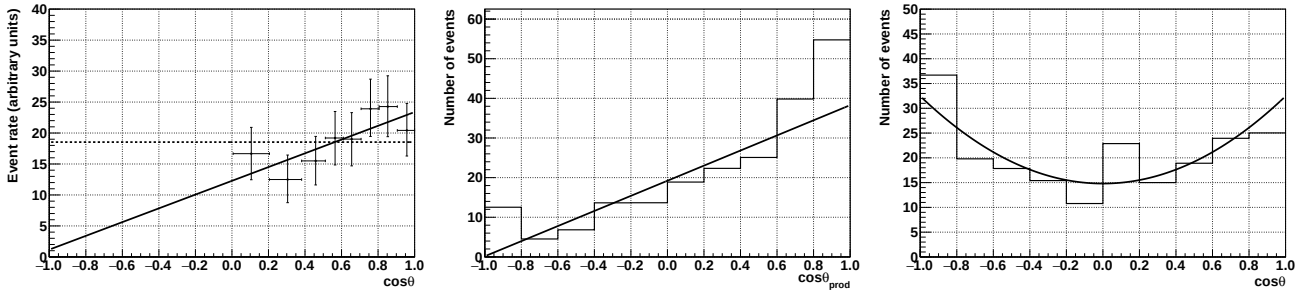

(a) (b) (c)

Figure 3.35.: The angular dependence used in the Monte Carlo simulation. (a) The center-of-mass production angle for $\pi^- p \to \phi n$. Data points are taken from [95]. The dotted and solid lines indicate the fit results of the constant and linear function, respectively. (b) The production angular distribution of $\Lambda(1520)$. Data points are taken from [93]. It should be noted that $\theta_{\rm prod}$ is defined as the angle measured from the opposite direction of the incident pion in [93]. The fit result with the linear function is also shown. (c) The decay angular distribution of $\Lambda(1520)$. Data points are taken from [93]. The fit result with the quadratic function is also shown.

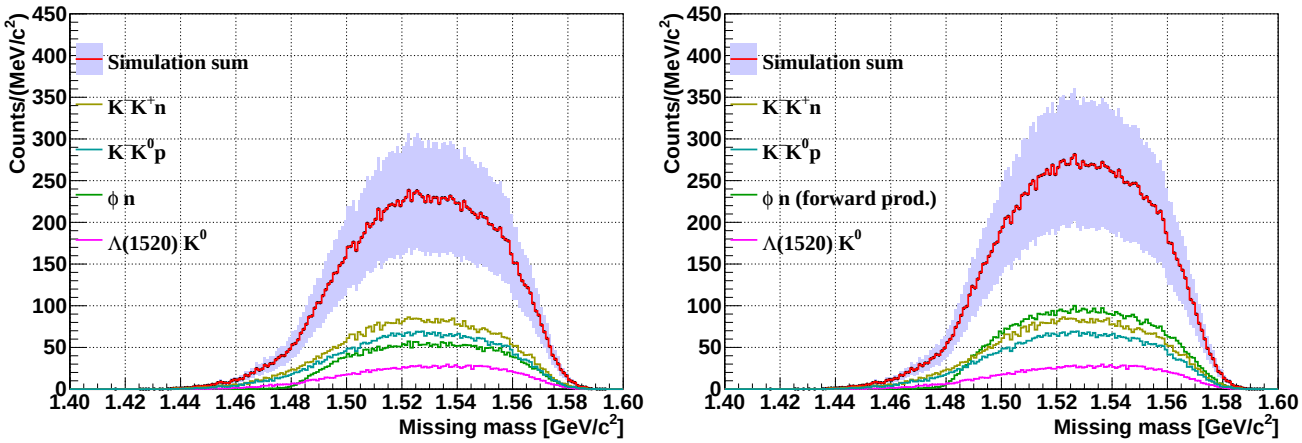

(a)ϕ production is isotropic in the center-of-mass system.

(b)ϕ production is forward peaking in the center-of-mass system.

Figure 3.36.: The background shape of the associated reactions estimated by the Monte Carlo simulation based on the Geant4. The yellow and cyan histograms mean the contribution of the 3-body phase space of K^-K^+n and K^-K^0p, respectively. The green and magenta histograms correspond to ϕ production and $\Lambda(1520)$ production, respectively. The sum of these channels is shown as the red histogram with errors.

differential cross section is in good agreement with the past experimental result.

3.7. Systematic errors

The systematic error of the cross section was estimated from the acceptance of the SKS and the run dependence of the experimental efficiency. The acceptance error of the SKS was assumed to be ±1%. The fluctuation of the efficiencies was estimated to be ±9%. In total, linear sum of the two, i.e. ±10%, was adopted for the systematic error of Θ production run.

3.8. Energy accuracy and resolution

In this section, the calibration of the momentum scales of the SKS and the beam spectrometer are described in detail. Then, on the basis of the analysis, the accuracy and resolution of $p(\pi^-, K^-)X$ missing mass are discussed.

3.8.1. Beam-through data

In order to examine the linearity of the scattered particle's momentum, π^- beam-through data without a target [1] were taken at several central momenta from 0.75 GeV/c to 0.95 GeV/c. The magnet setting of the SKS was fixed at 2.5 T. Figure 3.38 (a) shows the peak position of the momentum difference between the two spectrometers ($\Delta p = p_{SKS} - p_{K1.8}$) as a function of the central momentum of the beam spectrometer. The offset common to all the beam-through data ($\sim$ 4 MeV/c, as shown in Fig.

[1]The target chamber and the vessel were yet installed.

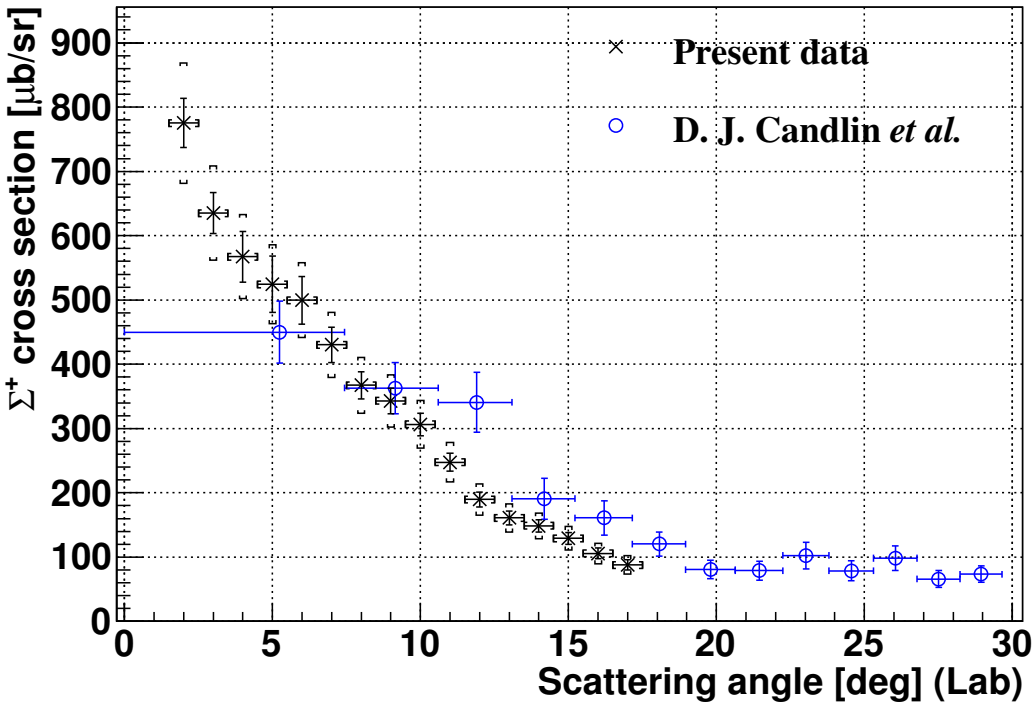

(a) The differential cross sections of Σ^+ production. The angular distribution in old experiment is cited from [96].

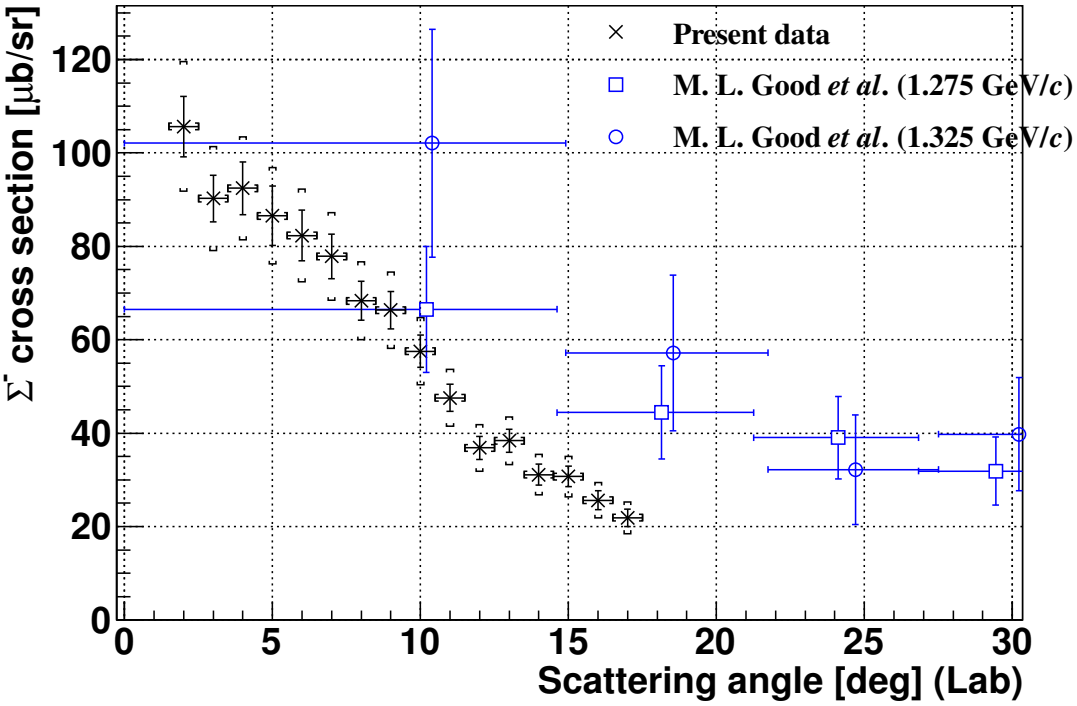

(b) The differential cross sections of Σ^- production. The angular distributions in old experiment are cited from [97].

Figure 3.37.: The differential cross sections of $\Sigma^\pm$ production. The error bar with and without the square bracket of the present experiment includes the only statistical error and both the statistical and the systematic error, respectively.

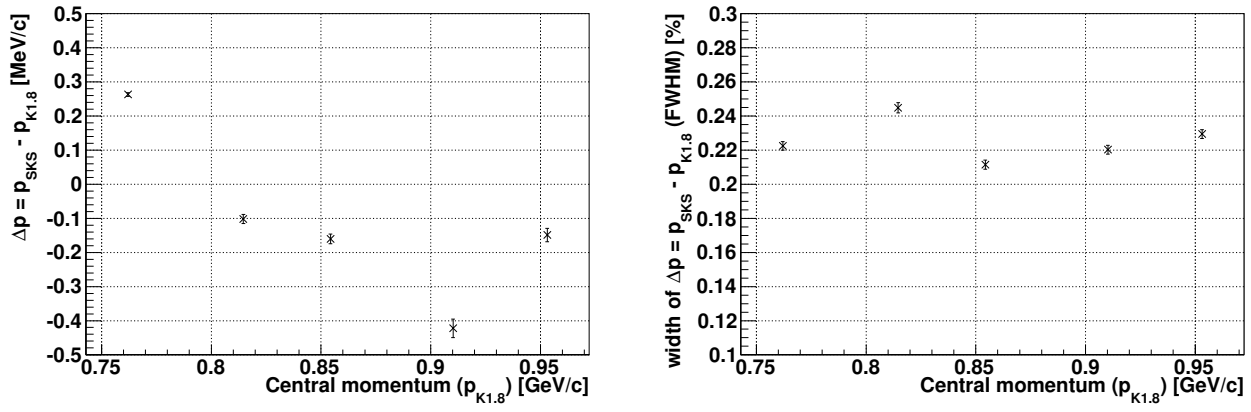

(a) (b)

Figure 3.38.: (a) The momentum difference between the two spectrometers and (b) its width as a function of the central momentum of the beam line spectrometer, where the common momentum offset of ~ 4 MeV/c were subtracted.

3.39), was introduced to minimize the averaged momentum difference. Energy calibration method is described in detail in Sec. 3.8.5

Figure 3.38 (b) shows the variance of the momentum difference Δp as a function of the central momentum of the QQDQQ. This value ($\sigma_{\Delta p}$) gives the momentum resolution including the effect of the two spectrometers and the energy loss straggling occupied in the materials according to the error propagation rule.

$$\sigma^2_{\Delta p} = \sigma^2_{SKS} + \sigma^2_{K1.8} + \sigma^2_{\Delta E\ stragg.} \tag{3.43}$$

The value of $\sigma_{\Delta p}/p$ was 0.2 % (FWHM). The momentum dependence of the resolution was negligibly small.

3.8.2. Energy loss correction

In order to examine the effects of the target energy loss and its straggling, π^- beam through data without and with a target were taken at 0.75–0.95 GeV/c. As an example, Figure 3.40 (a) shows a distribution of the energy difference measured by the beam spectrometer and the SKS without (hatched histogram) and with (black histogram) the liquid hydrogen target for a 0.85 GeV/c π^- beam. The measured energy losses were compared with three kinds of calculations; the Bethe-Bloch formula, the most probable energy loss, and their arithmetic mean. In the present analysis, materials between the two spectrometers were considered as summarized in Table 3.5.

The step lengths and its corresponding energy losses in each material except BH2 were numerically integrated event by event from the vertex position, whereas the energy loss in BH2 (ΔE_{BH2}) was assumed to be proportional to the number of hit segments along the beam track (N_{hit}) multiplied by the energy loss in the segment thickness(ΔE_{seg}) as follows.

$$\Delta E_{BH2} = N_{hit} \times \Delta E_{seg} \tag{3.44}$$

Figure 3.40 shows the comparison between the measured energy loss and the three kinds of calculations. An example of the energy loss distribution after the correction for the LH2 target is shown in

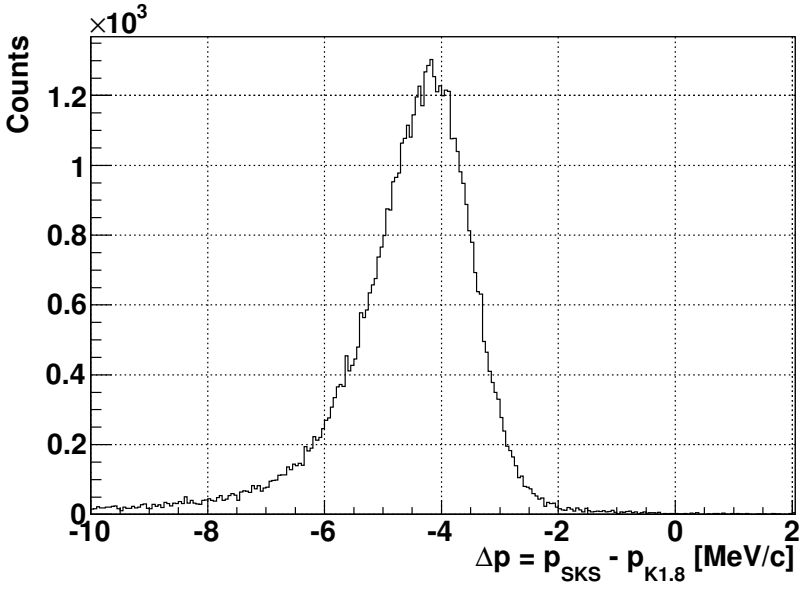

Figure 3.39.: The momentum difference between the two spectrometers without any offset shift. The beam momentum setting was 0.85 GeV/c.

Table 3.5.: Energy loss and straggling at the scattering angle of $\theta = 5°$ for Σ production data.

material	density [g/cm^3]	mass thickness [g/cm^2]	energy loss [MeV]	energy straggling [MeV]
Q13 to Target				
Air	0.001205	0.19 ± 0.01	0.32 ± 0.01	0.058 ± 0.001
Chamber gas	0.00185	0.033 ± 0.001	0.047 ± 0.001	0.0093 ± 0.0001
Mylar	1.4	0.20 ± 0.04	0.298 ± 0.001	0.058 ± 0.001
Carbon (graphite)	2.21	0.053 ± 0.001	0.081 ± 0.001	0.058 ± 0.001
Plastic scintillator	1.032	0.56 ± 0.18	1.08 ± 0.33	0.196 ± 0.058
LH2	0.0708	0.77 ± 0.24	3.43 ± 0.16	0.59 ± 0.08
Target to SKS				
Air	0.001205	0.085 ± 0.025	0.14 ± 0.03	0.033 ± 0.001
Chamber gas	0.00185	0.025 ± 0.001	0.0343 ± 0.0006	0.0093 ± 0.0001
Mylar	1.4	0.162 ± 0.093	0.205 ± 0.004	0.048 ± 0.003
Carbon (graphite)	2.21	0.087 ± 0.01	0.205 ± 0.004	0.048 ± 0.003
All			5.8 ± 0.4	1.07 ± 0.08

colored lines in Fig.3.40(a). The mean value of the energy loss distribution are shown in Fig.3.40(b) for the data with the momenta of ± 0.85 GeV/c. The obtained values from the data agreed well with any calculations in the error bar. Among the three calculation methods, the arithmetic mean of the Bethe-Bloch and the most probable energy loss was adopted for the missing mass calculation.

3.8.3. Energy fluctuation in materials

The energy straggling in materials which occupied the space from the exit of the last Q-magnet of K1.8 beam spectrometer to the entrance of SKS (i.e. wire chambers, mylar sheets, BH2, LH2, the container of LH2 and air) was estimated by using Landau distribution. To test the validity of the estimation, the measured energy loss straggling in BH2 and LH2 was calculated from the width broadening of the energy difference ΔE. Figure 3.41 (a) shows the difference of squares of ΔE between the tracks passing through one segment of BH2 and those passing through two segments of BH2. In Fig. 3.41 (b), the difference of squares of ΔE between the data with LH2 and without LH2 are shown. The estimation of the energy fluctuation based on the Landau distribution agreed well with the measured values. Therefore, the Landau fluctuations were applied to other materials besides BH2 and LH2.

3.8.4. Momentum correction

In the KEK-PS experiment using the SKS, it was known that there was the correlation between reconstructed momenta (P^{track}_{SKS}) and scattered directions ($\frac{dx}{dz}, \frac{dy}{dz}$) and those correlation caused the energy resolution worse. In the present analysis, such correlation was investigated in elementary process of Σ production reaction $p(\pi^{\pm}, K^{+})\Sigma^{\pm}$. Figures 3.42 and 3.43 show scattered plots between the missing mass for the $p(\pi, K)\Sigma$ reaction and $\frac{dx}{dz}$ or $\frac{dy}{dz}$. In order to improve the energy resolution, the momentum correction for the scattered kaon is expressed by the following equation;

$$P^{cor}_{SKS} = P^{track}_{SKS} + dP_{loss} + \sum_{k=0}^{3} a_k \cdot \left(\frac{dx}{dz}\right)^k + \sum_{k=0}^{4} b_k \cdot \left(\frac{dy}{dz}\right)^k + c \tag{3.45}$$

where P^{cor}_{SKS} is the corrected kaon's momentum at the reaction point. dP_{loss} is the term due to the energy loss. a_k and b_k are the correlation coefficients and c is the energy offset to be determined finally. In the correction procedure, P^{cor}_{SKS} was estimated assuming the kinematics of the $p(\pi^{\pm}, K^{+})\Sigma^{\pm}$ reaction, which can have correlation with neither $\frac{dx}{dy}$ nor $\frac{dy}{dz}$. Thus, the correction coefficients, a_k and b_k, were solved by minimizing the difference of the estimated P^{cor}_{SKS} and P^{track}_{SKS}. In the momentum correction for K^{-} in the SKS, it was assumed that the same correction parameters as those of $p(\pi^{\pm}, K^{+})\Sigma^{\pm}$ were applicable to the $p(\pi^{-}, K^{-})$ reaction data.

The beam momentum was corrected by the following equation;

$$P^{cor}_{K1.8} = f_{D4} \cdot (P^{track}_{K1.8} + d) - dP_{loss} \tag{3.46}$$

where $P^{cor}_{K1.8}$ is the corrected π momentum at the reaction point. $P^{track}_{K1.8}$ is the reconstructed momentum by the beam spectrometer. f_{D4} represents the normalization factor due to the time fluctuation of the dipole magnetic field. dP_{loss} is the estimated momentum loss and d is the energy offset. In the present experiment, the power supply system of D4 magnet affected by the electrical noise from the operation of J-PARC Main Ring, therefore, f_{D4} had the time dependence correlated with the spill cycle. Figure

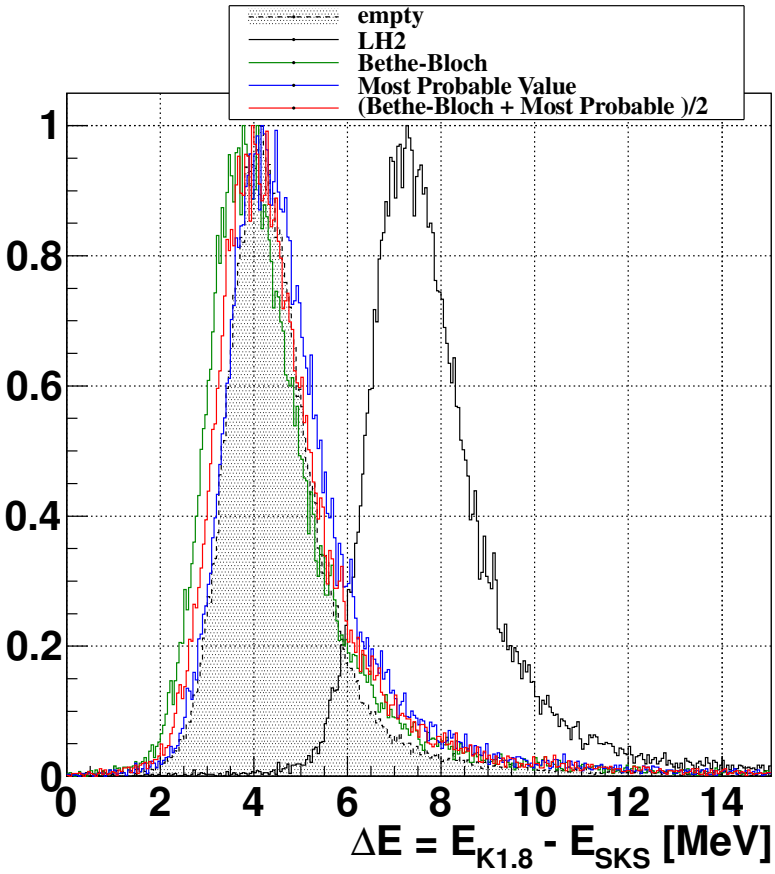

(a)

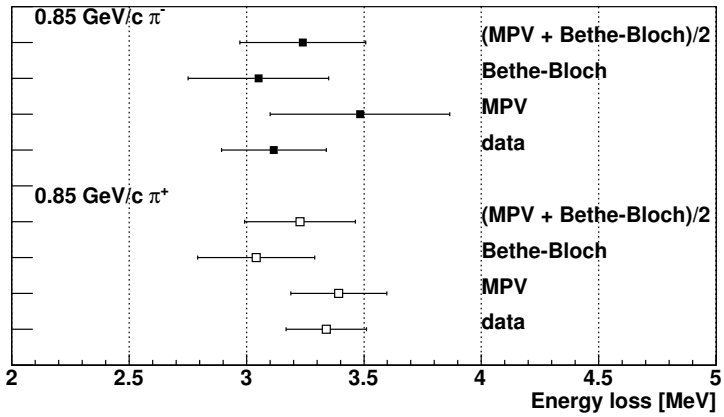

(b)

Figure 3.40.: Comparison of three kinds of energy loss calculation; the Bethe-Bloch formula, the most probable energy loss and their mean values. (a): Energy difference of the π^- beam at 0.85 GeV/c between the two spectrometers before offset correction. Hatched and black histogram corresponds to the measured distribution without the LH2 target and with the LH2 target, respectively. Colored lines are calculated histograms after the correction for the energy loss in the LH2 target. (b): Energy loss in the LH2 target and its correction for $\pi^{\pm}$ beams at 0.85 GeV/c

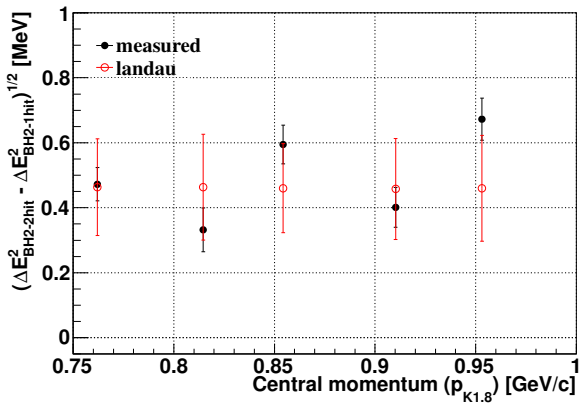

(a) difference of energy fluctuation in BH2 for π^- beams.

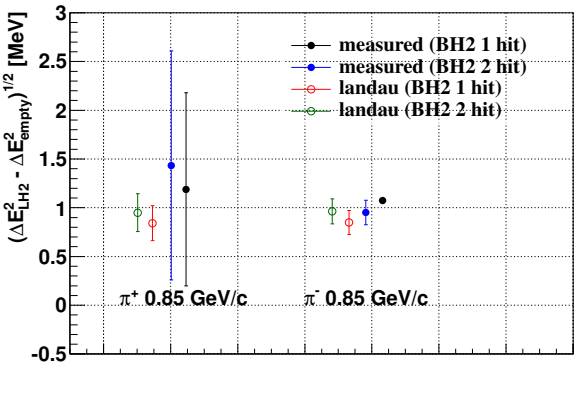

(b) difference of energy fluctuation in LH2.

Figure 3.41.: Measured energy-loss straggling difference in materials compared with a calculation based on the Landau distribution.

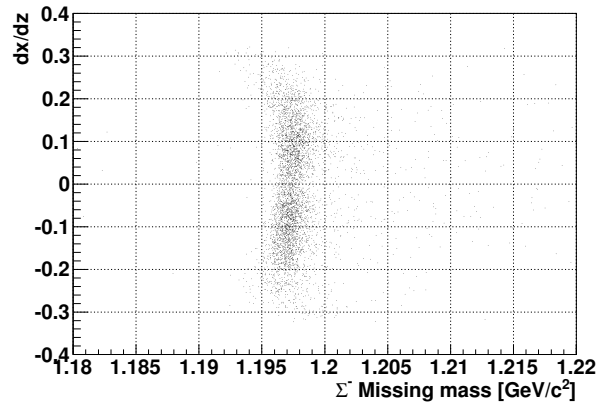

(a)

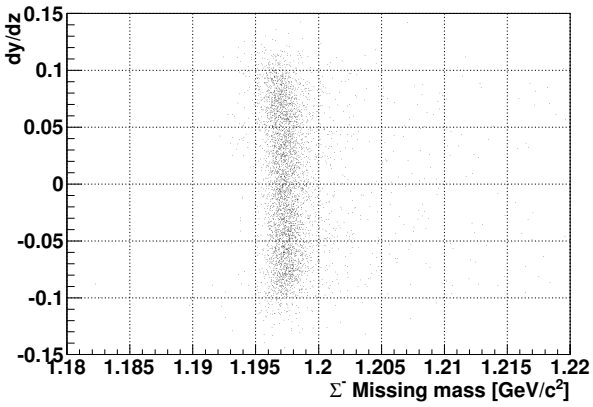

(b)

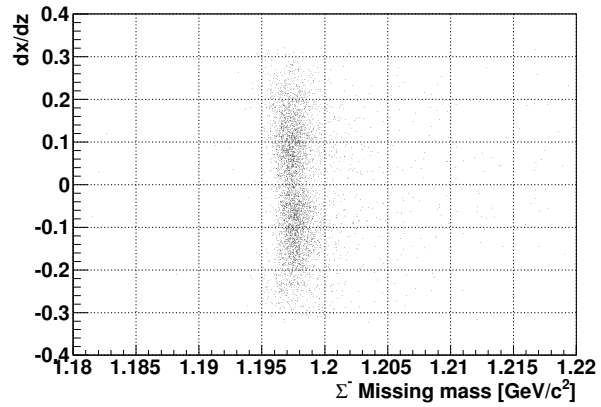

(c)

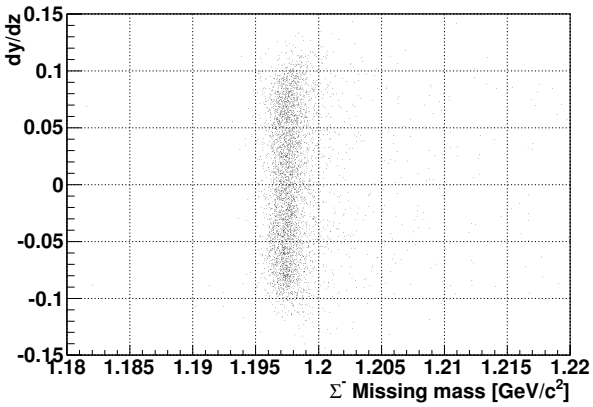

(d)

Figure 3.42.: Scatter plot between the scattering angle in the horizontal direction ($\frac{dx}{dz}$) or the vertical direction ($\frac{dy}{dz}$) and the missing mass of Σ^- in the $p(\pi^-, K^+)$ reaction. (a), (b): before correcting correlation. (c), (d): after correction.

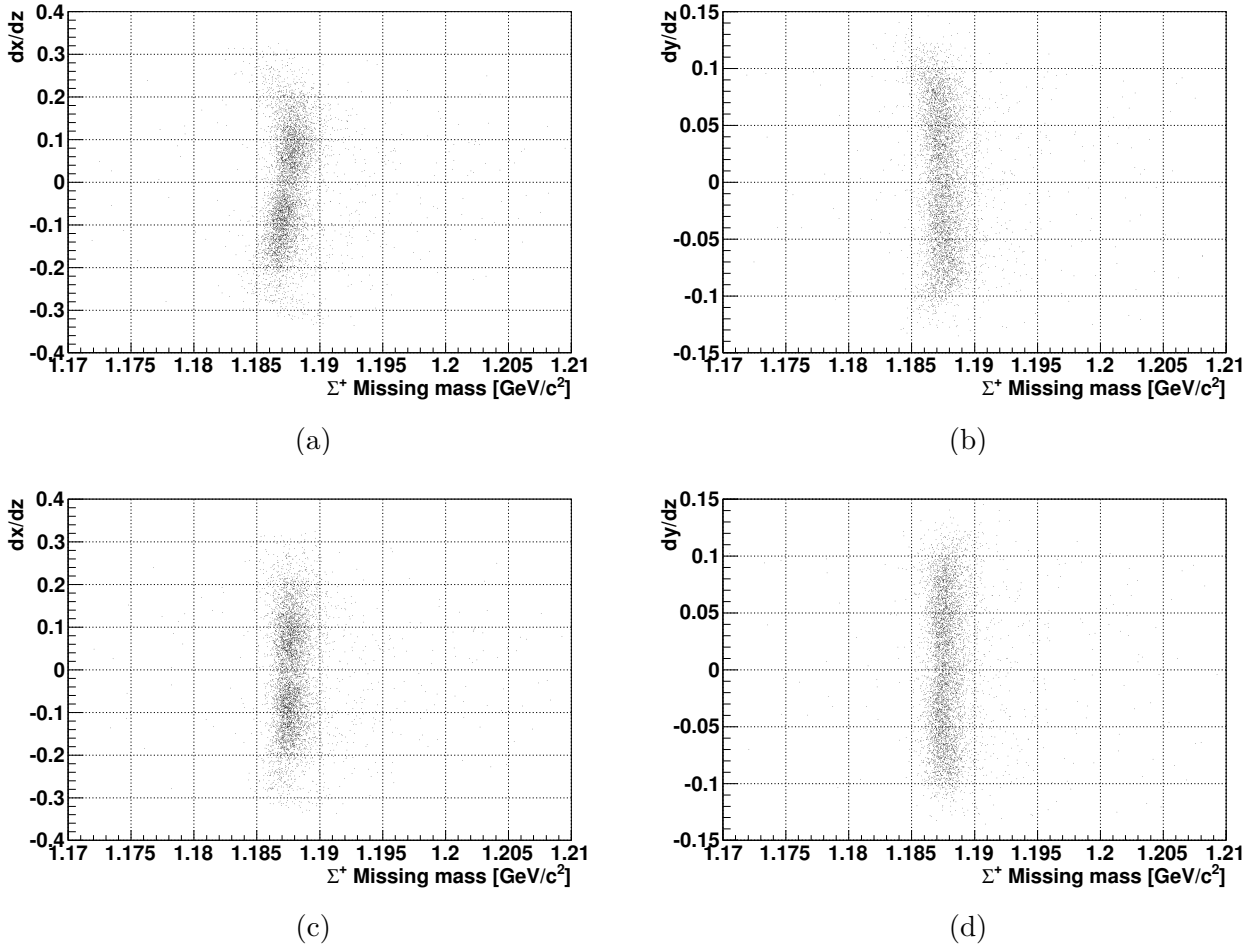

Figure 3.43.: Scatter plot between the scattering angle in the horizontal direction ($\frac{dx}{dz}$) or the vertical direction ($\frac{dy}{dz}$) and the missing mass of Σ^+ in the $p(\pi^+, K^+)$ reaction. (a), (b): before correcting correlation. (c), (d): after correction.

3.44 shows the scatter plot of the field strength normalized by the central value vs. the timestamp in the spill together with the operation pattern of the J-PARC Main Ring. The correction function f_{D4} is shown in red line. The fluctuation of $\Delta B/B \sim 10^{-4}$ was observed at the beginning of the beam extraction from MR. However, no significant difference was observed between with and without this correction due to low statistics of $\Sigma^{\pm}$ production data. Therefore, this correction could be ignored in the beam momentum correction.

3.8.5. Energy calibration

The absolute momentum offsets, which were denoted by the constants c and d in Eq. (3.45), (3.46), were determined by the $\pi^{\pm}$ beam-through data without filling LH2 at several central momenta (-0.75 GeV/c to -0.95 GeV/c, and $+0.85$ GeV/c) and the $p(\pi^{\pm}, K^{+})\Sigma^{\pm}$ reaction data. In the present analysis, the different momentum offset values were assumed for the positive and negative polarities of the magnetic field, therefore there were four parameters, i.e. $c_{\pm}$ and $d_{\pm}$, to be determined, where the sign in the subscript means the magnet polarity. The figure of merit (FoM) was set as the summation of the momentum differences and the mass differences in quadrature with the same weights as follows;

$$FoM = \sum_{beam\ through\ data} (P^{cor}_{SKS} - P^{cor}_{K1.8})^2 + \left(M^{meas.}_{\Sigma^+} - M^{PDG}_{\Sigma^+}\right)^2 + \left(M^{meas.}_{\Sigma^-} - M^{PDG}_{\Sigma^-}\right)^2 \qquad (3.47)$$

where $M^{PDG}_{\Sigma^{\pm}}$ and $M^{meas.}_{\Sigma^{\pm}}$ are the mass of $\Sigma^{\pm}$ in PDG (1189.37 $\pm$ 0.07 MeV/c^2 for Σ^+, 1197.449$\pm$ 0.03 MeV/c^2 for Σ^-) [98] and the measured ones, respectively. Minimizing the Eq. (3.47), the error of the calibration was estimated to be $\pm$ 1.7 MeV/c^2. The offset correction parameters obtained by the minimization are summarized in Table 3.6. The missing mass spectra of the reaction $p(\pi^{\pm}, K^{+})$ after the all calibration procedures are shown in Fig. 3.46. Among the four parameters, c_{-} and d_{-} were used in the missing mass calculation of the $p(\pi^{-}, K^{-})X$ reaction. Figure 3.45 shows the momentum spectra of π beam and scattered K after the calibration.

3.9. Missing mass resolution

The experimental missing mass resolution ΔMM consists of the following four contributions;

$$\Delta MM^2 = \Delta^2_{Beam} + \Delta^2_{SKS} + \Delta^2_{\theta} + \Delta E^2_{stragg.} \qquad (3.48)$$

where the first term is the contribution from the momentum resolution of the beam line spectrometer (Δ_{Beam}), the second term is that of SKS (Δ_{SKS}), the third term comes from the resolution of the scattering angle (Δ_{θ}) and the last term is energy loss fluctuation in the materials ($\Delta E_{stragg.}$). Each

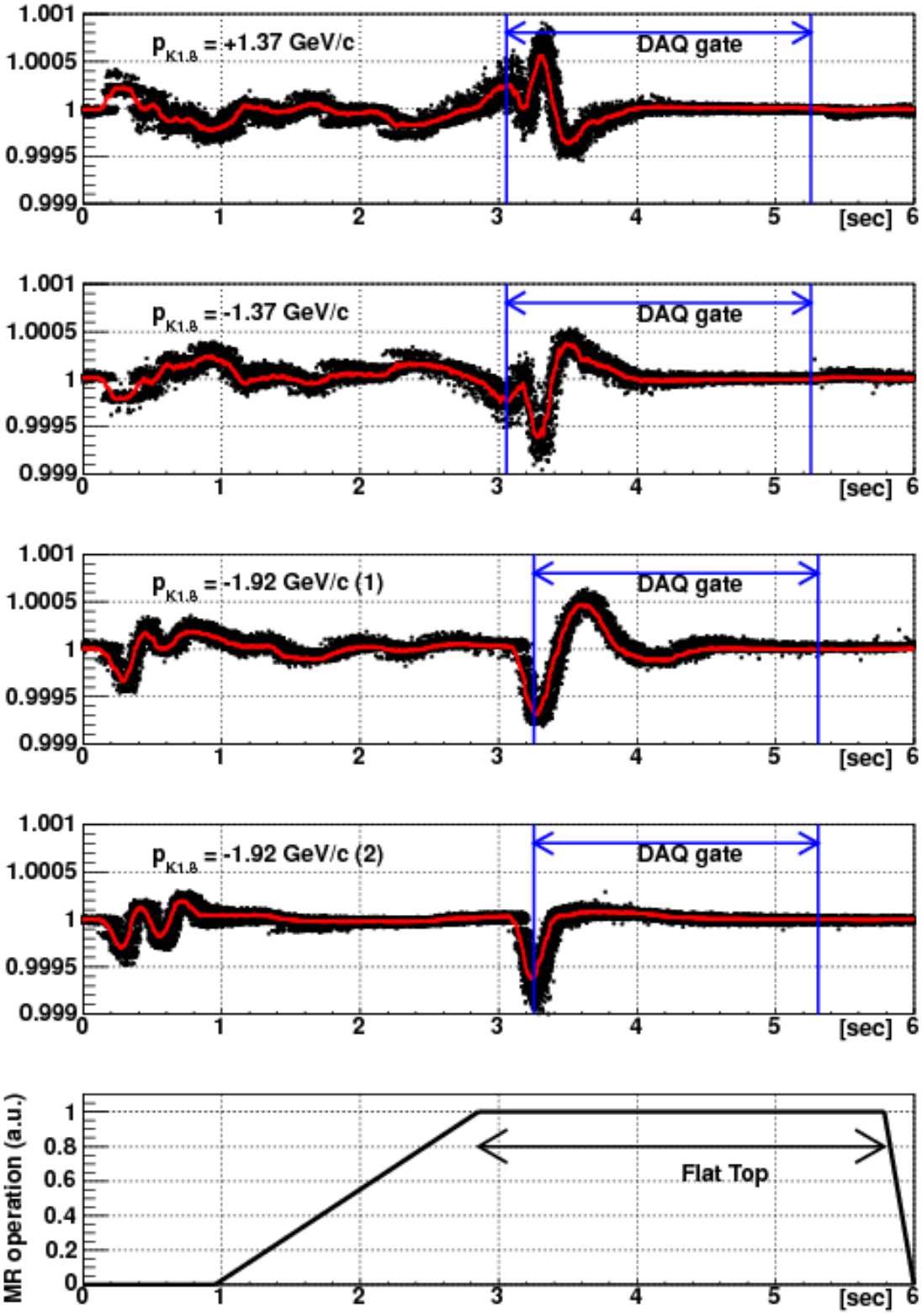

Figure 3.44.: Scatter plot of the fluctuation of normalized field value of K1.8 D4. The bottom figure shows the schematic of the MR operation pattern.

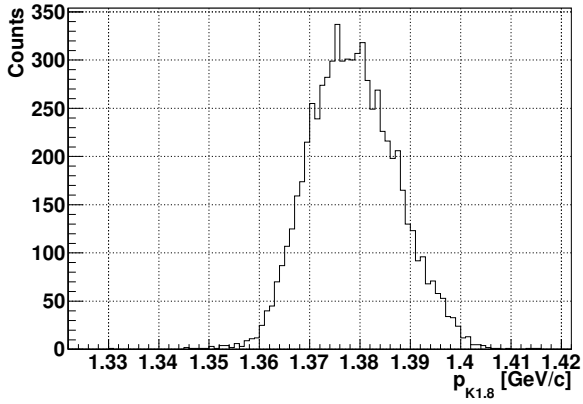

(a) π^+ beam momentum of the Σ^+ RUN.

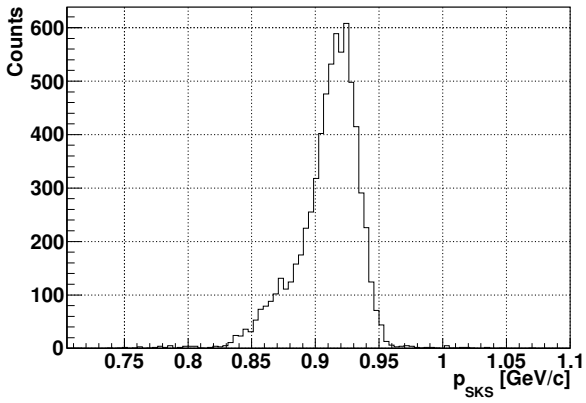

(b) Scattered K^+ momentum of the Σ^+ RUN.

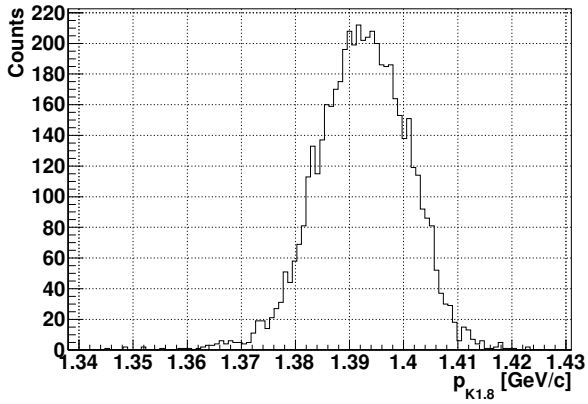

(c) π^- beam momentum of the Σ^- RUN.

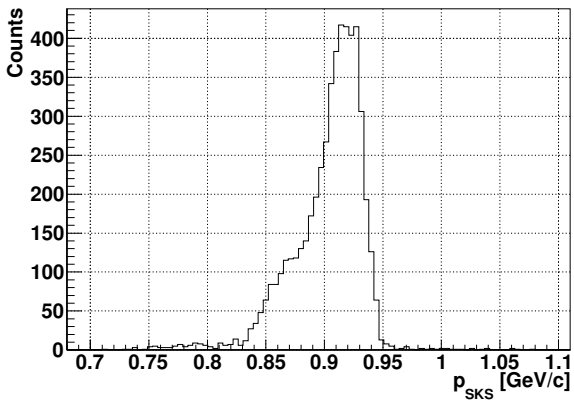

(d) Scattered K^+ momentum of the Σ^- RUN.

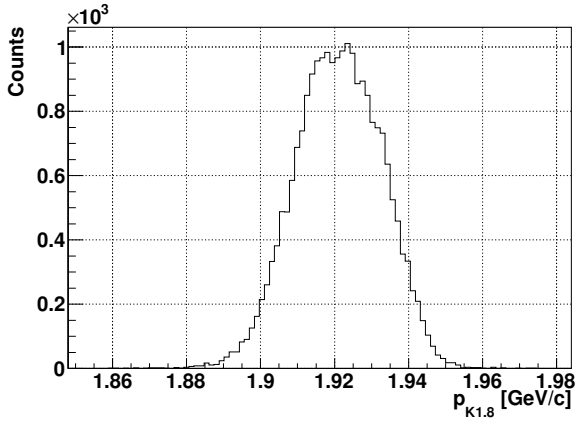

(e) π^- beam momentum of the Θ^+ RUN.

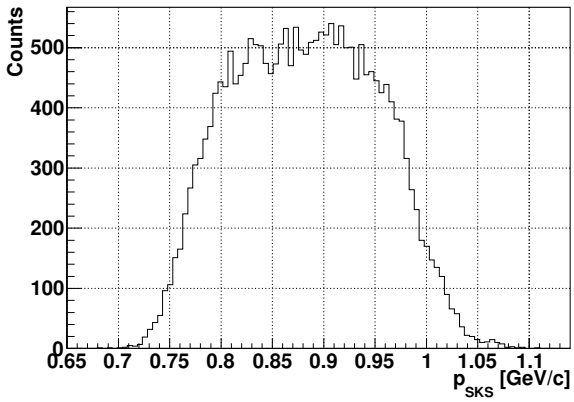

(f) Scattered K^- momentum of the Θ^+ RUN.

Figure 3.45.: Momentum spectra of π beam and scattered K after the energy calibration.

Table 3.6.: The relation between the magnetic field polarities and the four offset correction parameters together with the typical momenta. The right column means the accuracy, which corresponds to each term of the right hand side of Eq.3.47.

RUN condition	SKS [GeV/c]		K1.8 D4 [GeV/c]		before any correction $P^{cor}_{SKS} - P^{cor}_{K1.8}$ [MeV/c]	after correction
π^+ beam through	c_+	0.85	d_+	0.85	+0.39	−0.97
π^- beam through	c_-	0.75	d_-	0.75	−3.8	+0.39
π^- beam through	c_-	0.80	d_-	0.80	−4.2	+0.0017
π^- beam through	c_-	0.85	d_-	0.85	−4.2	−0.051
π^- beam through	c_-	0.90	d_-	0.90	−4.5	−0.31
π^- beam through	c_-	0.95	d_-	0.95	−4.2	−0.032
					$M^{meas.}_{\Sigma^\pm} - M^{PDG}_{\Sigma^\pm}$ [MeV/c^2]	
$p(\pi^+, K^+)\Sigma^+$	c_+	0.83-0.96	d_+	1.37	+1.9	−1.7
$p(\pi^-, K^+)\Sigma^-$	c_+	0.83-0.95	d_-	1.37	+3.7	+0.051

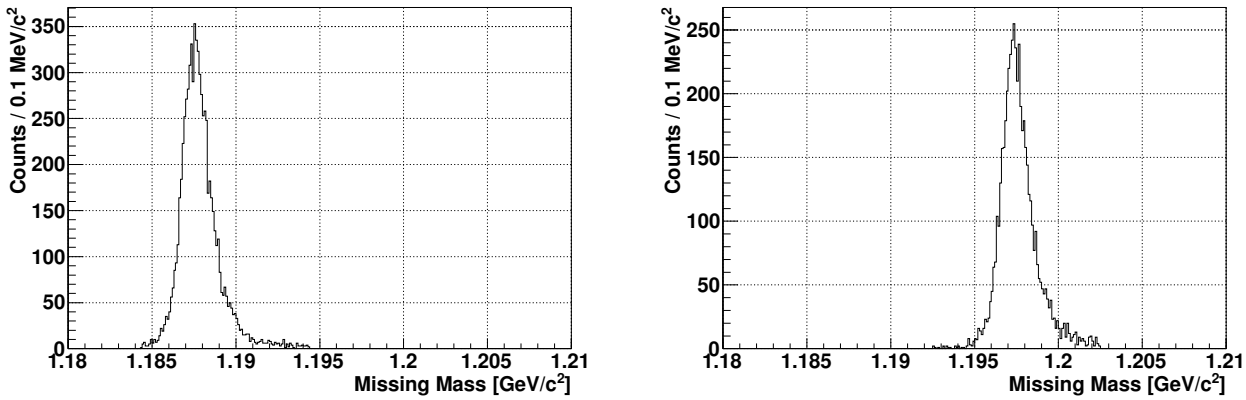

(a)Σ^+ missing mass

(b)Σ^- missing mass

Figure 3.46.: Missing mass spectra of the $p(\pi^+, K^+)$ reaction (a) and the $p(\pi^-, K^+)$ reaction (b).

component can be described as

$$\begin{aligned}
\Delta^2_{Beam} &= \left(\frac{\partial MM}{\partial p_{Beam}}\right)^2 \Delta p^2_{Beam} \\
&= \left(\frac{1}{MM}[\beta_\pi(M_p - E_K) + p_K \cos\theta]\right)^2 \Delta p^2_{Beam} \\
\Delta^2_{SKS} &= \left(\frac{\partial MM}{\partial p_{SKS}}\right)^2 \Delta p^2_{SKS} \\
&= \left(-\frac{1}{MM}[\beta_K(M_p + E_\pi) - p_\pi \cos\theta]\right)^2 \Delta p^2_{SKS} \\
\Delta^2_{\theta} &= \left(\frac{\partial MM}{\partial \theta}\right)^2 \Delta \theta^2 \\
&= \left(-\frac{p_\pi p_K}{MM}\sin\theta\right)^2 \Delta \theta^2,
\end{aligned}$$

where E_π and p_π are the total energy and momentum of a π, E_K and p_K are those of a K, M_p is the proton mass, and θ is the scattering angle of the reaction. Δp_{Beam} and Δp_{SKS} is the momentum resolution of the K1.8 beam line and the SKS spectrometer. $\Delta\theta$ is the resolution of the scattering angle.

The resolution of the scattering angle was estimated to be $\Delta\theta = 5.9$ mrad as stated in Sec. 3.3.2.

The effect of the energy loss straggling $\Delta E_{stragg.}$ was estimated by the Landau distribution as described in Sec. 3.8.3. The calculation included the energy loss straggling in all the materials between the two spectrometer. Furthermore, the difference of the path length in the LH2 target was considered using the reaction vertex point distribution. The mean value of the energy loss straggling in the LH2 target and in all the materials was estimated to be 0.56 MeV and 1.07 MeV for the $\Sigma^\pm$ data and 0.58 MeV and 1.08 MeV for the Θ^+ data, respectively.

The measured missing mass resolution of the Σ production was obtained to be $\Delta MM = 1.84 \pm 0.03 \pm 0.07$ MeV/c^2 (FWHM), where the first and the second error are the statistical and the systematic ones, respectively. The momentum resolutions of the two spectrometers were estimated so as to reproduce the measured missing mass of Σ and the width of the momentum differences in the beam through data assuming that the intrinsic momentum resolution ($\Delta p_{Beam}/p_{Beam}, \Delta p_{SKS}/p_{SKS}$) were constant in the momentum range of the present experiment, and that each momentum resolution composed of the sum of the intrinsic resolution and the contribution of the systematic uncertainty of the magnetic field as follows.

$$\left(\frac{\Delta p_{Beam}}{p_{Beam}}\right)^2 = \left(\frac{\Delta p_{Beam}}{p_{Beam}}\right)^2_{intr.} + \Delta^2_{B_{D4}} \tag{3.49}$$

$$\left(\frac{\Delta p_{Beam}}{p_{Beam}}\right)_{intr.} = c_B \tag{3.50}$$

$$\left(\frac{\Delta p_{SKS}}{p_{SKS}}\right)^2 = \left(\frac{\Delta p_{SKS}}{p_{SKS}}\right)^2_{intr.} + \Delta^2_{B_{SKS}} \tag{3.51}$$

$$\left(\frac{\Delta p_{SKS}}{p_{SKS}}\right)_{intr.} = c_S \tag{3.52}$$

where $\frac{\Delta p_{Beam}}{p_{Beam}}$ ($\frac{\Delta p_{SKS}}{p_{SKS}}$), $\frac{\Delta p_{Beam}}{p_{Beam}}_{intr.}$ ($\frac{\Delta p_{SKS}}{p_{SKS}}_{intr.}$), c_B (c_S) and $\Delta_{B_{D4}}$ ($\Delta_{B_{SKS}}$) are the expected momentum resolution of the beam π (scattered kaon), the intrinsic one, the constant coefficient and the

contribution from the field fluctuation of the K1.8 D4 magnet (SKS). These assumptions simplified the Eq.3.48 and Eq.3.43 to the followings,

$$\Delta MM^2 = A \cdot c_B^2 + B \cdot c_S^2 + C \tag{3.53}$$

$$\left(\frac{\sigma_{\Delta p}}{p}\right)^2 = c_B^2 + c_S^2 + D \tag{3.54}$$

where A,B,C and D are variables determined by kinematics and contributions from known fluctuation sources, respectively. If kinematics is given, Eq.3.53 and Eq.3.54 are depicted as an ellipse and a circle in the $c_B c_S$ plane, respectively. Therefore, the solution for (c_B, c_S) was obtained as the intersection of the two curves. Figure 3.47 shows such an example. The fluctuation $\Delta_{B_{D4}}$ were $\pm 3.0 \times 10^{-4}$ and $\pm 4.0 \times 10^{-4}$ at the beam momenta of 1.37 GeV/c and 1.92 GeV/c, respectively. For the SKS, the time dependence of the magnetic field was negligibly small. However, there was uncertainty from the field map difference between the measured value and the finite element calculation. The position dependence was estimated to be $\Delta_{B_{SKS}} = \pm 4.7 \times 10^{-4}$ [90]. The obtained values were $\Delta p_{Beam} = 9.3 \times 10^{-4}$ and 9.7×10^{-4} for the beam momenta of 1.37 GeV/c and 1.92 GeV/c, respectively, while the SKS momentum resolution $\Delta p_{SKS}/p$ was estimated to be 2.1×10^{-3}. Using these results, the missing mass resolution for the Θ was expected to be 1.72 MeV/c^2. The result is shown in Table 3.7. The present mass resolution was worse than the published one (1.4 MeV) [99]. The difference is due to the realistic evaluation of the beam momentum resolution. In [99], it was assumed that the beam momentum resolution was the design value of $\Delta p_{Beam}/p = 3.3 \times 10^{-4}$.

From the measurement of Σ peak, the missing mass resolution of the Θ^+ was estimated to be 1.7$\pm$0.03 MeV based on the Eq.3.48. Since the obtained missing mass for the beam momentum of 1.92 GeV/c spread more widely than that in the Σ production case, the kinematics in the Θ^+ production possibly have a systematic uncertainty due to the differential coefficient in the error propagation. In order to estimate such uncertainty, the mass distribution was sliced with a bin width of 10 MeV/c^2 in the range of 1500 – 1560 MeV/c^2. Figures 3.48 show the outgoing kaon momentum and its angular distribution for each mass bin, for which the differential coefficient $\frac{\partial MM}{\partial p_{Beam}}$, $\frac{\partial MM}{\partial p_{SKS}}$ and $\frac{\partial MM}{\partial \theta}$ were calculated. The uncertainty was found to be 0.13 MeV/c^2 for the missing mass resolution of the Θ^+ production. In addition to the uncertainty caused from the kinematics, an error originated from the correlation terms in the error propagation was estimated to be 0.17 MeV/c^2. The details of correlation effect is discussed in Appendix A. In conclusion, the missing mass resolution for Θ^+ was estimated to be $1.7 \pm 0.03 \pm 0.3$ MeV/c^2.

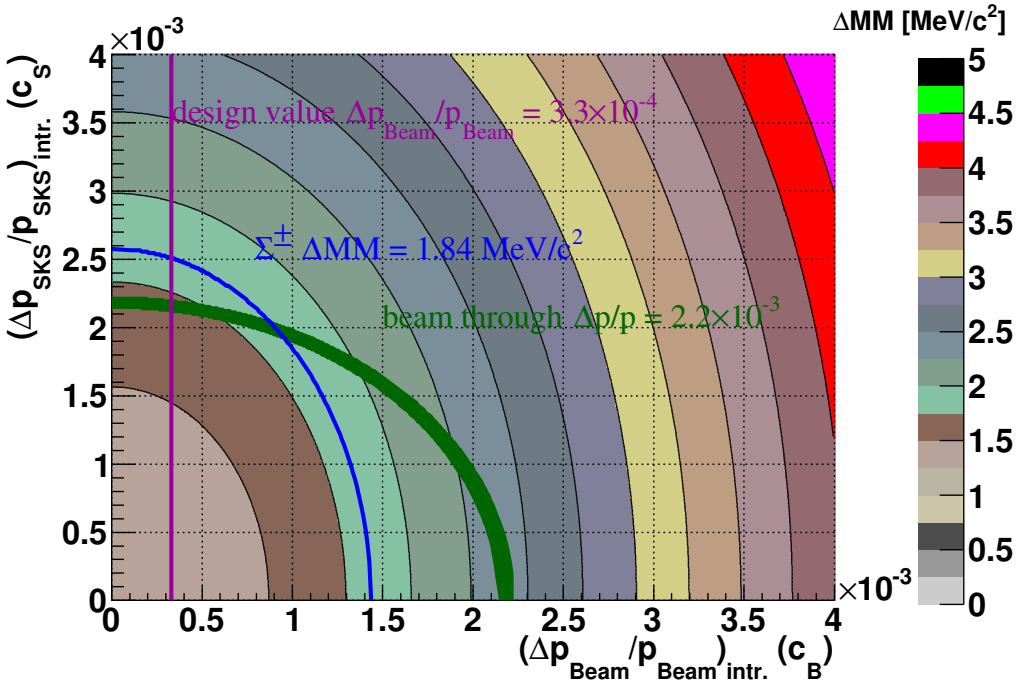

(a) $\Sigma^{\pm}$ RUN.

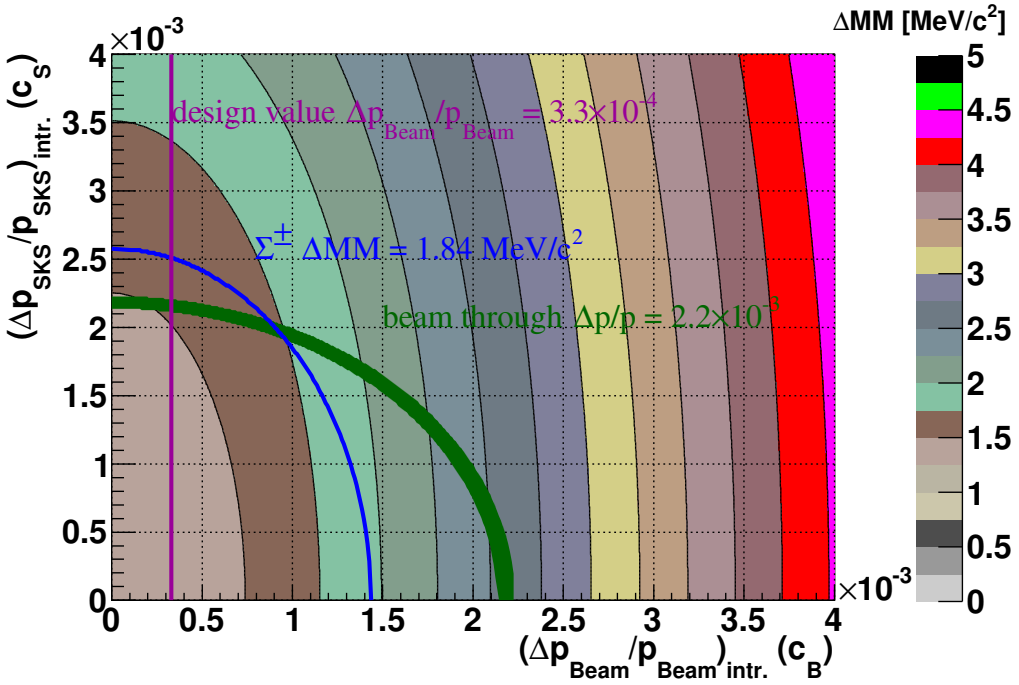

(b) Θ^{+} RUN.

Figure 3.47.: Missing mass resolution at $\theta = 5°$ as a function of the momentum resolution. The momenta of the π and the K are fixed at $p_{\pi} = 1.383$ GeV/c and $p_K = 0.920$ GeV/c for the $\Sigma^{\pm}$ production data, and $p_{\pi} = 1.923$ GeV/c and $p_K = 0.880$ GeV/c for the Θ^{+} production data, respectively. The constraint from the $\Sigma^{\pm}$ missing mass resolution is shown in the blue line while the constraint from the width of the momentum difference of the beam through data is shown in the green line. The magenta line corresponds to the beam momentum resolution of $\Delta p_{Beam}/p_{Beam}$ expected from the first order transfer matrix.

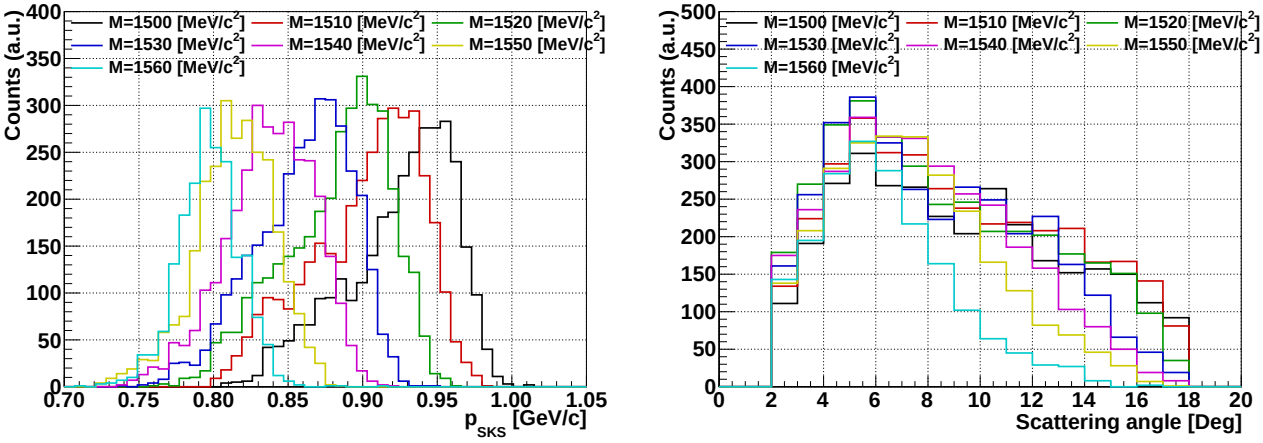

(a) (b)

Figure 3.48.: Scattered kaon momentum distribution (a) and scattering angle distribution (b) for sliced missing mass intervals.

Table 3.7.: The estimation of the missing mass resolution of Θ^+ in FWHM, where the values at the scattering angle of 5° is shown.

		$\Sigma^{\pm}$	Θ^+
$\frac{\Delta p_{Beam}}{p}$		9.3×10^{-4}	9.7×10^{-4}
Δp_{Beam}	[MeV/c]	1.29	1.86
$\left\|\frac{\partial MM}{\partial p_{Beam}}\right\|$		0.68	0.53
Δ_{Beam}	[MeV/c^2]	0.87	0.96
$\frac{\Delta p_{SKS}}{p}$		2.1×10^{-3}	2.1×10^{-3}
Δp_{SKS}	[MeV/c]	1.92	1.84
$\left\|\frac{\partial MM}{\partial p_{SKS}}\right\|$		0.57	0.38
Δ_{SKS}	[MeV/c^2]	1.09	0.70
$\Delta\theta$	[mrad]	5.9	5.9
$\left\|\frac{\partial MM}{\partial \theta}\right\|$	[MeV/c^2]	93.7	97.3
Δ_{θ}	[MeV/c^2]	0.55	0.57
$\Delta E_{stragg.}$(LH2)	[MeV]	0.59	0.58
$\Delta E_{stragg.}$(All)	[MeV]	1.07	1.08
ΔMM	[MeV/c^2]	$1.84 \pm 0.03 \pm 0.07$ (data)	$1.7 \pm 0.03 \pm 0.3$

4. Results and discussion

4.1. Missing mass spectrum

The missing mass spectrum for the $\pi^- p \to K^- X$ reaction with the beam momentum of 1.92 GeV/c is shown in Fig. 4.1, where the spectrum is presented in the experimental counts together with the backgrounds calculated by the Geant4 simulation. The vertical scale of the simulation data was normalized by the beam flux and the experimental efficiency factors. The error band of the simulated background spectrum is due to the error in past experimental results [93]. The present spectrum is well reproduced by the simulated background spectrum within the errors as shown in Fig. 4.1(a) and (b). The forward peaking ϕ production is favored to reproduce the data than the isotropic production of ϕ at this energy region. It should be noted that the cross section of phase space measured in the old bubble chamber experiment might have significant errors to which the difference between the background and data is attributed. The absolute cross section of the phase space should be scaled by 1.5–1.8 times to reproduce our missing mass spectrum.

($K^- K^+ n$ and $K^- K^0 p$), the scale factor of ∼1.5–1.8 is needed for the nonresonant cross sections as shown in Fig,4.1(c) and (d).

The differential cross section as a function of the missing mass MM was averaged over the scattering angle from 2° to 18° as

$$\overline{\left(\frac{d\sigma}{d\Omega}(MM)\right)}_{2^\circ-18^\circ} = \frac{\int_0^{2\pi} d\phi \int_{\theta=2^\circ}^{\theta=18^\circ} d(\cos\theta) \frac{d\sigma}{d\Omega}(MM,\theta,\phi)}{2\pi \times \int_{\theta=2^\circ}^{\theta=18^\circ} d(\cos\theta) \Delta\Omega(MM,\theta).} \tag{4.1}$$

where θ and ϕ are the polar angle and the azimuthal angle of the scattered K^- measured from the incident π^- direction in the laboratory frame, respectively. The angular averaged spectrum is shown in Fig. 4.2. There was no peak structure corresponding to the Θ^+ pentaquark in the mass region from 1.51 to 1.55 GeV/c^2.

4.2. Upper limit of production cross section

In order to obtain the upper limit of the production cross section of Θ^+, a Bayesian approach and the following steps were processed. First, the background level was estimated by the bin-by-bin fitting of the measured cross section plot in Fig. 4.2 with a Gaussian peak which has the fixed width of 1.7 MeV/c^2 (FWHM) on top of the background of the 2nd- or 3rd-order polynomials. Fitting results with the signal at 1.54 GeV/c^2 are illustrated in Fig. 4.3 as an example. There was no significant difference between the 2nd- and 3rd-order polynomial background shape. The fitting results with the 2nd-order polynomial background was adopted in the discussion below. The background subtracted spectrum is shown in Fig. 4.4, where the value in each bin (s_0) corresponds to the Gaussian area obtained by the above bin-by-bin fitting. Then, it is assumed that each bin follows a normal probability distribution

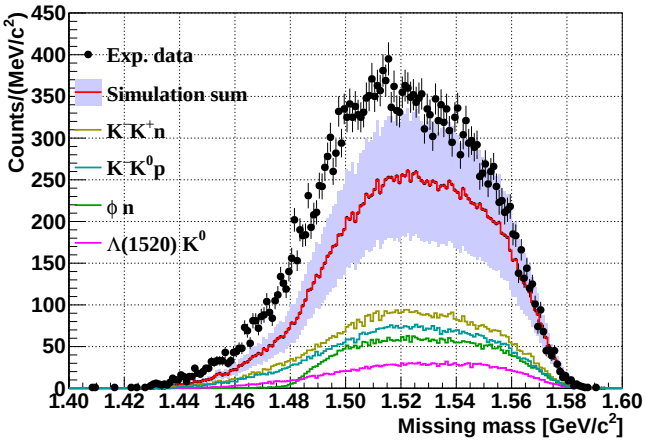

(a) isotropic ϕ production.

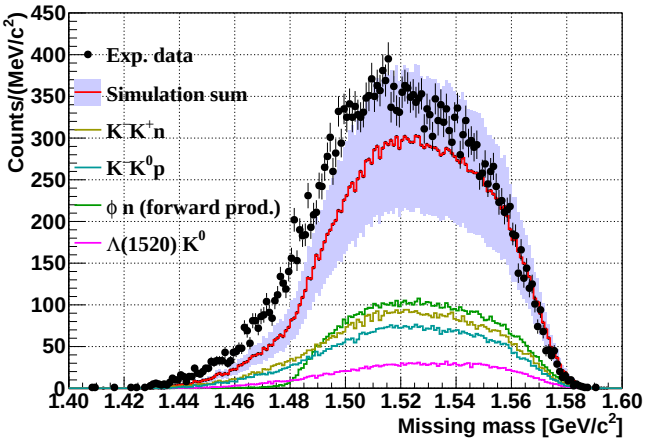

(b) forward peaking ϕ production.

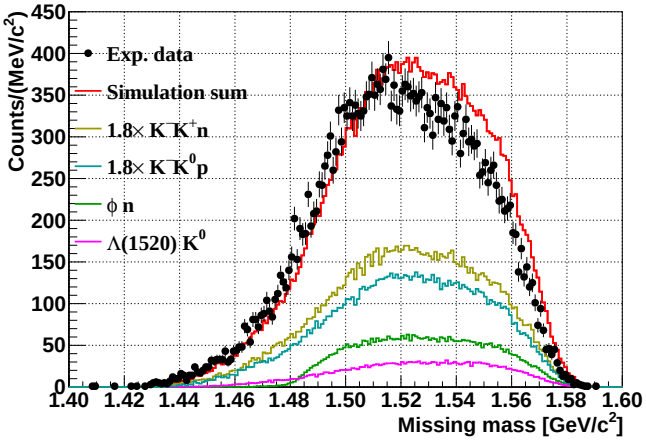

(c) isotropic ϕ production and 1.8 times larger for the nonresonant contributions.

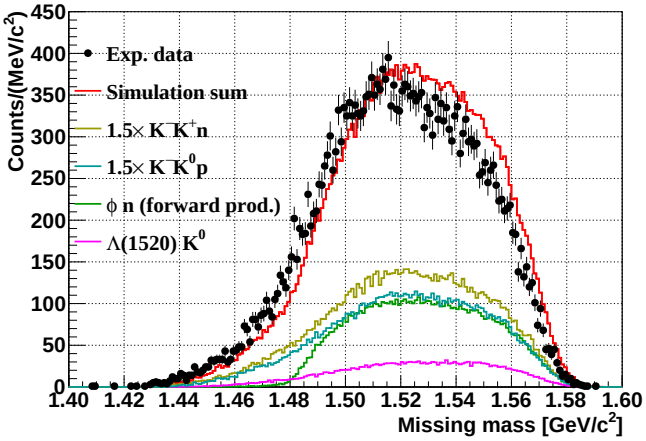

(d) forward peaking ϕ production and 1.5 times larger for the nonresonant contributions.

Figure 4.1.: The missing mass spectrum for the $\pi^- p \to K^- X$ reaction with the beam momentum of 1.92 GeV/c. The background spectra generated by the Geant4 simulation are also shown. The counts of the simulation are normalized by the π beam flux and the experimental efficiency factors. Error bars indicate only statistical uncertainty.

with the mean of s_0 and the rms of σ_s shown as the error bar. An upper limit $s_{\rm up}$ at confidence level (CL) $1-\alpha$ was obtained from the following equation

$$1-\alpha = \frac{\int_{-\infty}^{s_{\rm up}} L(s_0|s,\sigma_s)\pi(s)ds}{\int_{-\infty}^{+\infty} L(s_0|s,\sigma_s)\pi(s)ds} \tag{4.2}$$

where $L(s_0|s,\sigma_s)$ is the likelihood function for Gaussian distribution,

$$L(s_0|s,\sigma_s) = \frac{1}{\sqrt{2\pi}\sigma_s} e^{-\frac{1}{2}\left(\frac{s-s_0}{\sigma_s}\right)^2} \tag{4.3}$$

and $\pi(s)$ is the prior probability distribution function to constrain the signals to be non-negative,

$$\pi(s) = \begin{cases} 0 & s < 0 \\ 1 & s \geq 0 \end{cases} \tag{4.4}$$

Note that a well-known example for an upper limit of $s_{\rm up} \sim 1.28 \times \sigma_s$ can be obtained for $1-\alpha = 0.9$ (CL=90%) if the integrals in negative region of s in Eq. 4.2 are negligibly small due to the large mean s_0 .

Figure 4.4 shows the 90% confidence level upper limit of the cross section averaged over 2° to 18° in the laboratory frame. The upper limit of 0.27 μb/sr was obtained in the missing mass region of 1.51 to 1.55 GeV/c^2 for the experimental mass resolution of 1.7 MeV/c^2 (FWHM).

The difference between the present analysis and the previous one

The present analysis was performed keeping attention to improve the analysis efficiency compared to the previous result [90] which had been deteriorated by the bad time structure of the beam spill. The analysis efficiencies for the incident particle, the outgoing particle and the product of them were changed as 68.5% → 83.6%, 56.0% → 49.2% and 38.4% → 41.1%, respectively. Since the tracking method was improved to increase the tracking efficiency of beam particles, the analysis efficiency of beam particle was much improved. In the present analysis, the missing mass resolution was estimated to be 1.8 and 1.7 MeV/c^2 (FWHM) for $\Sigma^{\pm}$ and Θ^+, respectively, whereas the missing mass resolution was estimated to be 1.4 MeV/c^2 (FWHM) for Θ^+ in the previous analysis. The worse mass resolution for Θ^+ than that of the previous analysis was due to the updated estimation for the momentum resolution of the π^- beam, as described in Sec. 3.9. If the mass resolution was assumed to be 1.4 MeV/c^2, the upper limit decreased to 0.22 μb/sr as shown in Fig. 4.4(b).

4.3. Discussion

4.3.1. Upper limit of Θ^+ decay width

In this section, we discuss the upper bound of the decay width from the obtained upper limit of the cross section, and compared with the result obtained in other experiments.

Hyodo *et al.* [100] calculated the production cross section of the Θ^+ in the $\pi^- p \to K^- \Theta^+$ and the $K^+ p \to \pi^+ \Theta^+$ reactions using the effective Lagrangian approach at the tree level for $J^P = 1/2^{\pm}$ and $3/2^{\pm}$ cases. In their calculation, the isospin of Θ^+ is assumed to be $I = 0$. For the spin 1/2 cases,

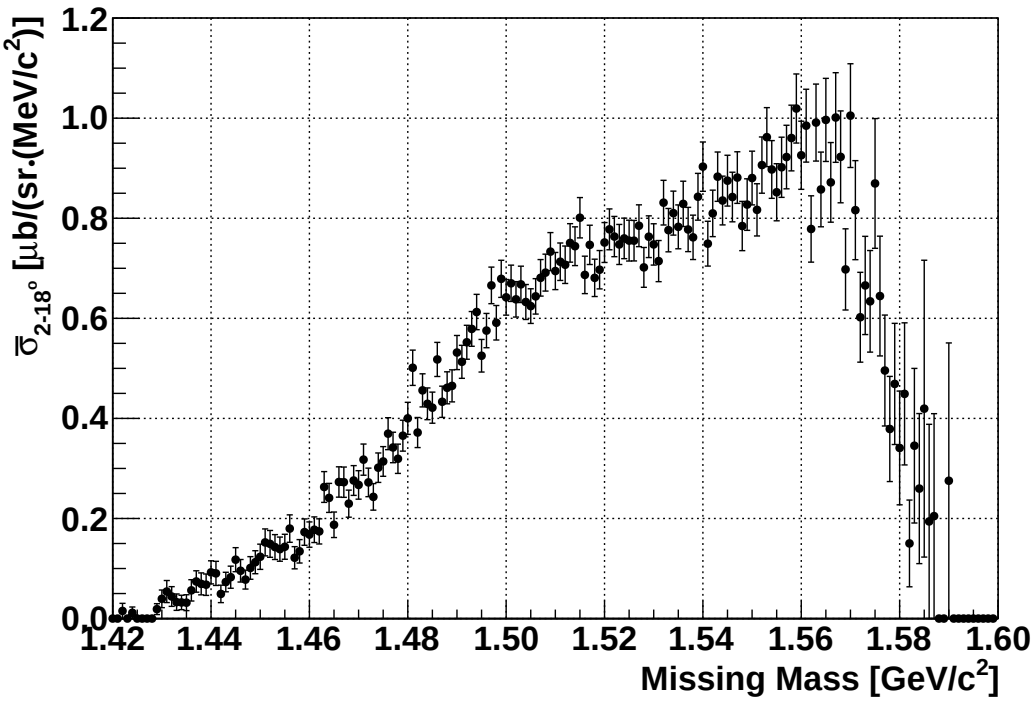

Figure 4.2.: The differential cross section of the missing mass spectrum for the $\pi^- p \to K^- X$ reaction averaged over 2° to 18° in the laboratory frame. Error bars indicate only statistical uncertainty.

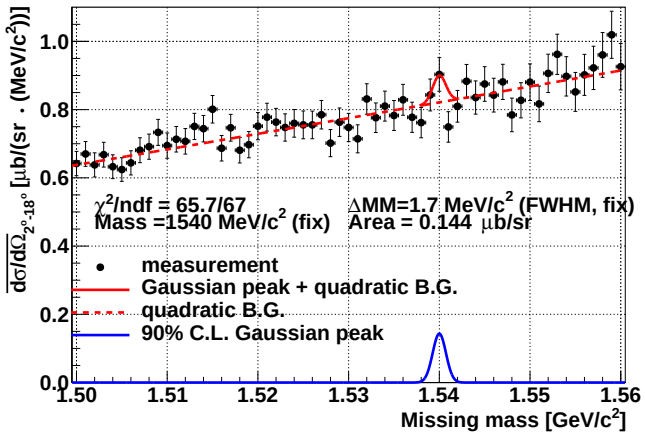

(a) 2nd order polynomial background.

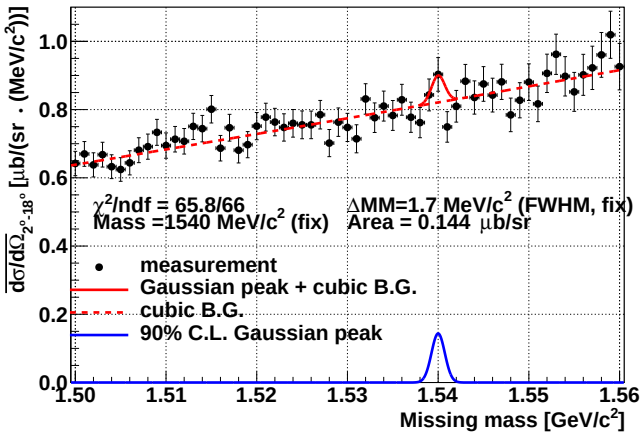

(b) 3rd order polynomial background.

Figure 4.3.: The missing mass spectrum of the $\pi^- p \to K^- X$ reaction with one of the fitting results (averaged over 2° to 18°). The fit function composed of a Gaussian peak shape with the fixed width of the mass resolution of 1.7 MeV/c^2 FWHM (red solid curve) and a polynomial function as a background shape (red dotted curve). The peak with the 90% confidence level upper limit was also shown (blue solid). Error bars indicate only statistical uncertainty.

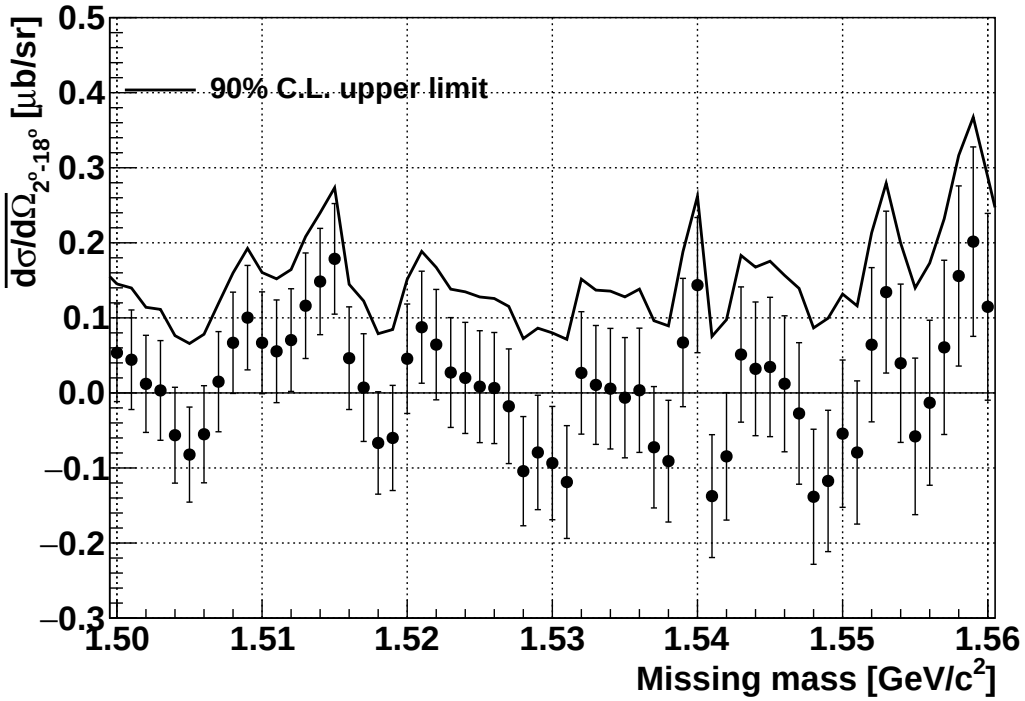

(a) mass resolution = 1.7 MeV/c^2 FWHM

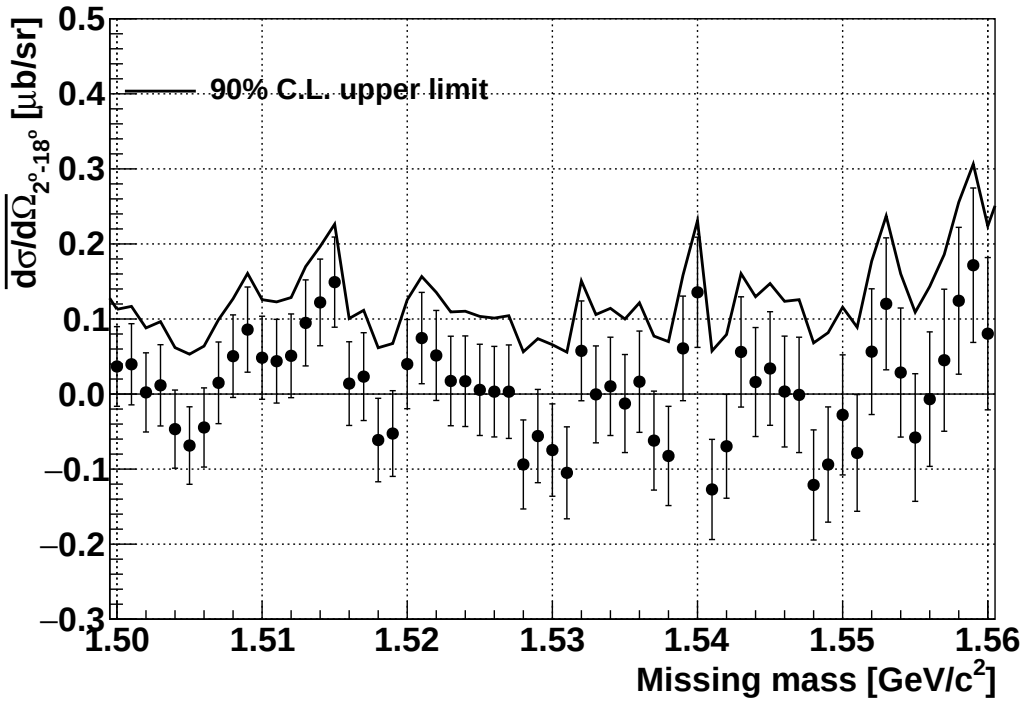

(b) mass resolution = 1.4 MeV/c^2 FWHM

Figure 4.4.: The 90% confidence level upper limit of the differential cross section of the $\pi^- p \to K^- \Theta^+$ reaction in the laboratory frame (averaged over $2° \leq \theta \leq 18°$). Error bars indicate only statistical uncertainty.

the Yukawa couplings for the meson-baryon vertices ($g_{KN\Theta}$ and $g_{\pi NN}$) were constructed in both the pseudoscalar (PS) scheme and pseudovector (PV) scheme in their calculation.

For spin 1/2 cases, the interaction Lagrangians in PS scheme are given by

$$\mathcal{L}^{1/2^\pm}_{KN\Theta} = g^{1/2^\pm}_{KN\Theta}\,\overline{\Theta}^{+}\,\Gamma\, KN + h.c., \tag{4.5}$$

$$\mathcal{L}_{\pi NN} = ig_{\pi NN}\overline{N}\gamma_5\boldsymbol{\pi}N, \tag{4.6}$$

$$g^{1/2^\pm}_{KN\Theta} = \sqrt{\frac{2\pi M_\Theta \Gamma_\Theta}{q(E_N \pm M_N)}}, \tag{4.7}$$

where Θ^+, N, K, $\boldsymbol{\pi}$ are the pentaquark, nucleon, kaon, and pion fields, respectively. $g^{1/2^\pm}_{KN\Theta}$ is the $KN\Theta$ coupling constant. $\Gamma = 1$ for negative parity, $\Gamma = i\gamma_5$ for positive parity, and $M_N(M_\Theta)$ is the mass of the nucleon (Θ^+). q is the magnitude of the relative three-momentum of the two particles in the final state and $E_N = \sqrt{q^2 + M_N^2}$. Γ_Θ is the decay width of Θ^+. The interaction Lagrangians in PV scheme are the derivative couplings

$$\mathcal{L}^{1/2^\pm}_{KN\Theta} = \frac{-ig^{*\pm}_A}{2f}\overline{\Theta}^{+}\Gamma\gamma_\mu\,\partial^\mu KN + h.c., \tag{4.8}$$

$$\mathcal{L}_{\pi NN} = \frac{g_A}{2f}\overline{N}\gamma_\mu\gamma_5\partial^\mu\boldsymbol{\pi}N, \tag{4.9}$$

$$g^{*\pm}_A = \frac{2f}{M_\Theta \pm M_N} g^{1/2^\pm}_{KN\Theta}, \tag{4.10}$$

where f, g_A, $g^{*\pm}_A$ are the meson decay constant, the axial coupling constant of the nucleon, and the transition axial coupling constant of the $\Theta^+ \to N$, respectively. Equation (4.10) shows the extended Goldberger-Treiman relations between $g^{*\pm}_A$ and $g_{KN\Theta}$ [102].

The interaction Lagrangian for the spin 3/2 case is given by

$$\mathcal{L}^{3/2^\pm}_{KN\Theta} = \frac{-ig^{3/2^\pm}_{KN\Theta}}{m_K}\overline{\Theta}^{+\mu}\gamma_5\,\partial_\mu KN + h.c., \tag{4.11}$$

$$g^{3/2^\pm}_{KN\Theta} = \sqrt{\frac{6\pi M_\Theta m_K^2 \Gamma_\Theta}{q^3(E_N \pm M_N)}}, \tag{4.12}$$

where the spin 3/2 pentaquark is denoted as the Rarita-Schwinger field $\Theta^{+\mu}$. Note that the Rarita-Schwinger field must be contracted with a derivative of meson field ($\partial_\mu K$) with respect to a 4-vector index, so as to construct the scalar Lagrangian. Therefore, the PS scheme is unphysical for spin 3/2 cases. For the πNN coupling, only the PV scheme was adopted in order to be consistent with the derivative coupling of Eq. (4.11).

In addition, phenomenological form factors were introduced to take into account the finite size of the hadrons, where two types of form factors, static type (F_s) and covariant type (F_c), were examined. The expression of F_s and F_c are described as Eq.1.1 and Eq.1.2. Since the K^* exchange term turned out to be negligibly small based on the experimental results [11,50], the differential cross section $d\sigma/d\Omega$ is simply proportional to the decay width Γ_Θ through the coupling constant $g_{KN\Theta}$:

$$\frac{d\sigma}{d\Omega} \propto g^2_{KN\Theta} \propto \Gamma_\Theta \tag{4.13}$$

The value of $g_{KN\Theta}$ corresponding to $\Gamma_\Theta = 1$ MeV at a mass of 1.54 GeV/c^2 was used in their calculation. The other uncertainty, coupling constants and the cutoff parameters of the form factor, were used

Table 4.1.: Total cross sections of the $\pi^- p \to K^- \Theta^+$ reaction and the $K^+ p \to \pi^+ \Theta^+$ reaction calculated by the pseudoscalar (PS) and pseudovector (PV) scheme [100]. Cutoff values are chosen to be $\Lambda_s = 500$ MeV ($\Lambda_c = 1800$) MeV for the static (covariant) form factors. The beam momentum of $p_\pi \sim 1920$ MeV/c ($p_K \sim 1200$ MeV/c) in the laboratory frame was used in the calculation. All the numbers are given in units of $\Gamma_{\Theta^+}/(1\text{ MeV})$ [μb].

	$\pi^- p \to K^- \Theta^+$		$K^+ p \to \pi^+ \Theta^+$	
$J^P = 1/2^+$	PS	PV	PS	PV
F_s	9.2	0.51	119	9.6
F_c	5.3	0.29	595	46
$J^P = 1/2^-$	PS	PV	PS	PV
F_s	0.18	0.40	1.9	4.2
F_c	0.10	0.23	9.6	20
$J^P = 3/2^+$		PV		PV
F_s		10		94
F_c		5.9		478
$J^P = 3/2^-$		PV		PV
F_s		5.5		8572
F_c		3.2		40544

as parameters and chosen to reproduce the known hyperon productions. The total production cross sections for the incident π^- momentum of 1.92 GeV/c and K^+ momentum of 1.2 GeV/c are summarized in Table 4.1. To explain the small cross sections in both $\pi^- p \to K^- \Theta^+$ and $K^+ p \to \pi^+ \Theta^+$ reactions reported by KEK experiments [49, 50], the spin 3/2 possibility is highly disfavored.

Figure 4.5 shows the differential cross sections in the center-of-mass frame for the spin 1/2 cases [100], whereas Fig.4.6 shows those of the spin 3/2 cases. In order to compare the theoretical calculation of the $\pi^- p \to K^- \Theta^+$ reaction with the present experiment, the differential cross sections from the theoretical model were converted to the laboratory frame and averaged over 2° to 18° as follows.

$$\overline{\left(\frac{d\sigma}{d\Omega}\right)}^{calc.}_{2^\circ - 18^\circ} = \left(\frac{\int_{2^\circ - 18^\circ} d(\cos\theta) \frac{d\sigma}{d\Omega}(\cos\theta)}{\int_{2^\circ - 18^\circ} d(\cos\theta)} \right)_{Lab} \tag{4.14}$$

$$= \frac{\left(\int_{2^\circ - 18^\circ} d(\cos\theta) \frac{d\sigma}{d\Omega}(\cos\theta) \right)_{Lab}}{0.048}. \tag{4.15}$$

For the $K^+ p \to \pi^+ \Theta^+$ reaction, the differential cross sections from the theoretical calculation was averaged over 2° to 22° in the laboratory frame, which was the acceptance of the KEK-PS E559.

$$\overline{\left(\frac{d\sigma}{d\Omega}\right)}^{calc.}_{2^\circ - 22^\circ} = \left(\frac{\int_{2^\circ - 22^\circ} d(\cos\theta) \frac{d\sigma}{d\Omega}(\cos\theta)}{\int_{2^\circ - 22^\circ} d(\cos\theta)} \right)_{Lab} \tag{4.16}$$

$$= \frac{\left(\int_{2^\circ - 22^\circ} d(\cos\theta) \frac{d\sigma}{d\Omega}(\cos\theta) \right)_{Lab}}{0.072}. \tag{4.17}$$

Figures 4.7, 4.8 and 4.9 show the differential cross section of the $\pi^- p \to K^- \Theta^+$ reaction as a function of the scattering angle in the laboratory frame for $J^P = 1/2^+$, $1/2^-$ and $3/2^\pm$ cases, respectively,

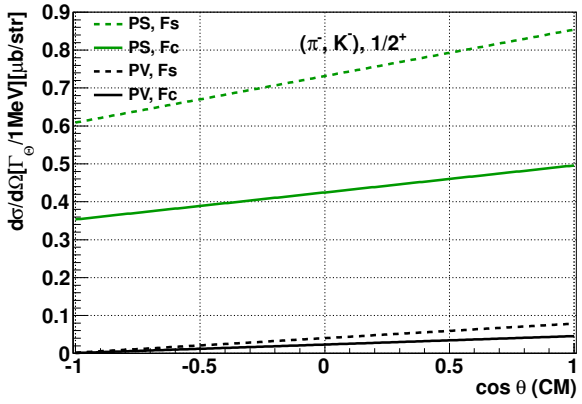

(a) $(\pi^-, K^-), 1/2^+$

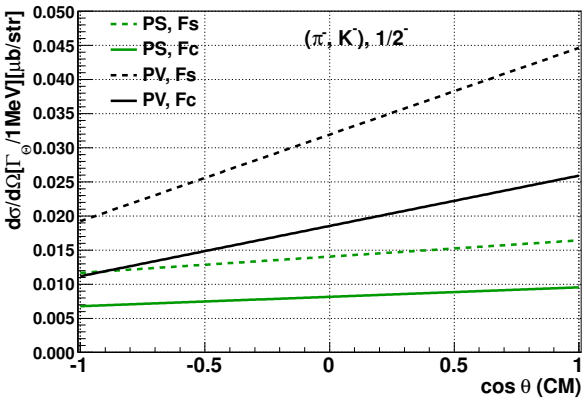

(b) $(\pi^-, K^-), 1/2^-$

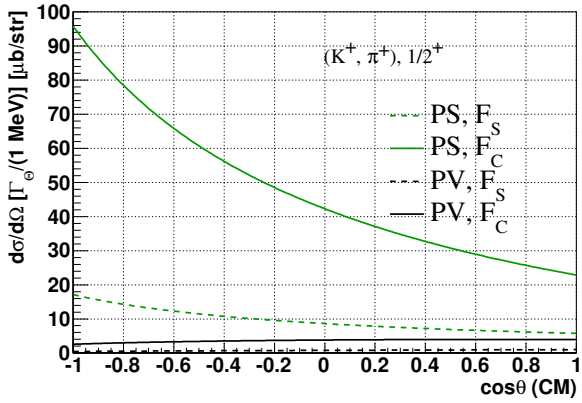

(c) $(K^+, \pi^+), 1/2^+$

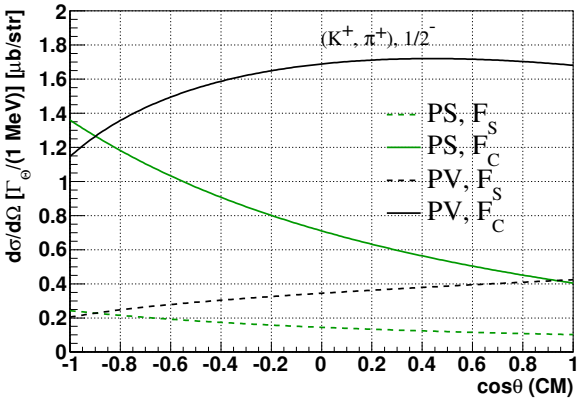

(d) $(K^+, \pi^+), 1/2^-$

Figure 4.5.: Differential cross sections of the $\pi^- p \to K^- \Theta^+$ and $K^+ p \to \pi^+ \Theta^+$ reaction calculated by hadronic model [100, 101] in the center-of-mass frame. Two coupling schemes, PS and PV are plotted together. The form factor of static (covariant) type with $\Lambda_s = 500$ MeV ($\Lambda_c = 1800$ MeV) is shown as dashed (solid) lines. The beam momenta of $p_\pi \sim 1.92$ GeV/c ($p_K \sim 1.2$ GeV/c) in the laboratory frame was used in the calculation.

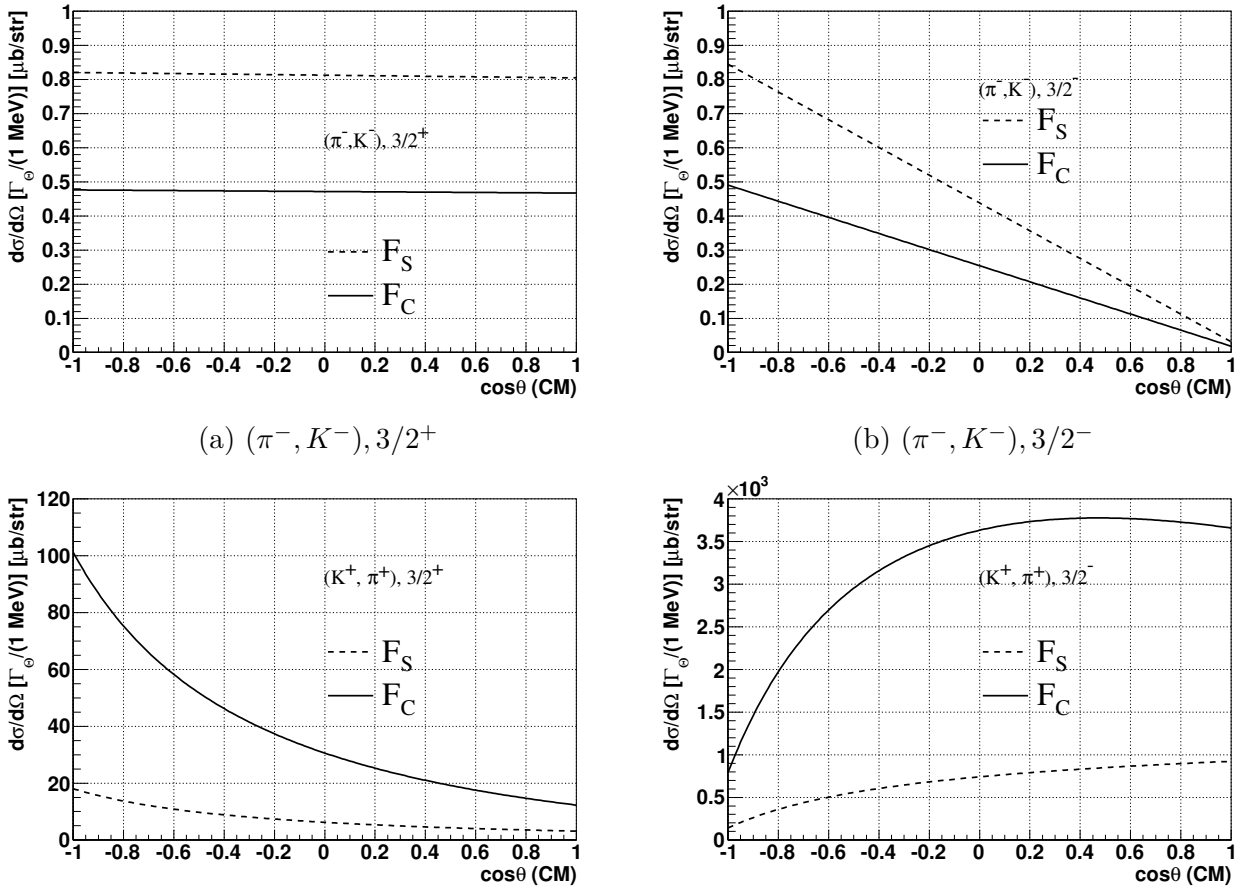

(a) $(\pi^-, K^-), 3/2^+$ (b) $(\pi^-, K^-), 3/2^-$

(c) $(K^+, \pi^+), 3/2^+$ (d) $(K^+, \pi^+), 3/2^-$

Figure 4.6.: Differential cross sections of the (π^-, K^-) and (K^+, π^+) reactions for spin 3/2 cases calculated by hadronic model [101]. Cutoff values are chosen to be $\Lambda_s = 500$ MeV ($\Lambda_c = 1800$) MeV for the static (covariant) form factors. The beam momentum of $p_\pi \sim 1920$ MeV/c ($p_K \sim 1200$ MeV/c) in the laboratory frame was used in the calculation. All the numbers are given in units of $\Gamma_{\Theta^+}/(1\text{ MeV})$ $[\mu b]$.

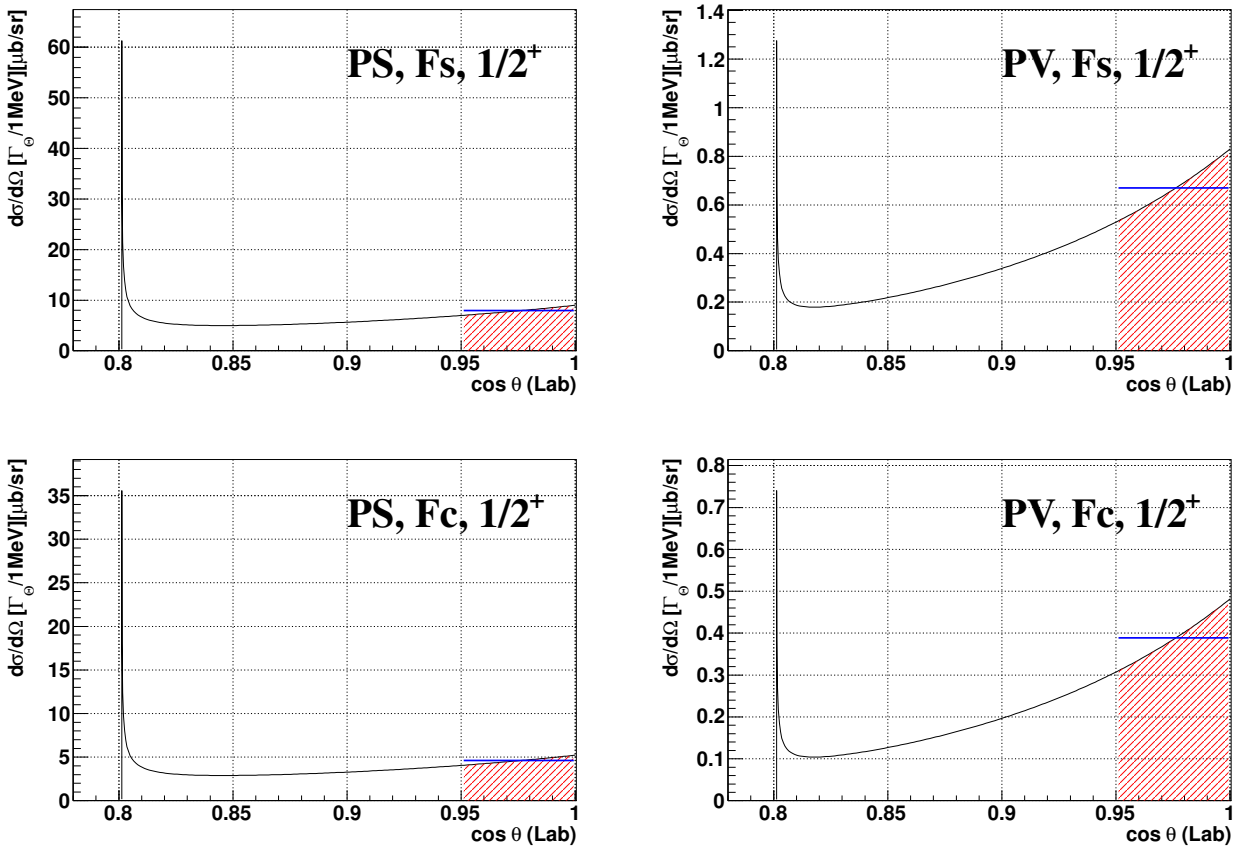

Figure 4.7.: Differential cross sections of the $\pi^- p \to K^- \Theta^+$ reaction in the laboratory frame for $J^P = 1/2^+$ cases. Cutoff values are chosen to be $\Lambda_s = 500$ MeV ($\Lambda_c = 1800$) MeV for the static (covariant) form factors. The beam momentum of $p_\pi \sim 1920$ MeV/c in the laboratory frame was used in the calculation.

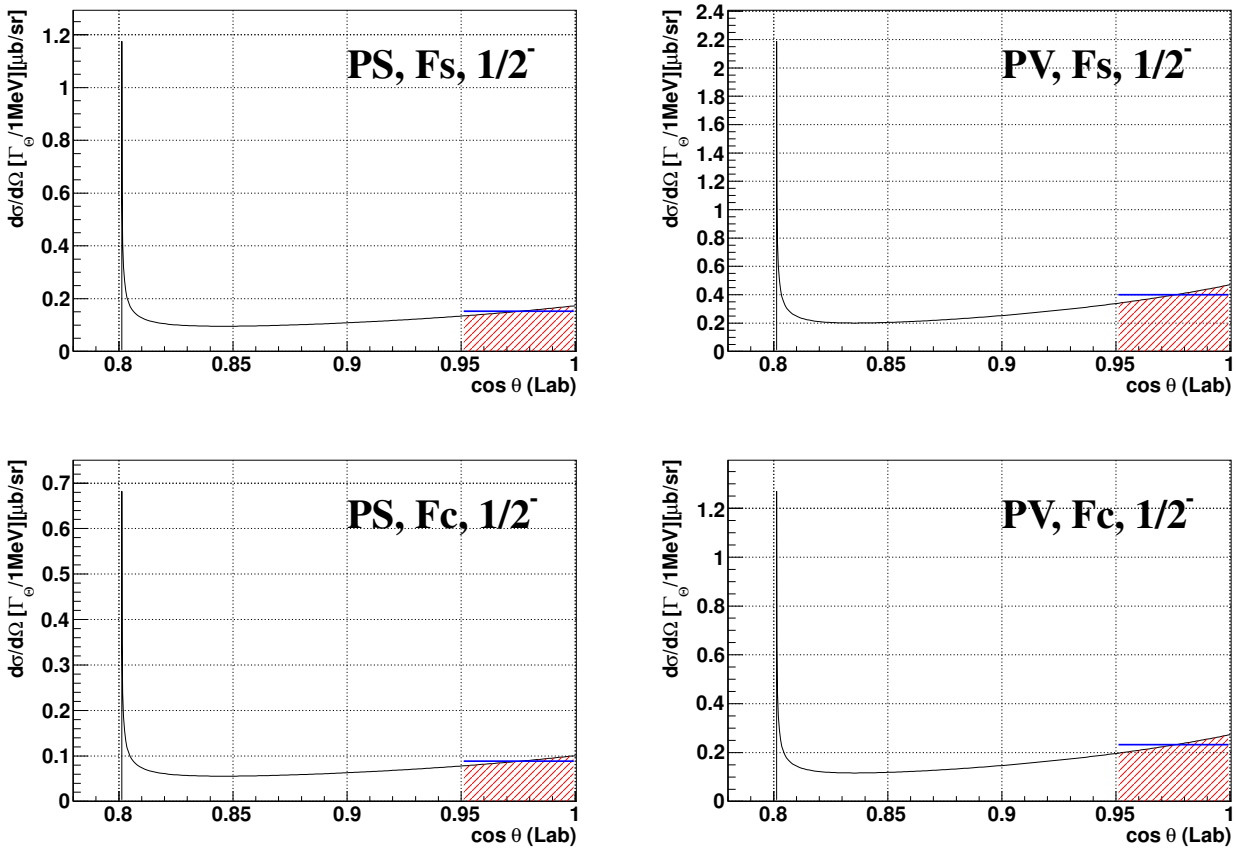

Figure 4.8.: Differential cross sections of the $\pi^- p \to K^- \Theta^+$ reaction in the laboratory frame for $J^P = 1/2^-$ cases. Cutoff values are chosen to be $\Lambda_s = 500$ MeV ($\Lambda_c = 1800$) MeV for the static (covariant) form factors. The beam momentum was of $p_\pi \sim 1920$ MeV/c in the laboratory frame was used in the calculation.

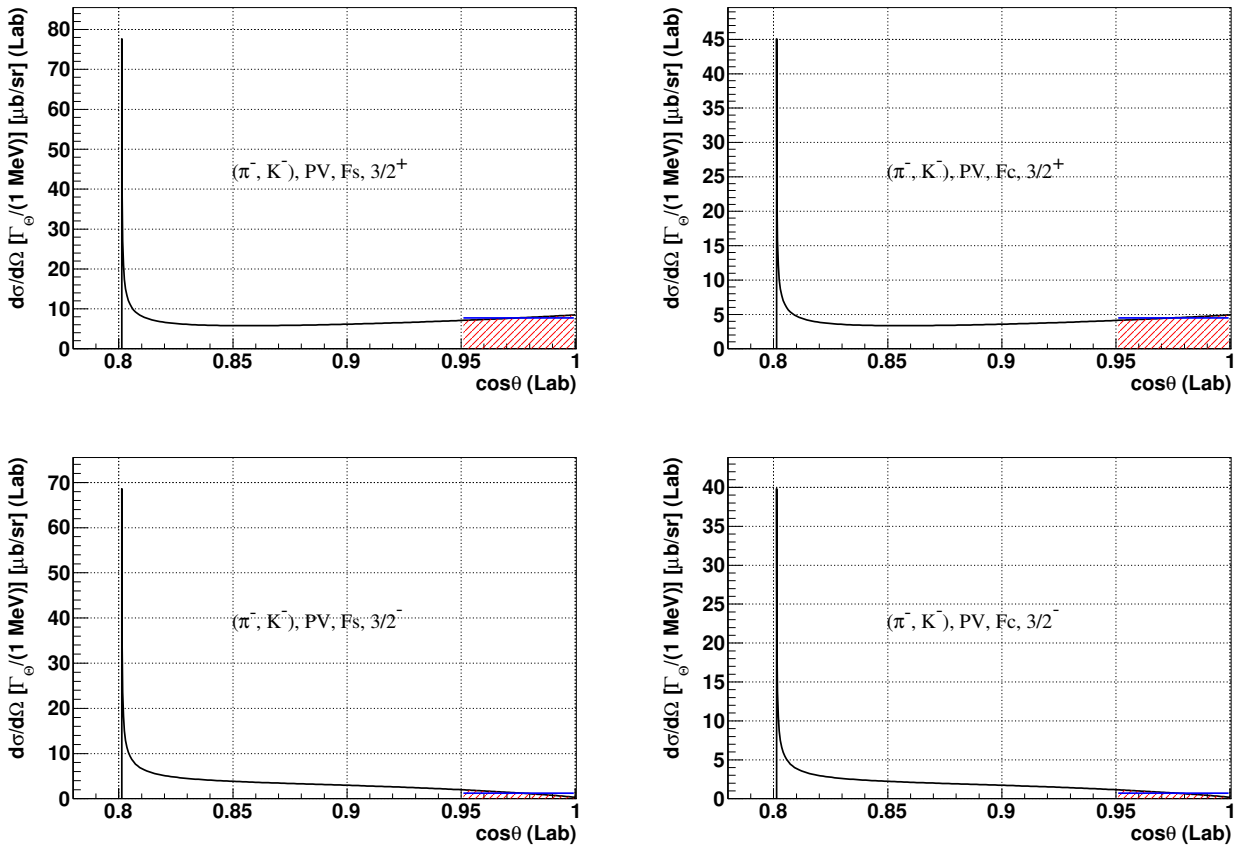

Figure 4.9.: Differential cross sections of the $\pi^- p \to K^- \Theta^+$ reaction in the laboratory frame for $J^P = 3/2^{\pm}$ cases. Cutoff values are chosen to be $\Lambda_s = 500$ MeV ($\Lambda_c = 1800$) MeV for the static (covariant) form factors. The beam momentum of $p_\pi \sim 1920$ MeV/c ($p_K \sim 1200$ GeV/c) in the laboratory frame was used in the calculation.

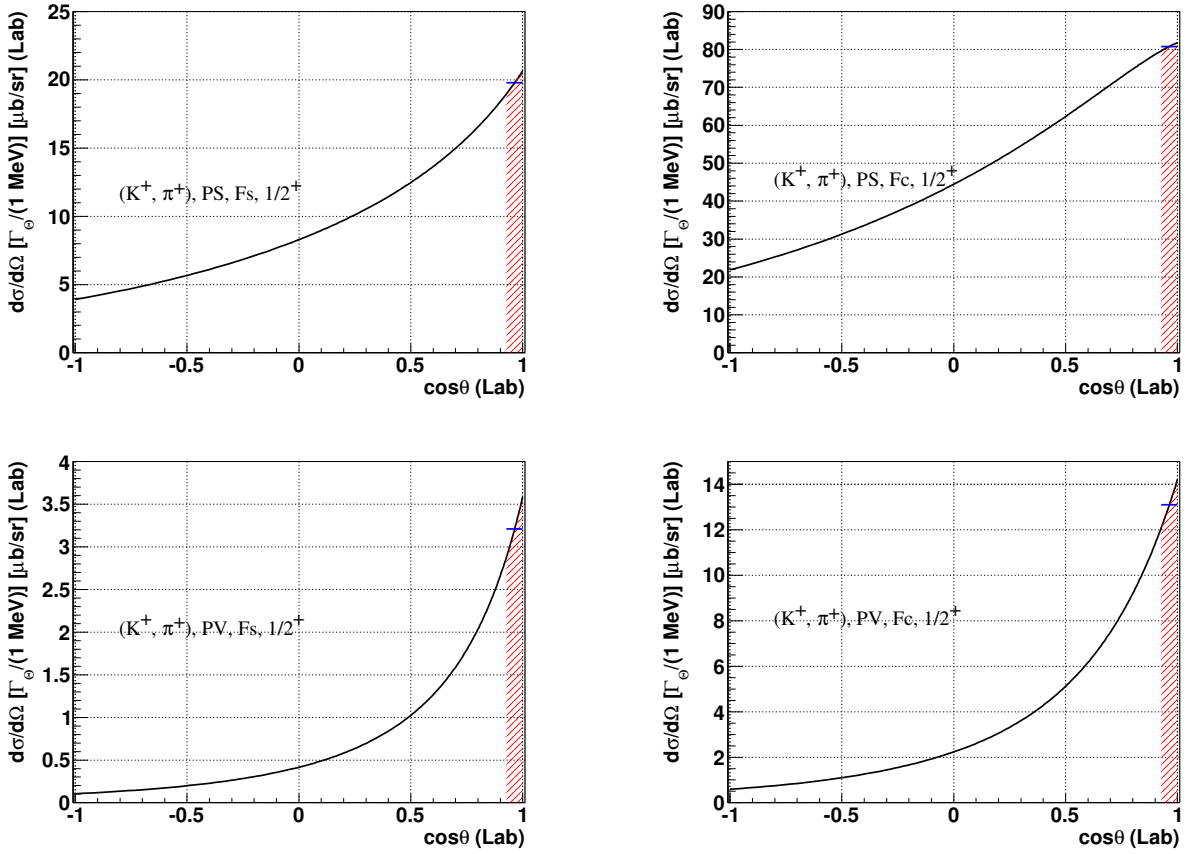

Figure 4.10.: Differential cross sections of the $K^+p \to \pi^+\Theta^+$ reaction in the laboratory frame for $J^P = 1/2^+$ cases. Cutoff values are chosen to be $\Lambda_s = 500$ MeV ($\Lambda_c = 1800$) MeV for the static (covariant) form factors. The beam momentum of $p_K \sim 1200$ GeV/c in the laboratory frame was used in the calculation.

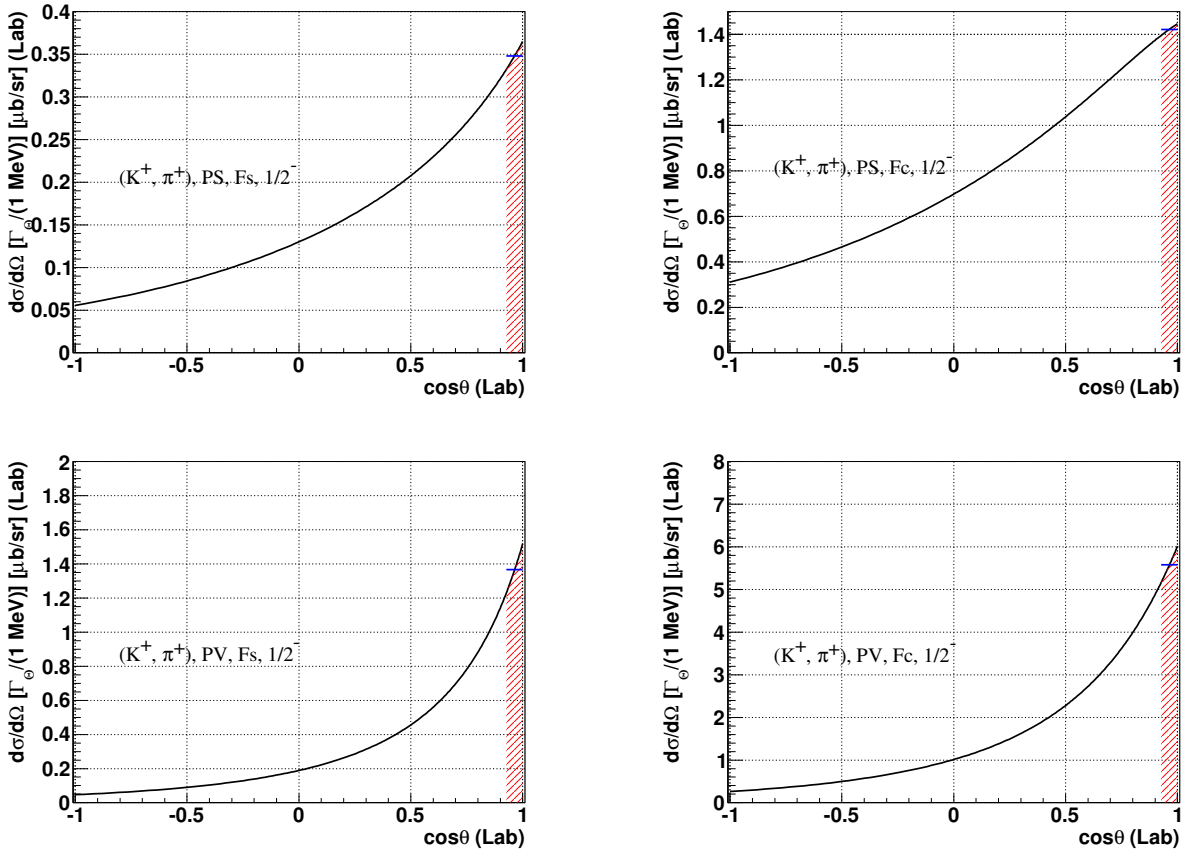

Figure 4.11.: Differential cross sections of the $K^+p \to \pi^+\Theta^+$ reaction in the laboratory frame for $J^P = 1/2^-$ cases. Cutoff values are chosen to be $\Lambda_s = 500$ MeV ($\Lambda_c = 1800$) MeV for the static (covariant) form factors. The beam momentum of $p_K \sim 1200$ GeV/c in the laboratory frame was used in the calculation.

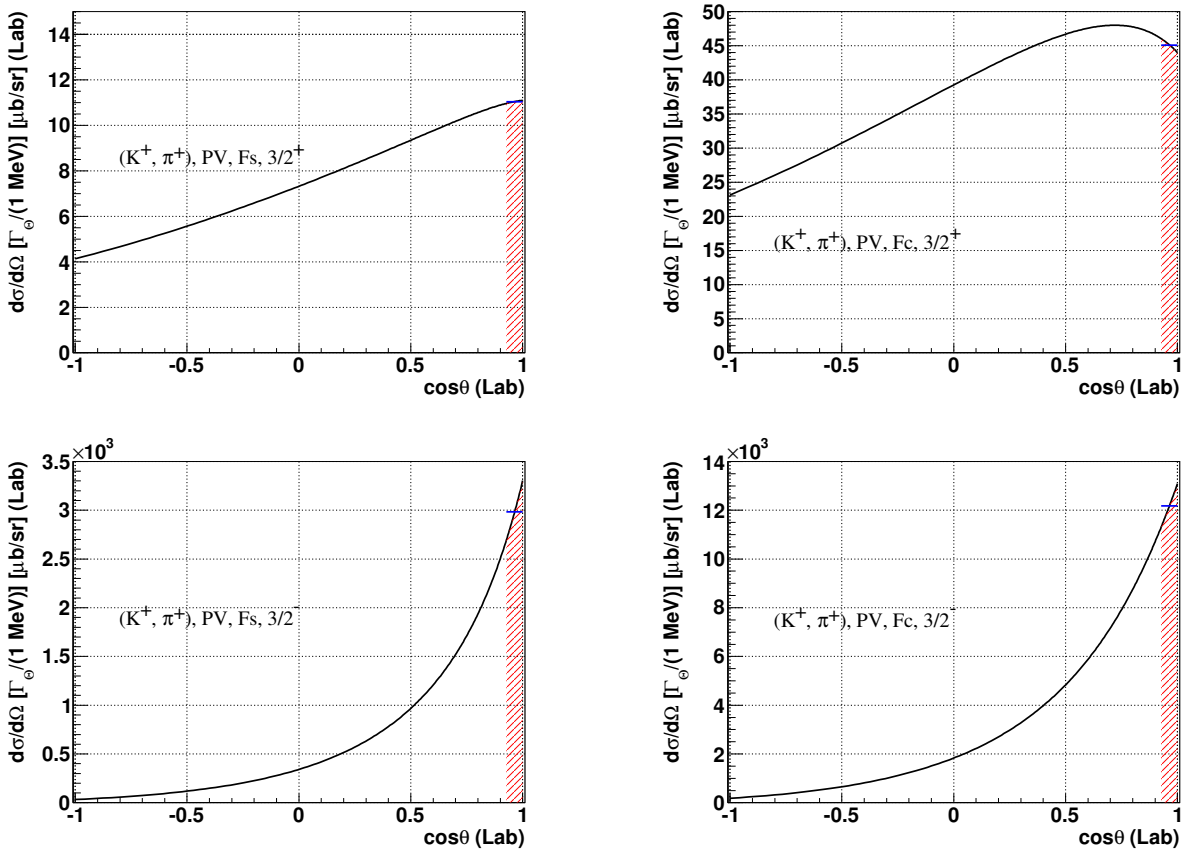

Figure 4.12.: Differential cross sections of the $K^+p \to \pi^+\Theta^+$ reaction in the laboratory frame for $J^P = 3/2^{\pm}$ cases. Cutoff values are chosen to be $\Lambda_s = 500$ MeV ($\Lambda_c = 1800$) MeV for the static (covariant) form factors. The beam momentum of $p_K \sim 1200$ GeV/c in the laboratory frame was used in the calculation.

Table 4.2.: Integrals of differential cross sections, averaged differential cross sections of the $\pi^- p \to K^- \Theta^+$ reaction in the laboratory frame derived from the hadronic model and corresponding 90% CL upper limits of Θ^+ decay width Γ_{Θ^+}, where integration and the averaging was performed over $\theta_{Lab} = 2^\circ - 18^\circ$. The numbers are given in units of $\Gamma_{\Theta^+}/(1\mathrm{MeV})$ [μb/sr] for the differential cross sections and in MeV/c^2 for the decay width, respectively.

	PS			PV		
	$\left(\int d(\cos\theta)\frac{d\sigma}{d\Omega}\right)_{Lab}$	$\overline{\left(\frac{d\sigma}{d\Omega}\right)}^{calc.}_{2^\circ-18^\circ}$	Γ_{Θ^+}	$\left(\int d(\cos\theta)\frac{d\sigma}{d\Omega}\right)_{Lab}$	$\overline{\left(\frac{d\sigma}{d\Omega}\right)}^{calc.}_{2^\circ-18^\circ}$	Γ_{Θ^+}
$J^P = 1/2^+$, F_s	0.38	7.9	0.034	0.032	0.67	0.41
$J^P = 1/2^+$, F_c	0.22	4.6	0.059	0.018	0.39	0.72
$J^P = 1/2^-$, F_s	0.0074	0.15	1.7	0.019	0.40	0.68
$J^P = 1/2^-$, F_c	0.0043	0.089	3.1	0.011	0.23	1.2
$J^P = 3/2^+$, F_s				0.37	7.8	0.035
$J^P = 3/2^+$, F_c				0.22	4.5	0.060
$J^P = 3/2^-$, F_s				0.060	1.2	0.22
$J^P = 3/2^-$, F_c				0.035	0.72	0.38

whereas Figs. 4.10, 4.11 and 4.12 show those of the $K^+ p \to \pi^+ \Theta^+$ reaction. The red hatched regions correspond to the numerator of the right hand side of Eqs.4.15 and 4.17. The blue horizontal line indicate the averaged differential cross section $\overline{\left(\frac{d\sigma}{d\Omega}\right)}^{calc.}_{2^\circ-18^\circ}$ and $\overline{\left(\frac{d\sigma}{d\Omega}\right)}^{calc.}_{2^\circ-22^\circ}$. The values of the integral of the differential cross section and the averaged ones are summarized in Table 4.2 and 4.3. Since the theoretical calculation was performed with the decay width of 1 MeV and the decay width is proportional to the differential cross section, the measured Θ^+ decay width is derived as,

$$\Gamma_\Theta[\mathrm{MeV}/c^2] = \begin{cases} \dfrac{\overline{\left(\frac{d\sigma}{d\Omega}\right)}^{meas.}_{2^\circ-18^\circ}}{\overline{\left(\frac{d\sigma}{d\Omega}\right)}^{calc.}_{2^\circ-18^\circ}} & \text{for } (\pi, K) \\ \\ \dfrac{\overline{\left(\frac{d\sigma}{d\Omega}\right)}^{meas.}_{2^\circ-22^\circ}}{\overline{\left(\frac{d\sigma}{d\Omega}\right)}^{calc.}_{2^\circ-22^\circ}} & \text{for } (K, \pi) \end{cases} \tag{4.18}$$

where $\overline{\left(\frac{d\sigma}{d\Omega}\right)}^{meas.}_{2^\circ-18^\circ}$ $\left(\overline{\left(\frac{d\sigma}{d\Omega}\right)}^{meas.}_{2^\circ-22^\circ}\right)$ is the differential cross section measured by the present experiment (KEK-PS E559). Although $\overline{\left(\frac{d\sigma}{d\Omega}\right)}^{calc.}_{2^\circ-18^\circ}$ $\left(\overline{\left(\frac{d\sigma}{d\Omega}\right)}^{calc.}_{2^\circ-22^\circ}\right)$ was derived at the fixed Θ^+ mass of 1.54 GeV/c^2 because the theoretical calculation by Hyodo was performed for that mass, we assumed that the same values were applicable to the measured mass region.

For the $\pi^- p \to K^- \Theta^+$ reaction, the 90% CL upper bounds of the decay width equivalent to the measured upper limit of the differential cross section of 0.27 μb/sr determined by the present experiment are listed in Table 4.2, whereas those of the $K^+ p \to \pi^+ \Theta^+$ reaction equivalent to the 90% CL upper limit of 3.5 μb/sr determined by KEK-PS E559 are listed in Table 4.3. For the $\pi^- p \to K^- \Theta^+$ reaction, the upper limits of the Θ^+ width were obtained to be 0.72, 3.1, 0.060 and 0.38 MeV for the $J^P = 1/2^+$, $1/2^-$, $3/2^+$ and $3/2^-$ cases from the present experiment, respectively. For the $K^+ p \to \pi^+ \Theta^+$ reaction, the upper limits of the width were found to be 1.1, 10, 0.32, 0.0012 MeV for the $J^P = 1/2^+$, $1/2^-$,

Table 4.3.: Integrals of differential cross sections, averaged differential cross sections of the $K^+p \to \pi^+\Theta^+$ reaction in the laboratory frame derived from the hadronic model with the experimental acceptance and 90% CL upper limits of Θ^+ decay width Γ_{Θ^+} corresponding to the KEK-PS E559 data, where the integration and the averaging were performed over $\theta_{Lab} = 2^\circ - 22^\circ$. The numbers are given in units of $\Gamma_{\Theta^+}/(1\text{MeV})[\mu\text{b/sr}]$ for the differential cross sections and in MeV for the decay width, respectively.

	PS			PV		
	$\left(\int d(\cos\theta)\frac{d\sigma}{d\Omega}\right)_{Lab}$	$\overline{\left(\frac{d\sigma}{d\Omega}\right)}^{calc.}_{2^\circ-22^\circ}$	Γ_{Θ^+}	$\left(\int d(\cos\theta)\frac{d\sigma}{d\Omega}\right)_{Lab}$	$\overline{\left(\frac{d\sigma}{d\Omega}\right)}^{calc.}_{2^\circ-22^\circ}$	Γ_{Θ^+}
$J^P = 1/2^+$, F_s	1.4	20	0.18	0.23	3.2	1.1
$J^P = 1/2^+$, F_c	5.8	81	0.043	0.95	13	0.27
$J^P = 1/2^-$, F_s	0.025	0.35	10	0.099	1.4	2.6
$J^P = 1/2^-$, F_c	0.10	1.4	2.5	0.40	5.6	0.63
$J^P = 3/2^+$, F_s				0.80	11	0.32
$J^P = 3/2^+$, F_c				3.3	45	0.078
$J^P = 3/2^-$, F_s				220	3000	0.0012
$J^P = 3/2^-$, F_c				880	12000	0.00029

Table 4.4.: The 90% upper limits of the Θ^+ decay width obtained by combining the result of the present experiment and KEK-PS E559.

	PS			PV		
	(π^-, K^-)	(K^+, π^+)	combined.	(π^-, K^-)	(K^+, π^+)	combined.
$J^P = 1/2^+$, F_s	0.034	0.18	0.034	0.41	1.1	0.41
$J^P = 1/2^+$, F_c	0.059	0.043	0.043	0.72	0.27	0.27
$J^P = 1/2^-$, F_s	1.7	10	1.7	0.68	2.6	0.68
$J^P = 1/2^-$, F_c	3.1	2.5	2.5	1.2	0.63	0.63
$J^P = 3/2^+$, F_s				0.035	0.32	0.035
$J^P = 3/2^+$, F_c				0.060	0.078	0.060
$J^P = 3/2^-$, F_s				0.22	0.0012	0.0012
$J^P = 3/2^-$, F_c				0.38	0.00029	0.00029

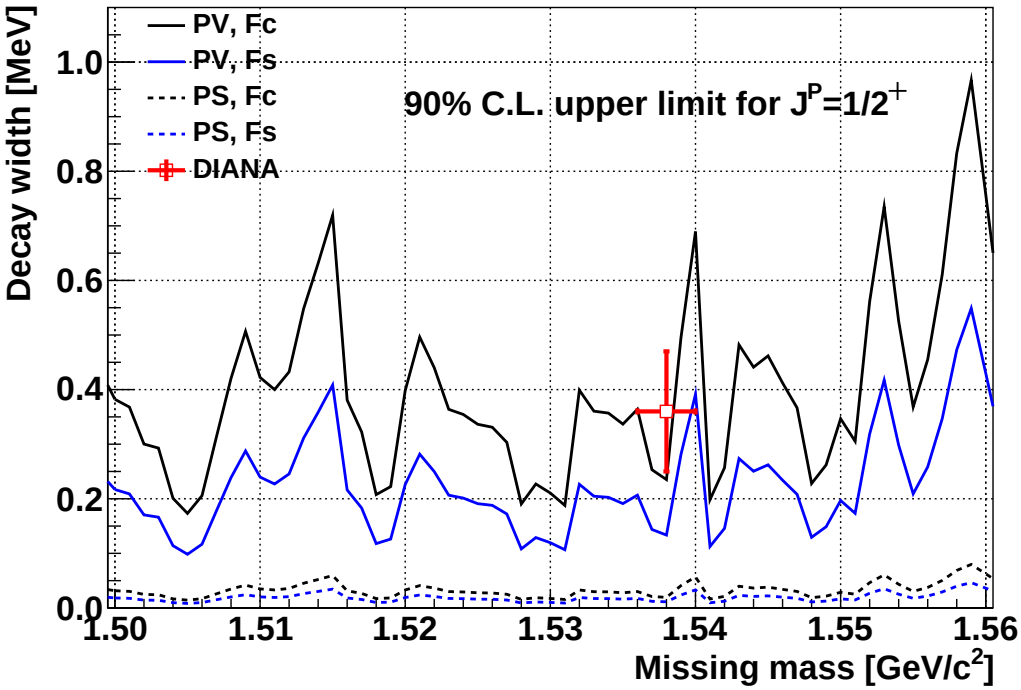

(a) $J^P = 1/2^+$ case.

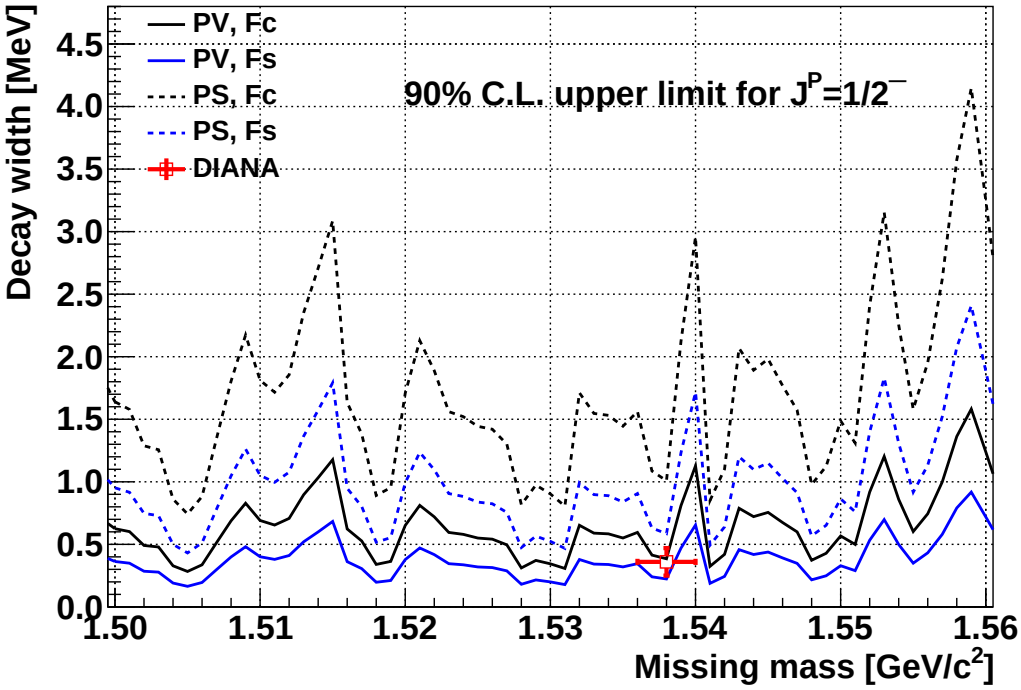

(b) $J^P = 1/2^-$ case.

Figure 4.13.: The 90% confidence level upper limit of the Θ^+ decay width (averaged over $2° \leq \theta \leq 18°$). The value in the latest report from DIANA is also shown.

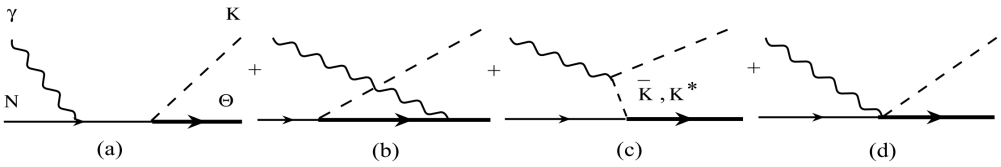

Figure 4.14.: Tree level diagrams for the $\gamma N \to \bar{K}\Theta^+$ reaction.

$3/2^+$ and $3/2^-$ cases from the KEK-PS E559, respectively. For combining the result of the (π^-, K^-) and the (K^+, π^+) reaction, the upper limits of the width were found to be 0.50, 2.5, 0.073, 0.0012 MeV for the $J^P = 1/2^+$, $1/2^-$, $3/2^+$ and $3/2^-$ cases, respectively (Table 4.4). As described above, the spin 3/2 possibility is highly disfavored. Using the combined result, we can update the upper limit of the decay width from 0.64 MeV set by Belle [34] to 0.41 MeV for the $J^P = 1/2^+$ case.

4.3.2. Comparison with DIANA

The DIANA collaboration at ITEP investigated the charge-exchange reaction $K^+\mathrm{Xe} \to K^0_s p\mathrm{Xe}'$ in the Xenon bubble chamber and observed an enhancement near 1538 MeV/c^2 in the pK^0_s invariant mass spectrum [14, 16–18]. In the latest report from DIANA, they measured the Θ^+ mass of 1538 ± 2 MeV/c^2 with the statistical significance of 6.3σ and determined the width of 0.36 ± 0.11 MeV [14]. The value of DIANA is shown in Fig. 4.13 together with the present results for the (π^-, K^-) reaction with the spin 1/2 cases. The present result is comparable with the DIANA's value for the positive parity case, though it cannot exclude the DIANA's observation.

4.3.3. Comparison with LEPS

The LEPS collaboration reported the evidence of the Θ^+ in the $\gamma d \to K^+K^-pn$ reaction [5, 9]. They said that the peak was seen at $1.524 \pm 0.002 + 0.003$ GeV/c^2 with the statistical significance of 5.1σ and the differential cross section was measured to be 12 ± 2 nb/sr in the center-of-mass frame using data taken in 2002-2003 [9] with the photon energy range from 2.0 to 2.4 GeV. In this subsection, a rough estimation of the decay width Γ_{Θ^+} will be given from the differential cross section measured by LEPS with the help of the theoretical calculation for the photon induced reaction.

Figure 4.14 shows tree level diagrams for the $\gamma N \to \bar{K}\Theta^+$ reaction. For the photon induced reaction, the anomalous magnetic moment of Θ^+ (κ_Θ), which is related to the $\gamma\Theta\Theta$ vertex, might cause another uncertainty. Figure 4.15 and 4.16 shows the total and differential cross sections of the $\gamma n \to K^-\Theta^+$ reaction using the effective Lagrangian [13, 103] in the center-of-mass frame for the $J^P = 1/2^\pm$ and $3/2^\pm$ cases. Two types of meson-baryon coupling, PS and PV are plotted in the solid and dashed curves, respectively. The black (red) line corresponds to $\kappa_\Theta = -0.8\mu_N(1.0\mu_N)$, $\Lambda = 0.85$ GeV (0.75 GeV) and the incident photon energy in the laboratory frame of $E_\gamma = 1.88$ GeV (2.0 GeV), where μ_N is the nuclear magneton. The $g_{KN\Theta}$ is normalized so that the decay width of Θ^+ is 1 MeV. For the $J^P = 3/2^\pm$ cases, the contact term, which is shown in Fig.4.14(d), plays a dominant role to enlarge the cross section. In those calculation, the coupling of $K^*N\Theta$ is assumed to be 0. Since the LEPS collaboration had estimated the differential cross section to be 12 nb/sr in the center-of-mass frame by assuming the isotropic distribution [9], the differential cross sections derived from the theoretical

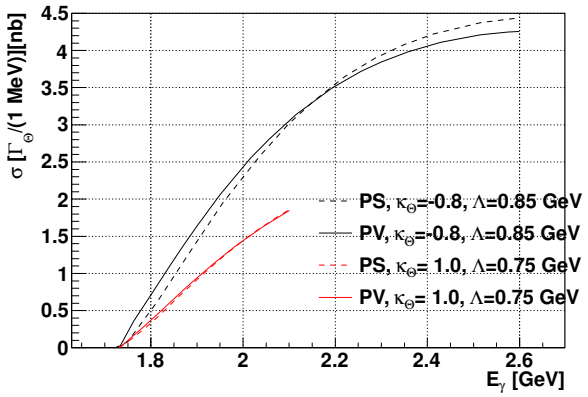

(a) Total cross section for $J^P = 1/2^+$.

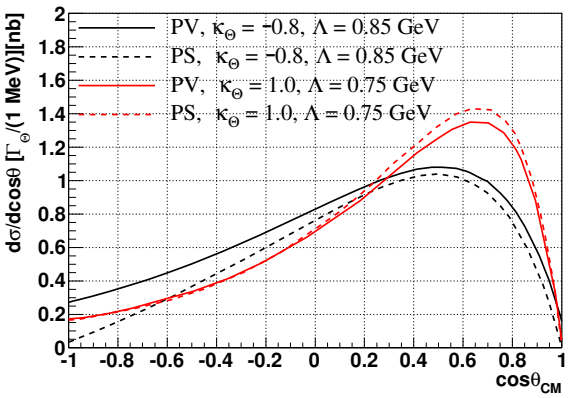

(b) Differential cross section for $J^P = 1/2^+$.

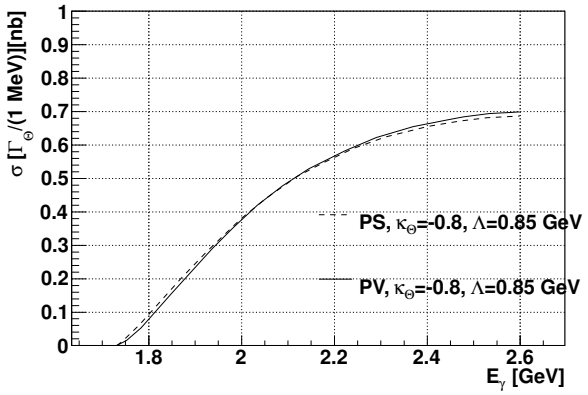

(c) Total cross section for $J^P = 1/2^-$.

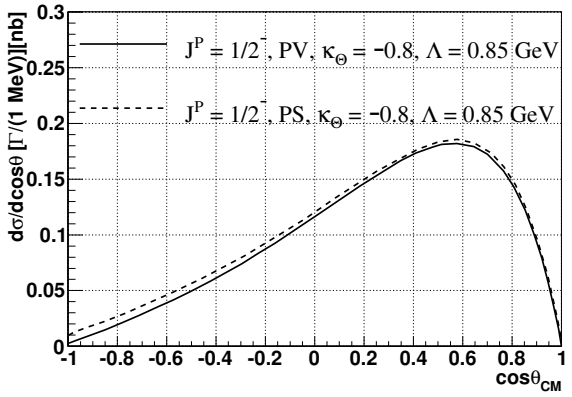

(d) Differential cross section for $J^P = 1/2^-$.

Figure 4.15.: Total and differential cross sections of the $\gamma n \to K^- \Theta^+$ reaction calculated by using effective Lagrangian [13, 103], where the coupling constant $g_{KN\Theta}$ is normalized so that it is equivalent to Θ^+ decay width of 1 MeV. (a),(b) : $1/2^+$ case. (c),(d) : $1/2^-$ case. Two coupling schemes, PS (solid line) and PV (dashed line) are plotted together with two parameter set of the cutoff Λ and κ_Θ. The black (red) line corresponds to $\kappa_\Theta = -0.8\mu_N(1.0\mu_N)$, $\Lambda = 0.85$ GeV (0.75 GeV). The differential cross section in the center of mass frame is given for the $E_\gamma = 1.88$ GeV (2.0 GeV) case and drawn in the black (red) line.

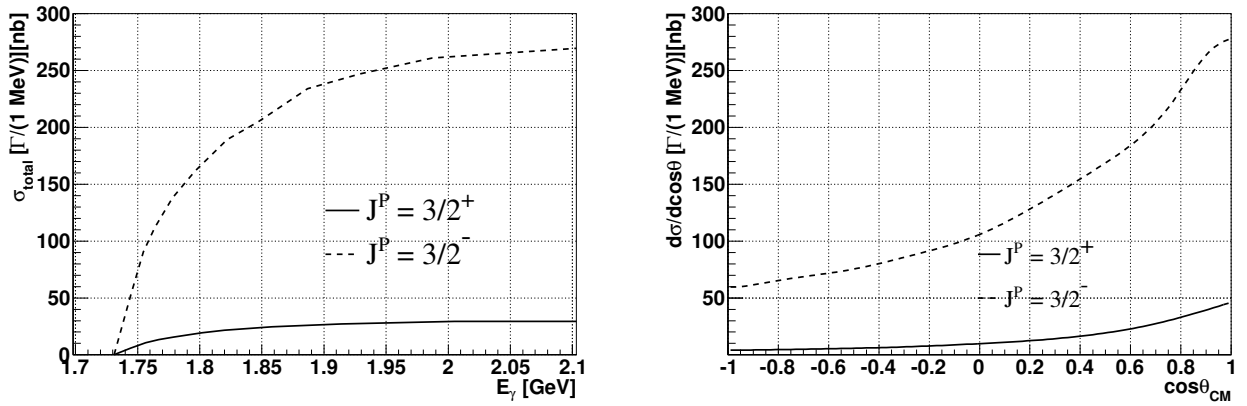

(a) Total cross sections. (b) Differential cross sections of $E_\gamma = 2.0$ GeV.

Figure 4.16.: Total and differential cross sections of the $\gamma n \to K^- \Theta^+$ reaction calculated by using effective Lagrangian for the spin 3/2 case [13]. The differential cross sections are given for the $E_\gamma = 2.0$ GeV case.

calculation were averaged over the LEPS acceptance ($\pm 20^\circ$ and $\pm 10^\circ$ in the horizontal and the vertical direction in the laboratory frame, respectively), which corresponds to $0 \lesssim \cos\theta_{CM} \leq 1$. Therefore, the decay width of Θ^+ was calculated as,

$$\Gamma_{\Theta^+}[\mathrm{MeV}] = \frac{12[\mathrm{nb/sr}]}{\overline{\left(\frac{d\sigma}{d\Omega}\right)}^{calc.}_{0^\circ - \theta^{max}_{CM}}} \tag{4.19}$$

$$\overline{\left(\frac{d\sigma}{d\Omega}\right)}^{calc.}_{0^\circ - \theta^{max}_{CM}} = \frac{\int_{0^\circ - \theta^{max}_{CM}} d(\cos\theta) \frac{d\sigma}{d\cos\theta}}{\int_{0^\circ - \theta_{CM}} d(\cos\theta)} \times \frac{1}{2\pi} \tag{4.20}$$

where θ^{max}_{CM} is the boundary for averaging the cross section and determined by the LEPS acceptance and the kinematics. In order to include the effect of the neutron Fermi motion in the deuteron and the energy dependence of the reaction, a couple of combination of the incident photon energy and the neutron momentum were investigated. Figure 4.17 shows the nucleon momentum distribution in the deuteron [104]. The mean and the rms of the distribution is $\sim$ 26 MeV/c and $\sim$ 26 MeV/c, respectively. 99% of the distribution is contained in the range of $0 - 125$ MeV/c. Thus, the case that neutron momentum of up to 0.125 GeV/c with the direction in parallel or antiparallel to the incident photon was examined. For the incident photon energy, 2.0, 2.1 and 2.4 GeV were used in the calculation because the photon energy region of LEPS was 2.0 – 2.4 GeV. In the present calculation, the angular dependence of the differential cross sections was assumed to have the calculated distribution as shown in Fig. 4.15(b)(d) and 4.16(b), whereas the energy dependence of the cross sections was scaled with the incident photon energy according to the calculation for the total cross section, which is shown in Fig. 4.15(a)(c) and 4.16(a). If the photon energy went out of the plotted range, the total cross section was linearly extrapolated from the value of the edge region.

Figure 4.18 shows the estimation of Γ_{Θ^+} for LEPS experiment [9]. The horizontal axis means the incident photon energy in the laboratory frame of the $\gamma n \to K^- \Theta^+$ reaction. The solid or dashed lines correspond to the case in which the target neutron is rest in the laboratory frame, while the hatched areas indicate the uncertainty from the Fermi motion. As seen in the figure, Γ_{Θ^+} decreases as the

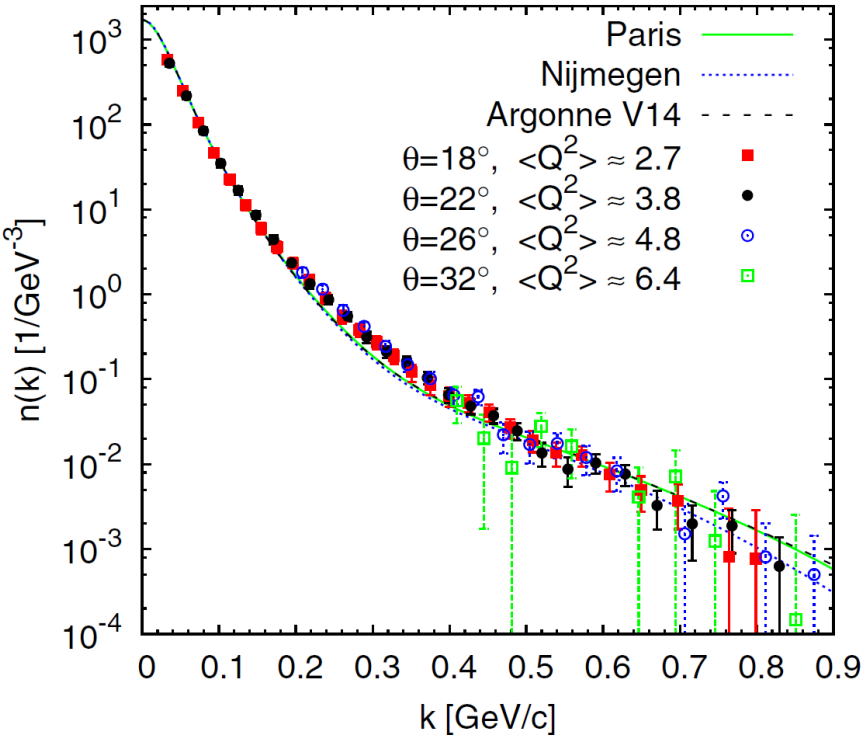

Figure 4.17.: The nucleon momentum distribution in the deuteron [104].

photon energy increases because the total cross section, or the denominator of Eq.4.19, grows up. For the $J^P = 1/2^+(1/2^-)$ case, the lower bound of the Γ_{Θ^+} is ∼20-30 MeV (∼150 MeV), which is too wide to observe the sharp peak structure in the spectrum obtained by the LEPS. On the other hand, the lower limit of the decay width for the $J^P = 3/2^+(3/2^-)$ case is ∼2.3 MeV (∼0.3 MeV). Thus, the LEPS data with the help of the theoretical model of the photo-production favors the spin 3/2 case. However, the spin 3/2 possibility conflicts the negative result of the present and the KEK-PS E559 experiments. Figure 4.19 illustrates the summary of the constraints on Γ_Θ. In conclusion, the current theoretical model can not explain the previous LEPS data and the meson-induced reaction simultaneously.

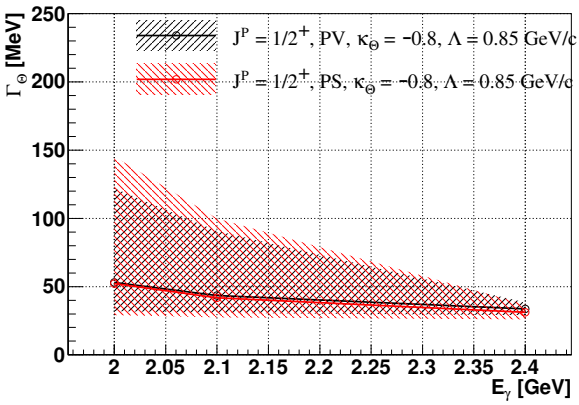

(a) $J^P = 1/2^+$, $\kappa_\Theta = -0.8$, $\Lambda = 0.85$ GeV

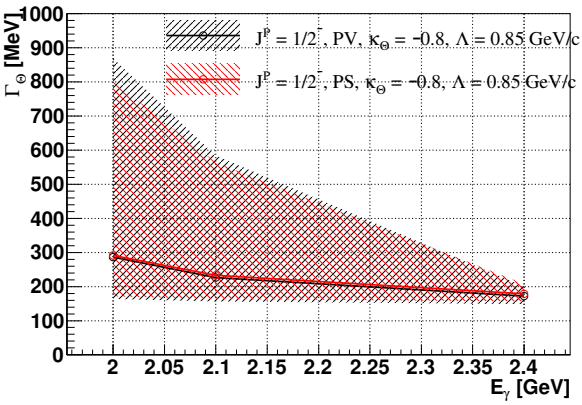

(b) $J^P = 1/2^-$, $\kappa_\Theta = -0.8$, $\Lambda = 0.85$ GeV

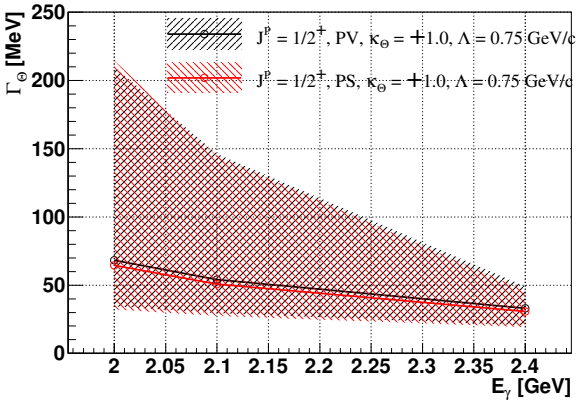

(c) $J^P = 1/2^+$, $\kappa_\Theta = 1.0$, $\Lambda = 0.75$ GeV

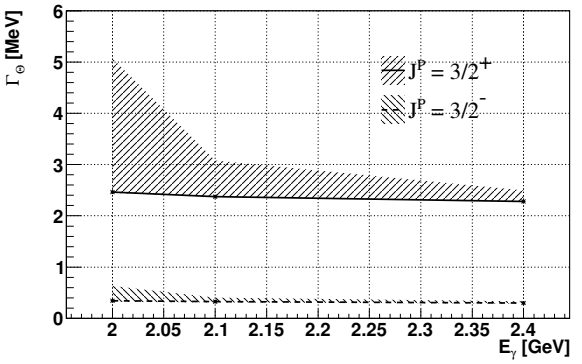

(d) $J^P = 3/2^\pm$, $\kappa_\Theta = 1.0$, $\Lambda = 0.85$ GeV

Figure 4.18.: Decay width estimation for the LEPS observation of 12 nb/sr in the center-of-mass frame. The solid or dashed lines correspond to the case in which the target neutron is rest in the laboratory frame.

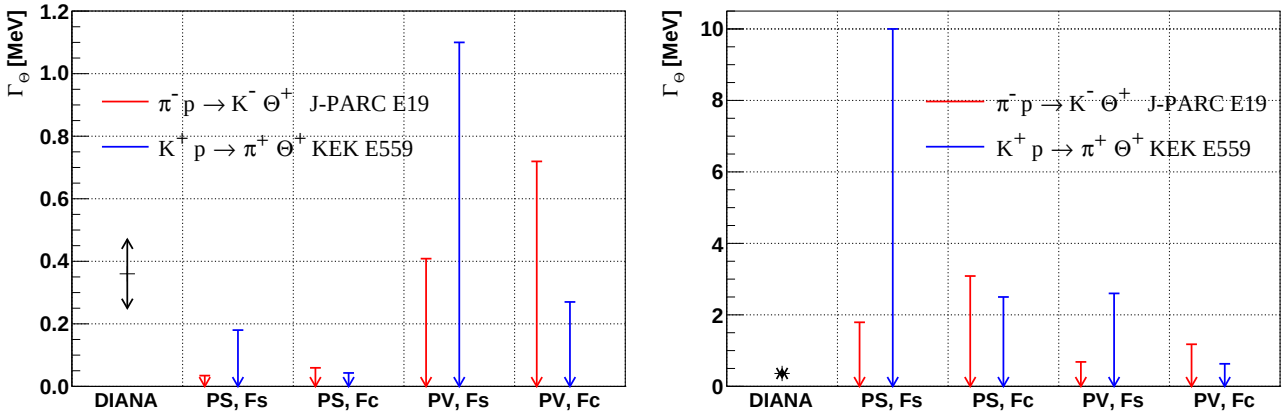

(a) $J^P = 1/2^+$ case.

(b) $J^P = 1/2^-$ case.

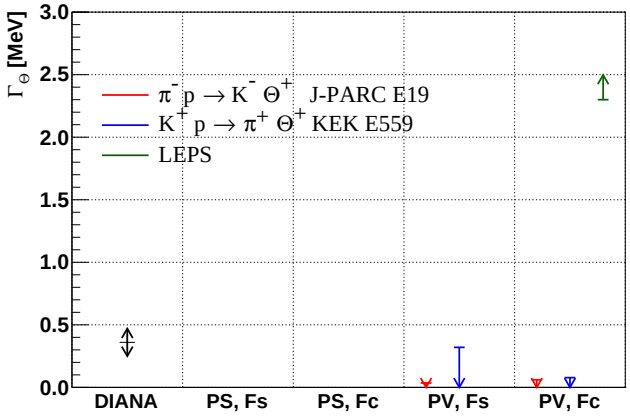

(c) $J^P = 3/2^+$ case.

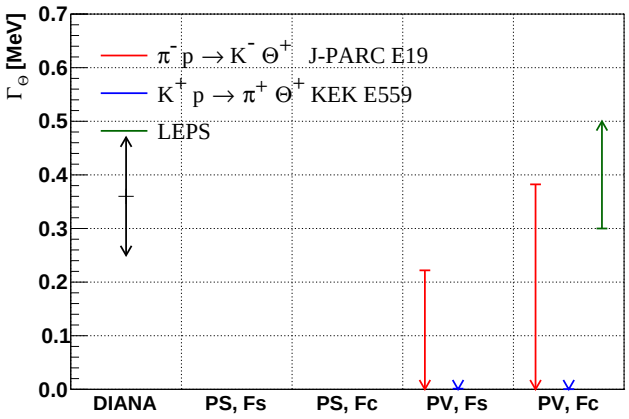

(d) $J^P = 3/2^-$ case.

Figure 4.19.: Comparison of the decay width Γ_{Θ^+}. The labels in horizontal axis, "PS, F_s", "PS, F_c", "PV, F_s", "PV, F_c", and DIANA, denote the combination of the coupling scheme and the form factor type and the result of DIANA, respectively. The arrows show the allowed regions. LEPS data for $J^P = 1/2^{\pm}$ cases are not plotted because they are far beyond the range.

5. Conclusion

The J-PARC E19 experiment has been carried out to search for the Θ^+ pentaquark with the missing mass spectroscopy in the $\pi^- p \to K^- X$ reaction at the K1.8 beam line of the J-PARC hadron facility. The goal of the present experiment was to confirm the existence or nonexistence of Θ^+ with better mass resolution and higher statistics than the previous experiment KEK-PS E522, which had reported the bump structure with the significance of 2.6σ in the $\pi^- p \to K^- X$ reaction.

The present data were taken from October to November in 2010 with two spectrometer systems with a good momentum resolution of $\frac{\Delta p}{p} \sim 10^{-3}$, which was realized with the K1.8 beam line spectrometer and the SKS spectrometer. In order to cope with the high intensity beam, detectors and a data acquisition system were upgraded. This experiment is the first physics experiment at the J-PARC hadron facility. A liquid hydrogen target was exposed to 7.8×10^{10} beam π^- with the momentum of 1.92 GeV/c. In addition to the $p(\pi^-, K^-)X$ reaction data, the $p(\pi^\pm, K^+)\Sigma^\pm$ reaction data with the beam momentum of 1.37 GeV/c were collected to evaluate the performance study and the calibration of the spectrometer systems.

The analysis was performed keeping attention to improve the analysis efficiency compared to the previous result [90] which had been deteriorated by the bad time structure of the beam spill. The tracking algorithm was improved by applying the Hough transformation to the beam line chamber at the most upstream part and requiring the tracks crossing the triggering segment of the timing counters. The analysis efficiencies for the incident particle, the outgoing particle and the product of them were improved as 68.5% $\to$ 83.6%, 56.0% $\to$ 49.2% and 38.4% $\to$ 41.1%, respectively. The missing mass resolution was estimated to be $1.84 \pm 0.03 \pm 0.07$ and $1.7 \pm 0.03 \pm 0.3$ MeV/c^2 (FWHM) for $\Sigma^\pm$ and Θ^+, respectively. The worse mass resolution for Θ^+ than that of published in [99] was due to the updated estimation for the momentum resolution of the π^- beam. The accuracy of the missing mass measurement was estimated to be 1.7 MeV/c^2. The measured differential cross section of Σ^+ is in good agreement with the past experimental data.

In the missing mass spectrum of the $\pi^- p \to K^- X$ reaction, there was no peak structure corresponding to the Θ^+. Therefore we have derived the upper limit of the differential cross section of Θ^+ production in the $\pi^- p \to K^- \Theta^+$ reaction. The 90% confidence level upper limit of the differential cross section for the scattering angle from 2^o to 18^o in the laboratory frame was obtained to be 0.27 μb/sr in the mass range from 1.51 to 1.55 GeV/c^2. The obtained result is smaller than the E522 result by an order of magnitude. Therefore, it is concluded that the observed bump structure by E522 collaboration was due to a statistical fluctuation.

According to the theoretical calculation from the hadronic model [100], the differential cross section is proportional to the Θ^+ decay width because the $t-$channel process with K^* exchange is negligible and the $s-$channel process is dominant. The 90% confidence level upper limit of the decay width was estimated to be 0.72 MeV (3.1 MeV) for the $J^P = 1/2^+(1/2^-)$ case. The obtained upper bound

did not update the severest one, 0.64 MeV, set by Belle [34] nor negate the DIANA measurement of 0.36 ± 0.11 MeV at the peak of 1538 MeV/c^2 [14] in the $K^+\mathrm{Xe} \to K^0_s p\mathrm{Xe}'$. Combined the result obtained in the K^+-induced reaction, the upper limit of Γ_{Θ^+} is estimated to be 0.41 MeV, which is the severest value among the experiments reporting negative results, however it is not enough small to exclude the DIANA result.

To compare the meson induced reaction with the photon induced one, the similar derivation of the decay width were applied to the differential cross section of the $\gamma n \to K^-\Theta^+$ reaction estimated to be 12 nb/sr in the center-of-mass frame by LEPS [9], using the theoretical calculation [13,103]. The lower bound of the decay width for the LEPS data were roughly estimated to be 20–30 MeV (150 MeV) for the $J^P = 1/2^+(1/2^-)$ case, and $\sim$2.3 MeV ($\sim$0.3 MeV) for the $J^P = 3/2^+(3/2^-)$ case, where the neutron Fermi motion in the deuteron is included in the estimation. There is a conflict between the meson beam experiments and the previous result of the LEPS. From the claimed narrow width by the LEPS experiment, the LEPS data favors the spin 3/2 assignment, while the cross sectoin upper limits obtained from the meson beam experiments already excluded that level of production in the case of spin 3/2 and spin 1/2 would be the only possibility left. Therefore, current theoretical models can not explain the previous LEPS data and the meson-induced reaction simultaneously.

Acknowledgments

I am deeply indebted to many people concerning the J-PARC E19 experiment.

First of all, I wish to express my sincere gratitude to my two supervisors; Prof. Tomofumi Nagae and Prof. Naohito Saito. Prof. Nagae guided me to the exciting field of strangeness nuclear physics. He gave me an opportunity to struggle with the construction of the J-PARC K1.8 experimental area from the earliest stage. He has encouraged me and given invaluable advice to complete this work. I have learned from him about not only the knowledge of physics but also attitudes of the nuclear physicist. I owe him for his patience to wait my output for a long time. After he moved to Kyoto university in July 2007, Prof. Saito became my supervisor in a doctor course. It is my great fortune that I could encounter his great insight and passion for physics as well as his leadership.

I would like to express my great thanks to Prof. Megumi Naruki, who is the spokesperson of the present experiment, and Prof. Toshiyuki Takahashi, who is one of the specialist of the experiment at SKS. They taught me many things about physics, techniques on the experiments and the analysis. They has supported me to brush up this dissertation through helpful discussions.

I express special thanks to Dr. Kotaro Shirotori, who had completed his doctoral dissertation by this experiment, for many things during the construction, commissioning and beam time shift. His intensive work for the E19 led to the success of the experiment. In addition, many catchwords, which he printed, encouraged everyone during the experiment.

I wish to thank members of Experimental Nuclear and Hadronic Physics (NH) group in Kyoto University. Mr. Atsushi Tokiyasu designed and constructed the new 3 mm spacing drift chamber. His tireless and creative efforts on the R&D overcame the technical problem with such a narrow pitch wire chamber. Mr. Manabu Moritsu developed the firmware of trigger receiver modules. Mr. Satoshi Adachi designed and fabricated the BGC and the BH2. Mr. Hitoshi Sugimura programmed the online monitor software. Mr. Yudai Ichikawa provided the alert system of LH2 target.

I would like to express my great thanks to the Strangeness Nuclear Physics group in Tohoku University. Dr. Koji Miwa is my friendly adviser from the start year of the graduate school. I was strongly affected by his love for the experimental physics. Dr. Mifuyu Ukai gave me continuous encouragement and useful advice. Dr. Kenji Hosomi arranged the matrix trigger and the monitor system for the spill duty factor. Mr. Ryotaro Honda provided the trigger timestamp system. Mr. Yoshio Yonemoto worked on the drift chamber calibration. Prof. Takeshi Koike and Mr. Takeshi Yamamoto relaxed and encouraged me many times. I also would like to thank other members of Tohoku group for their hard working and effective cooperation not only during the beam time but also in the preparation time for the repair of the BD chambers and alignment of the detectors: Ms. Misako Sato, Mr. Tomokazu Otani, Mr. Kazuya Yagi, Mr. Kenkoh Sugihara, Mr. Fumiki Hiruma, Mr. Akio Sasaki, and Mr. Yuki Matsumoto. I would like express thanks to Mr. Nobuyuki Chiga for designing and constructing the support frame for the downstream detectors.

I would like to thank Prof. Atsushi Sakaguchi, Mr. Kotaro Yoshida, Mr. Naoya Ishibashi and Mr. Toshiyuki Tanaka from Osaka University and Ms. Ruri Iwasaki from Nara Women's University for construction of the K1.8 experimental area and the SKS downstream detectors. I learned from Prof. Sakaguchi a lot of things about detectors. Ms. Iwasaki also provided the recording system of the magnetic field of the K1.8 D4 and the SKS.

I wish to thank to the group from Seoul National University. Prof. Kiyoshi Tanida gave me precious advice of physics. He was also concerned about everyone's health. Dr. Ryuta Kiuchi took charge of the construction of the K1.8 experimental area. He also kindly picked me up and drove back and forth between Tsukuba and Tokai. I would like to appreciate Dr. Choong Jae Yoon and Dr. Kim Mijung for their hard work and kindness.

I would like to acknowledge the SKS group of KEK. Dr. Kanae Aoki and Mr. Yutaka Kakiguchi maintained the SKS and its refrigerator system. Dr. Michiko Sekimoto kindly taught me helpful advice to construct and deal with wire chambers.

I would like to thank Dr. Shigeru Ishimoto and Dr. Shoji Suzuki for their great efforts to construct the liquid hydrogen target system and keep it running stably.

I am obliged to the staff members of J-PARC accelerator group and the hadron beam channel group: Prof. Kazuhiro Tanaka, Prof. Hiroyuki Noumi, Prof. Yoshinori Sato, Prof. Shinya Sawada, Prof. Masaharu Ieiri, Prof. Hitoshi Takahashi, Prof. Hiroaki Watanabe, Dr. Ryotaro Muto, Dr. Akihisa Toyoda, Dr. Masami Iio, Mr. Keizo Agari, Mr. Yutaka Yamanoi, Ms. Erina Hirose, Mr. Michifumi Minakawa and others. Without their supports, the present experiment would not be successfully running.

I am grateful to the KEK electronics system group. Dr. Youichi Igarashi was the chief member of the development for the new data acquisition system for the J-PARC hadron experiment. I leaned from him many things about the online software and debug methods of electronics hardware. Dr. Masahiro Ikeno provided the hardware design of the trigger/tag distribution modules. He also gave a lot of helps for the modification of the TKO-MHTDC. Without his helps, the module had a fatal error in the reset logic of the data buffer and had caused miserable statistics due to the long dead time. Dr. Tomohisa Uchida made the FPGA firmware of the FINESSE MWPC encoder. Past Prof. Takashi Taniguchi gave me practical techniques how to reduce a noise of a wire chamber. I also address my thanks to Dr. Kenta Itahashi from RIKEN, who is one of the core member of the hadron DAQ working group for valuable discussion of the specification of both software and hardware.

I would like thank Russian group, Dr. Petr Evtoukhovitch and Dr. Tsamalaidze Zviad for their hard working and their hospitality. I would like thank Italian group, Dr. Simonetta Marcello, Dr. Stefania Bufalino, Dr. Elena Botta and Dr. Alessandro Feliciello, for their cooperation during the data taking shift.

I want to address my gratitude to Dr. Tetsuo Hyodo and Prof. Makoto Oka for the theoretical calculation of the cross sections and valuable discussions.

I have joined two physics experiment and one test experiment at KEK-PS, E559/E566/T594, during the first year of my master course. I would address great thanks to Prof. Ken'ichi Imai, the spokesperson of E559, and Prof. Hirokazu Tamura, the spokesperson of E566, for providing me chances to participate in those experiment. I am thankful also all the members of those experiments. I would like to acknowledge Prof. Shuhei Ajimura, Prof. Kazuma Nakazawa, Dr. Takaomi Watanabe, Mr.

Tomohiro Kameyama Dr. Kenta Futatsukawa, Dr. Kyo Tsukada, Dr. Yusuke Miura, Dr. Yue Ma, Ms. Sari Kinoshita, Mr. Satoru Kamigaito, Mr. Katsuyuki Senzaka, Mr. Seishi Dairaku, Mr. Masashi Hayata, Mr. Kohei Shoji, Dr. Yoshichika Seki, and Prof. Kazuhiro Yamamoto. My experimental techniques and fundamentals had been trained and formed through those experiments. In addition, I learned from T594 experiment that it is important to visualize the data at online. I wish to thank to Dr. Takatsugu Ishikawa, Dr. Kotaku Suzuki and Dr. Ryo Hashimoto for their helps during the test experiment for the wire chambers at LNS.

I would like to express great appreciation to Dr. Tomofumi Maruta, Dr. Hiroyuki Fujioka, and Dr. Daisuke Nakajima, who were the seniors of Nagae's laboratory, Prof. Tsutomu Mibe, Dr. Hiromi Iinuma, Ms. Seiko Hirota, Mr. Takuya Kakurai and Mr. Sohtaro Kanda, who are the present and past members of Saito's laboratory, for their help, interesting discussions and the friendship. They also made me have fun of the daily life in Tsukuba by bringing me to the restaurants out side of KEK or sometimes holding drinking parties. I would like to express my gratitude to Ms. Hisako Ohata and Ms. Tomoko Iida for their secretarial support at KEK.

I am also deeply indebted to the members of the J-PARC E16 collaboration.

Special thanks are due to the Chief Scientist Dr. Hideto En'yo and Dr. Satoshi Yokkaichi, who gave me a chance to start my career although I had not finished the dissertation. Their support and understanding for the present work are greatly appreciated. I wish to thank Dr. Fuminori Sakuma, Dr. Kazuya Aoki, Dr. Yuhei Morino, Dr. Yoki Aramaki and Dr. Daisuke Kawama for their help and the friendship.

I would like to acknowledge Prof. Kyoichiro Ozawa. He encouraged and supported me to complete this work. He also read the drafts of this work carefully and gave me insightful comments. I am grateful to the members of Ozawa's laboratory: Mr. Yosuke Watanabe, Mr. Yusuke Komatsu, Mr. Shinichi Masumoto, Ms. Atsuko Takagi, Mr. Koki Kanno, Mr. Wataru Nakai, Mr. Yuki Obara, Mr. Takuya Shibukawa and Ms. Hikari Murakami.

I would like to express my gratitude to the secretaries of Radiation Laboratory of Riken Nishina Center, Ms. Noriko Kiyama, Ms. Keiko Suzuki and Ms. Mitsue Yamamoto for their support.

This analysis was performed on the Central Computing System of High Energy Accelerator Research Organization (KEKCC). I would like to acknowledge the support provided by Grant-in-Aid for JSPS Fellows.

Finally, my deepest appreciation goes to my family for their great support throughout my studies.

Bibliography

[1] D. Diakonov, V. Petrov, M. Polyakov, Z. Phys. A **359**, 305 (1997)

[2] R. Jaffe, F. Wilczek, Phys. Rev. Lett. **91**, 232003 (2003)

[3] T. Kishimoto, T. Sato, Prog. Theor. Phys. **116**, 241 (2006)

[4] M. V. Danilov *et al.*, Phys. Atom. Nucl. **71**, 605 (2008)

[5] T. Nakano *et al.*, Phys. Rev. Lett. **91**, 012002 (2003)

[6] A. I. Titov, *et al.*, Phys. Rev. C **70**, 042202 (2004)

[7] S. Stepanyan *et al.*, Phys. Rev. Lett. **91**, 252001 (2003)

[8] B. McKinnon *et al.*, Phys. Rev. Lett. **96** 212001 (2006)

[9] T. Nakano *et al.*, Phys. Rev. C **79**, 025210 (2009)

[10] J. Barth *et al.*, Phys. Lett. B **572**, 127 (2003)

[11] M. Battaglieri *et al.*, Phys. Rev. Lett. **96** 042001 (2006)

[12] R. De Vita *et al.*, Phys. Rev. D **74** 032001 (2006)

[13] S. I. Nam, A. Hosaka, H. C. Kim, Phys. Lett. B **633** 483 (2006)

[14] V. V. Barmin *et al.*, arXiv:1307.1653 [nucl-ex]

[15] V. Kubarovsky *et al.*, Phys. Rev. Lett. **92**, 032001 (2004)

[16] V. V. Barmin *et al.*, Phys. Atom. Nucl. **66**, 1715 (2003)

[17] V. V. Barmin *et al.*, Phys. Atom. Nucl. **70**, 35 (2007)

[18] V. V. Barmin *et al.*, Phys. Atom. Nucl. **73**, 1168 (2010)

[19] A. E. Asratyan *et al.*, Phys. Atom. Nucl. **67**, 682 (2004)

[20] P. Zh. Aslanyan, Nucl. Phys. A **755**, 375c (2005)

[21] A. Airapetian *et al.*, Phys. Lett. B **585**, 213 (2004)

[22] N. Abdel-Bary *et al.*, Phys. Lett. B **595**, 127 (2004)

[23] S. Chekanov *et al.*, Phys. Lett. B **591**, 7 (2004)

[24] L. Camilleri *et al.*, Nucl. Phys. B **143**, 129 (2005)

[25] A. Aleev *et al.*, arXiv:hep-ex/0401024

[26] A. Aleev *et al.*, arXiv:hep-ex/0509033

[27] J. Z. Bai *et al.*, Phys. Rev. D **70**, 012004 (2004)

[28] S. Schael *et al.*, Phys. Lett. B **599**, 1 (2004)

[29] S. Raducci *et al.*, DELPHI 2004-02 (CONF 683), (2004)

[30] P. Achard *et al.*, Eur. Phys. J. C **49**, 395 (2007)

[31] B. Aubert *et al.*, arXiv:hep-ex/0502004

[32] K. Goetzen *et al.*, Nucl. Phys. B (Proc. Suppl.) **164**, 117 (2007)

[33] K. Abe *et al.*, arXiv:hep-ex/0409010

[34] R. Mizuk *et al.*, arXiv:hep-ex/0411005

[35] D. O. Litvintsev *et al.*, Nucl. Phys. B (Proc. Suppl.) **142**, 374 (2005)

[36] Yu. M. Antipov *et al.*, Eur. Phys. J. A **21**, 455 (2004)

[37] I. Abt *et al.*, Phys. Rev. Lett. **93**, 212003 (2004)

[38] M. J. Longo *et al.*, Phys. Rev. D **70**, 111101(R) (2004)

[39] J. M. Link *et al.*, Phys. Rev. B **639**, 604 (2006)

[40] C. Pinkenburg *et al.*, J. Phys. G**30** S1201 (2004)

[41] M. I. Adamovich *et al.*, Phys. Rev. C **72** 055201 (2005)

[42] M. Zavertyev *et al.*, Nucl. Phys. A **755** 387c (2005)

[43] S. Niccolai *et al.*, Phys. Rev. Lett. **97** 032001 (2006)

[44] M. Abdel-Bary *et al.*, Phys. Lett. B **649** 252 (2007)

[45] O. Samoylov *et al.*, Eur. Phys. J. C **49** 499 (2007)

[46] J. Napolitano *et al.*, arXiv:hep-ex/0412031

[47] Y. Oh *et al.*, Phys. Rev. D **69**, 014009 (2004)

[48] Y. Oh *et al.*, Phys. Rev. D **69**, 074016 (2004)

[49] K. Miwa *et al.*, Phys. Lett. B **635**, 72 (2006)

[50] K. Miwa *et al.*, Phys. Rev. C **77**, 045203 (2008)

[51] M. Tomizawa, Nucl. Phys. B (Proc. Suppl.) **154**, 123 (2006)

[52] H. Oguri *et al.*, AIP Conf. Proc. **1390**, 235 (2011)

[53] M. Ikegami, Prog. Theor. Exp. Phys. 02B002 (2012)

[54] H. Hotchi *et al.*, Prog. Theor. Exp. Phys. 02B003 (2012)

[55] T. Koseki *et al.*, Prog. Theor. Exp. Phys. 02B004 (2012)

[56] K. Agari *et al.*, Prog. Theor. Exp. Phys. 02B008 (2012)

[57] J-PARC hadron beam line group, private communication

[58] Y. Yamanoi *et al.*, Proceedings of the 7th Annual Meeting of Particle Accelerator Society of Japan, (2010)

[59] J. R. Sanford, C. L. Wang, Brookhaven National Laboratory, AGS internal report, 11279 and 11479 (1967) C. L. Wang, Phys. Rev. Lett., **25**, pp.1068, pp.1536(errata) (1970)

[60] K. L. Brown *et al.*, CERN 80-04 (1980).

[61] U. Rohrer, PSI Graphic Transport Framework based on a CERN-SLAC-FERMILAB version by K. L. Brown *et al.*

[62] K. Agari *et al.*, Prog. Theor. Exp. Phys. 02B009 (2012)

[63] J-PARC K1.8 experimental group, private communication

[64] T. Takahashi *et al.*, Prog. Theor. Exp. Phys. 02B010 (2012)

[65] LPT-141 (hall probe), Digital Teslameter 151, Group-3, http://www.group3technology.com/meters/dtm151.php

[66] S. Adachi, Master thesis, Kyoto University, (2009)

[67] O. Sasaki, M. Yoshida, IEEE Trans. Nucl. Sci., **46**, 1871 (1999)

[68] H. Hotchi *et al.*, Phys. Rev. C **64**, 044302 (2001)

[69] T. Fukuda *et al.*, Nucl. Instrum. Meth. A **361**, 485 (1995)

[70] K. Aoki *et al.*, KEK-PREPRINT-2007-39, (2007); API Conf. Proc. **985**, 349 (2008)

[71] EFM-30P (NMR probe), EFM-3000AX (tesla meter), Echo Electronics, http://echo-denshi.co.jp/nmr_magnetic.htm

[72] ANSYS, http://www.ansys.com

[73] T. Hasegawa, Nucl. Instrum. Meth. **160**, 43 (1994)

[74] F. Suekane *et al.*, IEEE Trans. Nucl. Sci., **33**, 73 (1986); KEK-PREPRINT-1985-66, (1985)

[75] H. Nomura, Master thesis, Tohoku University, (2003)

[76] T. K. Ohska *et al.*, KEK REPORT 85-10

[77] VMEbus architecture. IEEE 1014/D1.0.

[78] Y. Igarashi *et al.*, IEEE Trans. Nucl. Sci., **52**, 2866 (2005)

[79] Y. Arai, Nucl. Instrum. Meth. A **453**, 365 (2000); ATLAS-Japan TDC group web page. http://www-atlas.kek.jp/tdc/

[80] M. Shiozawa *et al.*, Nuclear Science Symposium and Medical Imaging Conference, IEEE Conference Record, **2**, 632 (1994)

[81] Y. Igarashi *et al.*, IEEE Trans. Nucl. Sci., **57**, 618 (2010)

[82] ROOT — A data analysis framework. http://root.cern.ch/

[83] National Semiconductor, DS99R105/DS99R106 3–40 MHz DC-balanced 24 bit LVDS serializer and deserializer.

[84] T. Uchida, IEEE Trans. Nucl. Sci., **55**, 1631 (2008)

[85] S. Agostinelli *et al.*, Nucl. Instrum. Meth. A **206**, 250 (2003)

[86] P. V. C. Hough, U.S. Patent 3069654 (1962)

[87] S. Morinobu, private communication

[88] MINUIT - Function Minimization and Error Analysis, CERN Program Library Long Writeups D506 (1994)

[89] J. Myrhein, L. Bugge, Nucl. Instrum. Meth. **160**, 43 (1979)

[90] K. Shirotori, Doctoral Thesis, Tohoku University. (2011)

[91] K. L. Brown *et al.*, Decay TURTLE CERN 74-2 (1974), PSI Graphic Turtle Framework by U. Rohrer based on a CERN-SLAC-FERMILAB version by K. L. Brown et al.

[92] T. Hasegawa, Doctor thesis, University of Tokyo, INS-IM-15 (1994)

[93] O. I. Dahl *et al.*, Phys. Rev. **163**, 1377 (1967)

[94] K. A. Olive *et al.* [Particle Data Group Collaboration], Chin. Phys. C **38** 090001 (2014)

[95] H. Courant *et al.*, Phys. Rev. D **16**, 1 (1977)

[96] D. J. Candlin *et al.*, Nucl. Phys. B **226**, 1 (1983)

[97] M. L. Good, R. R. Kofler, Phys Rev. **183**, 1142 (1969)

[98] K. Nakamura *et al.* (Particle Data Group), J. Phys. G **37**, 075021 (2010)

[99] K. Shirotori, *et al.*, Phys. Rev. Lett. **109**, 132002 (2012)

[100] T. Hyodo, A. Hosaka, M. Oka, Prog. Theor. Phys. **128**, 523 (2012)

[101] T. Hyodo, private communication

[102] S. I. Nam, A. Hosaka, H. C. Kim, Phys. Lett. B **579** 43 (2004)

[103] S. I. Nam, A. Hosaka, H. C. Kim, J. Korean Phys. Soc. **49** 1928 (2006)

[104] N. Fomin, *et al.*, Phys. Rev. Lett. **108** 092502 (2012)

A. Effect of error correlation on missing mass resolution

A.1. Expression for the propagation of error

The missing mass resolution is decomposed to resolutions of the momentum reconstruction of the beam and scattered particles, a resolution of the scattering angle, and the uncertainties of the energy loss correction of the incoming pions and outgoing kaons. According to the error propagation rule, the missing mass resolution ΔMM is denoted as follows.

$$\Delta MM^2 = AVA^T \tag{A.1}$$

$$A = \left(\left(\frac{\partial MM}{\partial p_\pi}\right) \quad \left(\frac{\partial MM}{\partial E_\pi}\right) \quad \left(\frac{\partial MM}{\partial p_K}\right) \quad \left(\frac{\partial MM}{\partial E_K}\right) \quad \left(\frac{\partial MM}{\partial \theta}\right)\right) \tag{A.2}$$

$$V = \begin{pmatrix} \mathrm{cov}(p_\pi, p_\pi) & \mathrm{cov}(p_\pi, E_\pi) & \mathrm{cov}(p_\pi, p_K) & \mathrm{cov}(p_\pi, E_K) & \mathrm{cov}(p_\pi, \theta) \\ \mathrm{cov}(E_\pi, p_\pi) & \mathrm{cov}(E_\pi, E_\pi) & \mathrm{cov}(E_\pi, p_K) & \mathrm{cov}(E_\pi, E_K) & \mathrm{cov}(E_\pi, \theta) \\ \mathrm{cov}(p_K, p_\pi) & \mathrm{cov}(p_K, E_\pi) & \mathrm{cov}(p_K, p_K) & \mathrm{cov}(p_K, E_K) & \mathrm{cov}(p_K, \theta) \\ \mathrm{cov}(E_K, p_\pi) & \mathrm{cov}(E_K, E_\pi) & \mathrm{cov}(E_K, p_K) & \mathrm{cov}(E_K, E_K) & \mathrm{cov}(E_K, \theta) \\ \mathrm{cov}(\theta, p_\pi) & \mathrm{cov}(\theta, E_\pi) & \mathrm{cov}(\theta, p_K) & \mathrm{cov}(\theta, E_K) & \mathrm{cov}(\theta, \theta) \end{pmatrix} \tag{A.3}$$

$$\mathrm{cov}(X, Y) = E\left[(X - E(X))(Y - E(Y))\right] \tag{A.4}$$

$$\sigma_X = \sqrt{\mathrm{cov}(X, X)} \tag{A.5}$$

$$r_{XY} = \frac{\mathrm{cov}(X, Y)}{\sigma_X \sigma_Y} \tag{A.6}$$

where $p_\pi, E_\pi, p_K, p_K, \theta$ are the momentum and energy of the incoming pion, those of the outgoing kaon, and the scattering angle of the reaction, respectively. A and A^T is a matrix of derivatives and

its transpose. The derivatives ($\frac{\partial MM}{\partial p_\pi}$, $\frac{\partial MM}{\partial E_\pi}$, $\frac{\partial MM}{\partial p_K}$, $\frac{\partial MM}{\partial E_K}$, and $\frac{\partial MM}{\theta}$) are expressed as follows.

$$\frac{\partial MM}{\partial p_\pi} = \left(\frac{1}{MM}[\beta_\pi(M_p - E_K) + p_K \cos\theta] \right) \tag{A.7}$$

$$\frac{\partial MM}{\partial E_\pi} = \frac{\partial MM}{\partial p_\pi}\frac{\partial p_\pi}{\partial E_\pi} = \frac{\partial MM}{\partial p_\pi}\frac{1}{\beta_\pi} \tag{A.8}$$

$$= \left(\frac{1}{MM}[\beta_\pi(M_p - E_K) + p_K \cos\theta] \right) \frac{1}{\beta_\pi} \tag{A.9}$$

$$\frac{\partial MM}{\partial p_K} = \left(-\frac{1}{MM}[\beta_K(M_p + E_\pi) - p_\pi \cos\theta] \right) \tag{A.10}$$

$$\frac{\partial MM}{\partial E_K} = \frac{\partial MM}{\partial p_K}\frac{\partial p_K}{\partial E_K} = \frac{\partial MM}{\partial p_K}\frac{1}{\beta_K} \tag{A.11}$$

$$= \left(-\frac{1}{MM}[\beta_K(M_p + E_\pi) - p_\pi \cos\theta] \right) \frac{1}{\beta_K} \tag{A.12}$$

$$\frac{\partial MM}{\partial \theta} = \left(-\frac{p_\pi p_K}{MM} \sin\theta \right) \tag{A.13}$$

V is a covariance matrix and $E(X)$ is an expectation value of a variable X. σ_X is a standard deviation of X. r_{XY} is a correlation coefficient of X and Y. In eq. 3.48, only diagonal components are taken into account. In this chapter, contribution of the off-diagonal part is described.

A.2. Monte Carlo simulation

A.2.1. Simulation setup

The effect of the off-diagonal part was evaluated by a Monte Carlo simulation using Geant4. Event vertices of the $p(\pi, K)$ reaction were generated to reproduce the observed distribution in the liquid hydrogen target. The masses of Σ^- and Θ^+ were fixed at 1197.449 MeV/c^2 and 1540 MeV/c^2, respectively. The measured momentum distribution at the K1.8 beam line was utilized for the beam particles. In the two-body reaction, an isotropic scattering-angle distribution in the center of mass frame was assumed. To make the particle trajectories, the kaon trajectory was calculated from the vertex point to the downstream part of the SKS (black trajectory in Fig. A.1), whereas the pion was propagated from the vertex to the upstream part of the beam spectrometer. In the pion propagation, the trajectory from the vertex to the exit of the QQDQQ system was calculated with Geant4 (black trajectory in Fig. A.1), then, the pion was transported with the inverse of the transport matrix of K1.8 beam line optics, called downstream-to-upstream or D2U matrix in the beam particle analyses 3.2.2. (red solid trajectory in Fig. A.1), and finally the straight track at the upstream part of QQDQQ was extrapolated (red dotted trajectory in Fig. A.1). After the event generation, hit positions on each tracking plane were artificially smeared by a Gaussian distribution with a position resolution in the range of 100 μm to 1000 μm with a step size of 100 μm (i.e. $10 \times 10 = 100$ combinations of the tracker resolution were examined in the present evaluation). Finally, the event reconstruction was performed in the same procedure as described in Chapter 3 (blue and green trajectories for π and K in Fig. A.1, respectively). Figure A.2 shows the position resolution dependence of the reconstructed mass resolution. For both Σ^- and Θ^+, the reconstructed mass resolution was found to have strong linear dependence on the position resolution of the BCs, whereas there was a small correlation between the mass resolution and the position resolution of the SDCs.

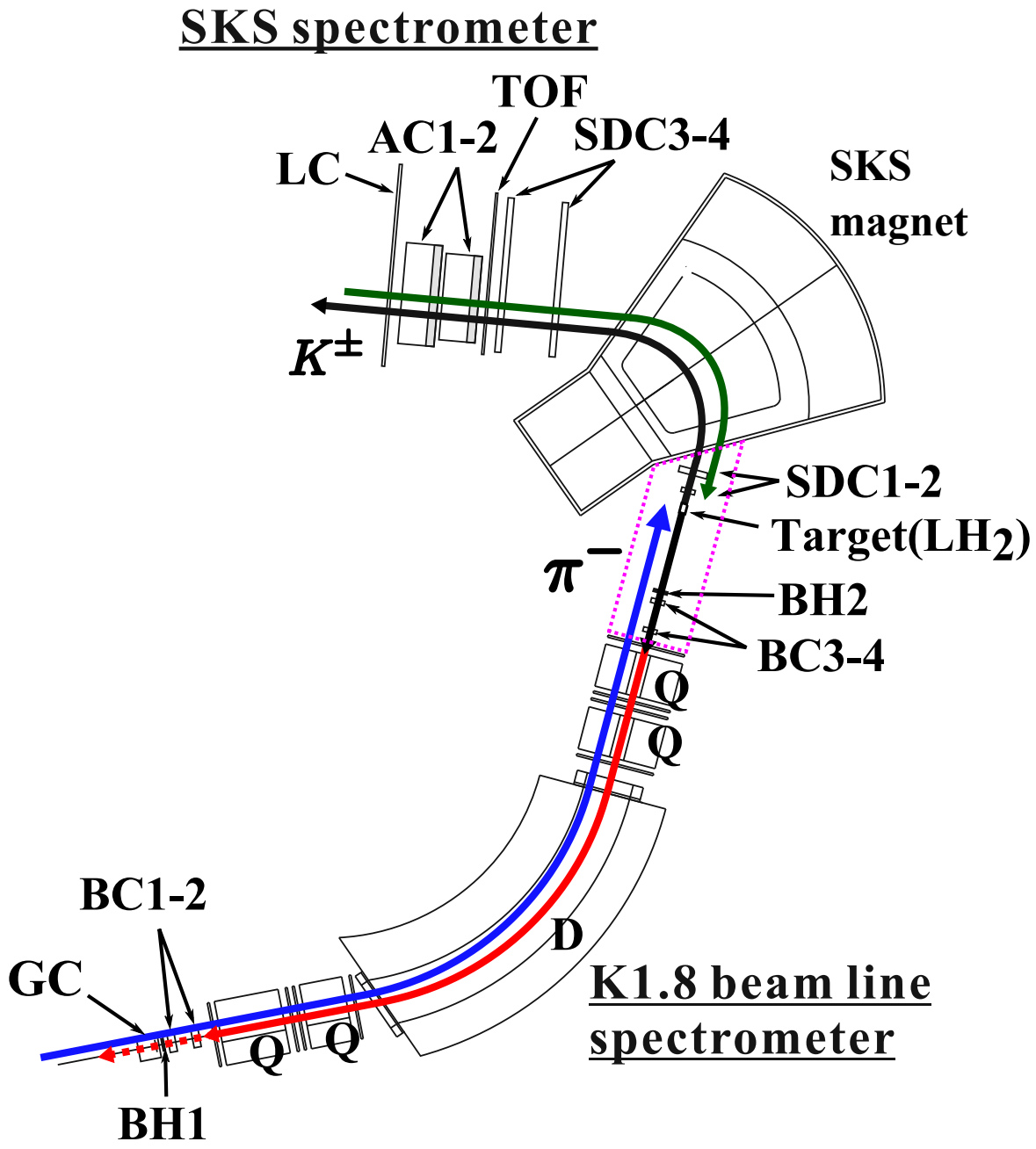

Figure A.1.: The schematic view of the reconstructed trajectories in the error correlation study. In the Monte Carlo simulation, pions and kaons were generated in the LH2 target and transported by Geant4 (black trajectories). Then, pions which reached at the exit of QQDQQ were transported by the inverse of the K1.8 transport matrix to the upstream part of the beam spectrometer (red solid trajectory) together with the straight track which was extrapolated to obtain hit positions of BC1-2 (red dotted trajectory). After the event generation and smearing of hit positions, the tracks and vertex reconstructions were performed (blue and green trajectories). The energy loss correction was taken into account only in the region surrounded by a magenta dotted line.

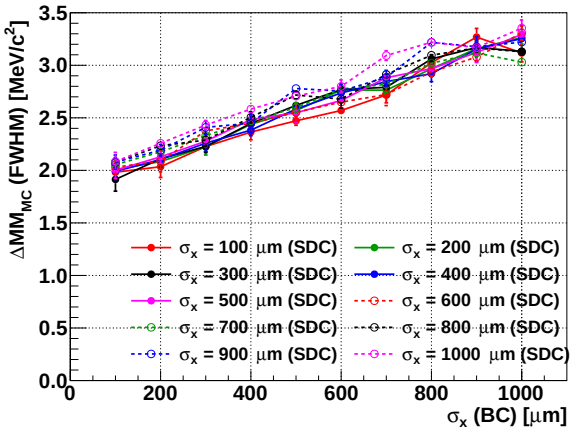

(a) Σ^- : σ_x(BC) vs ΔMM.

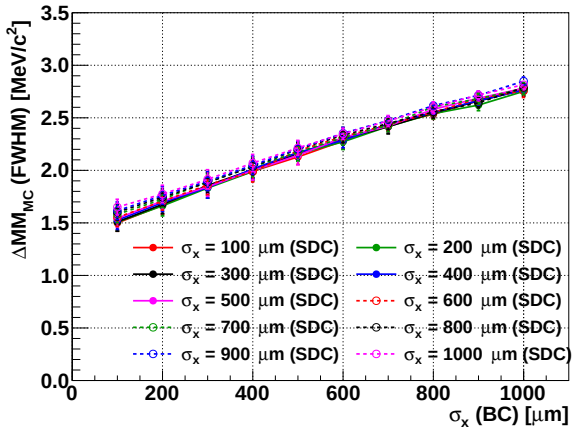

(b) Θ^+ : σ_x(BC) vs ΔMM.

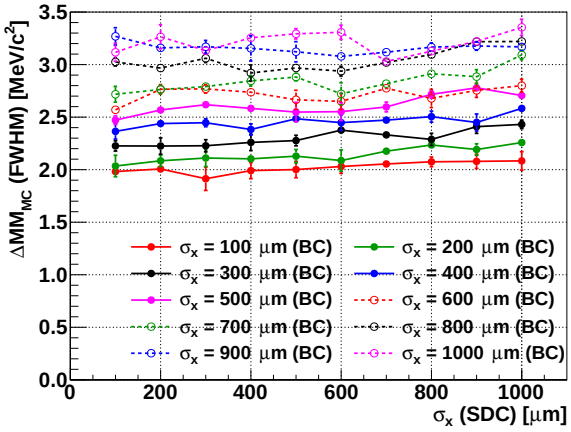

(c) Σ^- : σ_x(SDC) vs ΔMM.

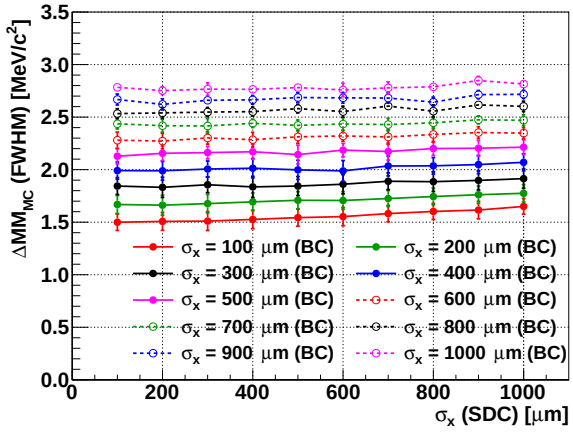

(d) Θ^+ : σ_x(SDC) vs ΔMM.

Figure A.2.: Position resolution dependence of the missing mass resolution. Missing mass resolution of (a), (c) Σ^- and (b), (d) Θ^+ productions. Top and bottom panels show the dependence of the BC and SDC resolutions, respectively.

A.2.2. Deviations

In the calculation of the variances and covariances, deviations of reconstructed values from generated values δp_π, δp_K, δE_π, δE_K and $\delta\theta$ were defined as follows:

$$\delta p_\pi = p_\pi^{\mathrm{recon.,g4-el}} - p_\pi^{\mathrm{gen.}} \tag{A.14}$$

$$\delta p_K = p_K^{\mathrm{recon.,g4-el}} - p_K^{\mathrm{gen.}} \tag{A.15}$$

$$\delta E_\pi = dE_\pi - dE_\pi^{\mathrm{g4}} \tag{A.16}$$

$$\delta E_K = dE_K - dE_K^{\mathrm{g4}} \tag{A.17}$$

$$\delta\theta = \theta^{\mathrm{recon.}} - \theta^{\mathrm{gen.}} \tag{A.18}$$

The superscript "recon." and "gen." indicate the value obtained by the track reconstruction and that of the event generation, respectively. The superscript "g4-el" denotes that the energy loss was corrected with the value which was provided by Geant4. δp_π (δp_K) included only the error of the tracking and separated from the error due to the energy loss fluctuation. dE_π (dE_K) denotes the pion (kaon) energy loss obtained by the same way as 3.8.2. dE_π^{g4} and dE_K^{g4} are the energy losses calculated by Geant4. The energy loss correction was considered in the same region as that of the present analysis, which is indicated with a magenta dotted line in Fig. A.1. The deviation distributions are displayed in Figs. A.3– A.7. Ten cases are shown as examples, in which the tracker resolution of BCs and SDCs are equal. The RMS of each plot was employed in the calculation of the variance. Note that contrary to the experimental data analysis (Sec. 3.9), the beam momentum resolution obtained by the simulation study reproduced almost the same value of the designed one. The reason why the momentum resolution in Sec. 3.9 was worse than the designed value is discussed in Sec. A.2.4.

A.2.3. Covariance and correlation coefficient

Contour plots of the deviations are shown in Figs. A.8 – A.17, where the position resolution of σ_x =300 μm was chosen as an example. Note that there is an obvious correlation between δE_π and δE_K as shown in Fig. A.13 because of the vertex point, and the path length in the LH2. There are also small correlation between $\delta\theta$ and δE_π (Fig. A.14) and between $\delta\theta$ and δE_K (Fig. A.17), which can be understood as a correlation between the scattering angle and the path length which makes the fluctuation of energy loss.

Significances of correlation coefficients were evaluated by a statistical test using Student's t-distribution. A statistic t_0 for a correlation coefficient r is defined as

$$t_0 = |r| \sqrt{\frac{N-2}{1-r^2}} \tag{A.19}$$

where $N-2$ is the number of degrees of freedom of $t-$distribution. In the t-test, a null hypothesis H_0 is defined as "the correlation coefficient r equals to zero". The definition of $p-$value is given as

$$p = \int_{-\infty}^{-t_0} f(t|H_0)dt + \int_{+t_0}^{+\infty} f(t|H_0)dt \tag{A.20}$$

$$= 2\int_{+t_0}^{+\infty} f(t|H_0)dt \tag{A.21}$$

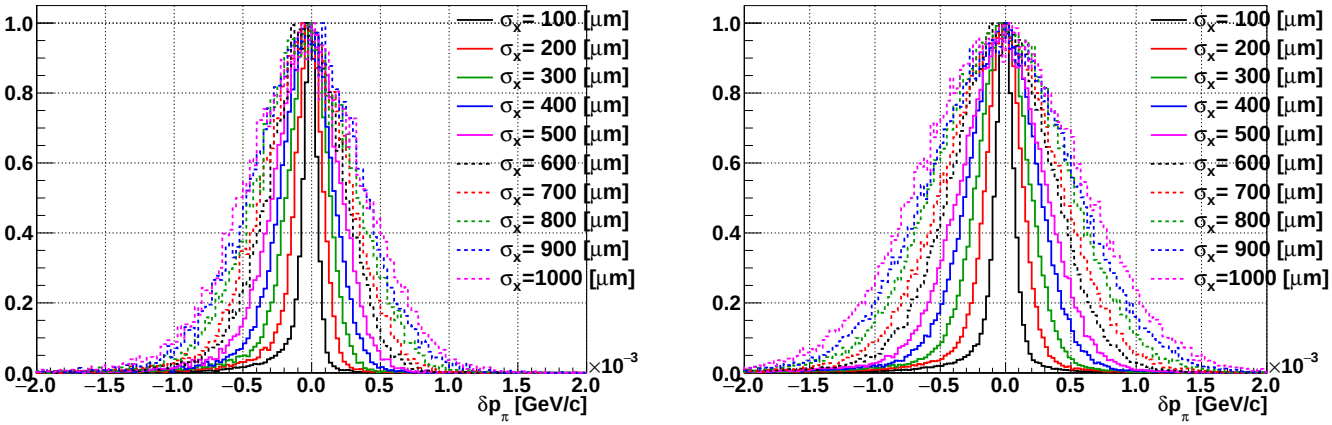

(a) Σ^- (b) Θ^+

Figure A.3.: Deviation distribution of the beam pion momenta δp_π.

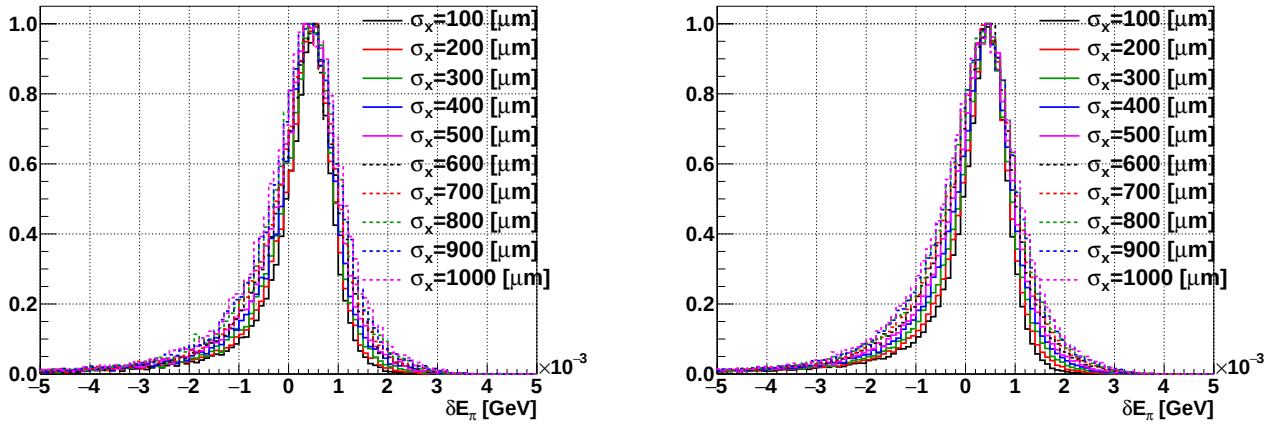

(a) Σ^- (b) Θ^+

Figure A.4.: Deviation distribution of the energy loss correction for the beam pion δE_π.

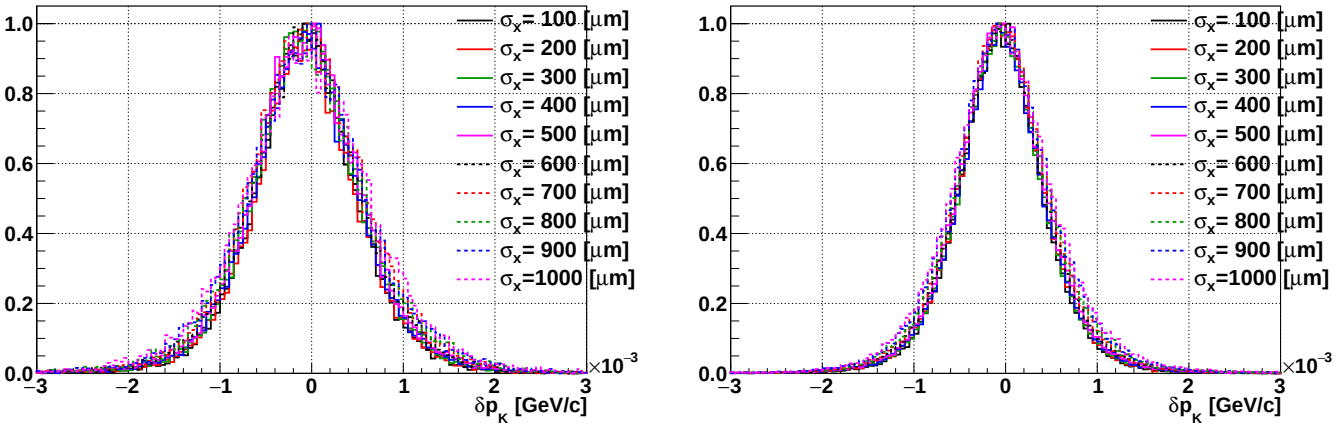

(a) Σ^- (b) Θ^+

Figure A.5.: Deviation distribution of the scattered kaon momentum δp_K.

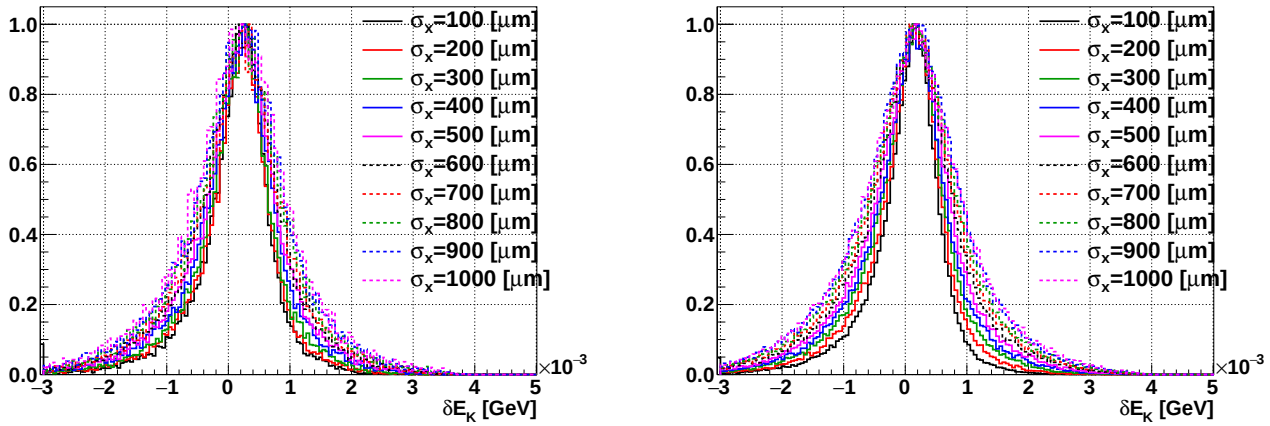

(a) Σ^- (b) Θ^+

Figure A.6.: Deviation distribution of the energy loss correction for the scattered kaon δE_K.

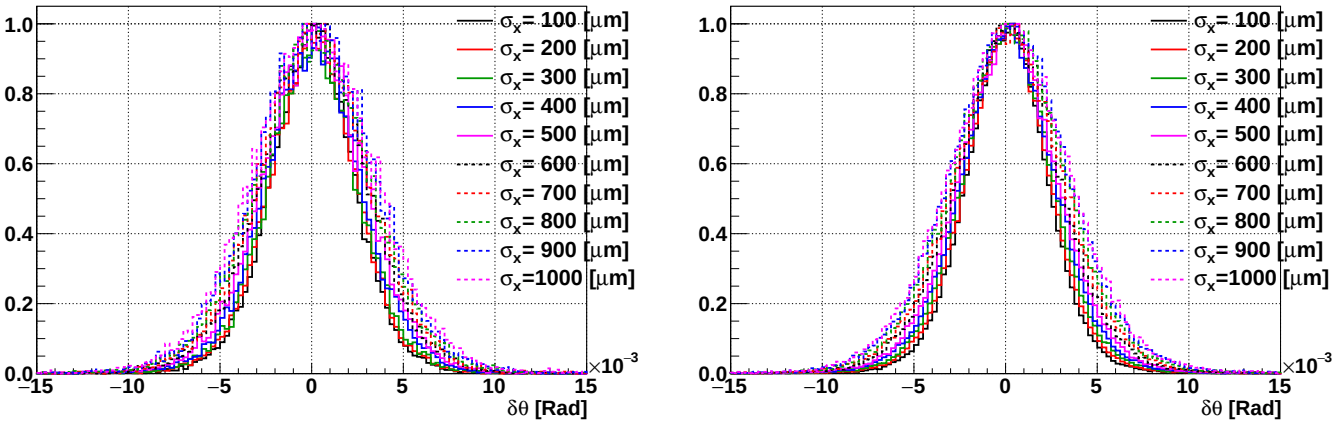

(a) Σ^- (b) Θ^+

Figure A.7.: Deviation distribution of the scattering angle $\delta\theta$.

where $f(t|H_0)$ is the $t-$distribution function under an assumption H_0. If the $p-$value is greater than a given significance level α, the statement that there is no correlation between the two variables is valid. On the other hand, if the $p-$value is less than α the hypothesis, H_0 is rejected. In other words, there is a correlation between the two variables.

The correlation coefficients and corresponding $p-$values of $t-$distribution obtained for the simulation data are shown in Figs. A.18 – A.27. There are statistical significant correlations with $\alpha = 0.05$ for cases of (δE_π, $\delta\theta$), (δE_K, $\delta\theta$) and (δE_π, δE_K), whereas the others have no correlation. Figures A.28 – A.37 display products of the deviations of two variables. The mean value of each plot was used in the calculation of the covariance.

A.2.4. Discussion

The missing mass distributions of the Monte Carlo simulation for Σ^- are shown in Fig. A.38. The experimental data (black histogram) is reproduced by the simulation results with the position resolution of less than 300 μm, though the width of the simulation data are slightly wider than that of the experimental data.

The width (FWHM) of the missing mass distribution was compared with the estimation by the error propagation. Since a relation between RMS and FWHM depends on the shape of the distribution (e.g. $2\sqrt{2\log 2}$ for a normal distribution), the scaling factor from RMS to FWHM was calculated using the mass distribution obtained by the simulation. The factors were smaller than that of a Gaussian distribution as shown in Figs. A.39, where black and red histograms correspond to the scale factor without energy loss and with energy loss, respectively.

Figures A.40 show the difference of the missing mass resolution (FWHM) between the width obtained from the full Monte Carlo simulation and the estimation by the error propagation without correlation terms, while Figs. A.41 show those for the error propagation with correlation. Although most of the values for the error propagation are slightly smaller than the widths of the simulation, the error propagation with correlation gives better estimation than that without correlation. The differences between the mass resolution with and without correlation is presented in Figs. A.42, which are estimated to be $\sim$0.18 MeV/c^2 for Σ^- and $\sim$0.10 MeV/c^2 for Θ^+, respectively.

Case for an explicit correlation between δp and δE

In the deviation definition of eqs. (A.14)–(A.17), no explicit correlation between δp_π (δp_K) and δE_π (δE_K) was considered as the same assumption is used in the experimental data analysis. In this subsection, the different definition for the uncertainty of the energy is discussed. The modified definition for δE_π and δE_K are as follows.

$$\delta E_\pi = E_\pi^{\text{recon.}} - E_\pi^{\text{gen.}} \tag{A.22}$$

$$\delta E_K = E_K^{\text{recon.}} - E_K^{\text{gen.}}, \tag{A.23}$$

where the superscript "recon." denotes the reconstructed energy at the vertex. In the new definition, δE_π (δE_K) contains not only the error of the energy loss correction but also the error of the momentum reconstruction, therefore, the contribution of correlation terms is non-zero (i.e. $\text{cov}(\delta p_\pi, \delta E_\pi) \neq 0$ and $\text{cov}(\delta p_K, \delta E_K) \neq 0$ by definition). The deviation distribution, contour plot, variance distribution,

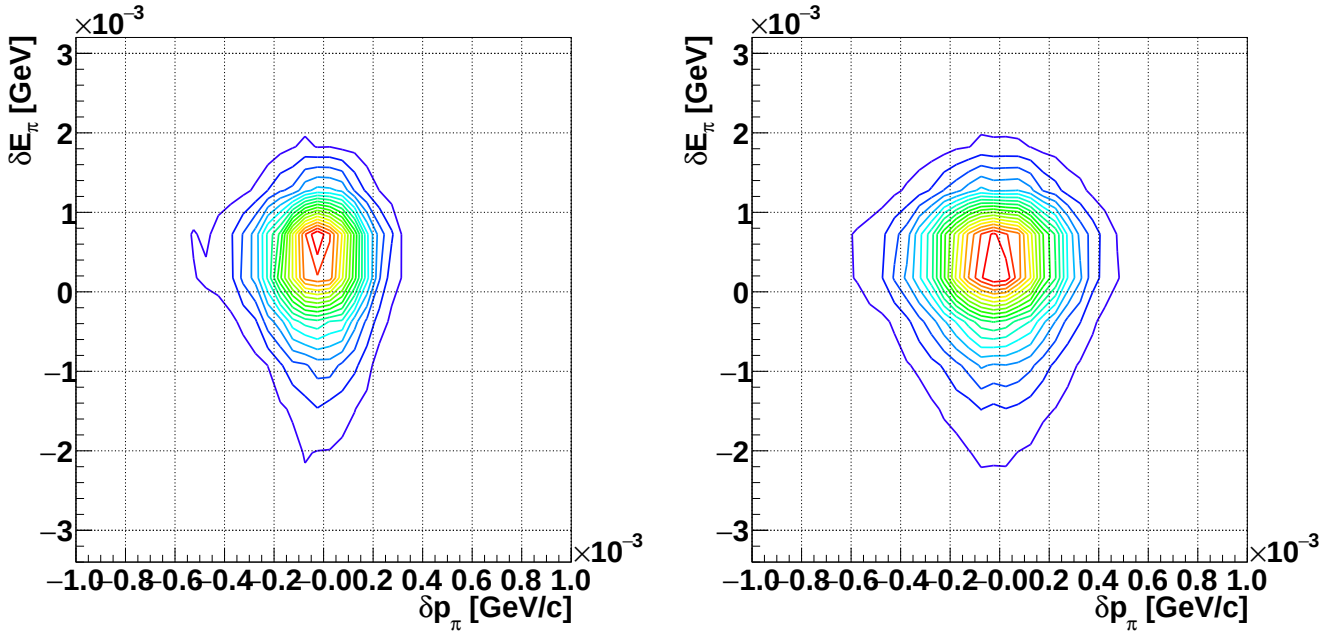

(a) Σ^- (b) Θ^+

Figure A.8.: Contour plot of the error distribution of the beam momentum δp_π and the energy correction for the beam δE_π.

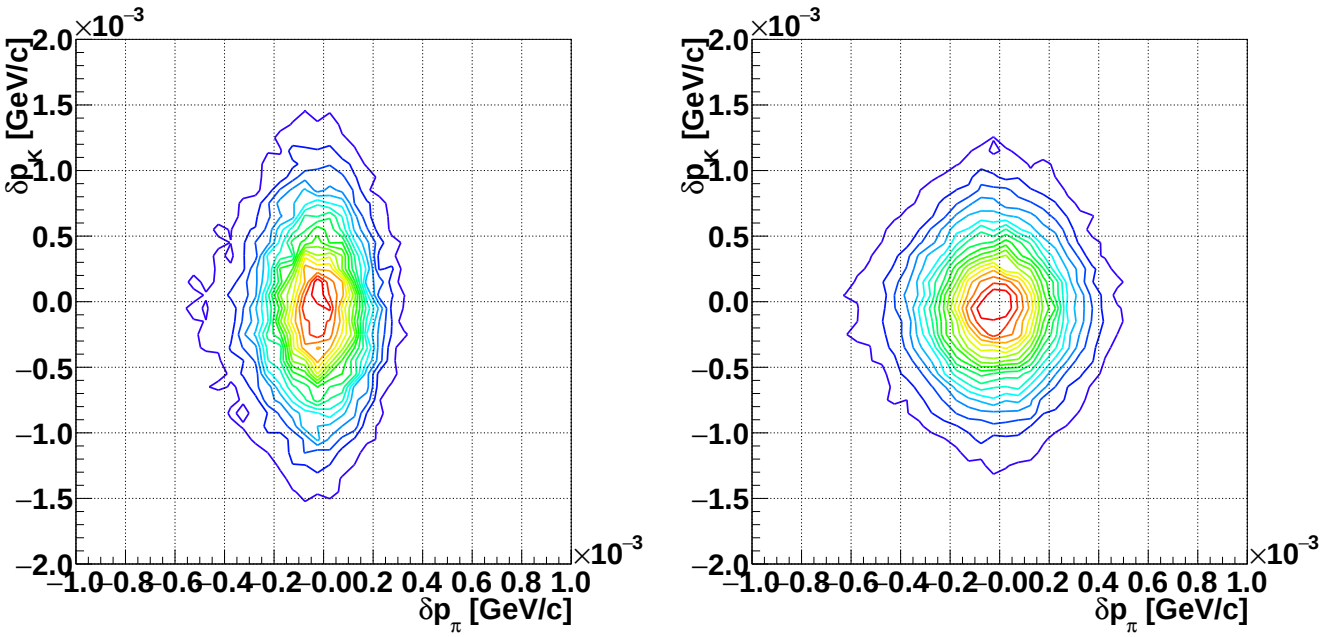

(a) Σ^- (b) Θ^+

Figure A.9.: Contour plot of the error distribution of the beam momentum δp_π and the scattered kaon momentum δp_K.

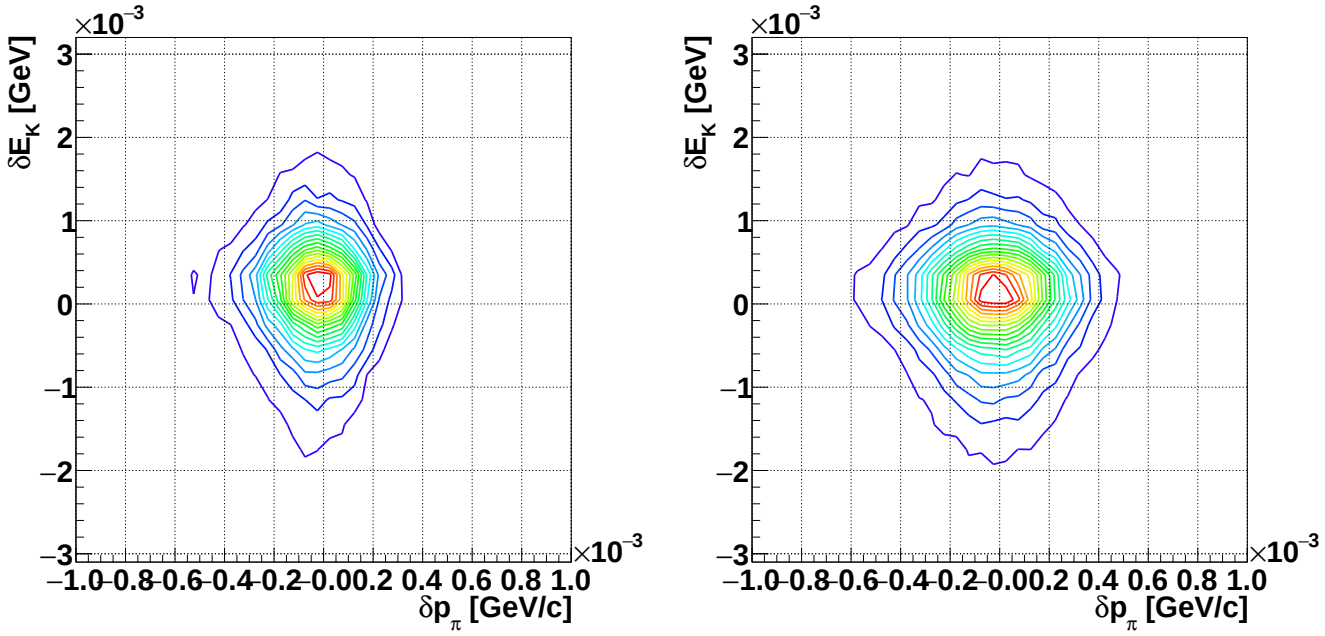

(a) Σ^- (b) Θ^+

Figure A.10.: Contour plot of the error distribution of the beam momentum δp_π and the energy loss correction for the scattered kaon δE_K.

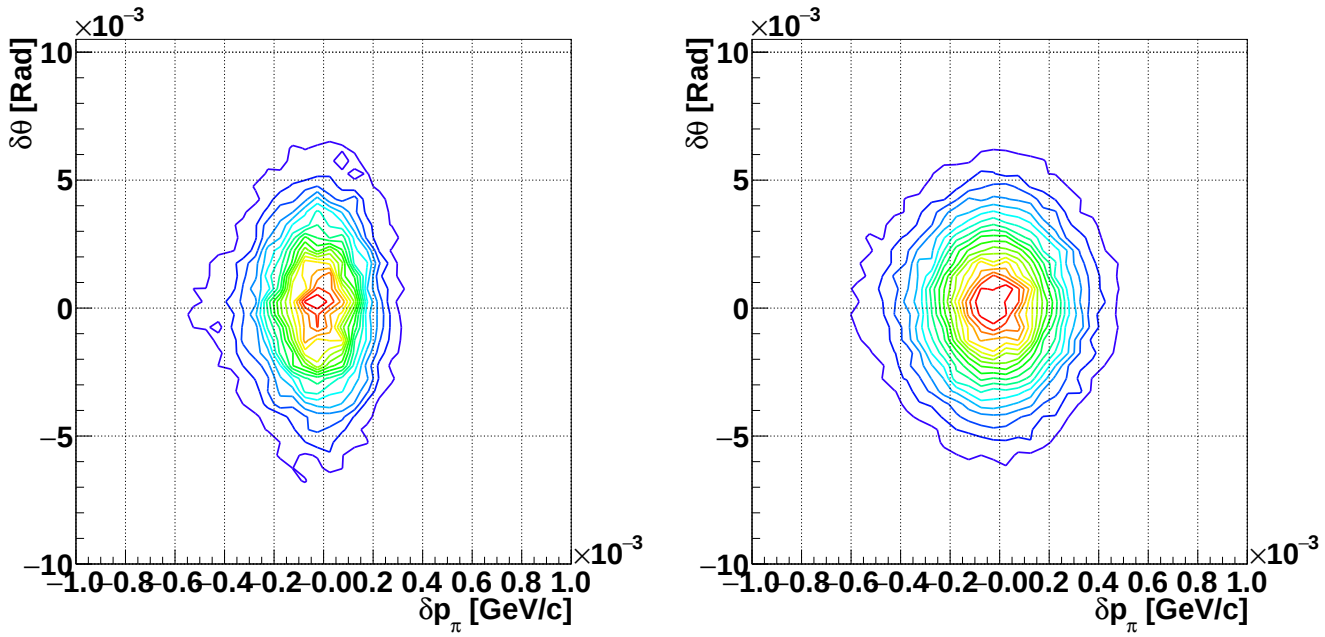

(a) Σ^- (b) Θ^+

Figure A.11.: Contour plot of the error distribution of the beam momentum δp_π and the scattering angle $\delta\theta$.

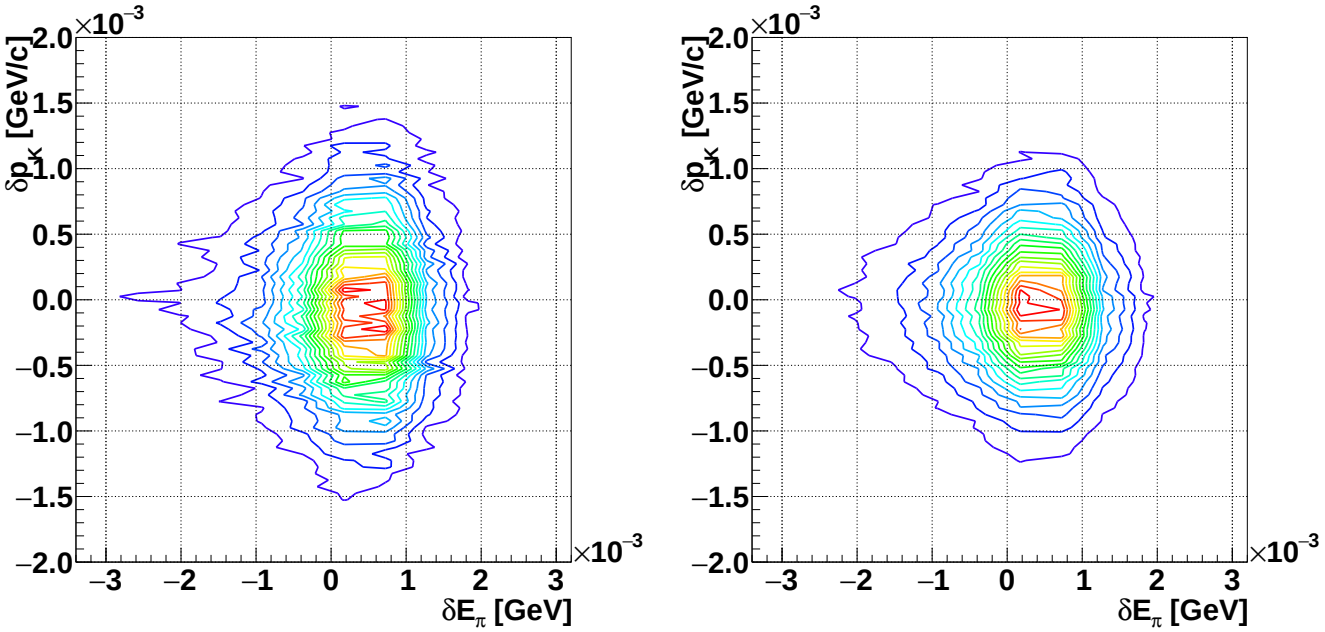

(a) Σ^- (b) Θ^+

Figure A.12.: Contour plot of the error distribution of the scattered kaon momentum δp_K and the energy loss correction of the beam pion δp_π.

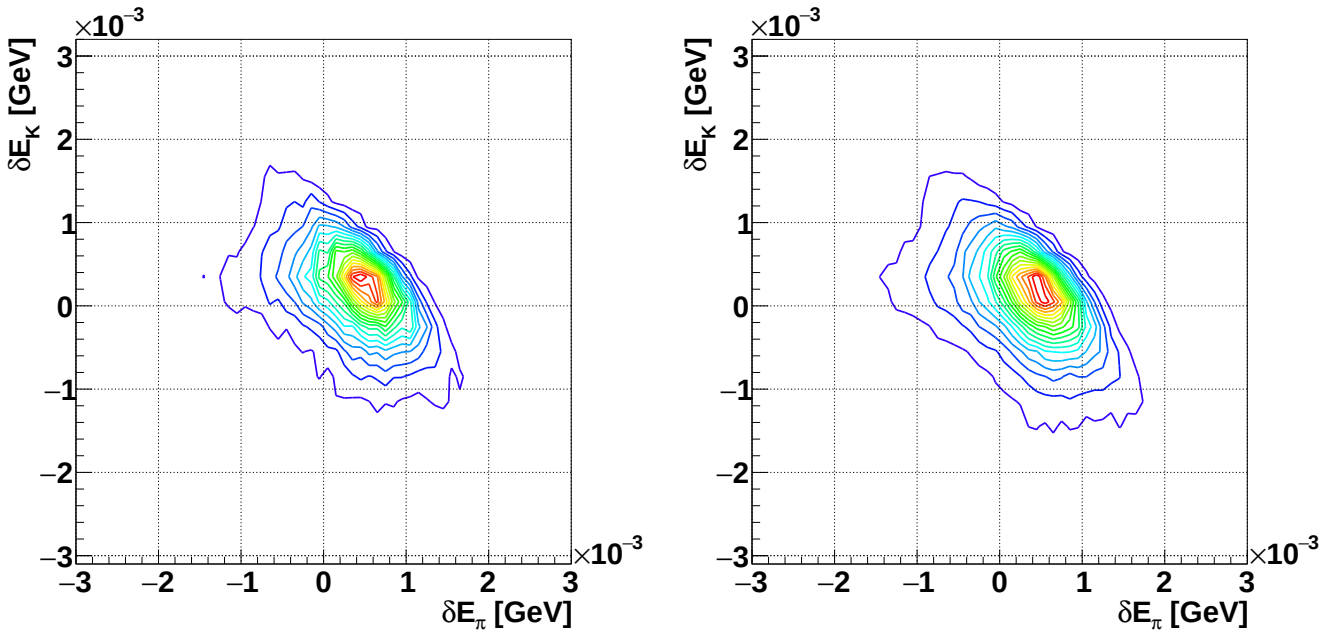

(a) Σ^- (b) Θ^+

Figure A.13.: Contour plot of the error distribution of the energy loss correction of the beam pion δE_π and that of the scattered kaon δE_K.

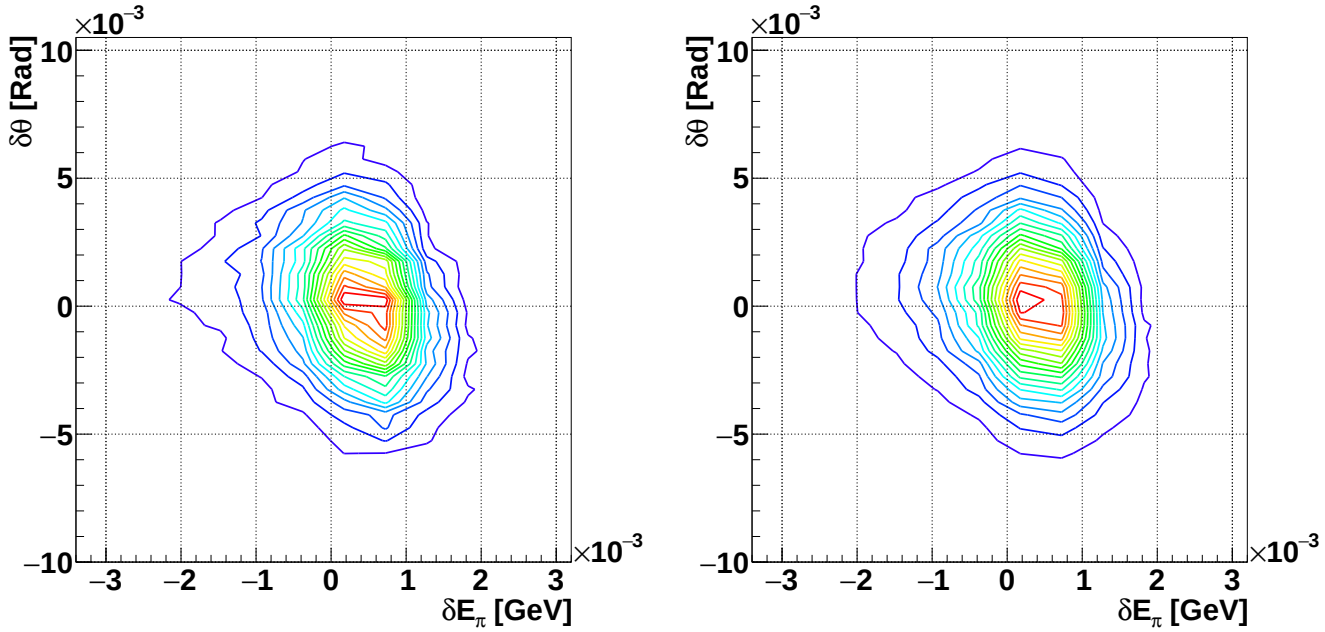

(a) Σ^- (b) Θ^+

Figure A.14.: Contour plot of the error distribution of the scattering angle $\delta\theta$ and the energy loss correction of the beam pion δE_π.

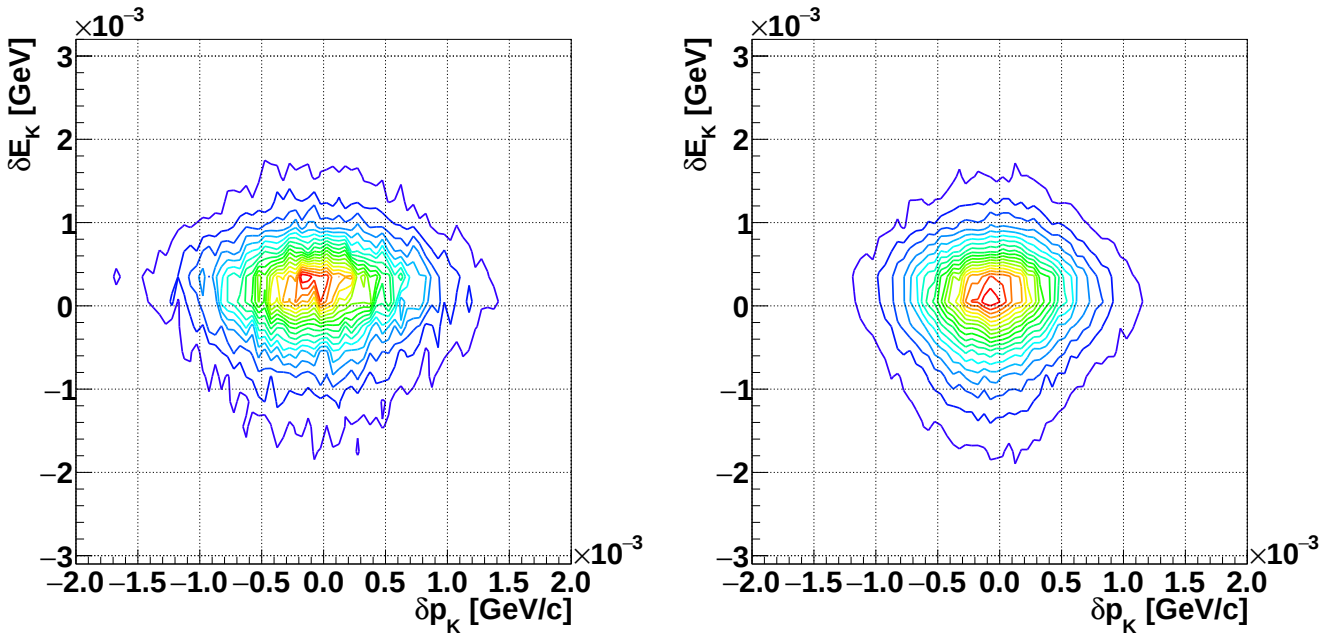

(a) Σ^- (b) Θ^+

Figure A.15.: Contour plot of the error distribution of the scattered kaon momentum δp_K and the energy loss correction of the scattered kaon δE_K.

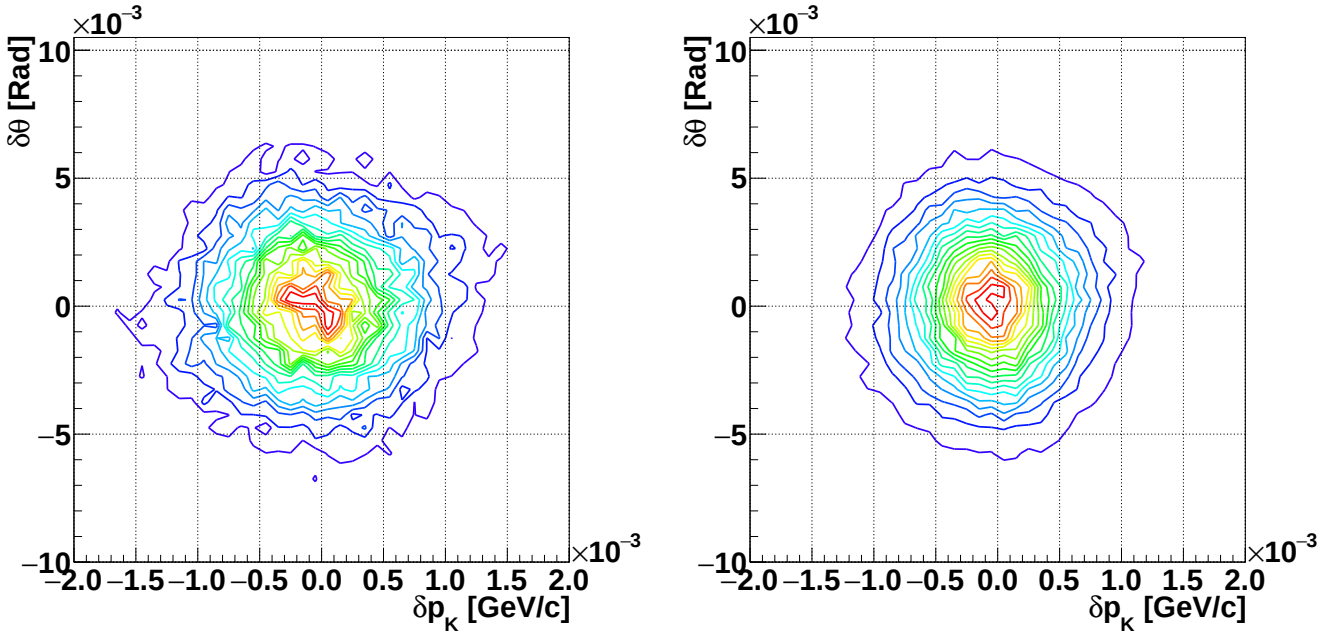

(a) Σ^- (b) Θ^+

Figure A.16.: Contour plot of the error distribution of the scattered kaon momentum δp_K and the scattering angle $\delta\theta$.

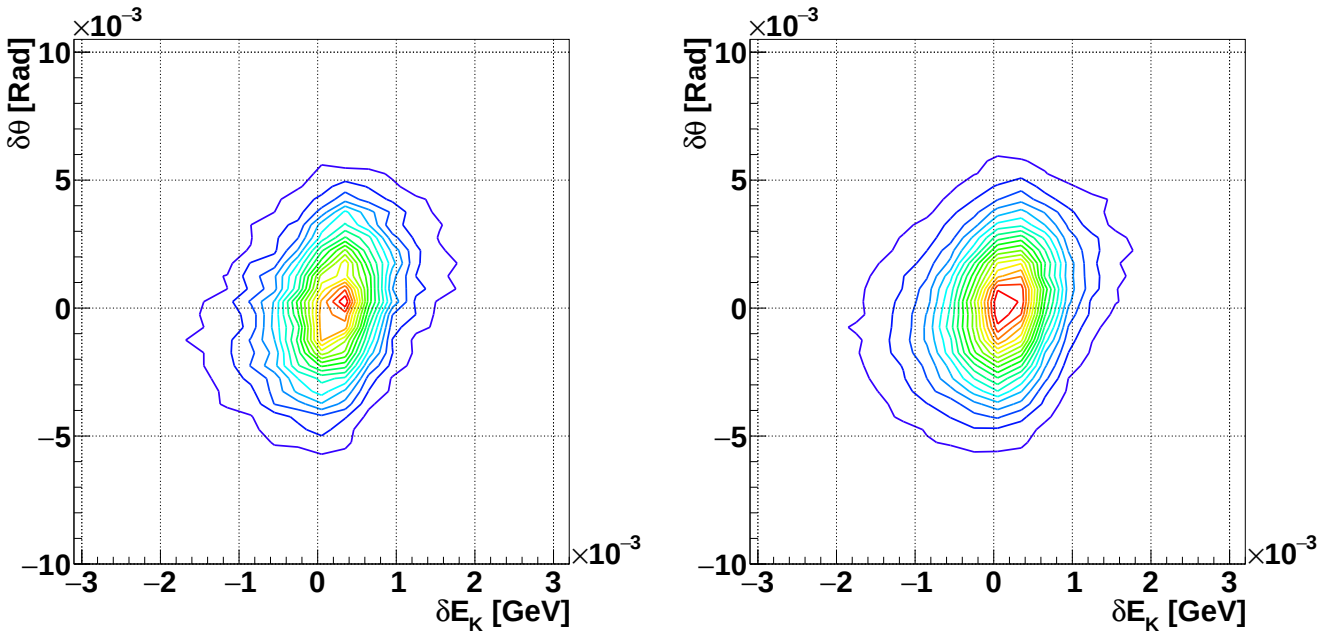

(a) Σ^- (b) Θ^+

Figure A.17.: Contour plot of the error distribution of the scattering angle $\delta\theta$ and the energy loss correction of the scattered kaon δE_K.

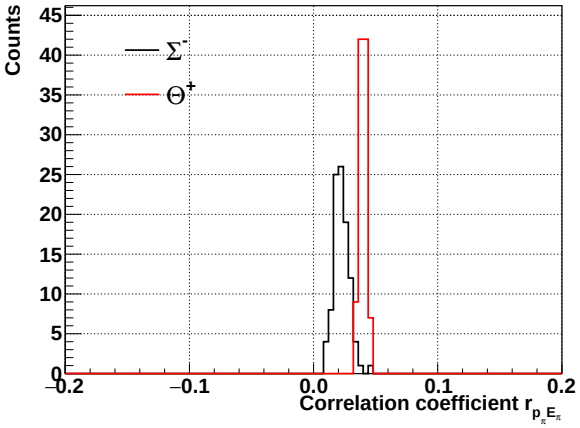

(a) Correlation coefficient

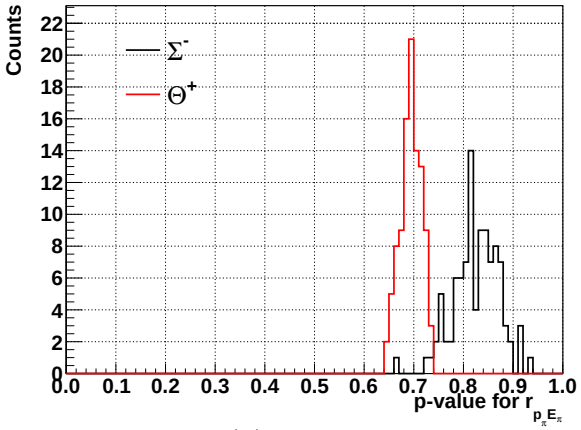

(b) $p-$value

Figure A.18.: Correlation coefficient $r_{\delta p_\pi \delta E_\pi}$ (a) and its $p-$value of $t-$distribution (b).

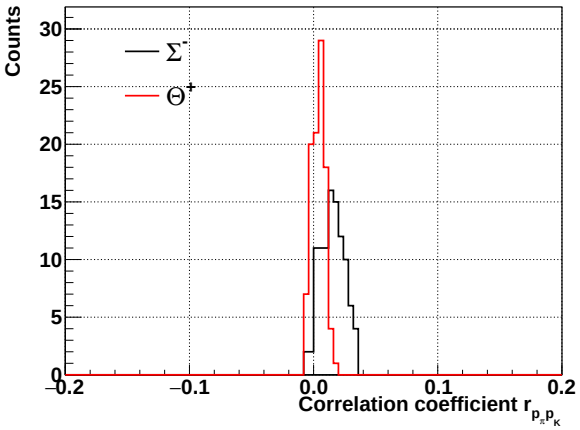

(a) Correlation coefficient

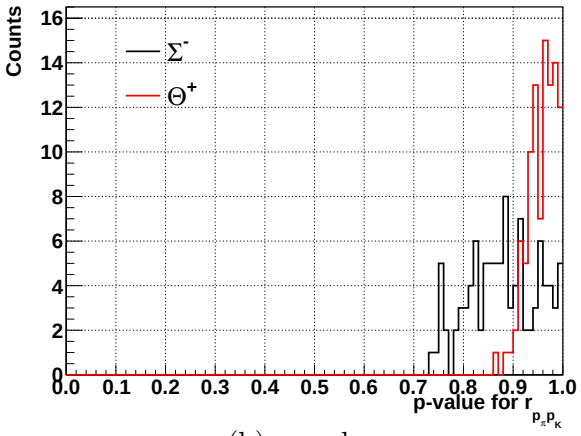

(b) $p-$value

Figure A.19.: Correlation coefficient $r_{\delta p_\pi \delta p_K}$ (a) and its $p-$value of $t-$distribution (b).

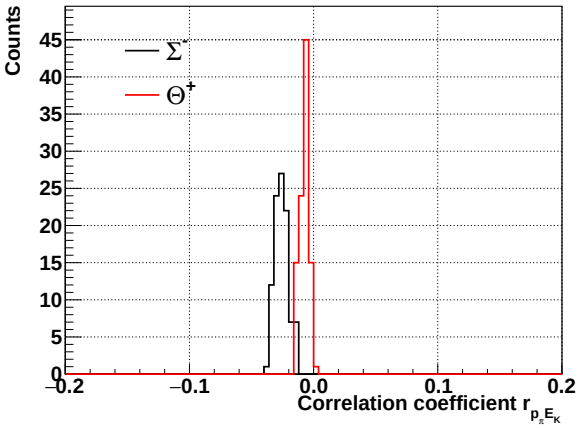

(a) Correlation coefficient

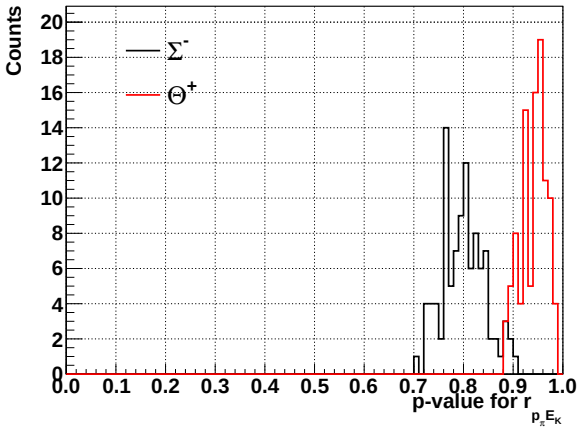

(b) $p-$value

Figure A.20.: Correlation coefficient $r_{\delta p_\pi \delta E_K}$ (a) and its $p-$value of $t-$distribution (b).

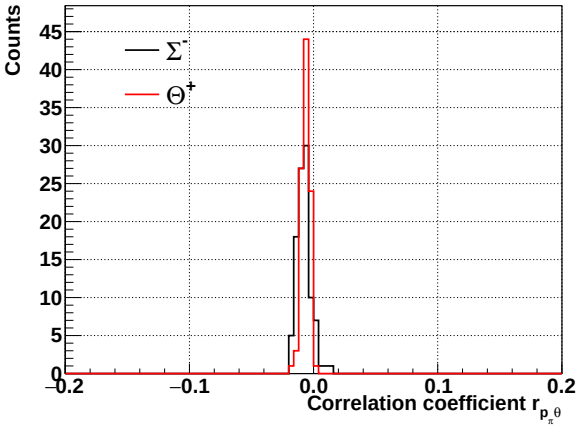

(a) Correlation coefficient

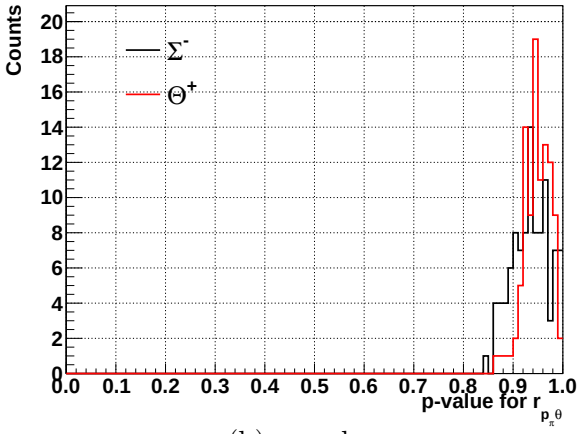

(b) $p-$value

Figure A.21.: Correlation coefficient $r_{\delta p_\pi \delta\theta}$ (a) and its $p-$value of $t-$distribution (b).

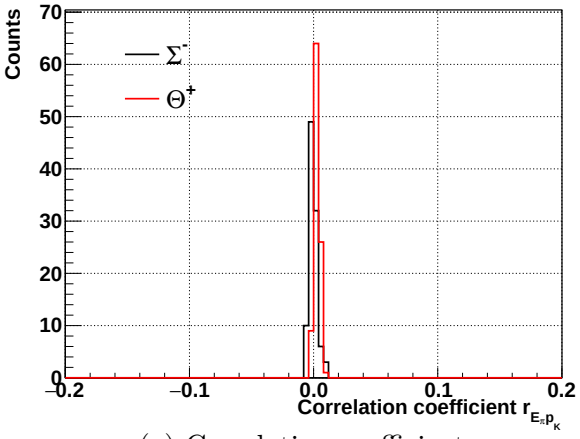

(a) Correlation coefficient

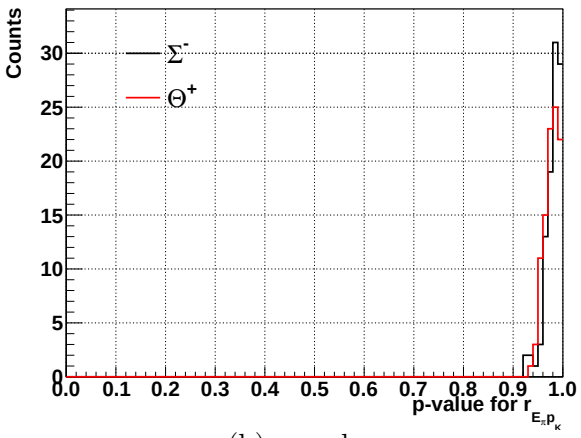

(b) $p-$value

Figure A.22.: Correlation coefficient $r_{\delta E_\pi \delta p_K}$ (a) and its $p-$value of $t-$distribution (b).

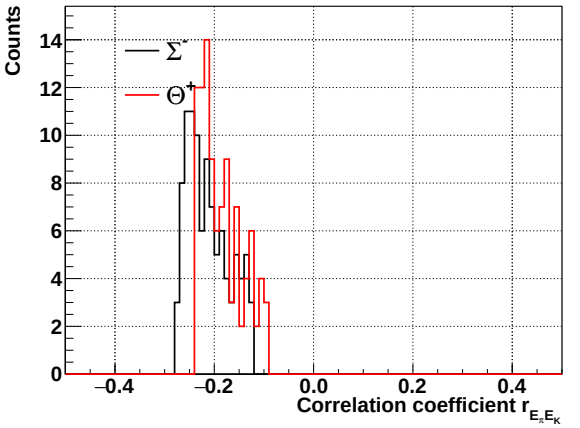

(a) Correlation coefficient

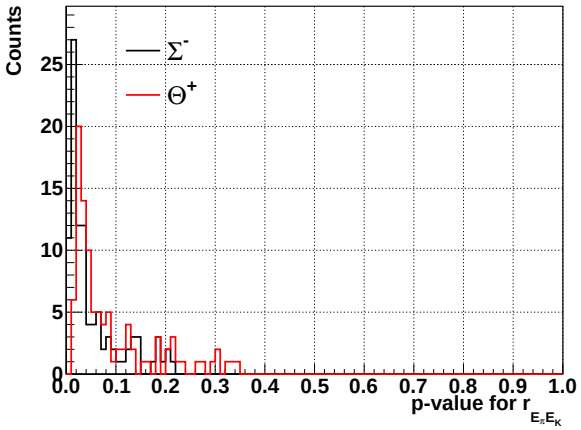

(b) $p-$value

Figure A.23.: Correlation coefficient $r_{\delta E_\pi \delta E_K}$ (a) and its $p-$value of $t-$distribution (b).

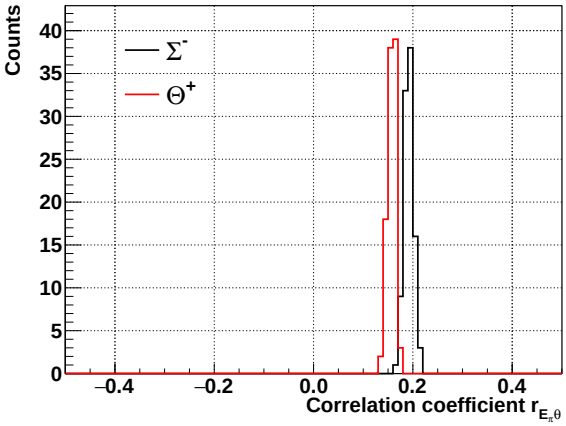

(a) Correlation coefficient

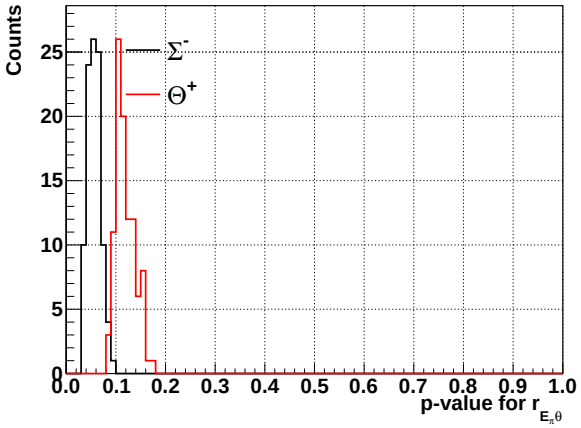

(b) $p-$value

Figure A.24.: Correlation coefficient $r_{\delta E_\pi \delta\theta}$ (a) and its $p-$value of $t-$distribution (b).

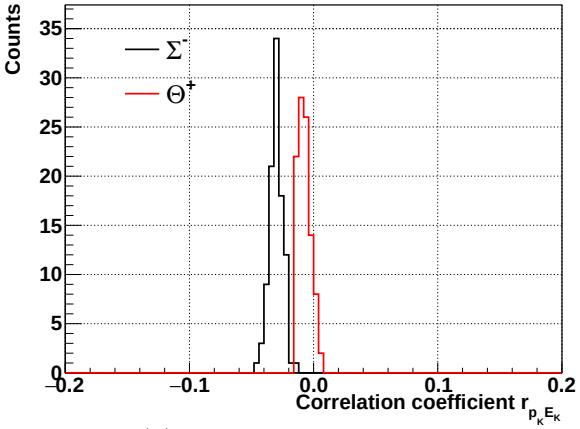

(a) Correlation coefficient

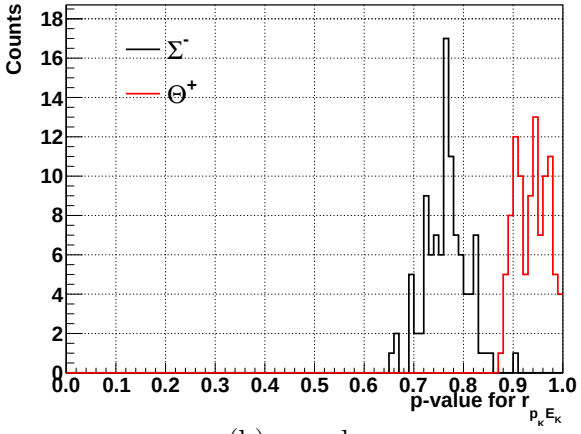

(b) $p-$value

Figure A.25.: Correlation coefficient $r_{\delta p_K \delta E_K}$ (a) and its $p-$value of $t-$distribution (b).

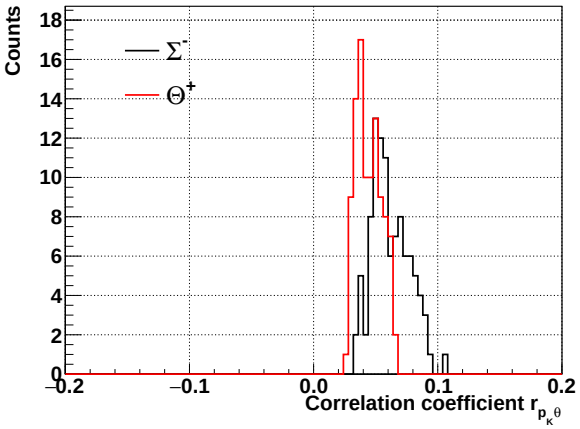

(a) Correlation coefficient

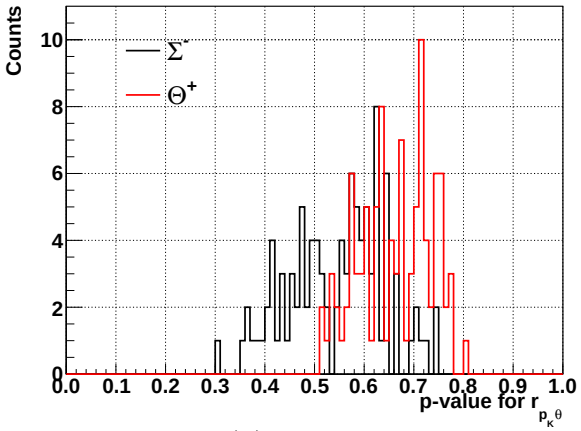

(b) $p-$value

Figure A.26.: Correlation coefficient $r_{\delta p_K \delta\theta}$ (a) and its $p-$value of $t-$distribution (b).

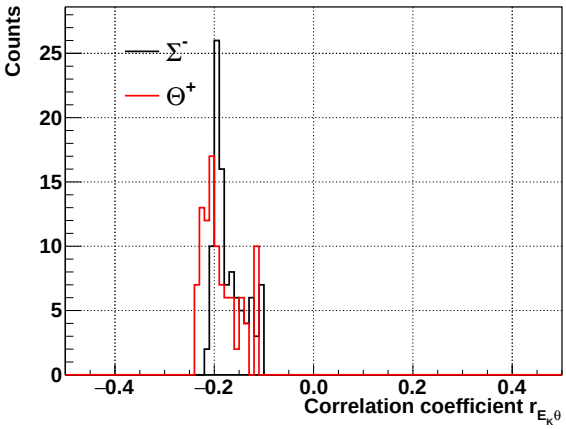

(a) Correlation coefficient

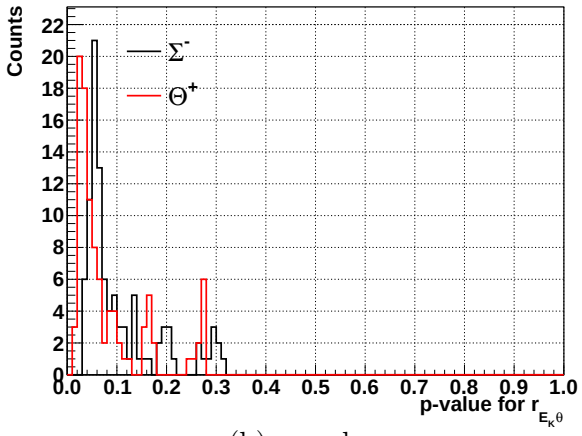

(b) $p-$value

Figure A.27.: Correlation coefficient $r_{\delta E_K \delta\theta}$ (a) and its $p-$value of $t-$distribution (b).

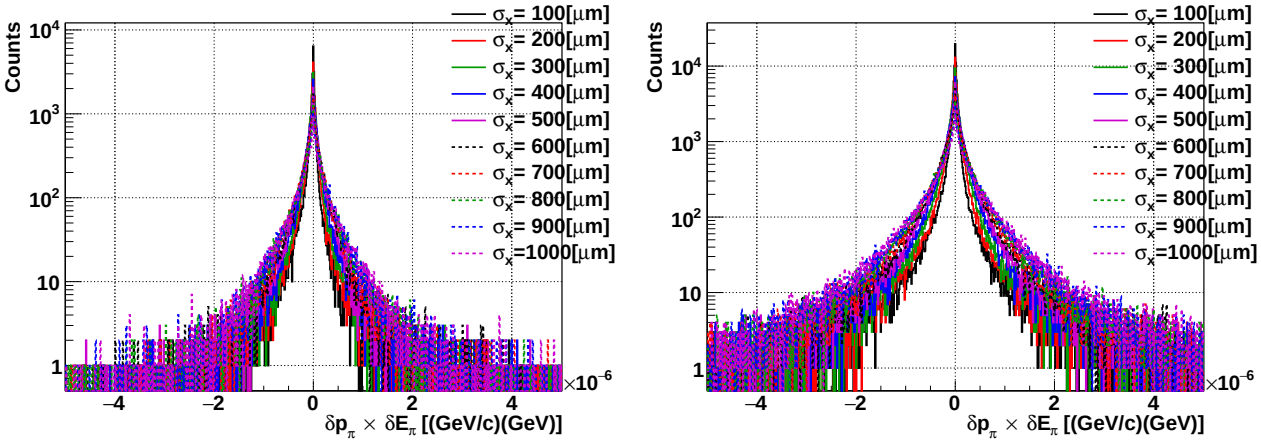

(a) Σ^- (b) Θ^+

Figure A.28.: Product of the deviations δp_π and δE_π.

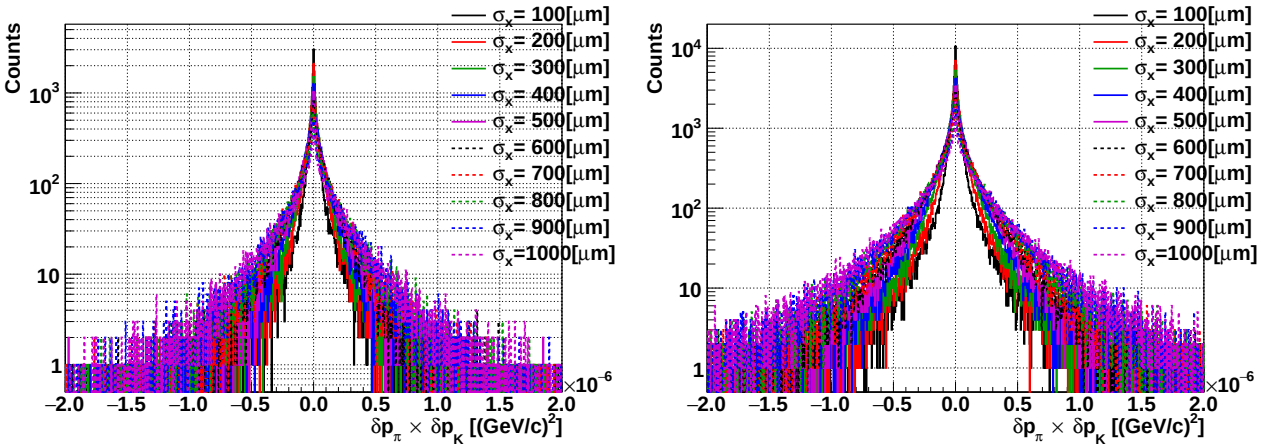

(a) Σ^- (b) Θ^+

Figure A.29.: Product of the deviations δp_π and δp_K.

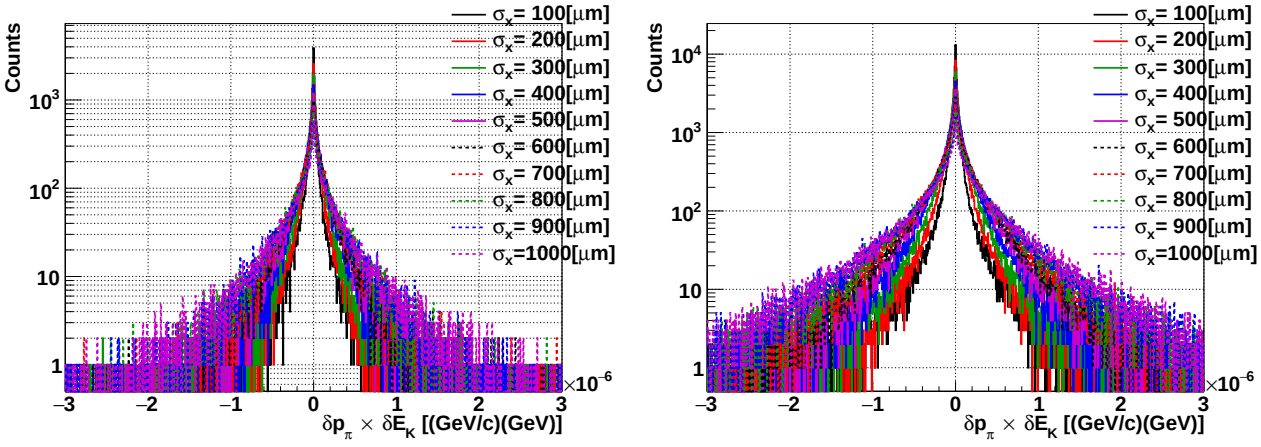

(a) Σ^- (b) Θ^+

Figure A.30.: Product of the deviations δp_π and δE_K.

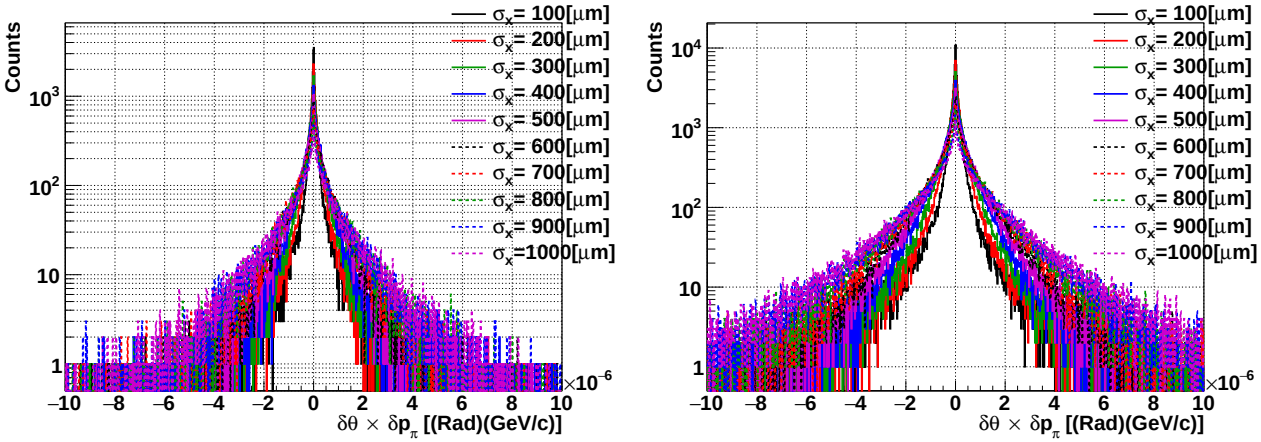

(a) Σ^- (b) Θ^+

Figure A.31.: Product of the deviations δp_π and $\delta\theta$.

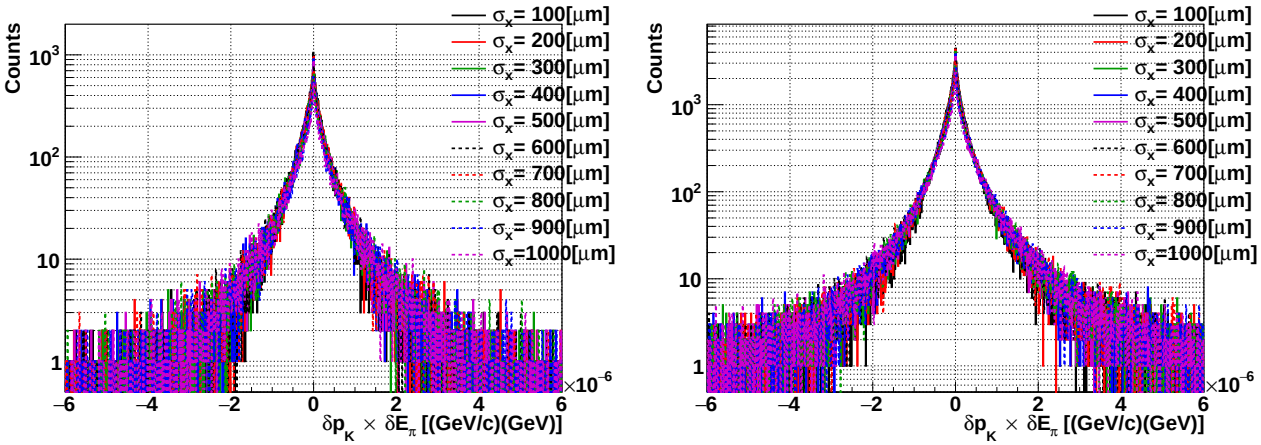

(a) Σ^- (b) Θ^+

Figure A.32.: Product of the deviations δE_π and δp_K.

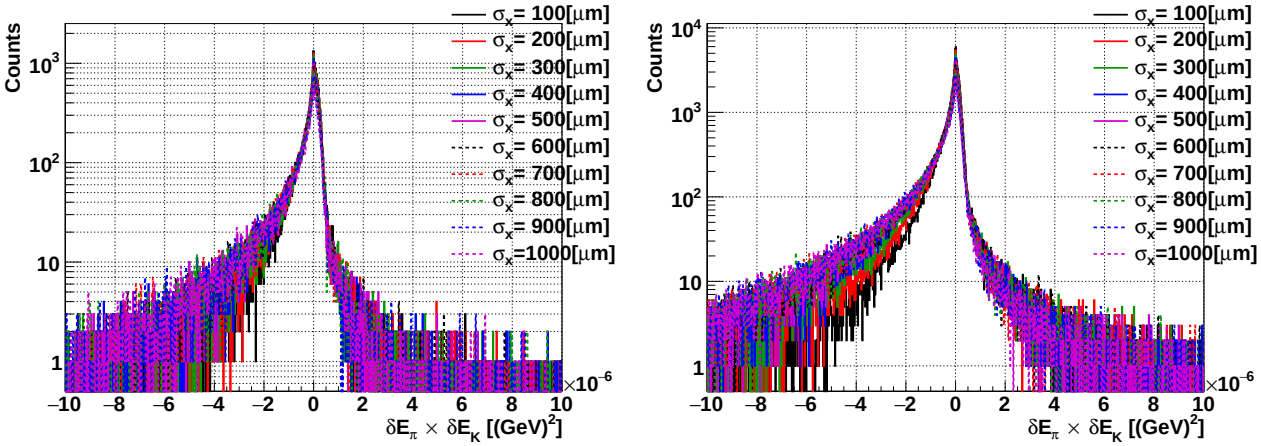

(a) Σ^- (b) Θ^+

Figure A.33.: Product of the deviations δE_π and δE_K.

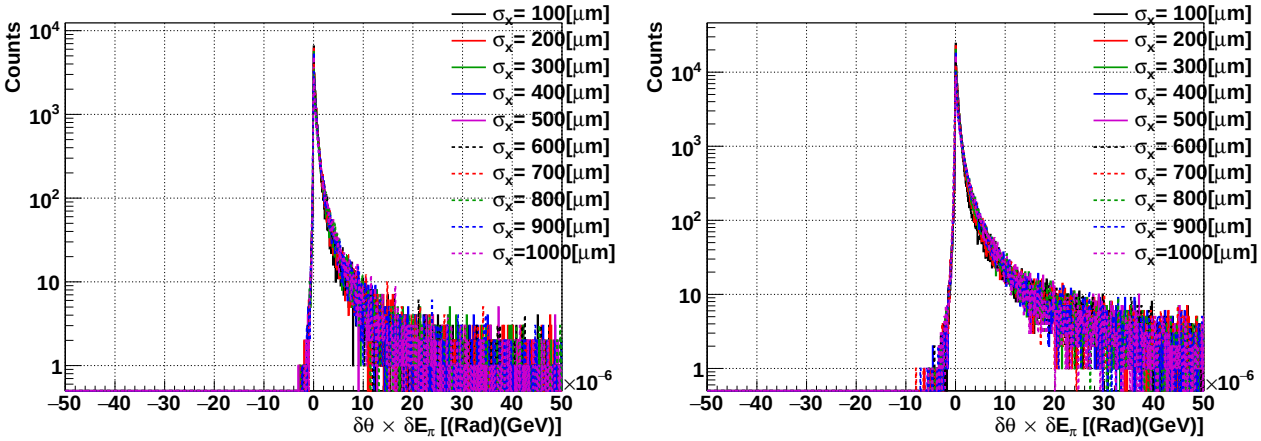

(a) Σ^- (b) Θ^+

Figure A.34.: Product of the deviations δE_π and $\delta\theta$.

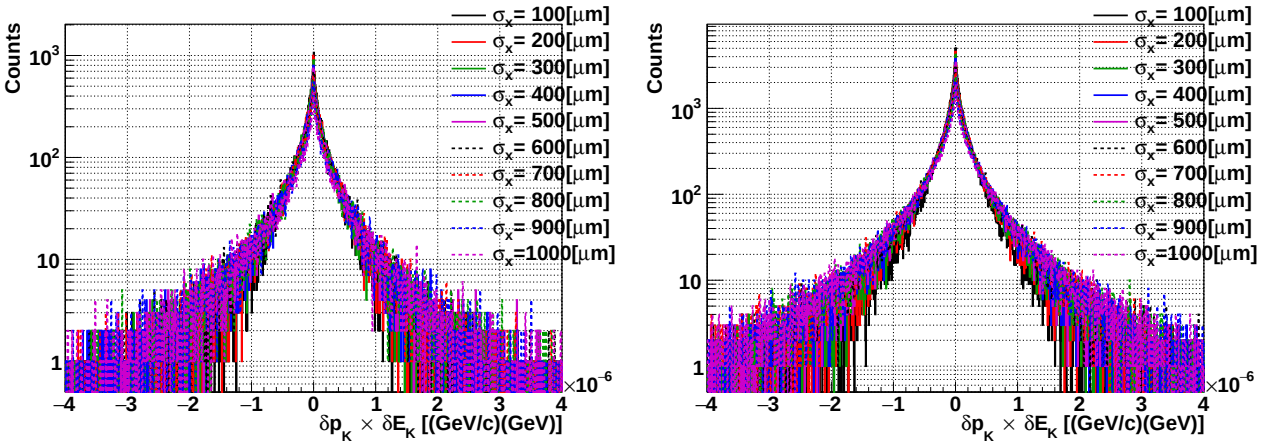

(a) Σ^- (b) Θ^+

Figure A.35.: Product of the deviations δp_K and δE_K.

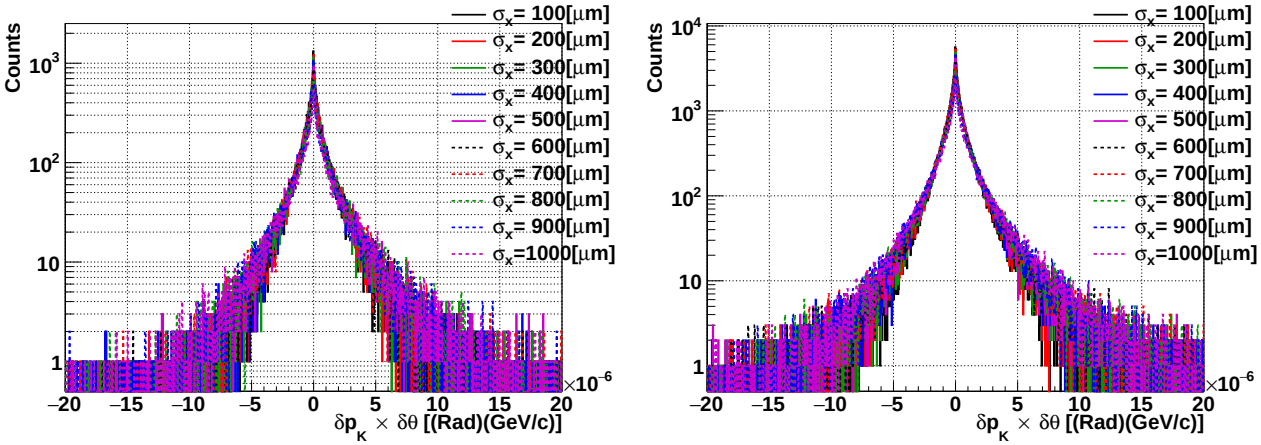

(a) Σ^- (b) Θ^+

Figure A.36.: Product of the deviations δp_K and $\delta\theta$.

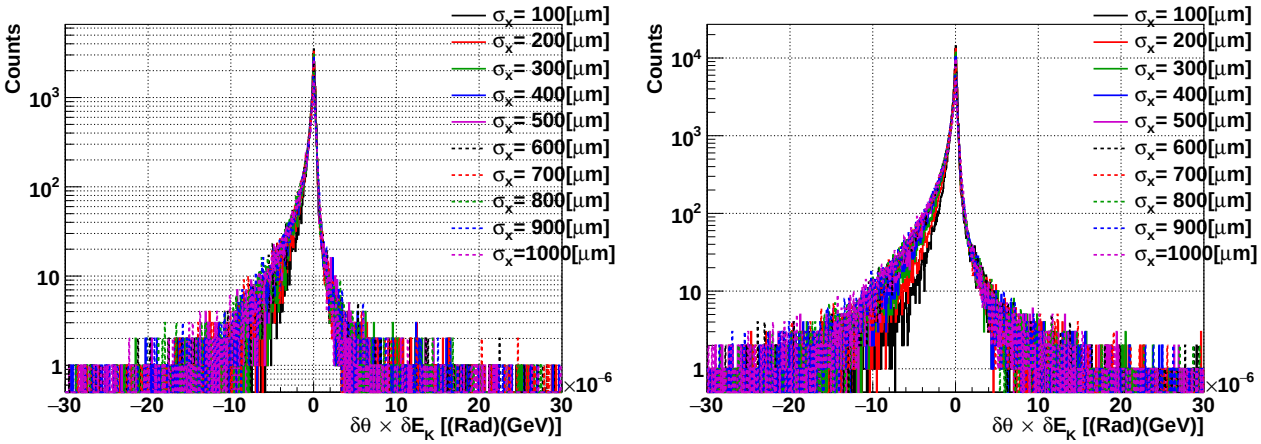

(a) Σ^- (b) Θ^+

Figure A.37.: Product of the deviations δE_K and $\delta\theta$.

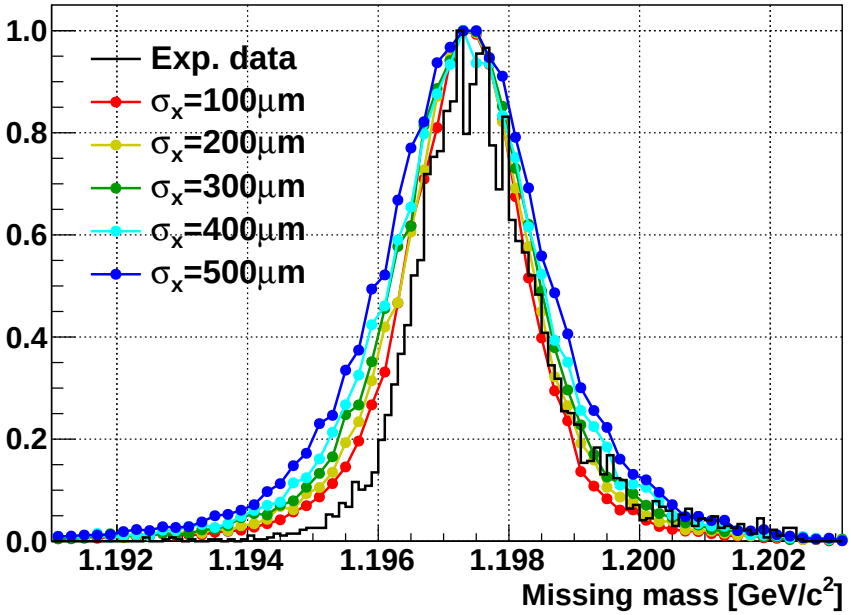

Figure A.38.: Missing mass spectra of the simulation study (colored curves) for Σ^-. The results of the present experiment is also shown as the black histogram. Among 100 data set of the simulation results, 5 data set are shown as examples.

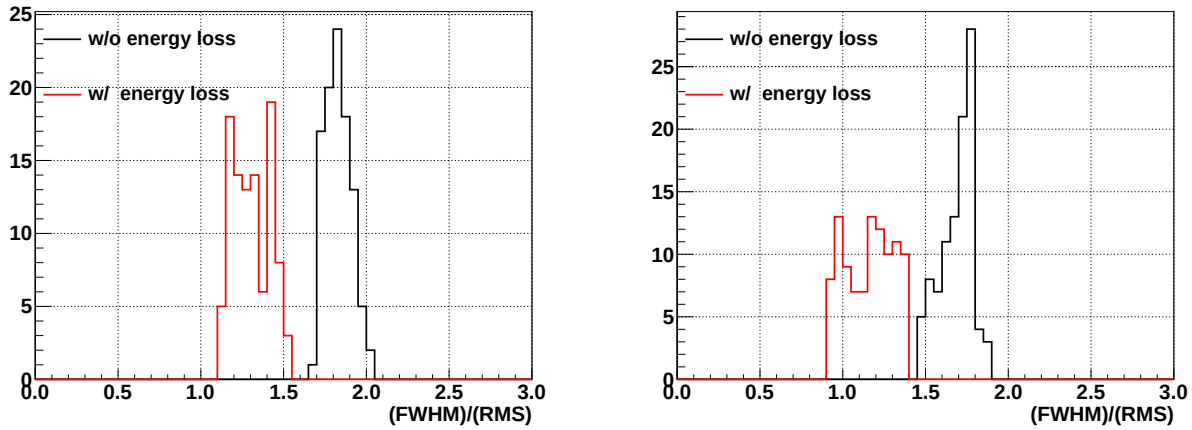

(a) Σ^- (b) Θ^+

Figure A.39.: Scale factor from RMS to FWHM obtained by the simulation. (Black) Without energy loss. (Red) With energy loss.

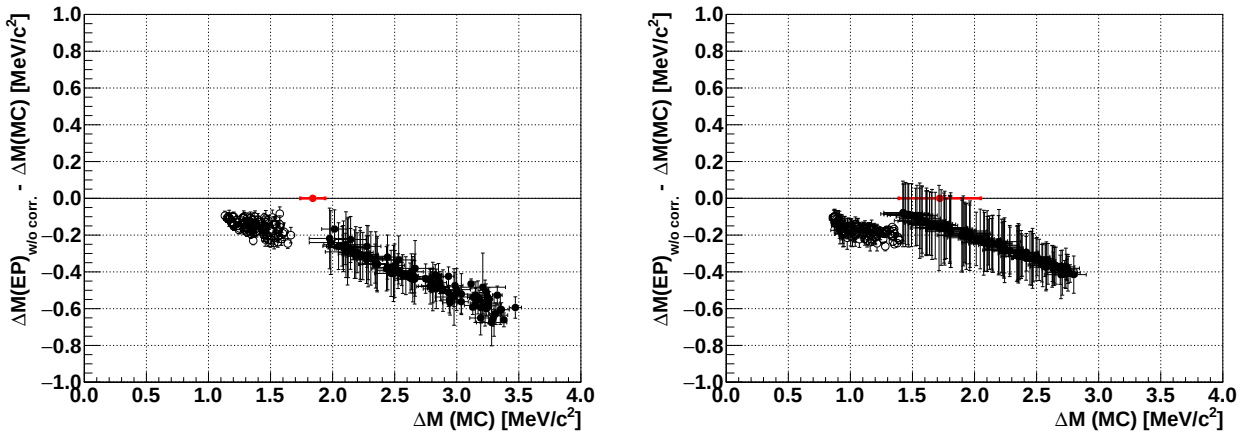

(a) Σ^- (b) Θ^+

Figure A.40.: Difference of the missing mass resolution (FWHM) between the width of the Monte Carlo result (MC) and the estimation by the error propagation (EP) without correlation terms. (Open circles) : Without energy loss. (Filled circles) : With energy loss. The mass resolution for the experimental data is also shown as a red point. The error bar of the experimental data represents the sum of the statistic and systematic ones.

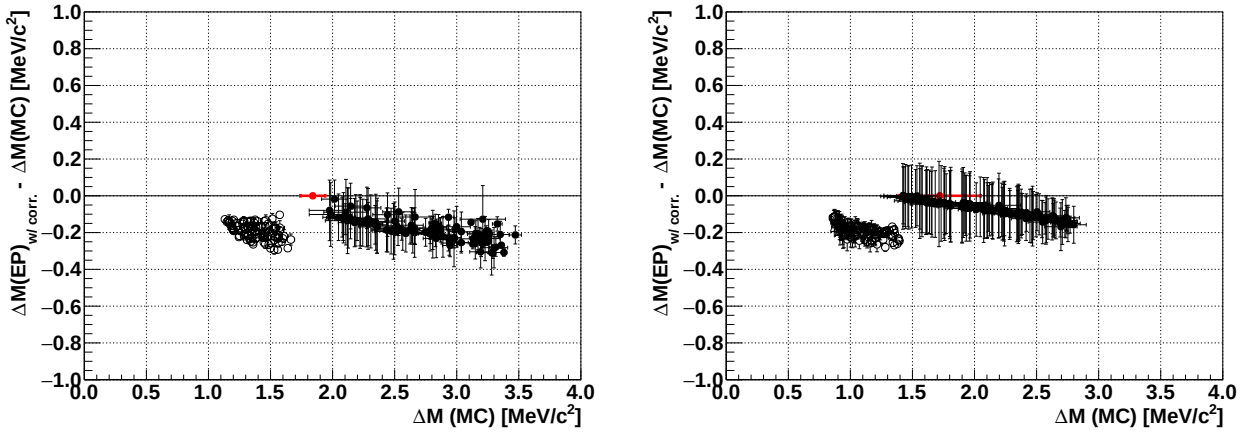

(a) Σ^- (b) Θ^+

Figure A.41.: Difference of the missing mass resolution (FWHM) between the width of the Monte Carlo result (MC) and the estimation by the error propagation (EP) with correlation terms. (Open circles) : Without energy loss. (Filled circles) : With energy loss. The mass resolution for the experimental data is also shown as a red point. The error bar of the experimental data represents the sum of the statistic and systematic ones.

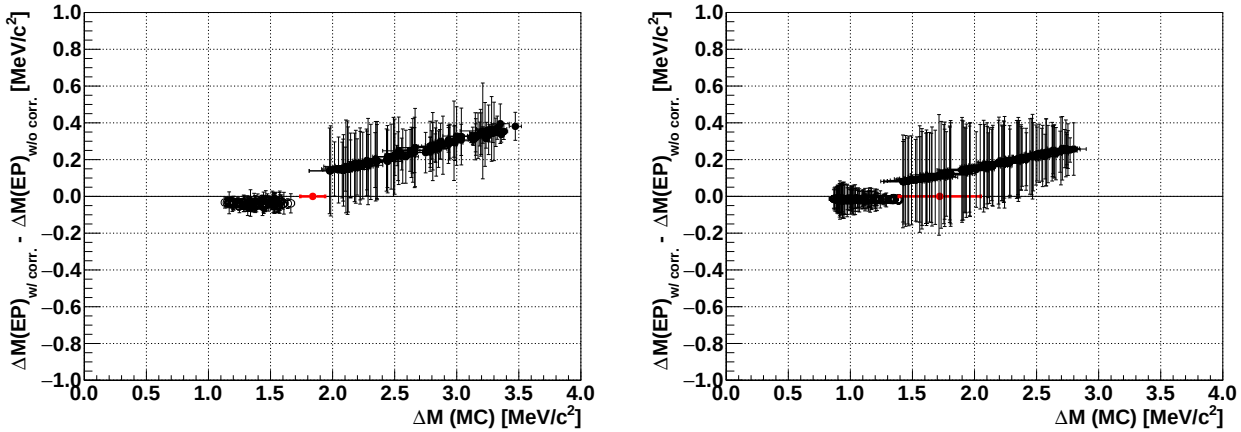

(a) Σ^- (b) Θ^+

Figure A.42.: Comparison between the missing mass resolution estimated with correlation and without correlation. (Open circles) : Without energy loss. (Filled circles) : With energy loss. The mass resolution for the experimental data is also shown as a red point. The error bar of the experimental data represents the sum of the statistic and systematic ones.

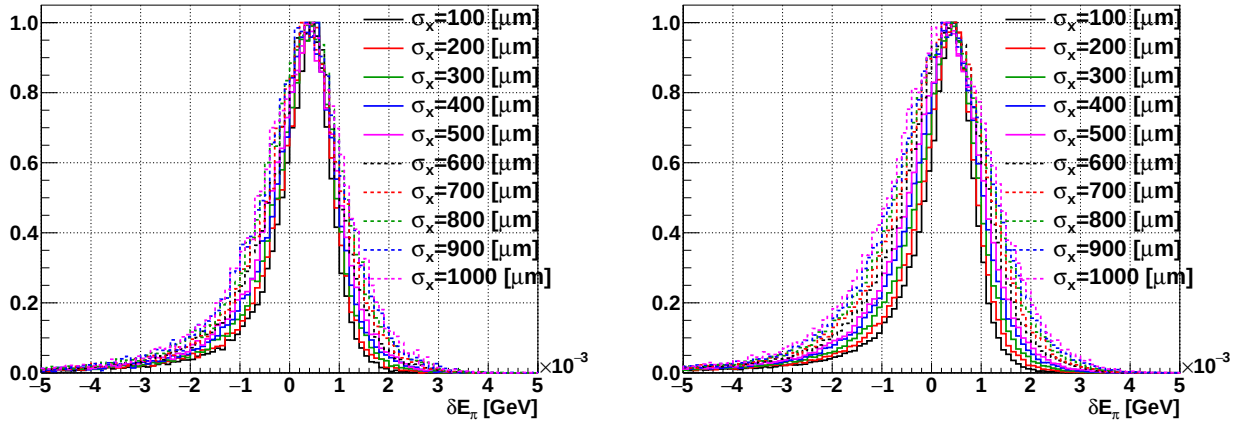

(a) Σ^- (b) Θ^+

Figure A.43.: Deviation distribution of the energy loss correction for the beam pion δE_π (for the case of $\mathrm{cov}(\delta p_\pi, \delta E_\pi) \neq 0$ and $\mathrm{cov}(\delta p_K, \delta E_K) \neq 0$ by definition).

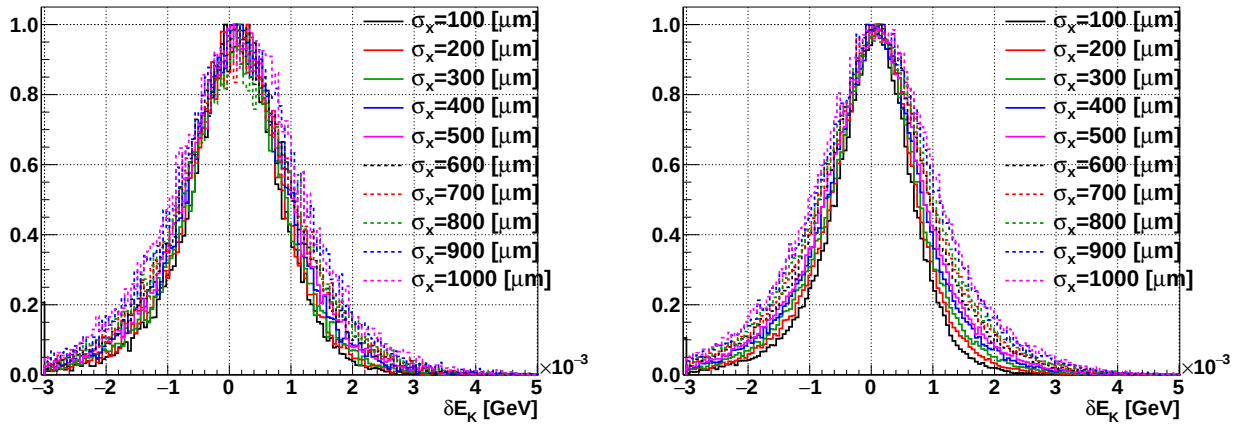

(a) Σ^- (b) Θ^+

Figure A.44.: Deviation distribution of the energy loss correction for the scattered kaon δE_K (for the case of $\mathrm{cov}(\delta p_\pi, \delta E_\pi) \neq 0$ and $\mathrm{cov}(\delta p_K, \delta E_K) \neq 0$ by definition).

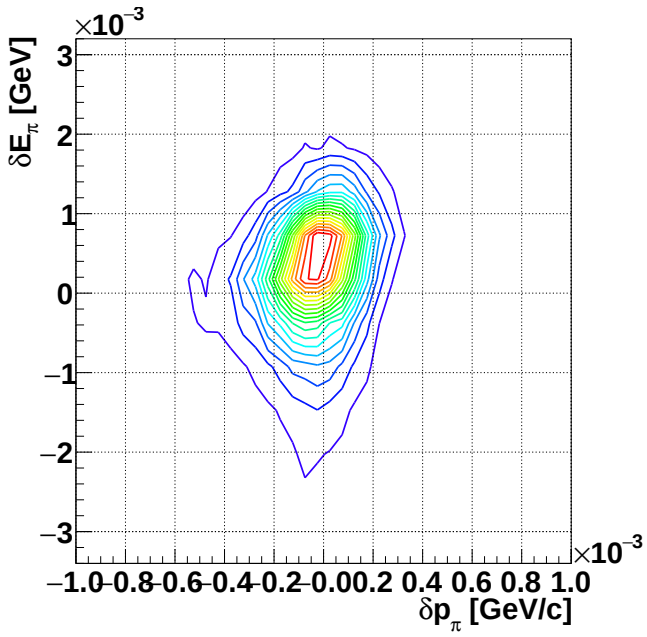

(a) Σ^-

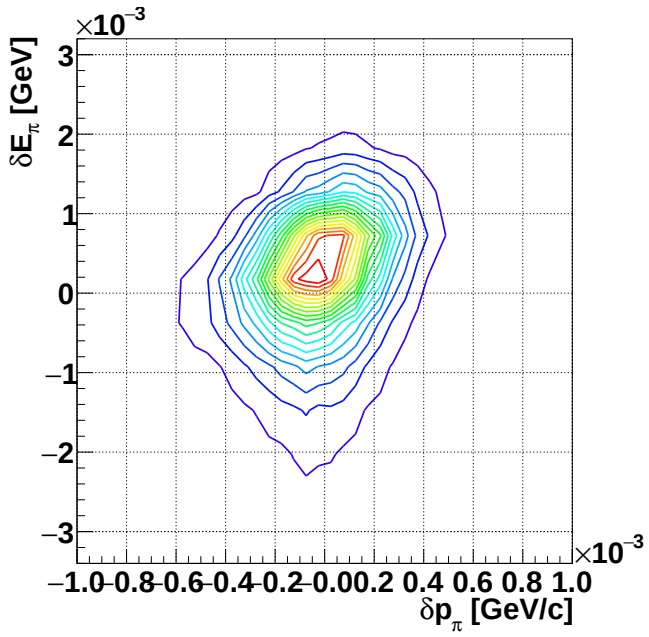

(b) Θ^+

Figure A.45.: Contour plot of the error distribution of the beam momentum δp_π and the energy correction for the beam δE_π (for the case of $\mathrm{cov}(\delta p_\pi, \delta E_\pi) \neq 0$ and $\mathrm{cov}(\delta p_K, \delta E_K) \neq 0$ by definition).

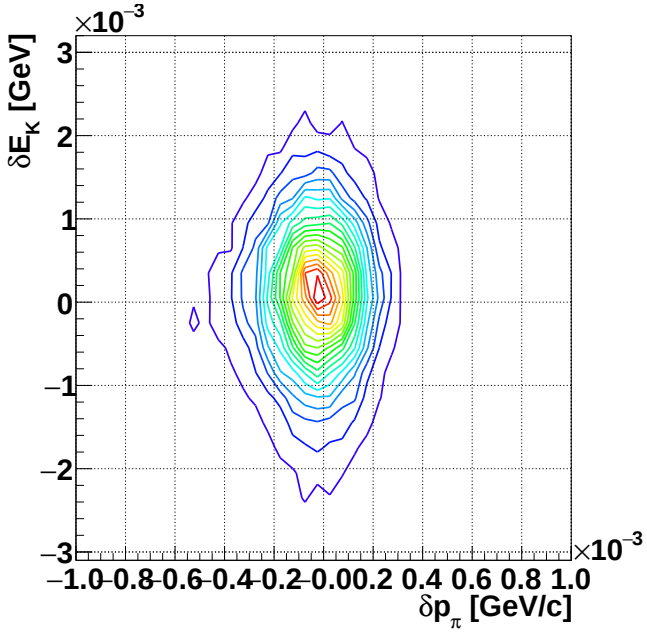

(a) Σ^-

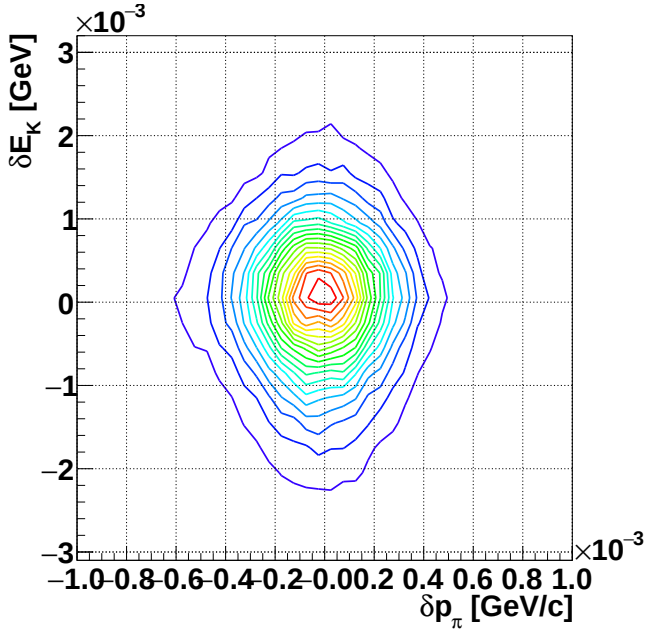

(b) Θ^+

Figure A.46.: Contour plot of the error distribution of the beam momentum δp_π and the energy loss correction for the scattered kaon δE_K (for the case of $\mathrm{cov}(\delta p_\pi, \delta E_\pi) \neq 0$ and $\mathrm{cov}(\delta p_K, \delta E_K) \neq 0$ by definition).

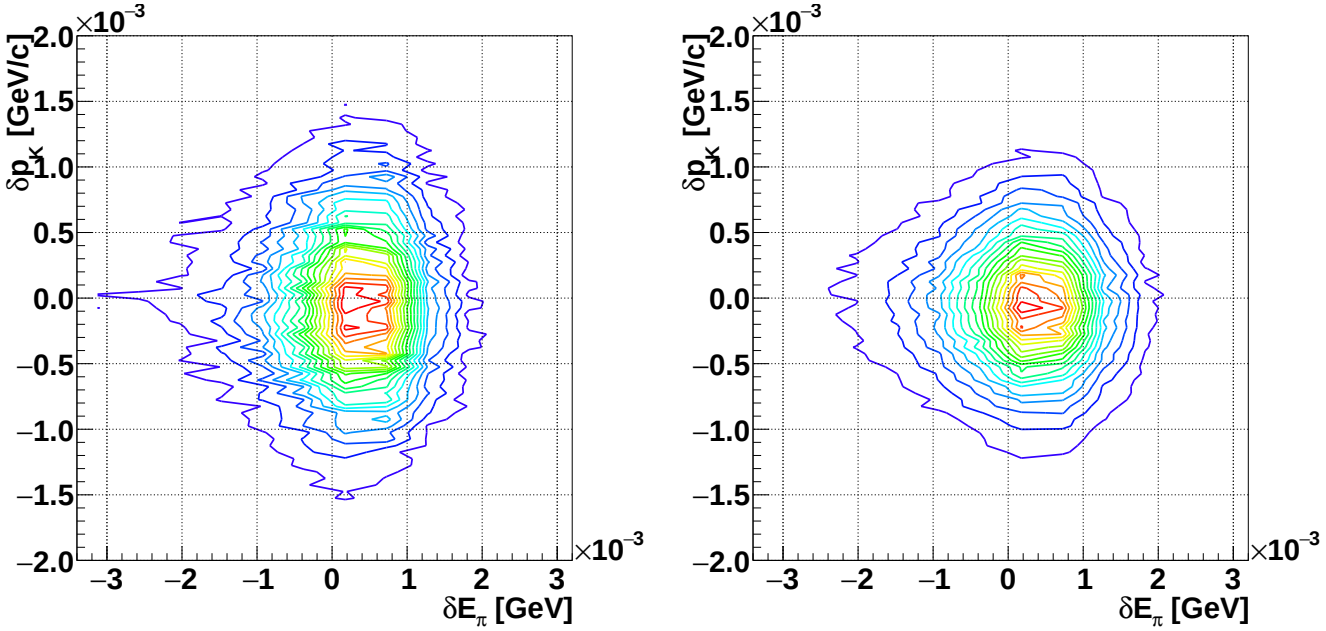

(a) Σ^- (b) Θ^+

Figure A.47.: Contour plot of the error distribution of the scattered kaon momentum δp_K and the energy loss correction of the beam pion δp_π (for the case of $\mathrm{cov}(\delta p_\pi, \delta E_\pi) \neq 0$ and $\mathrm{cov}(\delta p_K, \delta E_K) \neq 0$ by definition).

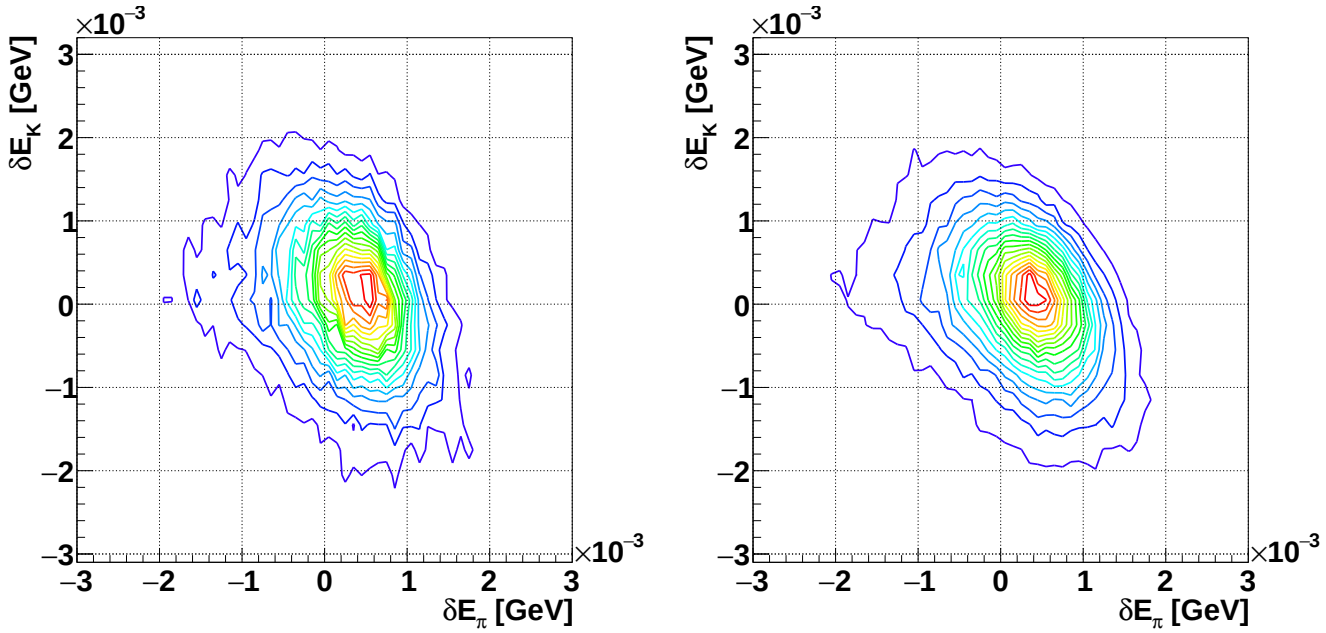

(a) Σ^- (b) Θ^+

Figure A.48.: Contour plot of the error distribution of the energy loss correction of the beam pion δE_π and that of the scattered kaon δE_K (for the case of $\mathrm{cov}(\delta p_\pi, \delta E_\pi) \neq 0$ and $\mathrm{cov}(\delta p_K, \delta E_K) \neq 0$ by definition).

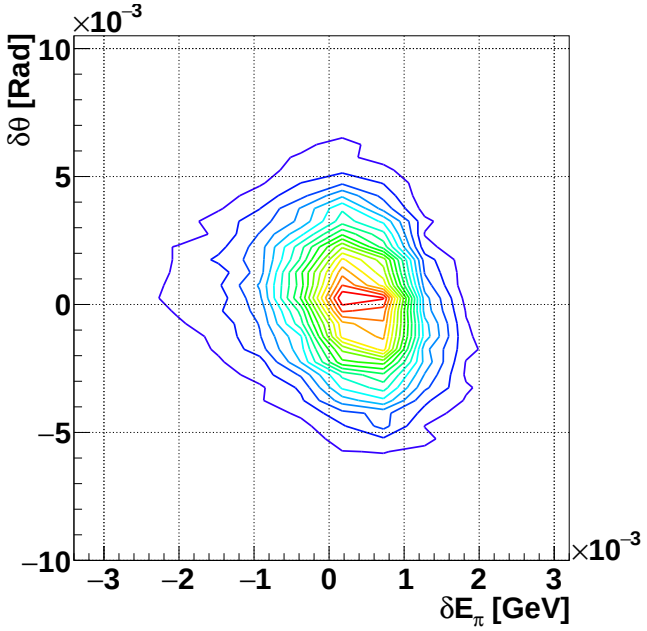

(a) Σ^-

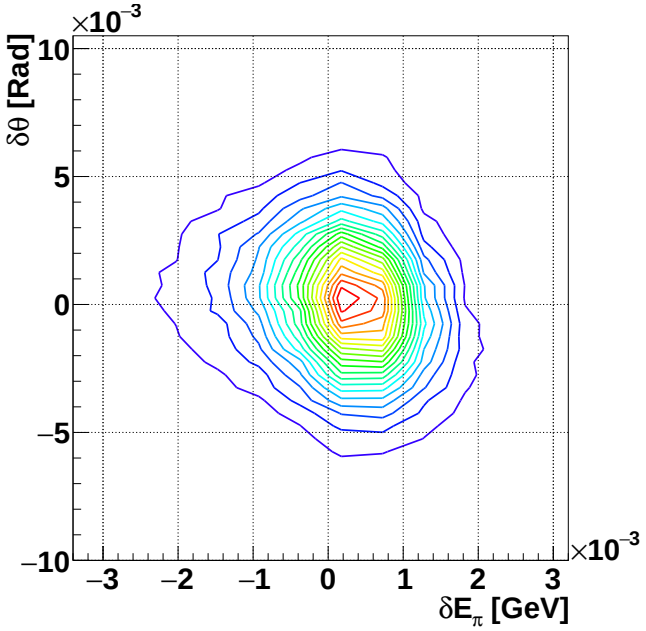

(b) Θ^+

Figure A.49.: Contour plot of the error distribution of the scattering angle $\delta\theta$ and the energy loss correction of the beam pion δE_π (for the case of $\mathrm{cov}(\delta p_\pi, \delta E_\pi) \neq 0$ and $\mathrm{cov}(\delta p_K, \delta E_K) \neq 0$ by definition).

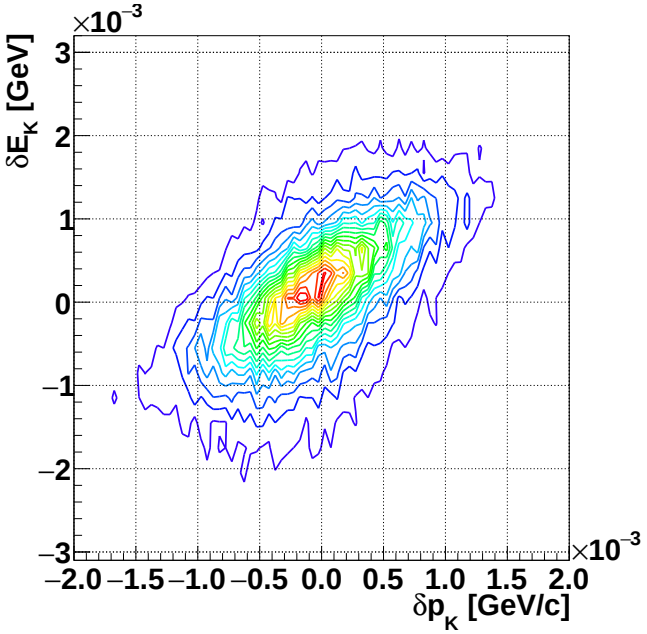

(a) Σ^-

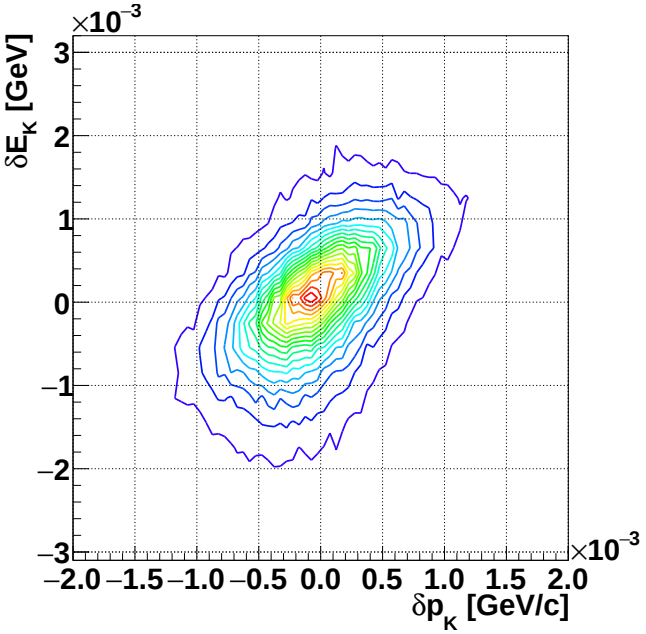

(b) Θ^+

Figure A.50.: Contour plot of the error distribution of the scattered kaon momentum δp_K and the energy loss correction of the scattered kaon δE_K (for the case of $\mathrm{cov}(\delta p_\pi, \delta E_\pi) \neq 0$ and $\mathrm{cov}(\delta p_K, \delta E_K) \neq 0$ by definition).

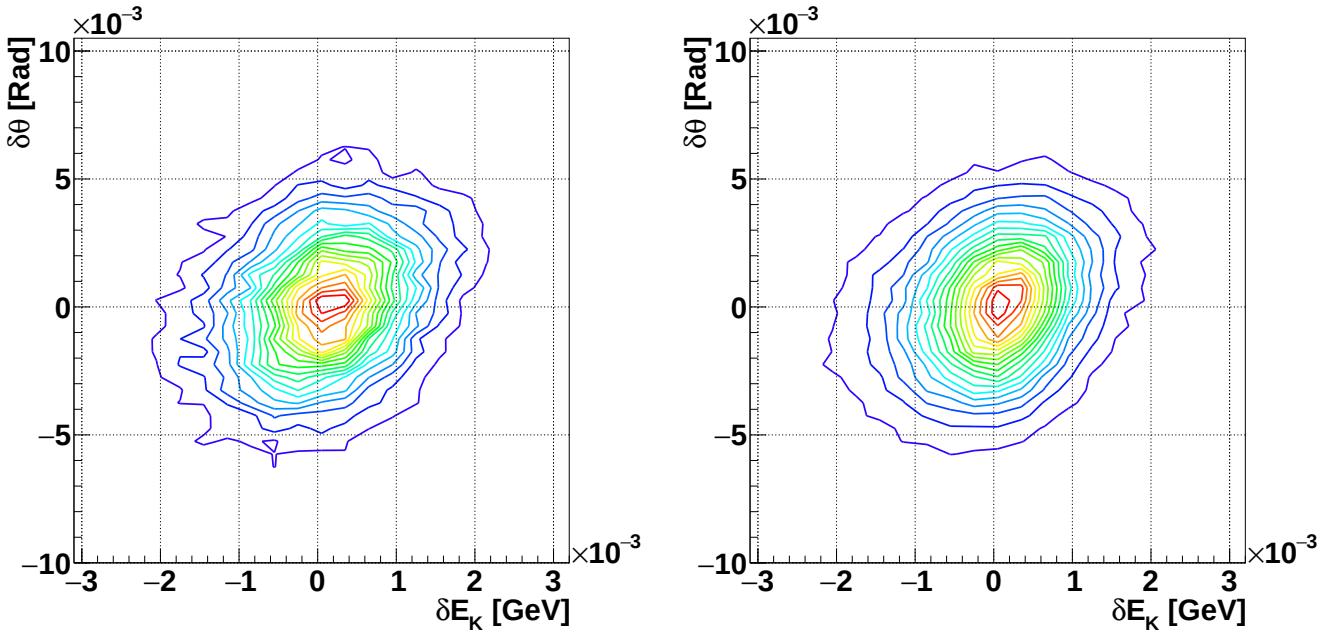

(a) Σ^- (b) Θ^+

Figure A.51.: Contour plot of the error distribution of the scattering angle $\delta\theta$ and the energy loss correction of the scattered kaon δE_K (for the case of $\mathrm{cov}(\delta p_\pi, \delta E_\pi) \neq 0$ and $\mathrm{cov}(\delta p_K, \delta E_K) \neq 0$ by definition).

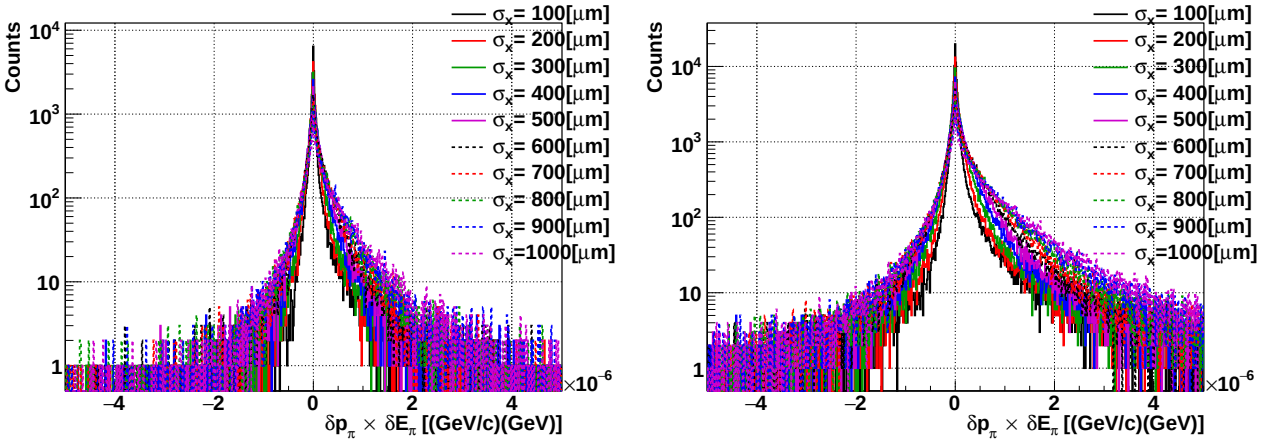

(a) Σ^- (b) Θ^+

Figure A.52.: Product of the deviations δp_π and δE_π (for the case of $\mathrm{cov}(\delta p_\pi, \delta E_\pi) \neq 0$ and $\mathrm{cov}(\delta p_K, \delta E_K) \neq 0$ by definition).

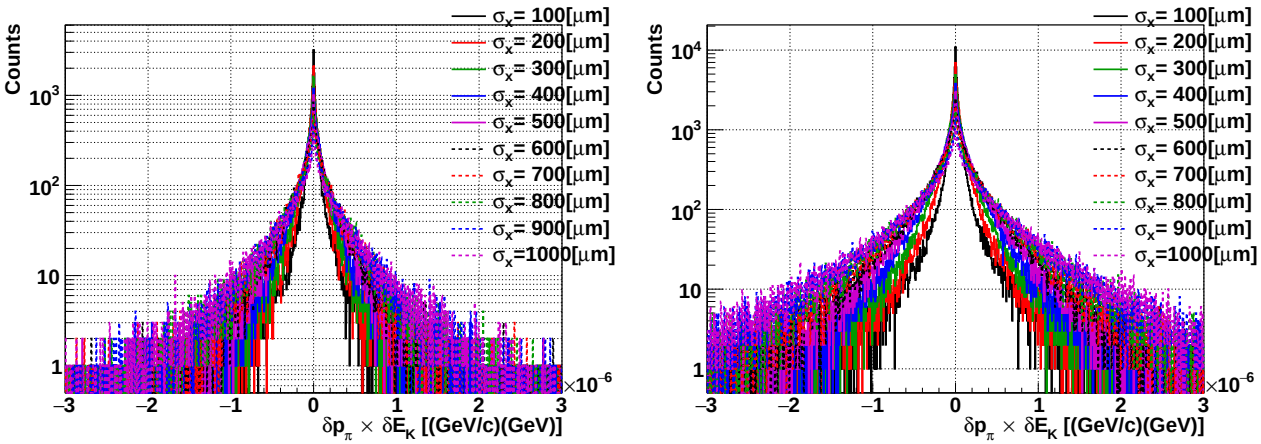

(a) Σ^- (b) Θ^+

Figure A.53.: Product of the deviations δp_π and δE_K (for the case of $\mathrm{cov}(\delta p_\pi, \delta E_\pi) \neq 0$ and $\mathrm{cov}(\delta p_K, \delta E_K) \neq 0$ by definition).

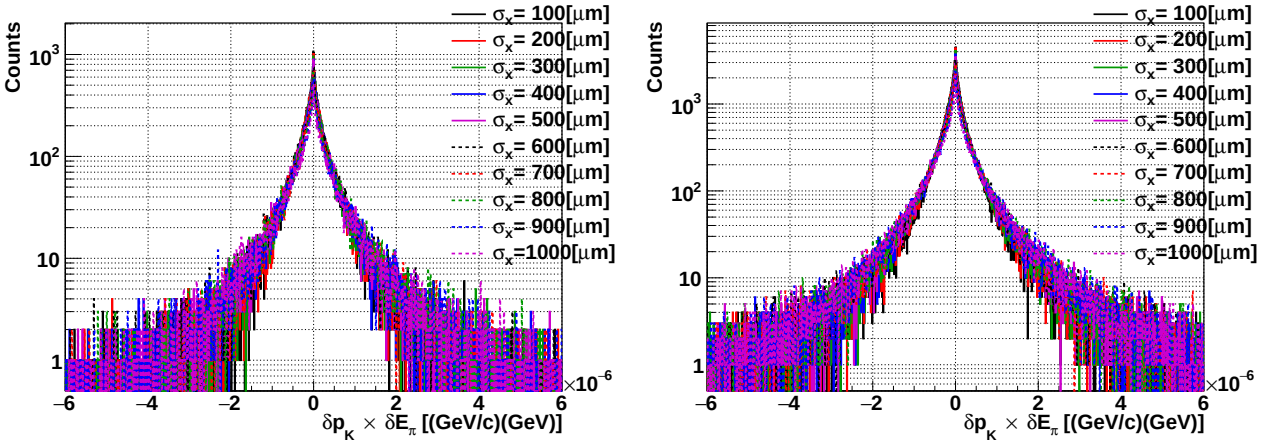

(a) Σ^- (b) Θ^+

Figure A.54.: Product of the deviations δE_π and δp_K (for the case of $\mathrm{cov}(\delta p_\pi, \delta E_\pi) \neq 0$ and $\mathrm{cov}(\delta p_K, \delta E_K) \neq 0$ by definition).

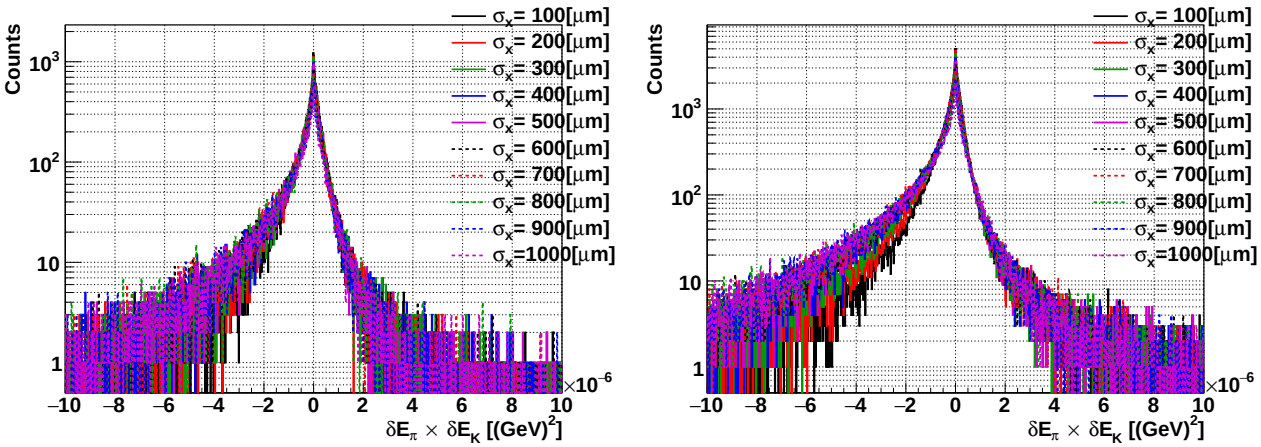

(a) Σ^- (b) Θ^+

Figure A.55.: Product of the deviations δE_π and δE_K (for the case of $\mathrm{cov}(\delta p_\pi, \delta E_\pi) \neq 0$ and $\mathrm{cov}(\delta p_K, \delta E_K) \neq 0$ by definition).

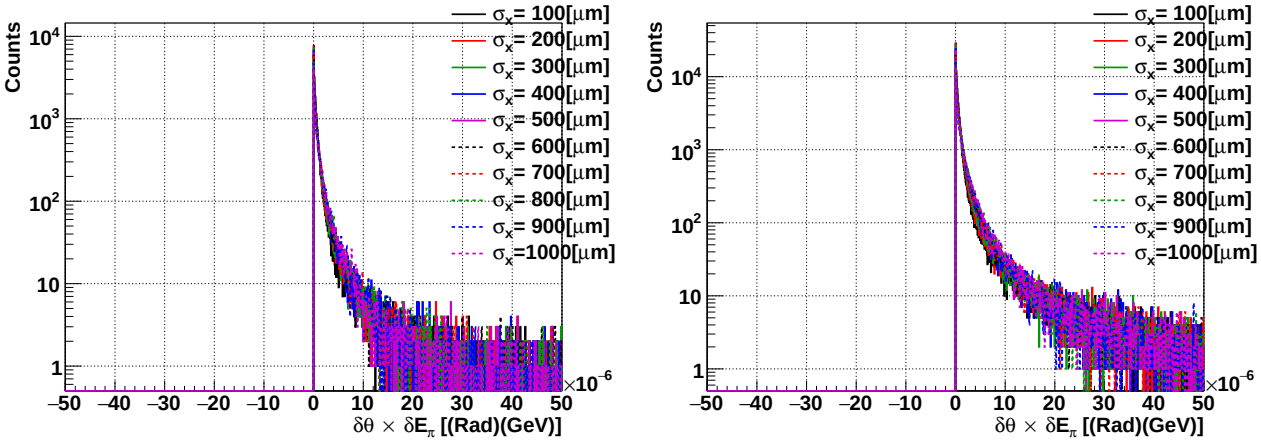

(a) Σ^- (b) Θ^+

Figure A.56.: Product of the deviations δE_π and $\delta\theta$ (for the case of $\mathrm{cov}(\delta p_\pi, \delta E_\pi) \neq 0$ and $\mathrm{cov}(\delta p_K, \delta E_K) \neq 0$ by definition).

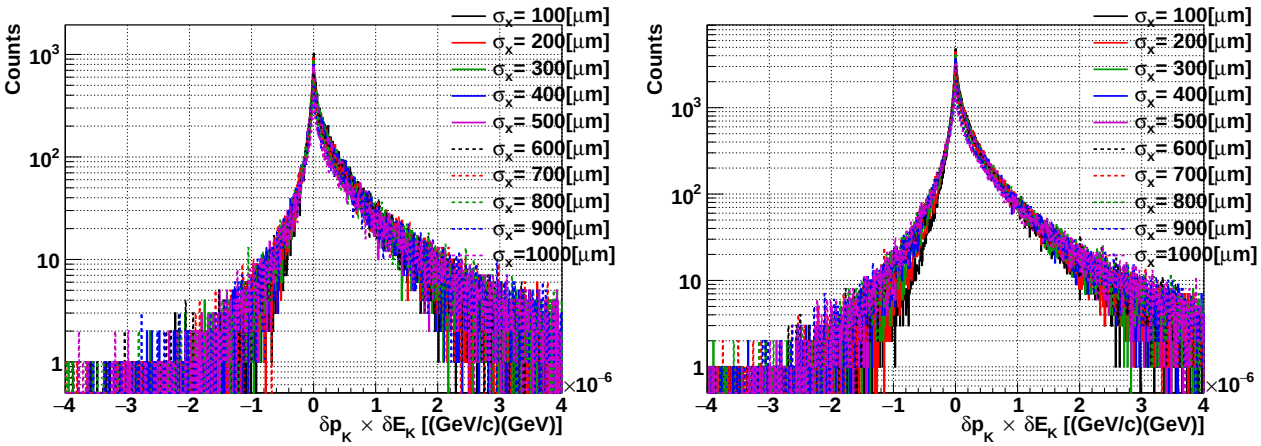

(a) Σ^- (b) Θ^+

Figure A.57.: Product of the deviations δp_K and δE_K (for the case of $\mathrm{cov}(\delta p_\pi, \delta E_\pi) \neq 0$ and $\mathrm{cov}(\delta p_K, \delta E_K) \neq 0$ by definition).

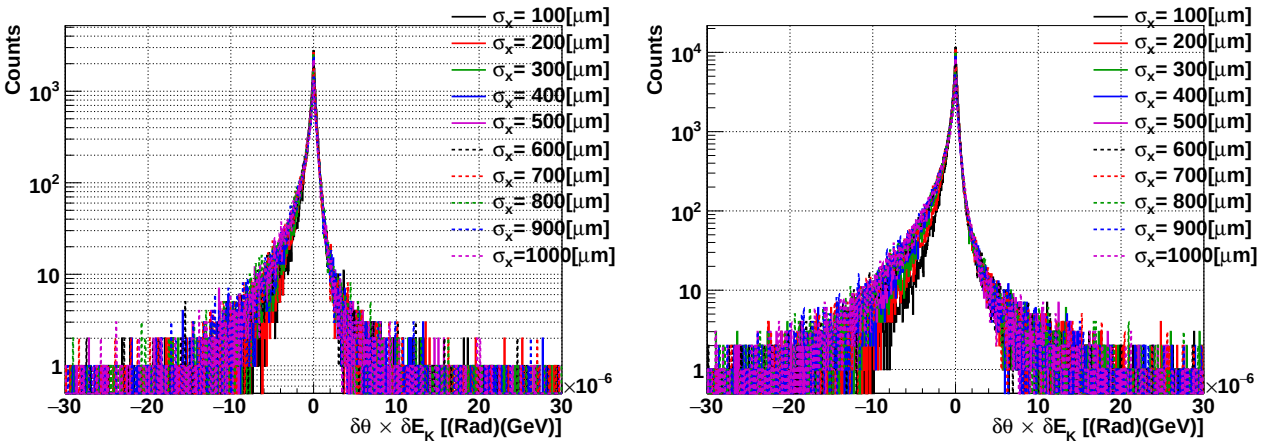

(a) Σ^- (b) Θ^+

Figure A.58.: Product of the deviations δE_K and $\delta\theta$ (for the case of $\mathrm{cov}(\delta p_\pi, \delta E_\pi) \neq 0$ and $\mathrm{cov}(\delta p_K, \delta E_K) \neq 0$ by definition).

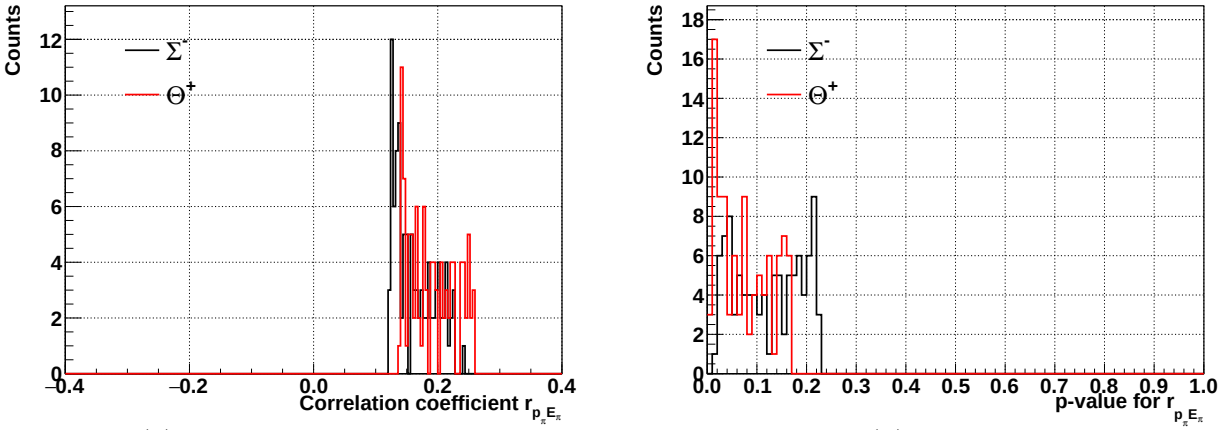

(a) Correlation coefficient (b) $p-$value

Figure A.59.: Correlation coefficient $r_{\delta p_\pi \delta E_\pi}$ (a) and its $p-$value of $t-$distribution (b) (for the case of $\mathrm{cov}(\delta p_\pi, \delta E_\pi) \neq 0$ and $\mathrm{cov}(\delta p_K, \delta E_K) \neq 0$ by definition).

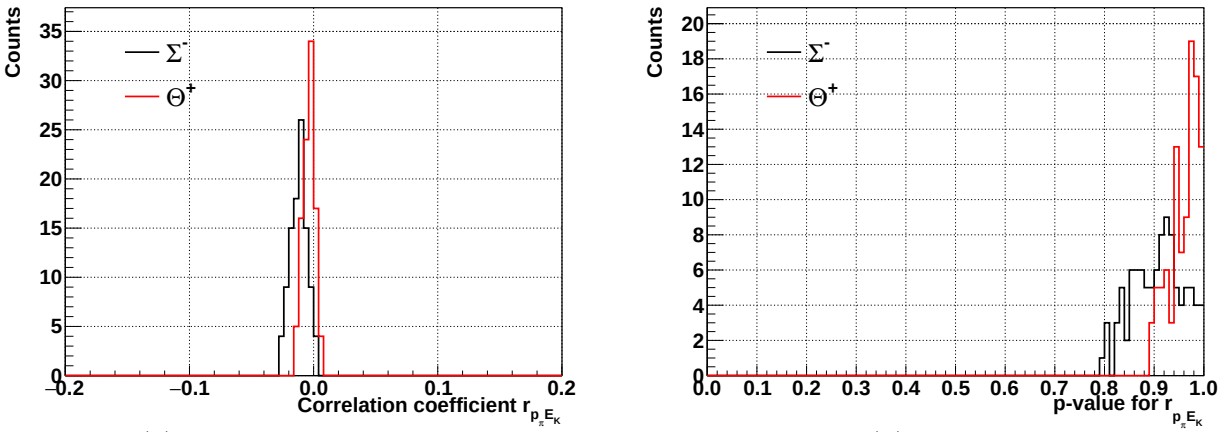

(a) Correlation coefficient (b) $p-$value

Figure A.60.: Correlation coefficient $r_{\delta p_\pi \delta E_K}$ (a) and its $p-$value of $t-$distribution (b) (for the case of $\mathrm{cov}(\delta p_\pi, \delta E_\pi) \neq 0$ and $\mathrm{cov}(\delta p_K, \delta E_K) \neq 0$ by definition).

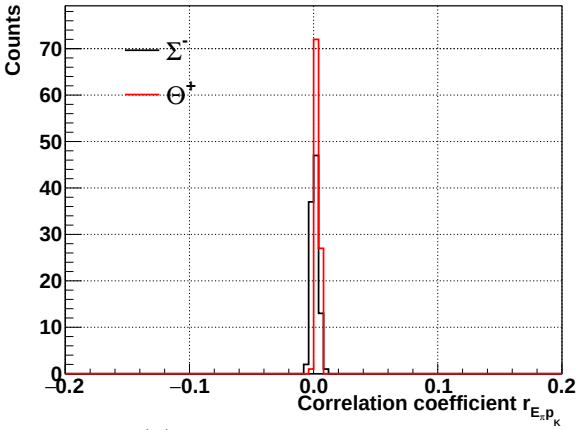

(a) Correlation coefficient

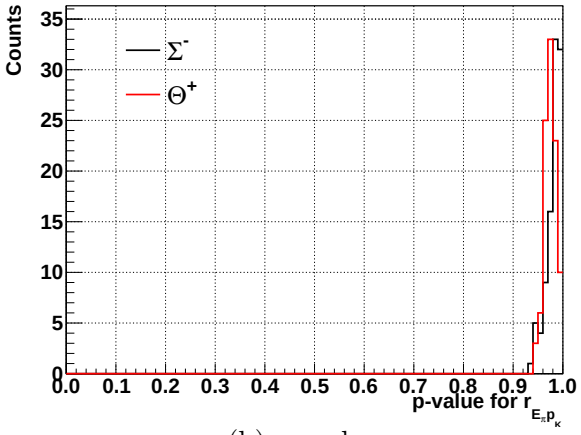

(b) $p-$value

Figure A.61.: Correlation coefficient $r_{\delta E_\pi \delta p_K}$ (a) and its $p-$value of $t-$distribution (b) (for the case of $\mathrm{cov}(\delta p_\pi, \delta E_\pi) \neq 0$ and $\mathrm{cov}(\delta p_K, \delta E_K) \neq 0$ by definition).

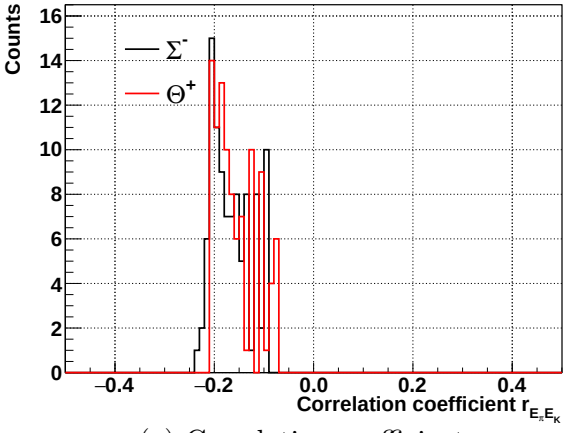

(a) Correlation coefficient

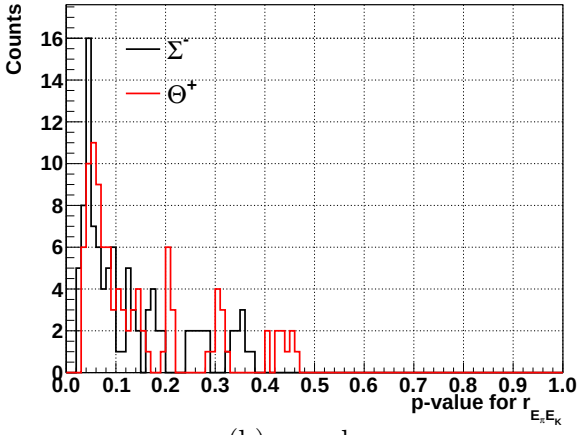

(b) $p-$value

Figure A.62.: Correlation coefficient $r_{\delta E_\pi \delta E_K}$ (a) and its $p-$value of $t-$distribution (b) (for the case of $\mathrm{cov}(\delta p_\pi, \delta E_\pi) \neq 0$ and $\mathrm{cov}(\delta p_K, \delta E_K) \neq 0$ by definition).

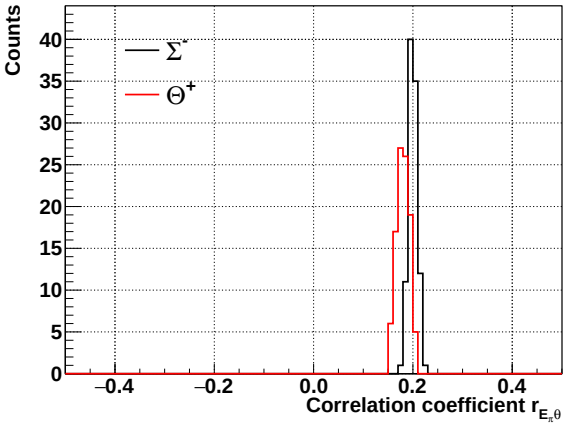

(a) Correlation coefficient

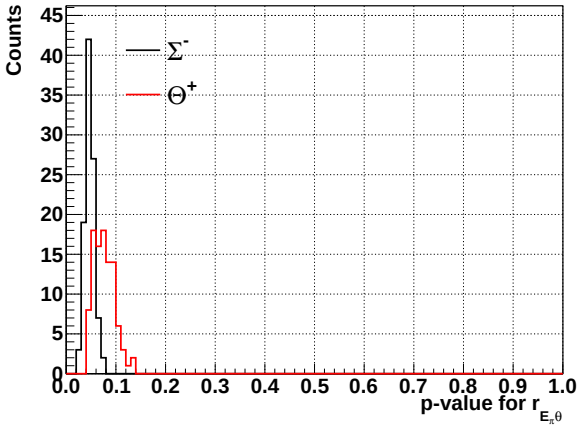

(b) $p-$value

Figure A.63.: Correlation coefficient $r_{\delta E_\pi \delta\theta}$ (a) and its $p-$value of $t-$distribution (b) (for the case of $\mathrm{cov}(\delta p_\pi, \delta E_\pi) \neq 0$ and $\mathrm{cov}(\delta p_K, \delta E_K) \neq 0$ by definition).

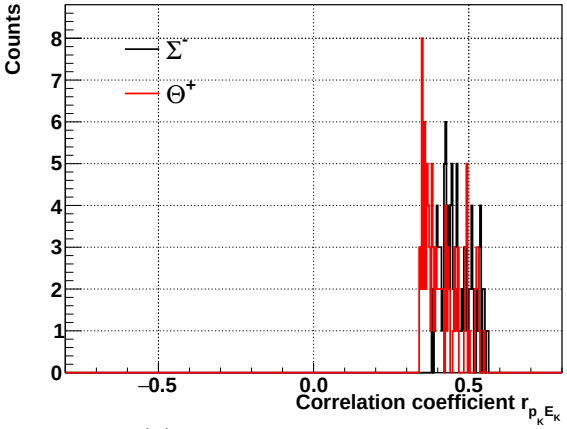

(a) Correlation coefficient

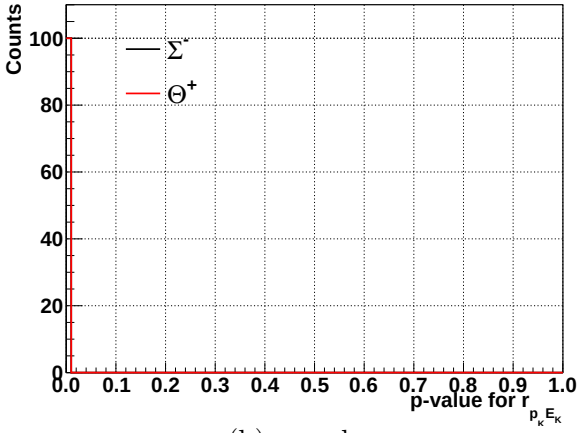

(b) $p-$value

Figure A.64.: Correlation coefficient $r_{\delta p_K \delta E_K}$ (a) and its $p-$value of $t-$distribution (b) (for the case of $\mathrm{cov}(\delta p_\pi, \delta E_\pi) \neq 0$ and $\mathrm{cov}(\delta p_K, \delta E_K) \neq 0$ by definition).

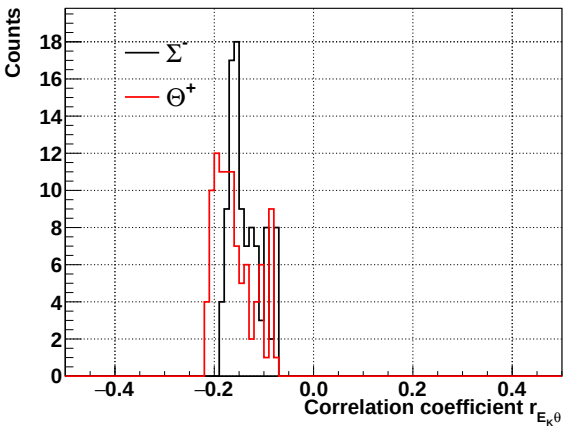

(a) Correlation coefficient

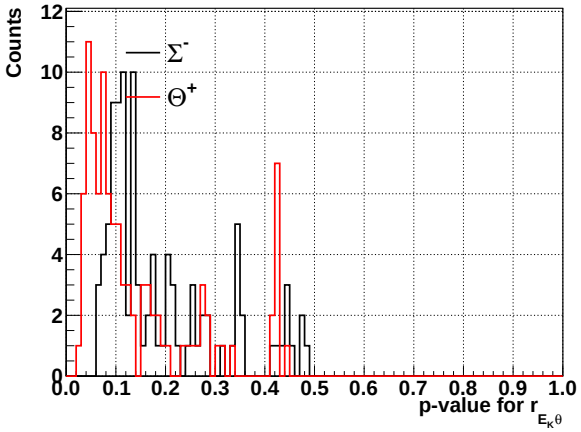

(b) $p-$value

Figure A.65.: Correlation coefficient $r_{\delta E_K \delta\theta}$ (a) and its $p-$value of $t-$distribution (b) (for the case of $\mathrm{cov}(\delta p_\pi, \delta E_\pi) \neq 0$ and $\mathrm{cov}(\delta p_K, \delta E_K) \neq 0$ by definition).

the correlation coefficients and $p-$values are displayed in Figs. A.43–A.44, A.45–A.51, A.52–A.58, A. 59–A.65, respectively. In addition to the error correlations between δE_π and δE_K, and $\delta E_{\pi(K)}$ and $\delta\theta$, the correlations between $\delta p_{\pi(K)}$ and $\delta E_{\pi(K)}$, are clearly seen in Figs. A.45, A.50, A.59 and A.64, as expected.

Figures A.66–A.67 show the difference of the missing mass resolution for the second definition of $\delta E_{\pi(K)}$. The second definition of $\delta E_{\pi(K)}$ reproduces the width of the Monte Carlo result better than that of the first definition as shown in Fig. A.66. The difference between the mass resolution with and without correlation are $\sim$0.20 MeV/c^2 for Σ^- and $\sim$0.17 MeV/c^2 for Θ^+, respectively.

In the experimental data analysis (Sec. 3.9), the effect of correlation was ignored and the resolutions of the momenta was determined so as to reproduce the mass resolution of the Σ hyperons (and the beam-through data). It can be interpreted as that the contribution of the correlation terms was incorporated into the momentum resolutions, which caused the momentum resolutions worse than the designed values.

A.3. Summary

Based on the Monte Carlo simulation, the contribution of correlation terms in the error propagation of the mass resolution estimation was studied. There were non-zero correlations between the error of scattering angle and the energy loss straggling, and between the energy loss stragglings of the beam and scattered particles. The contributions of correlation to the missing mass resolution were $\sim$ 0.20 MeV/c^2 for Σ^- and $\sim$0.17 MeV/c^2 for Θ^+, respectively. The difference was taken into account as a systematic error in the present analysis (Sec. 3.9).

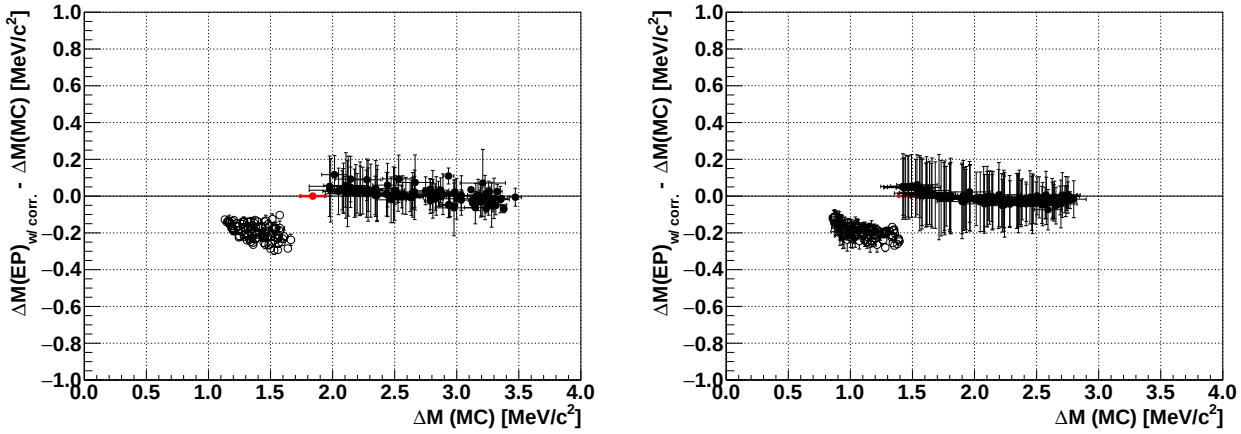

(a) Σ^- (b) Θ^+

Figure A.66.: Difference of the missing mass resolution (FWHM) between the width of the Monte Carlo result (MC) and the estimation by the error propagation (EP) with correlation terms (for the case of $\mathrm{cov}(\delta p_\pi, \delta E_\pi) \neq 0$ and $\mathrm{cov}(\delta p_K, \delta E_K) \neq 0$ by definition). (Open circles) : Without energy loss. (Filled circles) : With energy loss. The mass resolution for the experimental data is also shown as a red point. The error bar of the experimental data represents the sum of the statistic and systematic ones.

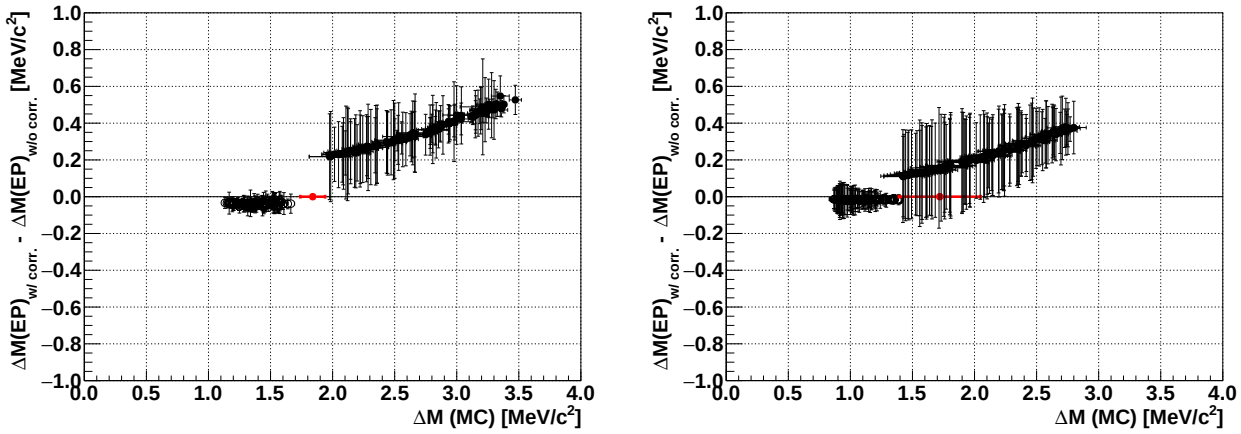

(a) Σ^- (b) Θ^+

Figure A.67.: Comparison between the missing mass resolution estimated with correlation and without correlation (for the case of $\mathrm{cov}(\delta p_\pi, \delta E_\pi) \neq 0$ and $\mathrm{cov}(\delta p_K, \delta E_K) \neq 0$ by definition). (Open circles) : Without energy loss. (Filled circles) : With energy loss. The mass resolution for the experimental data is also shown as a red point. The error bar of the experimental data represents the sum of the statistic and systematic ones.

B. Contribution of a calibration error to the missing mass resolution

An effect of the uncertainty of the absolute scale of the momentum to the missing mass resolution was evaluated by a Monte Carlo simulation. First, $\Sigma^-(1197.449\ \mathrm{MeV}/c^2)$ or $\Theta^+(1540\ \mathrm{MeV}/c^2)$ were generated with a zero decay width in the $p(\pi, K)$ reaction. Second, a magnitude of the momentum of π and/or K was shifted, whereas the directions of the momenta were not changed from the generated ones. The introduced momentum shifts, δp_π and δp_K, were varied with 1 MeV/c per step in range of -15 to +15 MeV/c and -12 to +12 MeV/c, respectively. Then, the missing mass calculation was performed with the shifted momenta. Finally, only contribution from errors of a momentum offset correction to the width broadening was examined.

Figures B.1,B.2 display examples of the mass shift distribution for Σ^- and Θ^+, respectively. The shift of the momentum causes not only a shift of the mean value of the missing mass but also a tail of the distribution. The FWHM was computed for each histogram. Figures B.3(a) and (b) show the width broadening due to the momentum shift for Σ^- and Θ^+ productions, respectively. The contributions were found to be $0.15\pm0.04\ \mathrm{MeV}/c^2$ and $0.18\pm0.07\ \mathrm{MeV}/c^2$, respectively. These values were smaller by an order of magnitude compared with the missing mass resolution. Therefore, they were regarded as having negligible impact on the mass resolution and peak search.

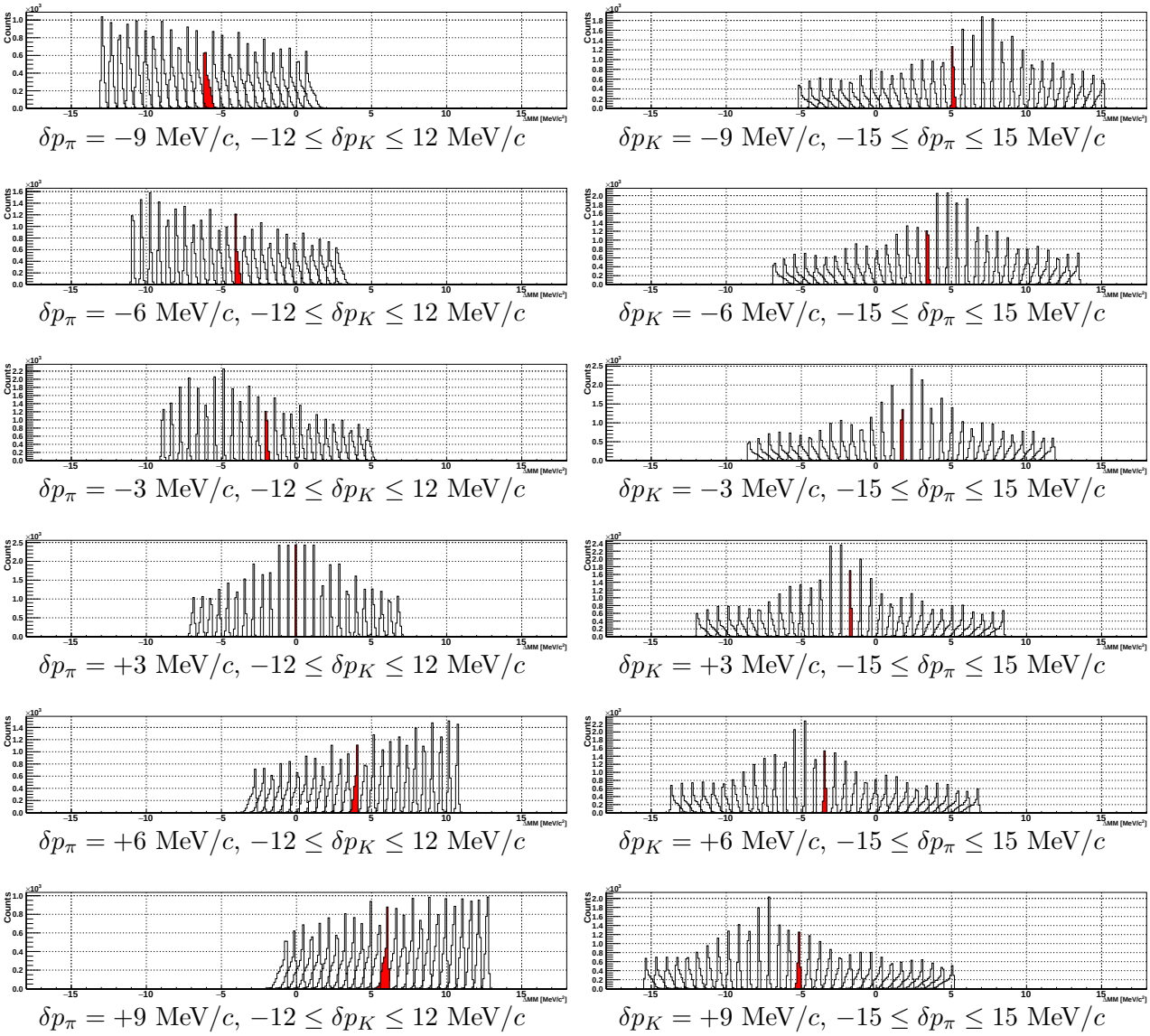

Figure B.1.: Missing mass spectra deformed by the momentum shift dp_π and dp_K (Σ^-). The horizontal axes is a mass shift from 1197.449 MeV/c^2. (Left) δp_π is fixed at the denoted value and δp_K is varied with 1 MeV/c per step. The case of $\delta p_K = 0$ is filled with red color as a guide. (Right) δp_K is fixed at the denoted value and δp_π is varied with 1 MeV/c per step. The case of $\delta p_\pi = 0$ is filled with red color as a guide.

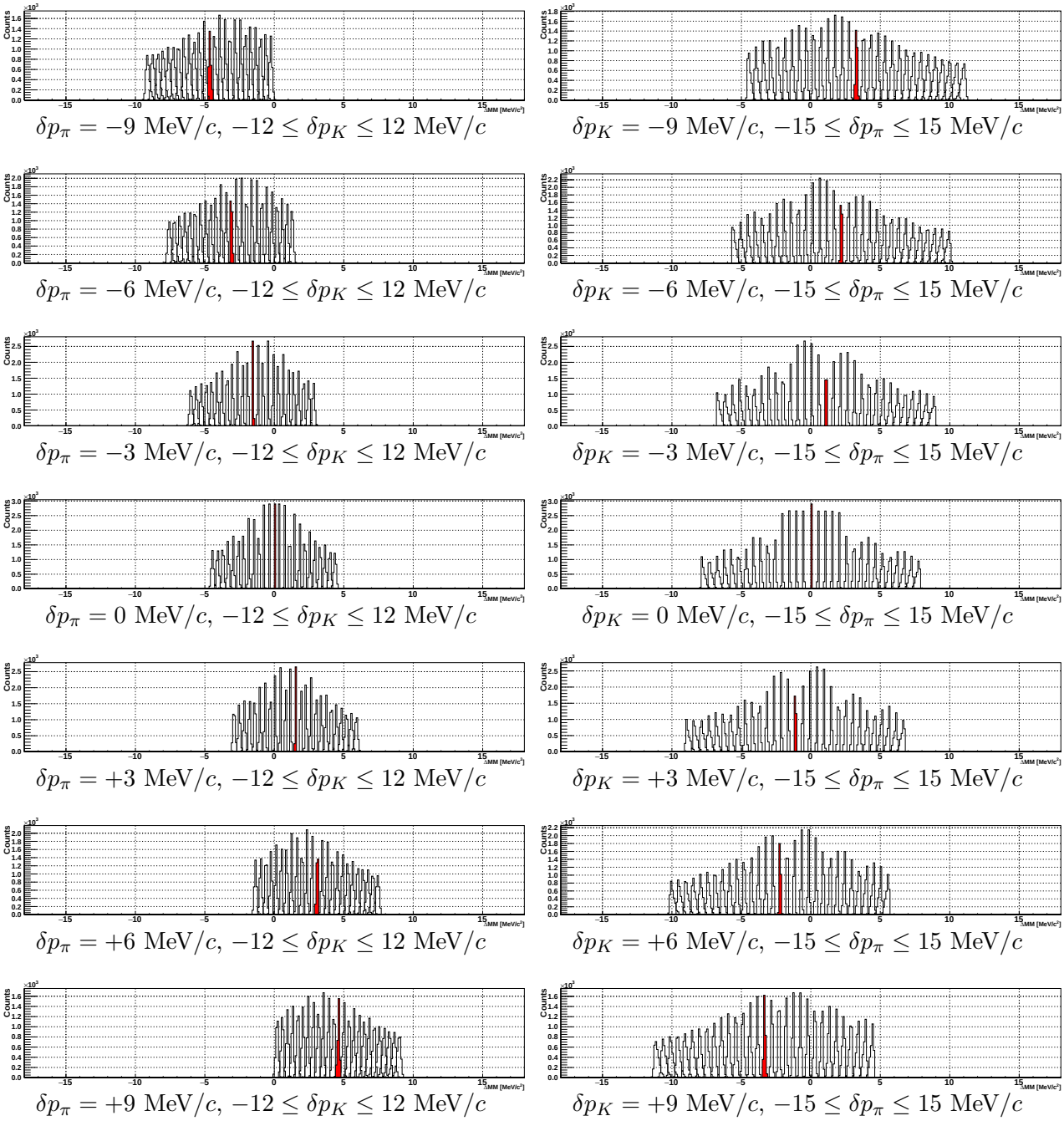

Figure B.2.: Missing mass spectra deformed by the momentum shift dp_π and dp_K (Θ^+). The horizontal axes mean a mass shift from 1540 MeV/c^2. (Left) δp_π is fixed at the denoted value and δp_K is varied with 1 MeV/c per step. The case of $\delta p_K = 0$ is filled with red color as a guide. (Right) δp_K is fixed at the denoted value and δp_π is varied with 1 MeV/c per step. The case of $\delta p_\pi = 0$ is filled with red color as a guide.

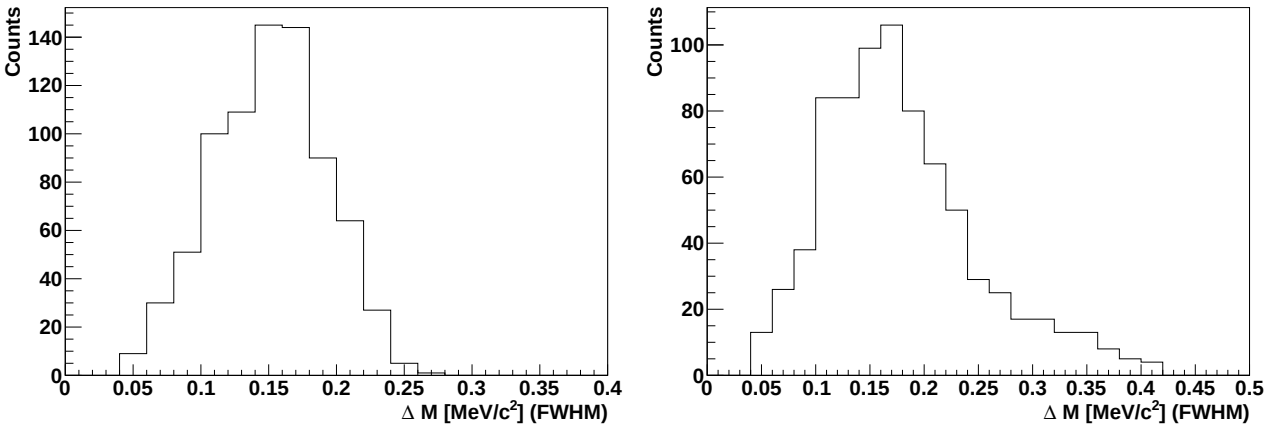

(a) Σ^- production. (b) Θ^+ production.

Figure B.3.: Width broadening due to the momentum shift for Σ^- production (a) and Θ^+ production (b).

C. Difference between the present analysis and the published paper

The difference between the present analysis and the published paper [99] is described in this chapter.

The missing mass spectra before the efficiency and acceptance correction are displayed in Fig. C. 1(a). The scattering-angle range of 2° to 15° was chosen for the present analysis to be compared with [99]. The black and red points are obtained by the present analysis and [99], respectively. Figure C.1(b) shows the normalized missing mass spectra, where the data points were normalized so as to a integral becomes unity. The two plots were overlapped within the error bars. After the efficiency and acceptance correction, however, there was the difference between the results of the two analysis as shown in Fig. C.4(a).

There are two main reasons. The first is the systematic difference of an acceptance table for the outgoing particles. In the present experiment, some of the outgoing particles hit on PMTs of the ACs and their magnetic shield cases. In order to eliminate those events easily in the efficiency correction, the corresponding segments of the TOF and LC were not used in the data taking and offline analysis. Therefore the acceptance table and solid angle should be calculated considering the condition, which are shown in Figs. 3.30 and 3.31, respectively. In the published paper, on the other hand, the acceptance table and solid angle were calculated with all of the TOF and LC segments, which is shown in Figs. C. 2 and C.3, respectively. The present analysis takes into account the effect of events hitting the outside sensitive area of the ACs correctly, compared with the previous analysis. The second reason is the systematic uncertainty of the efficiency evaluation of the SDC3–4 tracking. In Sec.3.4.5, the SDC3–4 tracking efficiency was evaluated with outgoing proton tracks. The efficiency estimated with outgoing pion tracks was found to be higher by ∼8 %, which is thought to be an uncertainty of the tracking efficiency.

Figure C.4 shows those systematic effects on the Θ^+ differential cross section. In all of the panels, the black plot shows the result published in [99]. The colored plots indicate the differential cross section with the acceptance used in the present analysis and the lower SDC3-4 tracking efficiency (Fig C.4 (a)), with the acceptance used in the present analysis and the higher SDC3-4 tracking efficiency (Fig C.4 (b)), with the acceptance used in [99] and the lower SDC3-4 tracking efficiency (Fig C.4 (c)) and with the acceptance used in [99] and the higher SDC3-4 tracking efficiency (Fig C.4 (d)), respectively. The present analysis agreed with [99] within the error bars as shown in Fig. C.4(d), if the same acceptance and tracking efficiency used. Therefore the difference of the present result and [99] can be explained by the systematic treatment of the data and the most conservative result (red points in Fig. C.4(a)) was adopted in the present analysis.

To compare the measured upper limits, the peak search was performed in the same scattered-angle region as that of the previous analysis. Examples of the peak search in the mass spectra, the upper limits on the Θ^+ production cross section and Θ^+ decay width for spin 1/2 cases with the scattering-

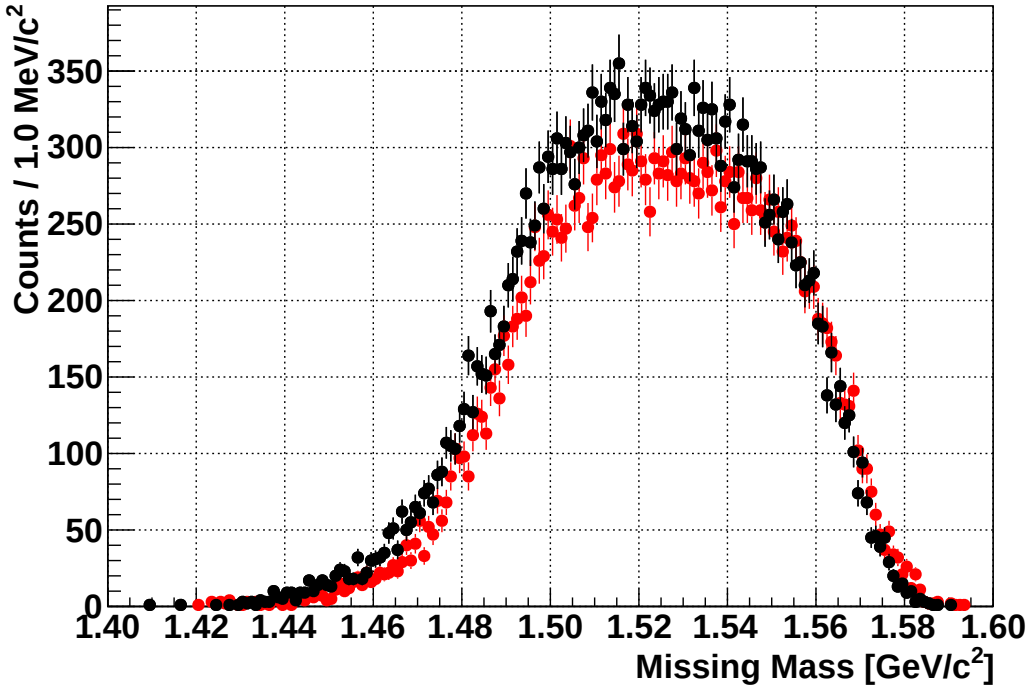

(a) Missing mass spectra of the present and previous analysis [99]

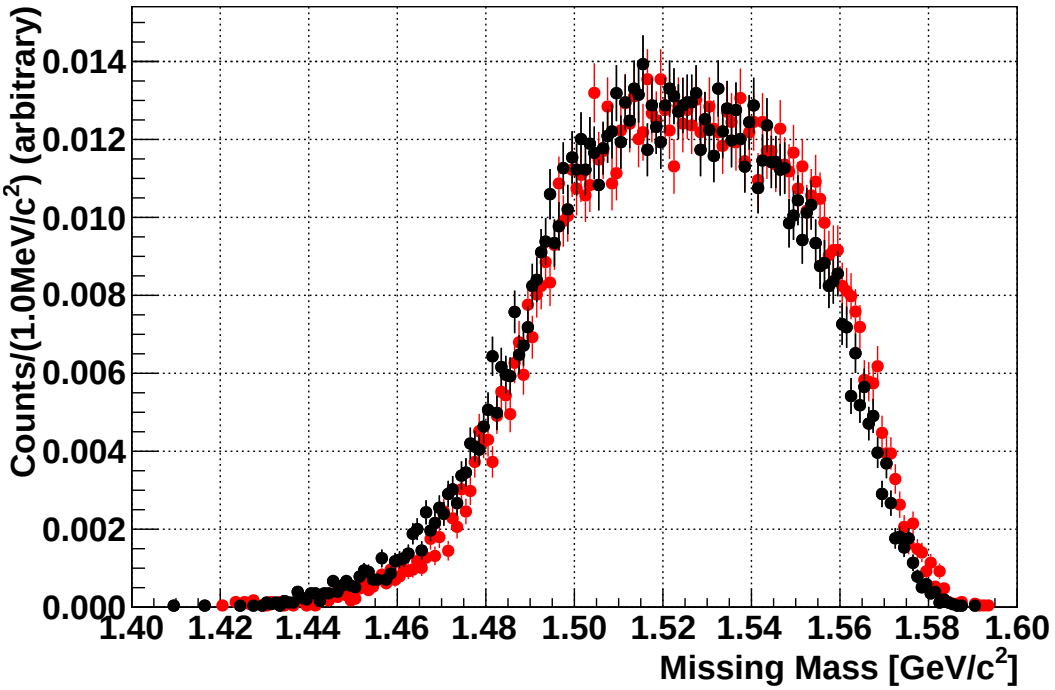

(b) Normalized missing mass spectra of the present and previous analysis [99]. The integral of each spectrum was normalized to 1.

Figure C.1.: Missing mass spectra obtained by the present analysis (black) and the literature [99] (red). The acceptance and efficiency corrections were not applied. (b) Normalized spectra whose integral is unity.

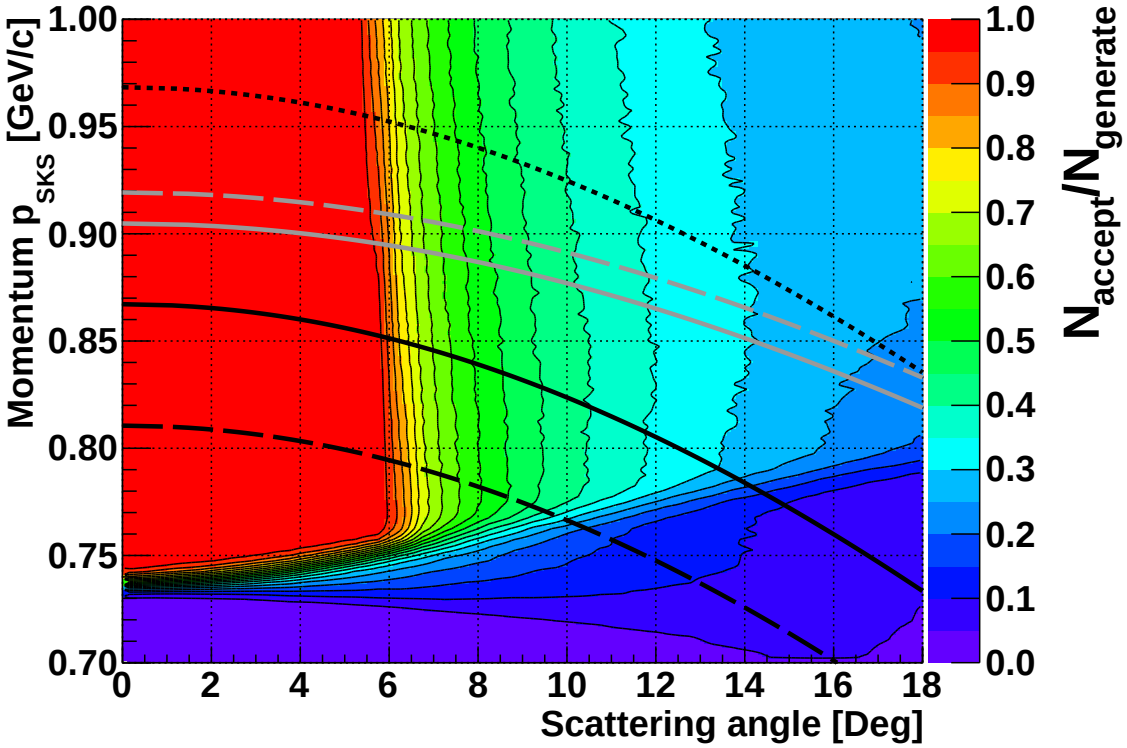

Figure C.2.: An acceptance of SKS with all segments of TOF and LC (used in [99]). The black dotted, solid and dashed lines correspond to the kinematics of the $\pi^- p \to K^- \Theta^+$ reaction at $p_\pi = 1.92$ GeV/c with the Θ^+ masses of 1500, 1540 and 1560 MeV/c^2, respectively. The gray dashed and solid lines correspond to the kinematics of the $\pi^+ p \to K^+ \Sigma^+$ and $\pi^- p \to K^+ \Sigma^-$ reactions at $p_\pi = 1.37$ GeV/c, respectively.

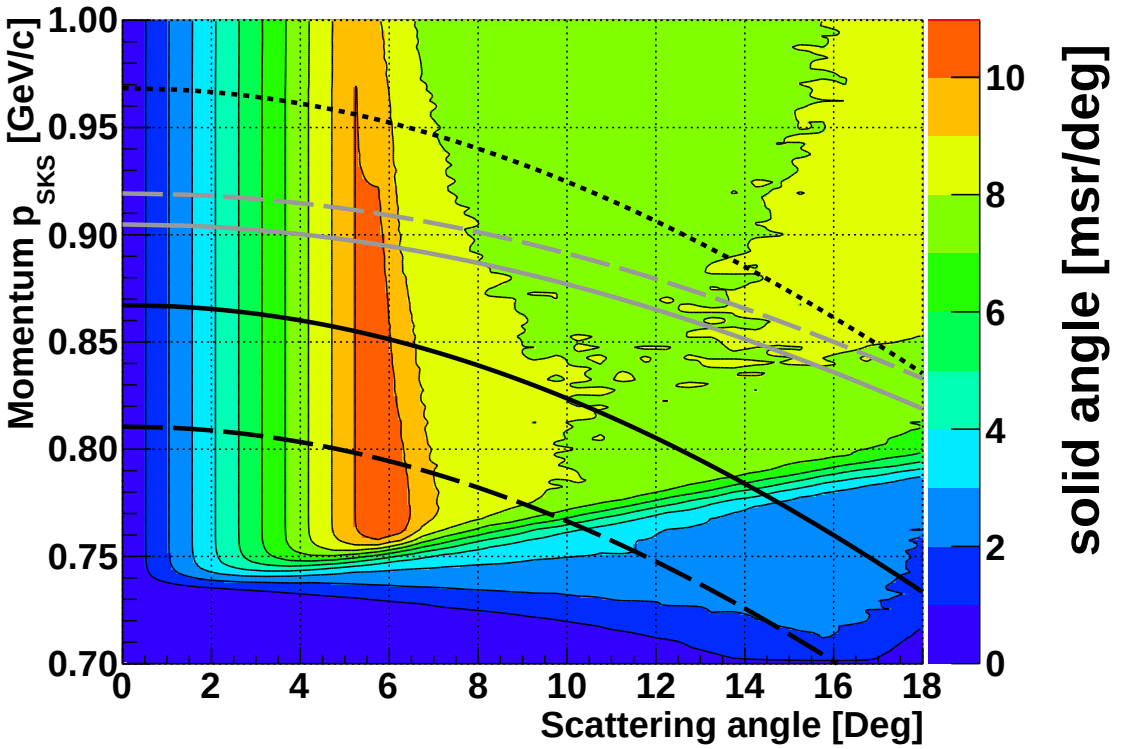

Figure C.3.: A solid angle of SKS with all segments of TOF and LC (used in [99]). The black dotted, solid and dashed lines correspond to the kinematics of the $\pi^- p \to K^- \Theta^+$ reaction at $p_\pi = 1.92$ GeV/c with the Θ^+ masses of 1500, 1540 and 1560 MeV/c^2, respectively. The gray dashed and solid lines correspond to the kinematics of the $\pi^+ p \to K^+ \Sigma^+$ and $\pi^- p \to K^+ \Sigma^-$ reactions at $p_\pi = 1.37$ GeV/c, respectively.

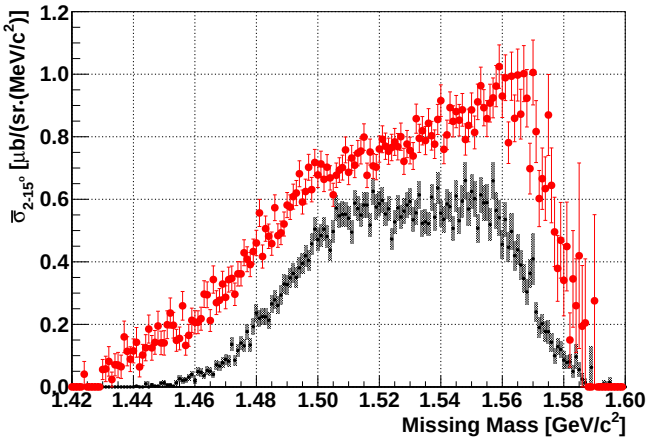

(a) acceptance: with TOF, LC cut.
SDC34 tracking: bad efficiency

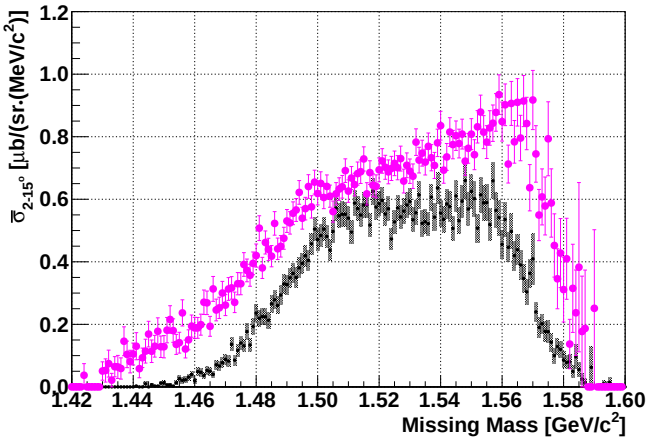

(b) acceptance: with TOF, LC cut.
SDC34 tracking: good efficiency

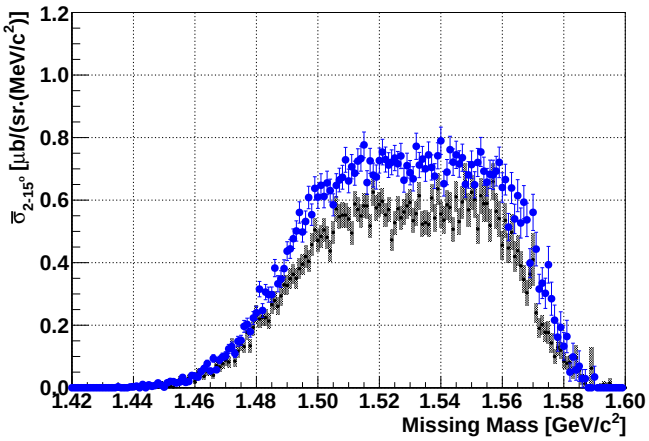

(c) acceptance: all TOF, LC segments.
SDC34 tracking: bad efficiency

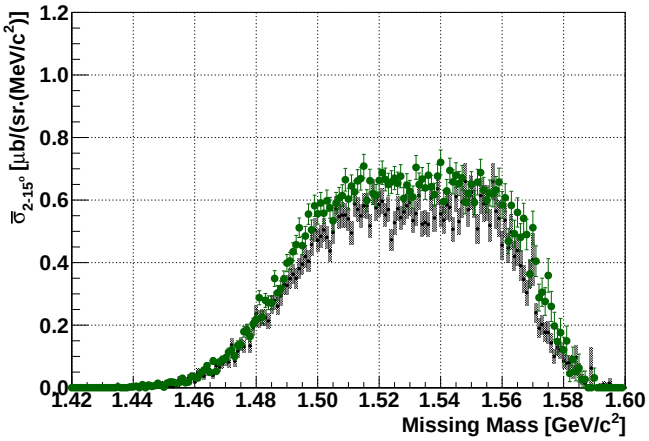

(d) acceptance: all TOF, LC segments.
SDC34 tracking: good efficiency

Figure C.4.: Systematic effects of the acceptance table and the SDC34 tracking efficiency on the differential cross section of the Θ^+ production. The Black plot shows the data published in [99]. The error bars are statistical only.

angle range of 2° to 15° were presented in Figs. C.5, C.6 and C.7, respectively. The systematic error between the results of $2° \leq \theta \leq 18°$ and $2° \leq \theta \leq 15°$ was less than 2%.

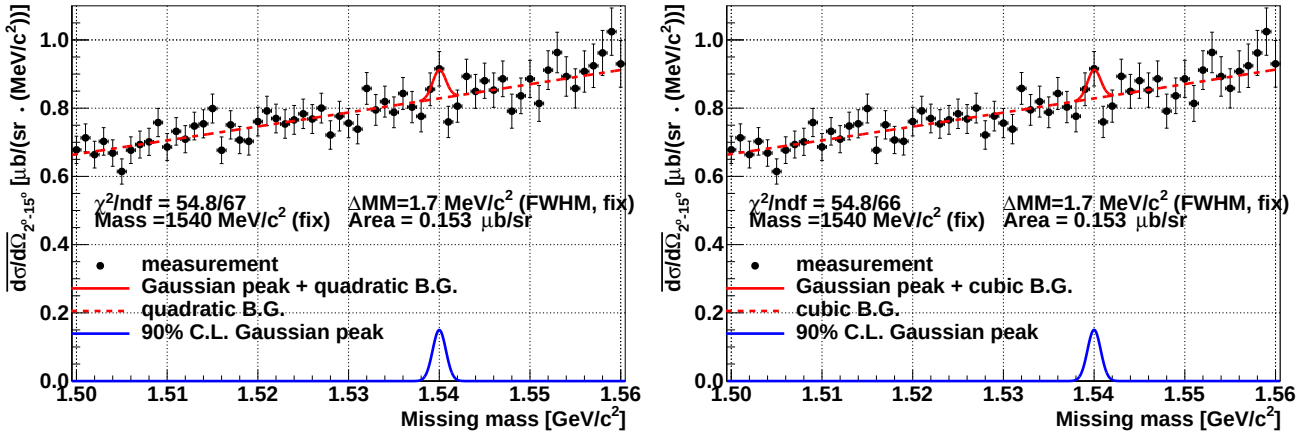

(a) 2nd order polynomial background. (b) 3rd order polynomial background.

Figure C.5.: The missing mass spectrum of the $\pi^- p \to K^- X$ reaction with one of the fitting results (averaged over 2° to 15°). The fit function composed of a Gaussian peak shape with the fixed width of the mass resolution of 1.7 MeV/c^2 FWHM (red solid curve) and polynomial functions as a background shape (red dotted curve). The peak with the 90% confidence level upper limit is shown together (blue solid).

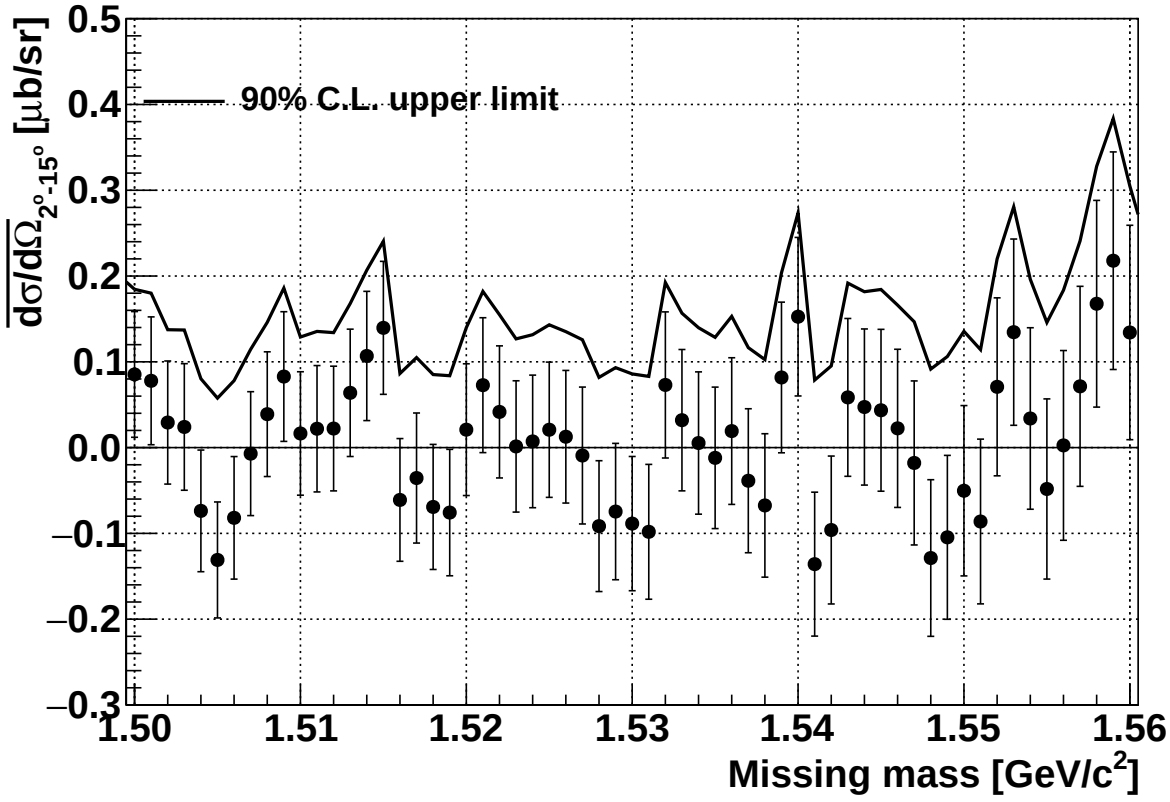

Figure C.6.: The 90% confidence level upper limit of the differential cross section of the $\pi^- p \to K^- \Theta^+$ reaction in the laboratory frame (averaged over $2^\circ \leq \theta \leq 15^\circ$).

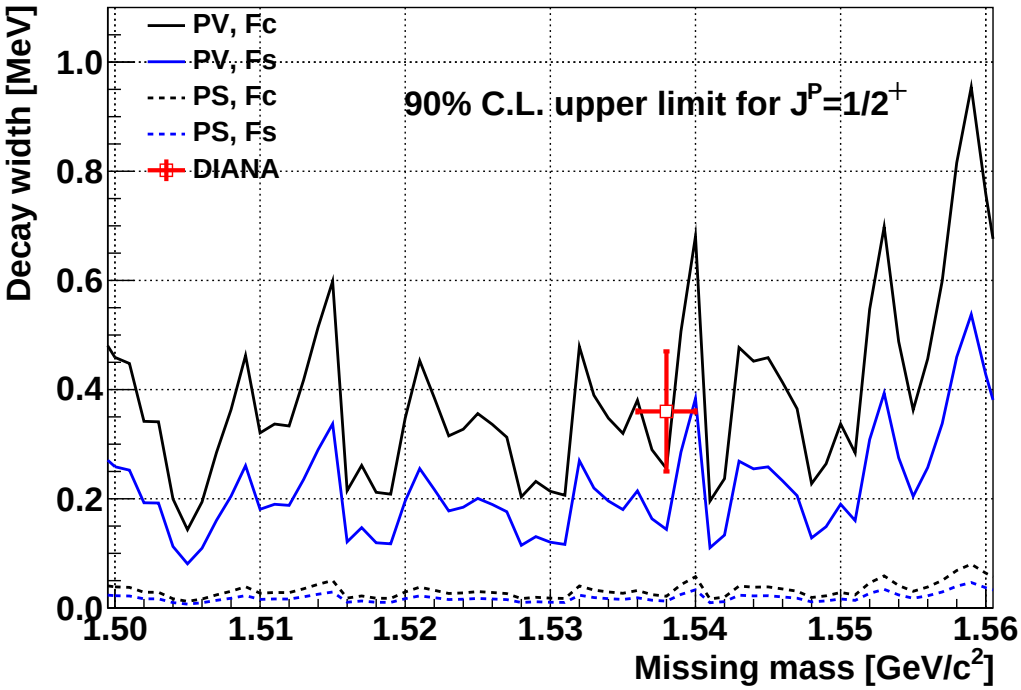

(a) $J^P = 1/2^+$ case.

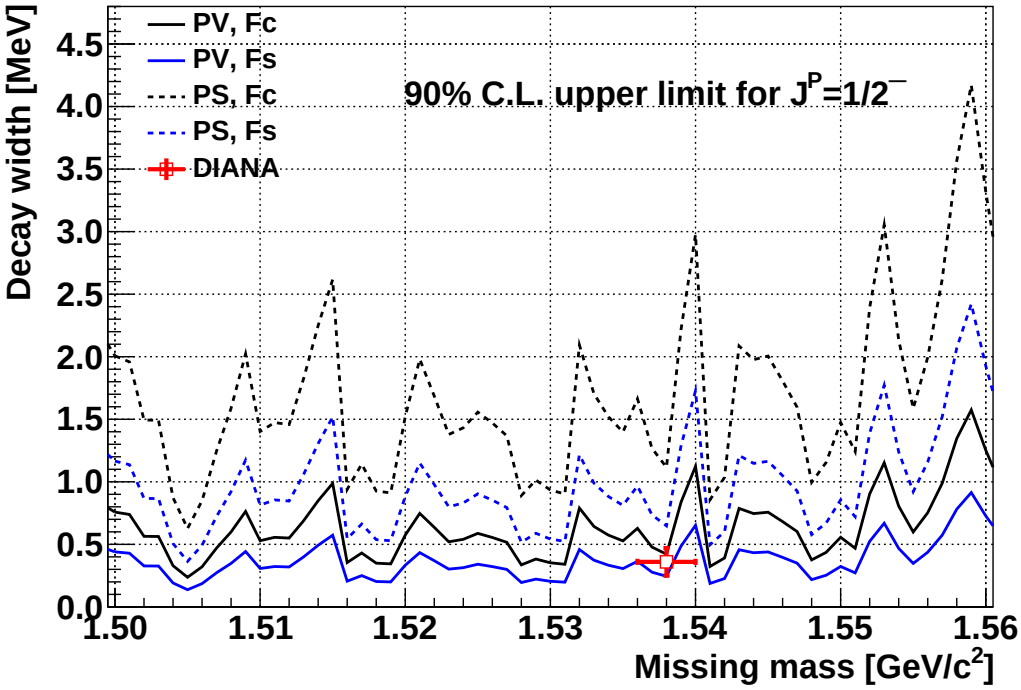

(b) $J^P = 1/2^-$ case.

Figure C.7.: The 90% confidence level upper limit of the Θ^+ decay width (averaged over $2° \leq \theta \leq 15°$). The value in the latest report from DIANA is also shown.